

AD _____

Award Number: W81XWH-10-1-0767

TITLE: A Partnership Training Program: Studying Targeted Drug Delivery
Using Nanoparticles in Breast Cancer Diagnosis and Therapy

PRINCIPAL INVESTIGATOR: Paul C. Wang, Ph.D.

CONTRACTING ORGANIZATION: Howard University
Washington, DC 20059

REPORT DATE: October 2013

TYPE OF REPORT: Revised Annual Summary

PREPARED FOR: U.S. Army Medical Research and Materiel Command
Fort Detrick, Maryland 21702-5012

DISTRIBUTION STATEMENT:

Approved for public release; distribution unlimited

The views, opinions and/or findings contained in this report are those of the author(s) and should not be construed as an official Department of the Army position, policy or decision unless so designated by other documentation.

REPORT DOCUMENTATION PAGE			Form Approved OMB No. 0704-0188		
Public reporting burden for this collection of information is estimated to average 1 hour per response, including the time for reviewing instructions, searching existing data sources, gathering and maintaining the data needed, and completing and reviewing this collection of information. Send comments regarding this burden estimate or any other aspect of this collection of information, including suggestions for reducing this burden to Department of Defense, Washington Headquarters Services, Directorate for Information Operations and Reports (0704-0188), 1215 Jefferson Davis Highway, Suite 1204, Arlington, VA 22202-4302. Respondents should be aware that notwithstanding any other provision of law, no person shall be subject to any penalty for failing to comply with a collection of information if it does not display a currently valid OMB control number. PLEASE DO NOT RETURN YOUR FORM TO THE ABOVE ADDRESS.					
1. REPORT DATE (DD-MM-YYYY) October 2013		2. REPORT TYPE Revised Annual Summary		3. DATES COVERED (From - To) 15 Sep 2012 - 14 Sep 2013	
4. TITLE AND SUBTITLE A Partnership Training Program: Studying Targeted Drug Delivery Using Nanoparticles in Breast Cancer Diagnostics and Therapy			5a. CONTRACT NUMBER		
			5b. GRANT NUMBER W81XWH-10-1-0767		
			5c. PROGRAM ELEMENT NUMBER		
6. AUTHOR(S) Paul C. Wang, Ph.D. Email: pwang@howard.edu			5d. PROJECT NUMBER		
			5e. TASK NUMBER		
			5f. WORK UNIT NUMBER		
7. PERFORMING ORGANIZATION NAME(S) AND ADDRESS(ES) Howard University Washington, DC 20059			8. PERFORMING ORGANIZATION REPORT NUMBER		
9. SPONSORING / MONITORING AGENCY NAME(S) AND ADDRESS(ES) U.S. Army Medical Research and Materiel Command Fort Detrick, Maryland 21702-5012			10. SPONSOR/MONITOR'S ACRONYM(S)		
			11. SPONSOR/MONITOR'S REPORT NUMBER(S)		
12. DISTRIBUTION / AVAILABILITY STATEMENT Approved for public release; distribution unlimited					
13. SUPPLEMENTARY NOTES					
14. ABSTRACT In the third year of this training grant, 10 faculty members, 5 postdocs, 9 graduate and 3 undergraduate students from 7 departments at the Howard University have been trained in the use of nanoparticles as targeted drug delivery vehicles for cancer diagnosis and therapy. Twelve seminars and workshops in cancer, molecular imaging, and nanomedicine have been offered. The trainees have received hands-on training in MRI, optical imaging, cell biology lab techniques, and small animal handling. The two research projects have progressed well. We have shown that the targeted nanocomplex, Tf-Lip-Mag significantly enhanced the MRI signals in MDA-MB-231 breast cancer tumors in mice. The image enhancement patterns are well correlated with histology, and could be used to evaluate tumor pathology in vivo. We have generated a bivalent single-chain variable fragment (scFv) recombinant immunotoxin, A-dmDT390-scFvDb(PSMA) with J591 antibody, against extracellular domain of PSMA in tumor epithelial cells in animal model. We published reviews on development, characterization and applications of nanoparticle in cancer imaging and therapy. We have published 8 papers and submitted 6 grant applications. There are 15 research projects utilizing the facility of the Nanomedicine Core. The Core has become a synergy center, drawing multidisciplinary research using nanotechnology for cancer research.					
15. SUBJECT TERMS training, nanotechnology, breast cancer, diagnosis, therapy, imaging, drug delivery					
16. SECURITY CLASSIFICATION OF:			17. LIMITATION OF ABSTRACT Unlimited	18. NUMBER OF PAGES 116	19a. NAME OF RESPONSIBLE PERSON
a. REPORT	b. ABSTRACT	c. THIS PAGE			19b. TELEPHONE NUMBER (include area code)

Table of Contents

	<u>Page</u>
Cover.....	1
SF 298.....	2
Table of Contents.....	3
Introduction.....	4
Body.....	4
Key Research Accomplishments.....	15
Reportable Outcomes.....	15
Conclusion.....	17
References.....	19
Appendices.....	21

A Partnership Training Program – Studying Targeted Drug Delivery Nanoparticles in Breast Cancer Diagnosis and Therapy

I. INTRODUCTION

In this program, we proposed to establish a Nanomedicine Core to train faculty and students at Howard University to pursue molecular imaging of breast cancer using nanoparticles as targeted drug delivery vehicles. This is a partnership with the Johns Hopkins University In Vivo Cellular Molecular Imaging Center and the Nanotechnology Characterization Lab at NCI-Frederick. At Howard University, this partnership involves a multidisciplinary consortium of four departments: Radiology, Radiation Oncology, Molecular Biology and Biochemistry, and Electrical Engineering. The program has two components, a research component and a broad training component. The Howard University trainees will obtain training through collaborative research and by participation in a broad based training program. Renowned experts in nanomedicine and molecular imaging will participate in the training through mentoring research, seminars, workshops, and by offering laboratory internships. This transfer of nanomedicine techniques will support ongoing, long-term breast cancer research at Howard University. The major goal is to provide faculty trainees and their students at Howard with updated nanomedicine techniques to apply to independent breast cancer research, thus enhancing their ability to educate the next generation of scientists. The program objectives are:

1. Train new researchers in breast cancer using modern nanomedicine techniques.
2. Offer lectures, seminars, workshops, and laboratory internships in nanotechnology and molecular imaging.
3. Conduct two proposed research projects.
4. Establish a Nanomedicine Core to support long-term sustainable research.
5. Research concept development and submission of competitive grants in breast cancer imaging.

II. BODY

Molecular imaging and functional MRI continue to provide new insights into the etiology, diagnosis, and treatment of breast cancer. In clinic, these methods have made a significant impact in breast cancer diagnosis and in monitoring response to therapy. As our understanding of breast cancer advances, we further recognize the complexities of this disease and the urgent need for individualized characterization and treatment. Recent exciting advances in the application of MR methods for breast cancer research have resulted from the development of contrast agents (CAs) that generate receptor-targeted or molecular-targeted contrast. Targeted CAs can be directed to cell surface receptors using antibodies [1, 2] or ‘smart’ agents activated by specific enzymes, or based on the expression of detectable reporters [3, 4]. These molecular imaging capabilities, in combination with the strong functional imaging capabilities of MR methods, allow molecular-functional characterization of cancer and the physiological microenvironment of tumors [5]. Non-invasive MR can play an important role in the molecular-functional characterization of breast cancer for detection, drug delivery, development of therapeutics, and monitoring of treatment response. Lately, the development of nanotechnology has also had a dramatic impact on diagnosis and treatment [6-8]. Among many possible applications of nanotechnology in medicine, the use of various nanomaterials as pharmaceutical delivery systems for drugs, DNA, and imaging agents has gained increasing attention. Many nanoparticle-based drug delivery and drug targeting systems have been approved by FDA or are under development [9-11]. Their use aims to

minimize drug degradation, prevent undesirable side effects, and increase drug bioavailability and the fraction of drug dosage delivered to the pathological area.

In order to achieve the goals of this training program, we have proposed conducting two research projects and a broad-based training program to train researchers at Howard University in the field of the application of nanotechnology in targeted drug delivery. In conjunction with these activities, we also proposed establishing a University Nanomedicine Core to promote and facilitate campus-wide research and training. The following progress report is a summary of the accomplishments for the third year in the areas: (i) research, (ii) training, (iii) establishment of Nanomedicine Core, and (iv) alignment with the Statement of Work.

II.1. Research Projects

Project 1: Study the physicochemical characteristics of nanoparticles as MR contrast agent delivery system with the dynamic contrast enhancement pattern for clinical applications

MRI Dynamic Contrast Enhancement Patterns in Solid Tumor

The advances in MRI have led to increasing use of parametric images, which are designed to display physiological, pathological, and morphological features of tissue along with anatomical details. Dynamic contrast enhanced magnetic resonance imaging (DCE-MRI) using Gd-DTPA as a contrast agent (CA) has been used for the assessment of the malignancy of tumors. The DCE-MRI involves acquisition of a series of MR images before, during and after i.v. injection of a CA. The dynamic changes in the MR image intensity reveals details of microenvironment inside the tumor. It has been used successfully for tumor detection and staging. We proposed to further enhance the DCE-MRI is to utilize a nanoparticle specific targeted delivery of the CA to the cancer cells, thereby, improving the specificity of tumor detection. We also proposed to study the impacts of physiochemical properties of nanoparticles to the DCE-MRI.

Transferrin receptor (TfR) is found to be overexpressed on the surface of many cancer cells including breast cancer. The elevated expression of TfR correlates with the malignancy of tumors. It has been widely used to explore for receptor-mediated delivery of anticancer agents. Encapsulating MRI CA within Tf based tumor-targeted liposomal complex offers potential advantages for enhanced sensitivity, detection of metastases, and diagnosis of cancer. In this year, we have used a liposome (Lip) complex modified with Tf on the surface as a ligand for specific targeting and CA (Magnevist) inside to be the payload (Tf-Lip-Mag) for DCE-MRI. We have studied the relationship of MRI dynamic contrast enhancement patterns with tumor pathology and tumor vasculature after i.v. administration of the nanocomplex Tf-Lip-Mag.

MDA-MB-231-Luc breast cancer cells were grown to 70% confluence. 1×10^7 PC-3M-Luc cells in 100 μ L saline buffer were inoculated in the flank of 6–8 weeks athymic nude mice. The DCE-MRI studies were conducted when xenograft tumors grew to 8–10 mm in diameter using a Bruker 9.4 T, 89 mm NMR spectrometer. The imaging sequence used was a multi-slice multi echo (MSME) sequence. Free Magnevist or Tf-Lip-Mag nanocomplex (0.3 mmol/kg) was systematically administrated by tail vein injection and images were acquired every 2.5 minutes for the 120 minutes. First, the animal was given an injection of Magnevist alone for obtaining a control DCE-MRI. Forty eight hours later after the original Magnevist was clear out, the same animal was used in the targeted DCE-MRI study with Tf-Lip-Mag nanocomplex.

The enhancement was observed immediately after administration and increased gradually, reaching to the maximum at 60–80 minutes. Representative DCE-MRI images of MDA-MB-231 mouse

xenografts are shown in Figure 1. Images obtained 60 minutes after Magnevist and Tf-Lip-Mag administration show significant differences in enhancement patterns. Greater image contrast of tumor observed for imaging with Tf-Lip-Magnevist than using Magnevist alone. Although the observed increasing signal intensity and greater contrast induced by nanocomplex compared to the CA alone are very promising, the underlying mechanisms of this heterogeneous and prolonged image enhancement are currently under further investigations.

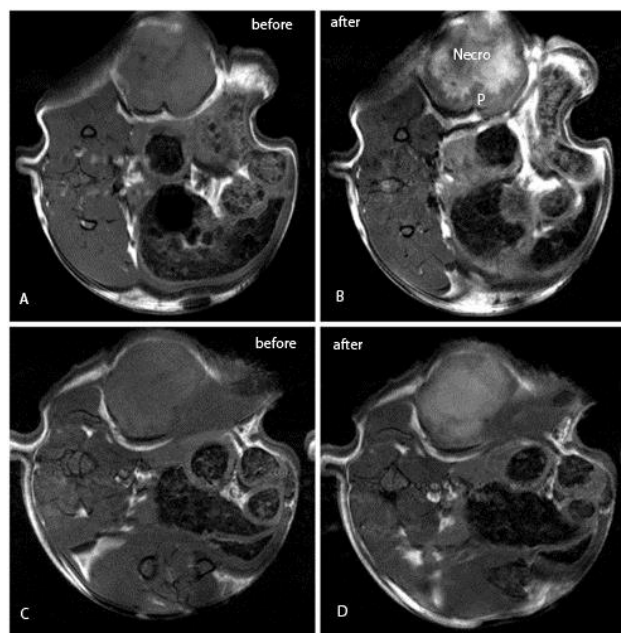


Fig. 1. DCE-MRI images of the same mouse (MDA-MB-231 solid tumor xenograft) studied with the Tf-Lip-Mag nanocomplex (upper row A and B) and with Magnevist alone (bottom row C and D), before (A and C) and after either Tf-Lip-Mag (B) or Magnevist (D) injection. High image contrast enhancement in the Tf-Lip-Mag study (B) indicates the tumor heterogeneity and uneven distribution of viable cancer cells.

Figure 2 displays the nanocomplex-mediated dynamic contrast enhancement in different parts of the tumor which is well correlated with the pathological findings. We have assessed the images of tumors in three different regions: peripheral region with abundant of blood vessels, deep-seated non-necrotic region away from blood supply, and the necrotic region. In the peripheral region, because of the abundant blood vessels the nanocomplexes were at first leaking out into this region. The image intensity increases in this region first, and then the CA gradually diffuses into the second deeper region and image intensity gradually increases with time. The third region, necrotic area, serves as a sink for CA accumulation due to lack of washout mechanisms.

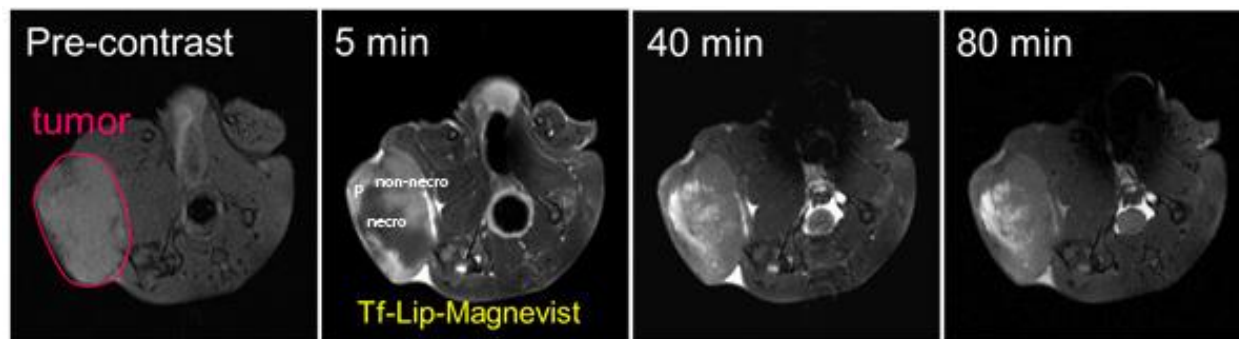


Fig. 2. Dynamic Contrast Enhancement for targeted delivery of MRI contrast agent (Tf-Lip-Magnevist) in mouse MDA-MB-231 breast cancer tumor model.

Figure 3 shows the dynamic image intensity ratio of tumor to muscle from these three regions after Tf-Lip-Mag or Magnevist i.v. administration. There is a significant signal intensity increase in the peripheral region during the first 10 minutes after injection. This is the initial stage of the CA distribution in tumor. During this time the Tf-Lip-Mag starts leaking out from the leaky blood vessels into the extravascular extracellular space (EES). Then, the nanocomplexes enter into cancer cells through endocytosis and release the CA in the cytoplasm. The contrast level in the deeper tumor tissues containing viable cells gradually increases with time, and the rate of the contrast enhancing observed in the necrotic area is higher than in the viable deep tissues. The untrapped nanoprobe and/or already released free Magnevist in EES gradually diffuse into the necrotic area from the viable tumor cells. The necrotic area becomes a depot of CA.

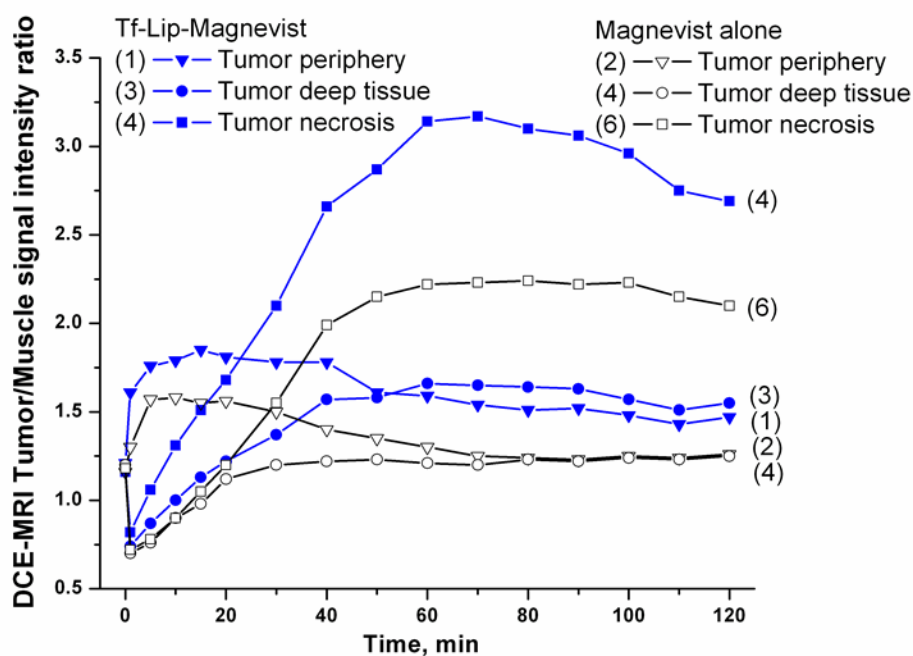


Fig. 3. Typical DCE-MRI curves show the MRI image intensities increase initially and later decrease at various rates for different regions in the tumor using either Tf-Lip-Mag liposomal nanocomplex or Magnevist. These distinct differences are due to the specific targeting and prolong retention of the Tf-Lip-Mag liposomal nanocomplex in the tumor.

Impacts of Physicochemical Properties of Nanoparticles to MRI-DCE Pattern

In order to understand the underlying mechanism of dynamic contrast enhancement pattern of nanocomplex targeted delivery of contrast agent, it is necessary to examine the impacts of physicochemical properties of nanoparticles to the uptake process both in vitro and in vivo. This year we have conducted a series of literature reviews to comprehend the uptake processes of various nanoparticles. We wrote a book chapter to discuss the design principles of targeted contrast agents in molecular MR imaging (Appendix 4.1). Molecular imaging utilizes molecular agents in traditional imaging

techniques, enabling visualization, characterization and measurement of biological processes at the molecular and cellular levels in humans and other living systems. The prospective of molecular imaging lies in its potential for selective potency by targeting biomarkers or molecular targets. The success of molecular imaging agent depends on well-controlled high-quality of synthesis, target selection and detailed characterization of the agent.

We also wrote a review on iron oxide-based MR contrast agents for MR cell tracking (Appendix 4.2). This review covered methods used to monitor the migration, homing, survival, and functionality of the transplanted cells in vivo. We wrote a review on the unique properties of nanoscale delivery formulation for innovative pharmaceutical development (Appendix 4.8). Nanomedicinal formulations are nanometer-sized carrier materials designed for increasing the drug tissue bioavailability, thereby improving the treatment of systemically applied chemotherapeutic drugs. In this review, we highlighted the nanomedicinal formulations that aim to improve the balance between the efficacy and the toxicity of therapeutic interventions. We wrote two papers; how a nanomaterial (carbon nanotube) interacts with cells (Appendix 4.4) and how surface chemistry mediates nanoparticle penetration in tumor spheroids (Appendix 4.5). The surface chemistry of gold nanorod is a key factor determining the cellular uptake and tissue penetration. The negatively charged gold nanorod could penetrate deeper into the tumor spheroids and positively charged gold nanorod.

Mathematical Model for MRI-DCE of Targeted Delivery of MR Contrast Agent

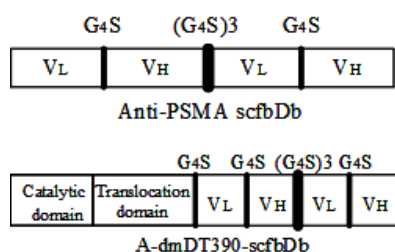
There is an apparent, distinct difference in MR image dynamic contrast enhancement pattern for targeted and untargeted delivery of contrast agent to tumors. A mathematical model describing pharmacokinetics of the contrast agent in and out of various compartments inside the solid tumor will be very useful to portray the nanoparticle uptake process. Due to limited imaging resolution and tumor tissue heterogeneity, MR contrast agent concentrations at many pixels often represent a mixture of more than one distinct compartment. This pixel-wise partial volume effect would have a profound impact on the accuracy of pharmacokinetics that use traditional compartmental models. This year, through our collaborator Dr. Bhujwalla at Johns Hopkins, we have been introduced to a research group at Virginia Polytechnic Institute and State University (PI, Dr. Yue Wang) to use a convex analysis of mixtures (CAM) algorithm to explicitly mitigate partial volume effect in modeling MRI-DCE of targeted delivery of nanoparticles in solid tumor. Using this CAM compartmental modeling, Dr. Wang's group has demonstrated a significant improvement in the accuracy of kinetic parameter estimation. We hope to use this algorithm to analyze our Tf-Lip-Mag targeted DCE data to improve pharmacokinetic parameter estimation, separating tumor tissue into regions with differential CA kinetics on a pixel-by-pixel basis and revealing plausible tumor tissue heterogeneity patterns. This work will be continued in the next year.

Project 2: Development of Multifunctional Nanoparticles for Breast Cancer Diagnosis and Treatment – Using Anti-VEGFR-2 Immunotoxin as Dual Purpose Ligand and Chemotherapeutics as Encapsulated payload

Angiogenesis is a process of neovascular development, but unlike the normal blood vessel system, tumor neovasculature is chaotic and irregular. A large set of genes are aberrantly expressed during angiogenesis and some have been established as vascular surface targets for molecular imaging and antiangiogenic therapy including VEGFR and prostate-specific membrane antigen (PSMA). More recent success of the antiangiogenic treatment has spurred the strong demand for developing angiogenesis-targeted sensitive and specific imaging and therapeutic agents.

Immunotoxin represents a novel strategy for targeted therapy and has several advantages over conventional therapeutics, including high specificity, extraordinary potency, and no drug resistance. Recombinant immunotoxins (RITs) as the latest generation has been intensively generated by fusing the antibody variable domains with the mutant forms of bacterial toxins. Development of RITs is driven by the ability to genetically design the antibody fragments and the toxin with recombinant DNA techniques. Compared with full antibody-drug conjugates, RITs have a smaller molecular size, more efficient penetration capability, greater efficacy, and fewer side effects.

PSMA is an integral, non-shed, type II transmembrane glycoprotein with a large extracellular domain. PSMA is not only highly expressed in prostate cancers, but also in the endothelial cells of tumor blood vessels in other human cancers including breast cancer. Various studies have established PSMA as an optimal target for angiogenic imaging and anti-angiogenic therapy. Taking advantage of the unique expression of PSMA and the high specificity of J591 antibody against the extracellular domain of PSMA, we generated a bivalent single-chain variable fragment (scFv) immunotoxin (designated as A-dmDT390-scfbDb(PSMA)). This novel RIT comprised a mutated diphtheria toxin (DT) moiety (DT390) and a bivalent scFv fold-back format diabody (scfbDb) with the scfbDb fused to the toxin C-terminus (Fig.1). The scfbDb consisted of two scFv fragments and its fold-back structure was formed by preventing dimer formation between the V_L/V_H domains through reducing the V_L/V_H linker to five residues (G₄S), while permitting interactions between the distal and proximal V_L/V_H domains from different scFv fragments by placing a longer peptide linker ((G₄S)₃) between the two scFv. The fold-back format had a significantly higher binding affinity with PSMA than the bivalent tandem scFv and scFv formats at a ratio of 7:2.5:1.



The scfbDb and the RIT were successfully expressed with a DT-resistant *Pichia* expression system and purified following a four-step purification scheme: diafiltration, capture by hydrophobic chromatography, borate anion exchange chromatography, and anion exchange chromatography. The purity of the final product was greater than 95%. The raw yield was ~120 mg/L and the purified yield was ~90.8 mg/L after a 163-hour induction period.

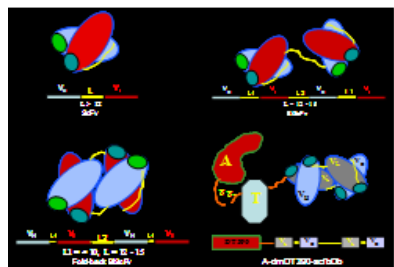


Fig. 1: Schema of fold-back format diabody and RIT. The upper and middle panels show the sequential arrangement of the diabody (scfbDb) and the RIT (A-dmDT390-scfbDb), respectively. The lower panel shows the cartoon structures of the scFv, bivalent tandem scFv (biscFv), scfbDb, and fold-back RIT.

Study of Recombinant immunotoxins as Dual Purpose Ligand and Chemotherapy

Following generation, we confirmed the purity of the diabody and the RIT with gel electrophoresis, presenting as a single band. The molecular sizes of the diabody and RIT were estimated to be 54.6 kDa and 97.1 kDa, respectively. We then characterized the RIT with PSMA-expressing LNCaP and PSMA-absent PC-3 cancer cells. Confocal microscopy and flow cytometry demonstrated that the diabody efficiently mediated the entry of the truncated toxin to the cytosol of PSMA-positive LNCaP cells, but not to the PSMA-negative PC-3 cells after incubation of the RIT with cancer cells (Fig. 2A and 2B). Cellular internalization and intracellular retention of the fold-back RIT was time- and dose-dependent in LNCaP cells. The RIT exhibited a high cytotoxicity against LNCaP cells. The IC₅₀ was measured with MTT

assay to be ~ 0.57 nM against LNCaP cells after incubation for 48 h, but no obvious cytotoxicity was detected against PC-3 cells even at concentration levels up to 100 nM (Fig. 2C). Flow cytometry and anti-annexin V immunostaining further revealed that the RIT induced the cell cycle arrest in S phase and cell apoptosis in a dose-dependent manner.

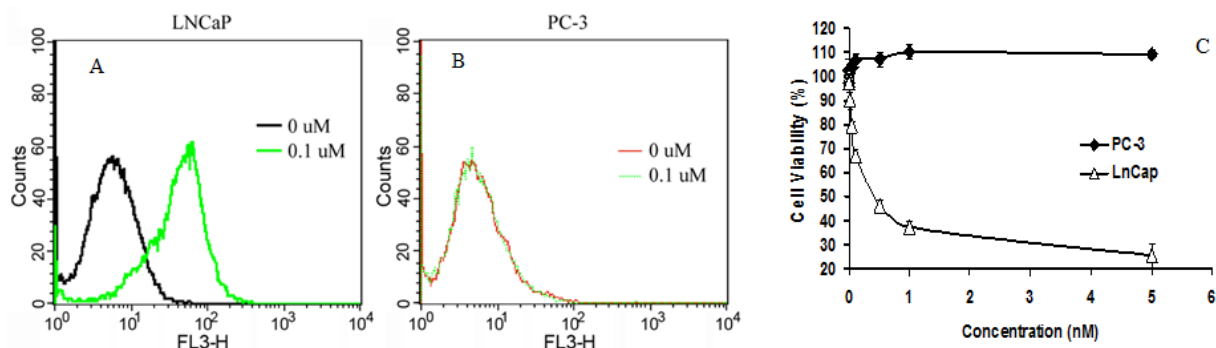


Fig. 2: 2A and 2B demonstrate internalization and accumulation of the RIT in LNCaP cells (2A), but not in PC-3 cells (2B) with flow cytometry. 2C shows the extremely high cytotoxicity of the RIT to LNCaP cells but not to PC-3 cells with MTT assay.

As a proof-of-concept study, we tested the anti-tumor efficacy of the fold-back RIT in mice bearing LNCaP and PC-3 tumor xenografts. The RIT was given to mice intraperitoneally with a multiple dosing regimen of 200 μ g/kg, twice/day at a six-hour interval for six consecutive days. The growth of LNCaP xenografts was significantly inhibited but not the growth of PC-3 xenografts (Fig. 3). One month after treatment, the average weight of LNCaP xenografts was only 0.27 ± 0.09 g, which was significantly lower than the tumor weight in the control group (0.67 ± 0.11 g) ($P < 0.05$, Fig. 3C).

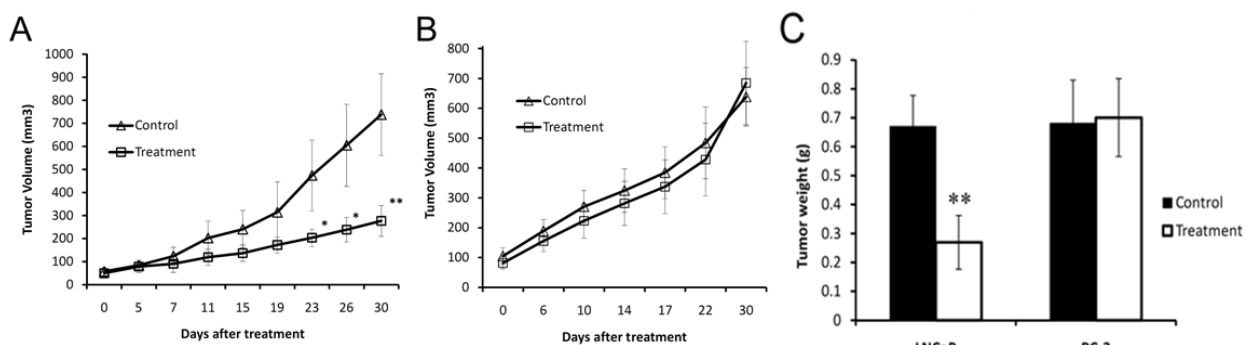


Fig. 3: Growth inhibition of the RIT on LNCaP, but not on PC-3 tumor xenografts. A: LNCaP tumor volume vs. days after treatment; B: PC-3 tumor volume vs. days after treatment; and C: Tumor weight after 30 days of treatment.

Plans for Next Year

PSMA-targeted RIT therapy represents a novel choice for anti-angiogenic therapy for breast cancer and others. However, challenges remain for solid tumor therapy because of the major issues of poor penetration ability and immunogenicity. In the coming year period, we will determine the potential side effects of the RIT in animals. At the same time, a novel formulation of the RIT, a pH-sensitive liposomal formulation, will be constructed (Fig. 4). We hypothesize that a pH-sensitive liposomal

formulation of this RIT will further enhance its anti-tumor efficacy, while reduce its immunogenicity and off-target toxicities by three mechanisms: increased circulation time, enhanced penetration ability through two-step targeting (enhanced permeability and retention effect in tumors and PSMA-mediated endocytosis), and shielding of the RIT surface. Liposomal shielding will prevent the interaction of the RIT with blood components and blood vessels, thereby minimize its immunogenicity and vascular damage. Use of pH-sensitive liposomes will allow the release of the encapsulated immunotoxin at the site of tumors because of the acidic environment in tumors. At the completion of these studies, we will have developed a well-formulated, fold-back format RIT with high sensitivity and specificity to cancers that overexpress PSMA.

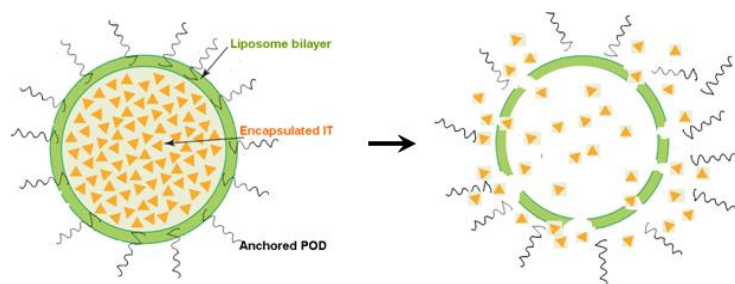


Fig. 4: Scheme of the liposomal formulation of the fold-back immunotoxin and release of the immunotoxin from collapsed liposome particles at the low pH environment of tumors.

II.2. Broad Based Training Components

The Molecular Imaging Laboratory has regular bi-weekly group meetings, journal clubs, and seminars. Some seminars have been arranged through webinars sponsored by the imaging vendors, thus giving an opportunity to the Howard University community to attend seminars given by experts from around the world, followed by very productive and fruitful local discussions. The bi-weekly group meetings engage participants in discussing the current status of research projects, analyzing the experimental issues of the current research, review progress, and exchange ideas, and have been the primary mode of interaction between Howard researchers and collaborating experts. The faculty trainees have also attended seminars at JHU ICMIC. The HU and JHU partnership leaders have been coordinating the training efforts through meetings and emails. Through participation in the Imaging Core-sponsored seminars and workshops, and interaction with Imaging Core staff, a multidisciplinary nanomedicine research community has been established and many fruitful exchanges of research ideas generated. Significant common synergies of interests have been identified, and much multidisciplinary research collaboration has developed. This year, due to establishment of the Nanomedicine Core through this funding support, there are more faculty members using the facility to conduct research in nanomedicine field. There are 10 faculty members from 7 departments and 9 scientists from the other institutions, including Children's National Medical Center and MedStar, who use the core facility to conduct these research projects. There are 3 undergraduate students, 9 graduate students and 5 postdoctoral fellows working with principle investigators on various research projects. The participants of the program have submitted grants to NIH, CDMRP, and NSF together with the partnership leaders. We believe that trainees engaged in this training program gain the interdisciplinary knowledge and skills they need to lead multidisciplinary research in the area of nanomedicine. The seminars and workshops organized at Howard University, as well as at the Johns Hopkins University and other institutions, are listed as following:

Seminars and workshops

1. Osteopontin Genotype as a Determinant of Muscle Remodeling: A Study of African American Young Adult Volunteers. Whitney Barfield, September 28, 2012
2. Nanoliposome: Preparation and Physical Properties Characterization. Alexandru Korotcov, October 12, 2012.
3. Workshop: Bruker 9.4 T MRI machine operation, October 16-17, 2012
4. MRI Dynamic Contrast Enhancement and Liposome, Alexandru Korotcov, December 18, 2012.
5. University Imaging Core Facility. Paul C. Wang, Ph.D., February 8, 2013, Joint Seminar with Children's National Medical Center.
6. Renal Oxygenation Levels Are Decreased in Peroxisome Proliferator Activated Receptor – α Knockout Mice during Angiotensin II Hypertension. Darah Wright (PhD student), April 1, 2013, Howard University Research Day.
7. Renal Oxygenation Levels Are Decreased in Peroxisome Proliferator Activated Receptor – α Knockout Mice during Angiotensin II Hypertension. Dexter Lee, Ph.D., April 3, 2013, Johnson Distinguished Lecture, Howard University.
8. Advantages of Multiple Modalities, Image Fusion and Data Analysis in Preclinical Small Animal Imaging. Sponsored by Bruker Corporation, May 20, 2013.
9. Applications of Nanotechnology in Medical Imaging and Targeted Drug Delivery. July 2, 2013, Fu Jen Catholic University/Catholic University of America Summer Program.
10. Discovering possible things that can be done and gaining background knowledge on bioinformatics. Joseph Arul, Ph. D., August 23, 2013.
11. An Anti-PSMA Bivalent Immunotoxin Exhibits Specificity and Efficacy for Prostate Cancer Imaging and Therapy. Fayun Zhang, Ph. D. September 8, 2013.
12. RCMI RTRN Webinar Research Resources Spotlight Series: Molecular Imaging Laboratory – Imaging Core facility. Paul Wang, PhD, September 26, 2103.

II.3. Nanomedicine Core

It is essential for Howard University to establish a basic infrastructure that is capable of supporting a sustainable long-term research program in the field of molecular imaging of breast cancer and nanomedicine. This infrastructure is necessary in order to provide the researchers with tools to perform the proposed researched projects, as well as to provide a broader research training experience for faculty and students. In the third year of this training program, we continued expansion the user base of the Nanomedicine Core to pursue the multidisciplinary biomedical research. There are 15 research projects that have been supported by the Nanomedicine Core, including projects in the initial phase of research. This year, we added two additional projects using computer modeling to study the process of nanoparticle docking to the intended targets in cancer cells and in animals. In addition, we have started using a convex analysis of mixtures algorithm to study compartmental modeling of MRI-DCE pattern of targeted delivery of nanoparticle containing MR contrast agent.

This year, Dr. Alexandru Korotcov, one of our junior faculty, has left the university and become an Imaging Scientist at the Uniformed Services University of the Health Sciences in Bethesda, Maryland working on posttraumatic stress disorder. Dr. Korotcov's new position is a more senior and permanent position. After joining the Uniformed Services University Dr. Korotcov has continued collaborating with our lab on various MRI research projects. At mean time, we have recruited Dr. Ping-Chang Lin from the University of Kansas Medical Center to continue Dr. Korotcov's function in the lab. Before working at

University of Kansas, Dr. Lin has worked at NIH Institute of Aging for five years. Dr. Lin is an MRI physicist received his PhD degree from UC Davis. Dr. Lin has a strong background in physical sciences and expertise in optical spectroscopy, NMR imaging and spectroscopy, and statistical analysis. While at NIH Institute of Aging, he studied neurological disorders using MRI and 1H MRS. He also used statistical approaches to investigate cartilage degradation and neocartilage growth using MRI and Fourier transform infrared imaging spectroscopy (FT-IRIS). Dr. Lin will be responsible for providing services to users conducting NMR imaging and spectroscopy studies.

Looking forward, Howard University Health Sciences has developed a Research Strategy Plan that outlines the direction of the Enterprise for the future, and envisions the development of biomedical research at Howard University to its full potential, with emphasis on health disparities research. This future plan embraces new research disciplines such as proteomics, computational biology, nanomedicine and genomics. To execute the University Research Strategy Plan and its commitment to the nanomedicine research, the University has started construction of a new Interdisciplinary Research Building to be completed in 2014 in which there will be a designated space for Nano biomedical imaging research. There will be lab space for nanomaterial fabrication with ultrastructure imaging and analytical instrument for physicochemical characterization of nanoparticles, molecular biology labs with incubators and hoods for cell culture and flow cytometry, and imaging suites for confocal microscope and future PET/CT machine. These new lab space and facilities will further enhance nanomedicine research capability at Howard University including breast cancer research.

II.4. Statement of Work Summary

The accomplishments aligned with the Statement-of-Work occurred in this reporting period is listed as following:

Research Component

- Task 1. To conduct Research Project 1 “Study the physicochemical characteristics of nanoparticles as MR contrast agent delivery system with the dynamic contrast enhancement pattern for clinical applications” (months 1-48).
- a. Purchase supplies for cell culture and materials for nanoparticles (months 1-2) (completed).
 - b. Construct liposome (Lip) nanoparticles with transferrin (Tf) as the ligand and encapsulated Gd-based MRI contrast agent (CA) inside as payload (months 3-9) (completed).
 - c. Characterize the physicochemical properties of nanoparticles, including size distribution, surface charge, encapsulation efficiency, and Tf linkage on the surface. Some of the measurements will be done at NCL, NCI-Frederick (months 6-12) (completed).
 - d. Study targeting efficiency of the liposome nanoparticle using MDA-MB-231 cells. Study the interactions of nanoparticles with breast cancer cells (months 13-24) (completed).
 - e. Study the correlation of the dynamic contrast enhancement (DCE) pattern with the distribution of Tf-liposome nanoparticles in tumor xenografts. Both MR and optical imaging will be used (30 mice) (months 25-36) (in progress).
 - f. Evaluate the potential clinical applications of the DCE pattern, focusing on the relationship between the DCE pattern and the tumor features of TfR expression level, permeability of neovasculatures, vascular density, tumor growth and necrosis (months 25-40) (in progress).
 - g. Data analysis and preparation of manuscripts for publication (months 40-48)

- Task 2. To conduct Research Project 2 “Develop multifunctional nanoparticles for breast cancer diagnosis and treatment – using anti-VEGFR-2 immunotoxin as dual purpose ligand and chemotherapeutics as encapsulated payload” (months 1-48).
- Purchase supplies and prepare for the study (months 1-2) (completed).
 - Define the efficacy of the anti-murine anti-VEGFR-2 immunotoxin in endothelial cell killing and vascular permeability increase in animal models (months 3-18) (completed).
 - Construct and characterize the targeted anti-VEGFR-2 immunotoxin multifunctional nanoparticles. Some of the work will be done at NCL (months 13-18) (completed).
 - Determine the biodistribution, pharmacokinetics and toxicity of the nanoparticles in healthy mice (8) and mice bearing with tumor xenografts (22). Optical imaging will be used. Measurements of biodistribution will be done at NCL and HNF (months 19-40) (in progress).
 - Define the synergistic effects of the targeted delivery, anti-angiogenics and chemotherapeutics in breast cancer animal models. Histological staining will be used to study the tumor vasculature (months 25-40) (in progress).
 - Data analysis and preparation of manuscripts for publication (months 40-48).
- Task 3. Research concept development and submission of competitive grants in breast cancer targeted imaging and therapy (months 37-48).

Broad Training Component

- Task 4. Provide opportunities to the faculty trainees in Howard University to update knowledge of nanomedicine (months 1-48) (in progress for all tasks).
- Biweekly group meetings at the Molecular Imaging Lab (months 1-48)
 - Monthly Seminar series at Howard University Cancer Center to be presented by the mentors and invited speakers (months 1-48).
 - Johns Hopkins University ICMIC Seminar Series organized by Dr. Bhujwalla (months 1-48).
 - To attend the biweekly Nanobiology Program Seminar Series at NCI-Frederick organized by Dr. Blumenthal (months 1-48).
 - Annual scientific meetings with mentors and trainees.
- Task 4. Train Howard faculty in advanced nanomedicine lab techniques (in progress for all tasks).
- Laboratory internships at the Johns Hopkins University and NCL, topics include molecular imaging and nano characterization techniques, 2-4 days each (months 1-36).
 - Workshop series. Topics include MR and optical imaging, SEM/TEM/AFM, optical instrumentation, drug design and liposome (months 1-48).
- Task 6. Administrative and communication affairs (coordinated by Drs. Wang and Bhujwalla) (Months 1-48) (in progress for all tasks).
- Status reports (quarterly and annual reports)
 - Research progress review (quarterly)

- c. Administrative meetings (biannually meetings)
- d. Coordination of seminars, workshops, and laboratory internships

III. KEY RESEARCH ACCOMPLISHMENTS

- We have shown that the targeted nanocomplex, Tf–Lip–Mag significantly enhanced the MRI signals in MDA-MB-231 breast cancer xenograft tumors in mice. The image enhancement was superior to that obtained using the contrast agent alone. This superior enhancement capability of the nanocomplex can be used to increase the sensitivity of detecting small tumors.
- The tumor MRI dynamic contrast enhancement patterns are well correlated with histology, and could be used to evaluate tumor pathology in vivo and provide very useful timely information for patient’s prognosis and response to treatment.
- Reviewed literature pertaining to the development, characterization and applications of nanoparticles in cancer imaging and therapy. Published one book chapter and two review articles.
- Analyzed the effect of single-walled carbon nanotubes (SWCNTs) on mitochondrial functions, including mitochondrial membrane potential, mitochondrial oxygen uptake and cytochrome c. We found that the mitochondrial membrane potential and oxygen uptake were greatly decreased and was accompanied by reduction of the cytochrome c.
- Studied the effect of the surface charge of nanoparticle on its cell penetration capability. We found that the negatively charged Au nanorod can penetrate deeper into the tumor spheroids and achieve a more significant thermal therapeutic benefit than positively charged Au nanorod.
- Generated a bivalent single-chain variable fragment (scFv) recombinant immunotoxin, A-dmDT390-scFvDb(PSMA) utilizing the high specificity of the J591 antibody against the extracellular domain of PSMA.
- Characterized the novel immunotoxin A-dmDT390-scFvDb(PSMA) with PSMA-expressing and absent prostate cancer cells, and further established its anti-tumor efficacy in animal models. Our results suggested that this novel immunotoxin is a promising candidate for anti-cancer therapy, especially for cancers that overexpress PSMA, including breast cancer.
- Designed and initiated a new project to determine the antiangiogenic efficacy of the A-dmDT390-scFvDb(PSMA).

IV. REPORTABLE OUTCOMES

Publications

1. Shan L, Gu XB, Wang PC. Design Principles of Nanoparticles as Contrast Agents for Magnetic Resonance Imaging. Nanopharmaceutics: The Potential Application of Nanomaterials. Chapter 11, Xing-Jie Liang (ed), World Scientific Publisher, 2012.
2. Wang PC, Shan L. Essential Elements to Consider for MRI Cell Tracking Studies with Iron Oxide based Labeling Agents. J Basic and Clinical Medicine 1(1)1-6, 2012.
3. Zhang RS, Zhou YF, Wang PC, Sridhar R. Evaluation of Tumor Cell Response to Hyperthermia with Bioluminescent Imaging. J Basic and Clinical Medicine 1(1)16-19, 2012.
4. Ma XW, Zhang LH, Wang LR, Xue X, Sun JH, Wu Y, Zou GZ, Wu X, Wang PC, Wamer WG, Yin JJ, Zheng KY, Liang XJ. Single-Walled Carbon Nanotubes Alter Cytochrome C Electron Transfer and Modulate Mitochondrial Function. ACS Nano 6(12)10486-96, 2012.

5. Jin SB, Ma XW, Ma HL, Zheng KY, Liu J, Hou SA, Meng J, Wang PC, Wu XC, Liang XL. Surface Chemistry-Mediated Penetration and Gold Nanorod Thermo-therapy in Multicellular Tumor Spheroids. *Nanoscale* 5(1)143-6, 2012.
6. Hu XX, Hao XH, Wu Y, Zhang JC, Zhang XN, Wang PC, Zou GZ, Liang XJ. Multifunctional Hybrid Silica Nanoparticles for Controlled Doxorubicin Loading and release With Thermal and pH Dual Response. *J Material Chem B* (1)1109-1118, 2013. PMC3609667
7. Zhang FY, Shan L, Liu YY, Neville D, Woo JH, Chen Y, Korotcov A, Lin S, Huang S, Sridhar R, Liang W, Wang PC. An Anti-PSMA Bivalent Immunotoxin Exhibits Specificity and Efficacy for Prostate Cancer Imaging and Therapy. *Adv. Healthcare Materials*, 2(5)736-44, 2013, PMID 23184611.
8. Kumar A, Chen F, Mozhi A, Zhang X, Zhao YY, Xue XD, Hao YL, Zhang ZN, Wang PC, Liang XJ. Innovative pharmaceutical development based on unique properties of nanoscale delivery formulation. *Nanoscale* (5)8307-25, 2103.

Presentations

1. Huang R, Gao RM, Drain CM, Wang PC, Gu XB, Imidazole-modified porphyrin ring (TIEBAP) for photodynamic therapy in cisplatin-resistant oral carcinoma cells in vitro and in vivo. 13th International RCMI Symposium on Health Disparity. San Juan, Puerto Rico, Dec 10-13, 2012.
2. Korotcov AV, Ishibashi N, Korotcova L, Chen Y, Lin S, Jonas RA, Wang PC. Cerebral white matter response to cardiopulmonary bypass in piglets. 13th International RCMI Symposium on Health Disparity. San Juan, Puerto Rico, Dec 10-13, 2012.
3. Lin S, Korotcov AV, Wu CS, Oh L, Wang PC. In vivo magnetic resonance imaging of multiple sclerosis mice. 13th International RCMI Symposium on Health Disparity. San Juan, Puerto Rico, Dec 10-13, 2012.
4. Wang PC. Introduction of Molecular Imaging laboratory at Howard University. 13th International RCMI Symposium on Health Disparity. San Juan, Puerto Rico, Dec 10-13, 2012.
5. Wright D, Lin S, Lin PC, Wu CS, Zhang D, Duerinckx A, Wang PC, Lee DL. Renal oxygenation levels are decreased in Peroxisome Proliferator Activated Receptor - α knockout mice during Angiotensin II hypertension. College of Medicine Research Day, Howard University, Washington DC, April 3, 2013.
6. Wright D, Lin S, Lin PC, Wu CS, Zhang D, Duerinckx A, Wang PC, Lee DL. Renal oxygenation levels are decreased in Peroxisome Proliferator Activated Receptor - α knockout mice during Angiotensin II hypertension. DB Johnson Distinguished Lecture, Howard University, Washington DC, April 3, 2013.
7. Zhang FY, Shan L, Liu YY, Neville D, Woo JH, Chen Y, Korotcov A, Lin S, Huang S, Sridhar R, Liang W, Wang PC. An Anti-PSMA Bivalent Immunotoxin Exhibits Specificity and Efficacy for Prostate Cancer Imaging and Therapy, ChinaNano 2013, Beijing, China, Sep 4-7, 2013.

Grants

1. NIH Mentored Clinical Scientist Development Award (K08)
Use of MRI/MRS to Assess for a Gamma-Glutamylcysteine Mediated in vivo Reduction in Hypoxic Stress-Induced Oxidative White Matter Injury in Mice
Dilip Nath (Children's Nat Med Centr, PI) Paul Wang (mentor) (09/17/2012 submitted, not funded)
2. NIH TR01
A Novel Non-invasive Device for Neuroregeneration in Dementia
Evaristus Nwulia (Psychiatry/Howard, PI), Paul Wang (co-PI) (09/22/2012 submitted, not funded)
3. NCRR/NIH/CTSA (part) GHUCCTS TTR

Development of An Anti-PSMA Fold-back Immunotoxin for Cancer Therapy

Liang Shan (8/3/2012 submitted, not funded)

4. NIH Exploratory/Developmental Research Grant Program (Parent R21)
Sheddable Bivalent Fold-back Format Immunotoxin for Prostate Cancer Therapy
Liang Shan (Radiology/Howard, PI) Paul Wang (co-PI) (06/03/2013 submitted, pending)
5. NSF
Howard University Center for Nanophotonics and Nanomaterials (NHCNN)
A Physics Frontiers for Study Interfacial Phenomena
Parbhakar Misra (Physics/Howard, PI) Paul Wang (co-PI) (08/05/2013 submitted, pending)
6. DoD W81XWH-13-PCRP-IDA
An Anti-PSMA Bivalent Fold-back Format Immunotoxin for Prostate Cancer Therapy
Liang Shan (Radiology/Howard, PI) Paul Wang (co-PI) (10/01/2013 submitted, pending)

V. CONCLUSIONS

In this year, we have shown that the targeted nanocomplex, Tf-Lip-Mag (~130 nm) significantly enhanced the MRI signals in MDA-MB-231 breast cancer xenograft tumors in mice. The image enhancement was superior to that obtained using the contrast agent alone. This superior enhancement capability of the nanocomplex can be used to increase the sensitivity of detecting small tumors. A much higher contrast in viable cells in the periphery of tumor was observed at the initial stage of the targeted DCE-MRI. The image intensity was persistently higher than the DCE-MRI of free CA and lasts for several hours. The nature of the elevated contrast level at the initial stage of targeted DCE-MRI in vivo may be due to receptor mediated endocytosis. The tumor enhancement patterns are well correlated with histology, and could be used to evaluate tumor pathology in vivo and provide very useful, timely information for the clinicians. In the future, specially formulated nanocomplex CA can be used to quantify the specific biomarkers expressed in tumors, which will be useful in determining the patient's prognosis and response to treatment.

This year, we also have reviewed literature pertaining to the development, characterization and applications of various nanoparticles in cancer imaging and therapy. We have analyzed the effects of single-walled carbon nanotubes (SWCNTs) on mitochondrial function. We have synthesized gold nanorods (Au NRs) with three different polymer coatings, and further investigated the relationship between the surface chemistry and the penetration ability of Au NRs in a multicellular tumor spheroid model. We have designed and synthesized temperature and pH dual responsive PNIPAM/AA@SiO₂ core-shell particles loaded with doxorubicin for improving drug delivery efficiency for cancer treatment. We have established a bioluminescent imaging technique to evaluate tumor cell response to hyperthermia utilizing luciferase-expressing MDA-MB-231-luc human breast cancer cells. We have generated a bivalent single-chain variable fragment (scFv) recombinant immunotoxin, A-dmDT390-scFvDb(PSMA) with J591 antibody, against extracellular domain of PSMA in tumor epithelial cells in animal model. Our results suggested that this novel immunotoxin is a promising candidate for anti-cancer therapy.

For the broad training component, the faculty members, and graduate and undergraduate students from different departments at Howard University have been trained in the use of nanoparticles as targeted drug delivery vehicles for cancer diagnosis and therapy. A total of 12 seminars and webinars, workshops and symposia in cancer, molecular imaging and nanomedicine have been offered in addition to the biweekly group meetings. The training activities have been coordinated by partnership leaders from Howard and John Hopkins Universities. This training program helps the participants gain useful

interdisciplinary knowledge and skills to conduct breast cancer research using nanotechnology. There are 10 faculty members from 7 departments and 9 scientists from the other institutions, including Children's National Medical Center and MedStar, who use the core facility to conduct these research projects. There are 3 undergraduate students, 9 graduate students and 5 postdoctoral fellows working with principle investigators on various research projects. This year, we initiated two additional projects: using computer modeling to study the docking process between nanoparticles and their intended targets in cancer cells, and using a convex analysis of mixtures algorithm to study compartmental modeling of MRI-DCE pattern of targeted delivery of nanoparticle containing MR contrast agent.

VI. REFERENCES

1. Pourtau L, Oliveira H, Thevenot J, Wan Y, Brisson AR, Sandre O, Miraux S, Thiaudiere E, Lecommandoux S. Antibody-Functionalized Magnetic Polymersomes: In vivo Targeting and Imaging of Bone Metastases using High Resolution MRI. *Advanced Healthcare Materials* 2013. Doi: 10.1002/adhm.201300061.
2. Gallo J, Long NJ, Aboagye EO. Magnetic nanoparticles as contrast agents in the diagnosis and treatment of cancer. *Chemical Society Reviews* 42(19): 7816-7833, 2013.
3. Gulaka PK, Yu JX, Liu L, Mason RP, Kodibagkar VD. Novel S-Gal analogs as ¹H MRI reporters for in vivo detection of β -galactosidase. *Magnetic Resonance Imaging* 31(6): 1006-1011, 2013.
4. Geninatti Crich S, Alberti D, Szabo I, Aime S, Djanashvili K. MRI visualization of melanoma cells by targeting overexpressed sialic acid with a Gd(III)-dota-en-pba imaging reporter. *Angewandte Chemie International Edition* 52(4): 1161-1164, 2013.
5. Penet MF, Glunde K, Jacobs MA, Pathak AP, Bhujwalla ZM. Molecular and functional MRI of the tumor microenvironment. *Journal of Nuclear Medicine* 49(5): 687-690, 2008.
6. Lammers T, Rizzo LY, Storm G, Kiessling F. Personalized nanomedicine. *Clinical Cancer Research* 18(18): 4889-4894, 2012.
7. Caruso F, Hyeon T, Rotello VM. Nanomedicine. *Chemical Society Reviews* 41(7): 2537-2538, 2012.
8. Lammers T, Aime S, Hennink WE, Storm G, Kiessling F. Theranostic nanomedicine. *Accounts of Chemical Research* 44(10): 1029-1038, 2011.
9. Kwon IK, Lee SC, Han B, Park K. Analysis on the current status of targeted drug delivery to tumors. *Journal of Controlled Release* 164(2): 108-114, 2012.
10. Sultana S, Khan MR, Kumar M, Kumar S, Ali M. Nanoparticles-mediated drug delivery approaches for cancer targeting: a review. *Journal of Drug Targeting* 21(2): 107-125, 2013.
11. Cheng Z, Al Zaki A, Hui JZ, Muzykantor VR, Tsourkas A. Multifunctional nanoparticles: cost versus benefit of adding targeting and imaging capabilities. *Science* 338(6109): 903-1020, 2012.
12. Xia Y, Yang P, Sun Y, Wu Y, Mayers B, Gates B, Yin Y, Kim F, Yan H. One-Dimensional Nanostructures: Synthesis, Characterization, and Applications. *Advanced Materials* 15 (5): 353-389, 2003.
13. Alivisatos AP. Semiconductor Clusters, Nanocrystals, and Quantum Dots. *Science* 271 (5251): 933-937, 1996.
14. Elghanian R, Storhoff JJ, Mucic RC, Letsinger RL, Mirkin CA. Selective Colorimetric Detection of Polynucleotides Based on the Distance-Dependent Optical Properties of Gold Nanoparticles. *Science* 277 (5329): 1078-1081, 1997.
15. Cao YC, Jin R, Mirkin CA. Nanoparticles with Raman Spectroscopic Fingerprints for DNA and RNA Detection. *Science* 297 (5586): 1536-1540, 2002.
16. Klostranec J M, Chan WCW. Quantum Dots in Biological and Biomedical Research: Recent Progress and Present Challenges. *Advanced Materials* 18 (15): 1953-1964, 2006.
17. Hirsch LR, Stafford RJ, Bankson JA, Sershen SR, Rivera B, Price RE, Hazle JD, Halas NJ, West JL. Nanoshell-mediated near-infrared thermal therapy of tumors under magnetic resonance guidance. *Proceedings of the National Academy of Sciences of the United States of America* 100 (23): 13549-13554, 2003.
18. Stefanini M, Wu F, Mac Gabhann F, Popel A. A compartment model of VEGF distribution in blood, healthy and diseased tissues. *BMC Systems Biology* 2 (1): 77, 2008.
19. Schenone S, Bondavalli F, Botta M. Antiangiogenic Agents: an Update on Small Molecule VEGFR Inhibitors. *Current Medicinal Chemistry* 14 (23): 2495-2516, 2007.

20. Kiselyov A, Balakin KV, Tkachenko SE. VEGF/VEGFR signalling as a target for inhibiting angiogenesis. *Expert Opinion on Investigational Drugs* 16 (1): 83-107, 2007.
21. Veeravagu A, Hsu AR, Cai W, Hou LC, Tse VCK, Chen X. Vascular Endothelial Growth Factor and Vascular Endothelial Growth Factor Receptor Inhibitors as Anti-Angiogenic Agents in Cancer Therapy. *Recent Patents on Anti-Cancer Drug Discovery* 2 (1): 59-71, 2007.
22. Lu D, Jimenez X, Zhang H, Wu Y, Bohlen P, Witte L, Zhu Z. Complete Inhibition of Vascular Endothelial Growth Factor (VEGF) Activities with a Bifunctional Diabody Directed against Both VEGF Kinase Receptors, fms-like Tyrosine Kinase Receptor and Kinase Insert Domain-containing Receptor. *Cancer Res* 61 (19): 7002-7008, 2001.

VII. APPENDICES

1. Research Projects Supported by the Nanomedicine Core
2. Personnel Received Pay for Research
3. Students Participated in Nanomedicine Core Supported Research Projects
4. Reprints of Publication
 - a) Shan L, Gu XB, Wang PC. Design Principles of Nanoparticles as Contrast Agents for Magnetic Resonance Imaging. *Nanopharmaceutics: The Potential Application of Nanomaterials*. Chapter 11, Xing-Jie Liang (ed), World Scientific Publisher, 2012.
 - b) Wang PC, Shan L. Essential Elements to Consider for MRI Cell Tracking Studies with Iron Oxide based Labeling Agents. *J Basic and Clinical Medicine* 1(1)1-6, 2012.
 - c) Zhang RS, Zhou YF, Wang PC, Sridhar R. Evaluation of Tumor Cell Response to Hyperthermia with Bioluminescent Imaging. *J Basic and Clinical Medicine* 1(1)16-19, 2012.
 - d) Ma XW, Zhang LH, Wang LR, Xue X, Sun JH, Wu Y, Zou GZ, Wu X, Wang PC, Wamer WG, Yin JJ, Zheng KY, Liang XJ. Single-Walled Carbon Nanotubes Alter Cytochrome C Electron Transfer and Modulate Mitochondrial Function. *ACS Nano* 6(12)10486-96, 2012.
 - e) Jin SB, Ma XW, Ma HL, Zheng KY, Liu J, Hou SA, Meng J, Wang PC, Wu XC, Liang XL. Surface Chemistry-Mediated Penetration and Gold Nanorod Thermotherapy in Multicellular Tumor Spheroids. *Nanoscale* 5(1)143-6, 2012.
 - f) Hu XX, Hao XH, Wu Y, Zhang JC, Zhang XN, Wang PC, Zou GZ, Liang XJ. Multifunctional Hybrid Silica Nanoparticles for Controlled Doxorubicin Loading and release With Thermal and pH Dual Response. *J Material Chem B* (1)1109-1118, 2013. PMC3609667
 - g) Zhang FY, Shan L, Liu YY, Neville D, Woo JH, Chen Y, Korotcov A, Lin S, Huang S, Sridhar R, Liang W, Wang PC. An Anti-PSMA Bivalent Immunotoxin Exhibits Specificity and Efficacy for Prostate Cancer Imaging and Therapy. *Adv. Healthcare Materials*, 2(5)736-44, 2013, PMID 23184611.
 - h) Kumar A, Chen F, Mozhi A, Zhang X, Zhao YY, Xue XD, Hao YL, Zhang ZN, Wang PC, Liang XJ. Innovative pharmaceutical development based on unique properties of nanoscale delivery formulation. *Nanoscale* (5)8307-25, 2103.
5. Reprints of Abstracts
 - a) Huang R, Gao RM, Drain CM, Wang PC, Gu XB, Imidazole-modified porphyrin ring (TIEBAP) for photodynamic therapy in cisplatin-resistant oral carcinoma cells in vitro and in vivo. 13th International RCMI Symposium on Health Disparity. San Juan, Puerto Rico, Dec 10-13, 2012.
 - b) Korotcov AV, Ishibashi N, Korotcova L, Chen Y, Lin S, Jonas RA, Wang PC. Cerebral white matter response to cardiopulmonary bypass in piglets. 13th International RCMI Symposium on Health Disparity. San Juan, Puerto Rico, Dec 10-13, 2012.
 - c) Lin S, Korotcov AV, Wu CS, Oh L, Wang PC. In vivo magnetic resonance imaging of multiple sclerosis mice. 13th International RCMI Symposium on Health Disparity. San Juan, Puerto Rico, Dec 10-13, 2012.
 - d) Wang PC. Introduction of Molecular Imaging laboratory at Howard University. 13th International RCMI Symposium on Health Disparity. San Juan, Puerto Rico, Dec 10-13, 2012.
 - e) Wright D, Lin S, Lin PC, Wu CS, Zhang D, Duerinckx A, Wang PC, Lee DL. Renal oxygenation levels are decreased in Peroxisome Proliferator Activated Receptor - α knockout mice during Angiotensin II hypertension. College of Medicine Research Day, Howard University, Washington DC, April 3, 2013.
 - f) Wright D, Lin S, Lin PC, Wu CS, Zhang D, Duerinckx A, Wang PC, Lee DL. Renal oxygenation levels are decreased in Peroxisome Proliferator Activated Receptor - α knockout mice during

Angiotensin II hypertension. DB Johnson Distinguished Lecture, Howard University, Washington DC, April 3, 2013.

- g) Zhang FY, Shan L, Liu YY, Neville D, Woo JH, Chen Y, Korotcov A, Lin S, Huang S, Sridhar R, Liang W, Wang PC. An Anti-PSMA Bivalent Immunotoxin Exhibits Specificity and Efficacy for Prostate Cancer Imaging and Therapy, ChinaNano 2013, Beijing, China, Sep 4-7, 2013.

6. Dr. Ping-Chang Lin's Curriculum Vitae

Appendix 1 Research Projects Supported by the Nanomedicine Core

1. Physicochemical Characteristics of Nanoparticles as MR Contrast Agent Delivery System with the Dynamic Contrast Enhancement Pattern for Clinical Applications (Wang PC, Korotcov A/ Radiology; Ping-Chang Lin/Radiology, Sridhar R/ Radiation Oncology; Bhujwala Z/Radiology/Johns Hopkins)
2. Develop multifunctional nanoparticles for breast cancer diagnosis and treatment – using anti-VEGFR-2 immunotoxin as dual purpose ligand and chemotherapeutics as encapsulated payload (Shan L/Radiology; Liu YY, Naville D/ NIH and Angimmune LLC).
3. Relativity simulation vs. 2D HSQC measurements of multiple fluorine compounds mixture (Ping-Chang Lin/Radiology)
4. Design of Multifunctional Polymeric Nanoparticles for Breast Cancer Diagnosis and Treatment (Akala E/Pharmacy)
5. Use of MRI/MRS to Assess for a Gamma-Glutamylcysteine Mediated in vivo Reduction in Hypoxic Stress-Induced Oxidative White Matter Injury in Mice (Costello J, Nath D, Jonas R/Children's National Medical Center, Phillipe-Auguste M/Med /Howard)
6. Use of MRI in Mouse brain tumor model and drug delivery (Nazarian J/Children's National Medical Center)
7. A Fluorescence Imaging Approach to Visualizing peripherally inserted central catheters (Shekhar, Raj/Children's National Medical Center)
8. Correlation of recruitment of osteogenic stem cells by stem cell derive factor 1(SDF-1) in damaged muscle (Zijun Zhang/Medstar Health Research Institute)
9. SPIOs with modified polymer-pHLIP peptide surface as an effective MRI-contrast agent for diagnosis of pancreatic tumor (Qibing Zhou/ Huazhong University of Science and Technology, Shan L/Radiology)
10. Efficiency of Brain Delivery of Novel Therapeutics Through the Olfactory Neuroepithelium (Nwulia E/Psychiatry)
11. Parallel computing in bioinformatics (Yayin Fan/Biochemistry, Joseph Arul/Fu Jen University)
12. Renal Oxygenation levels are Decreased in Peroxisome Proliferator Activated Receptor – α Knockout Mice during Angiotensin II Hypertension (Darah Wright, Dexter Lee/Physiology, Biophysics; Ping-Chang Lin, Stephen Lin/Radiology)
13. Anti-PSMA Diphtheria Immunotoxin for Prostate Cancer Imaging and Therapy (Shan L, /Radiology; Liu YY/ Angimmune LLC)
14. Osteopontin Genotype as a Determinant of Muscle Remodeling: A Study of African-American Young Adult Volunteers (Barfield W, Bond V/ Health and Human Performance, Wang PC, Williams L/Radiology, Hoffman EP/Children's National Medical Center)
15. Tissue-Specific Compartmental Analysis for Dynamic Contrast-Enhancement MR Imaging of Complex Tumors (Wang Y/Virginia Polytechnic Institute and State University, Bhujwala Z/Johns Hopkins, Wang PC/Howard)

Appendix 2 Personnel Received Pay in This Research Effort

- ☐ Paul C. Wang, Ph.D (PI)
- ☐ Alexandru V. Korotcov, PhD.
- ☐ Ping-Chang, Lin, Ph.D. (new)
- ☐ Chung-Shieh Wu, Ph.D.
- ☐ Yue Chen, B.S.

Appendix 3. Students Participated in Nanomedicine Core Supported Research Projects

Postdoctoral Fellows:

- Chung-Shieh Wu (Chemistry/Radiology)
- Bin Zhi (Anatomy)
- Javad Nazarian (Children's National Medical Center)
- Rohan Fernandes (Children's National Medical Center)
- Fayun Zhang (Radiology)

Predoctoral M.D./Ph.D./Dental Students:

- Belinda Hauser (Genetics)
- Whitney Barfield (Microbiology)
- Darah White (Physiology and Biophysics)
- Philipe Auguste (Medicine)
- Belinda Hauser (Dentistry)
- Xixue Hu (China Nat Nano Center)
- Shubin Jin (China Nat Nano Center)
- Xiao Ma (China Nat Nano Center)
- Anil Kumar (Radiology)

Undergraduate students:

- Akeem Moore (Biology)
- Sophia Huang (Pre-med)
- Kacey Davis (Anatomy)

Appendix 4. Reprints of Publication

1. Shan L, Gu XB, Wang PC. Design Principles of Nanoparticles as Contrast Agents for Magnetic Resonance Imaging. *Nanopharmaceutics: The Potential Application of Nanomaterials*. Chapter 11, Xing-Jie Liang (ed), World Scientific Publisher, 2012.
2. Wang PC, Shan L. Essential Elements to Consider for MRI Cell Tracking Studies with Iron Oxide based Labeling Agents. *J Basic and Clinical Medicine* 1(1)1-6, 2012.
3. Zhang RS, Zhou YF, Wang PC, Sridhar R. Evaluation of Tumor Cell Response to Hyperthermia with Bioluminescent Imaging. *J Basic and Clinical Medicine* 1(1)16-19, 2012.
4. Ma XW, Zhang LH, Wang LR, Xue X, Sun JH, Wu Y, Zou GZ, Wu X, Wang PC, Wamer WG, Yin JJ, Zheng KY, Liang XJ. Single-Walled Carbon Nanotubes Alter Cytochrome C Electron Transfer and Modulate Mitochondrial Function. *ACS Nano* 6(12)10486-96, 2012.
5. Jin SB, Ma XW, Ma HL, Zheng KY, Liu J, Hou SA, Meng J, Wang PC, Wu XC, Liang XL. Surface Chemistry-Mediated Penetration and Gold Nanorod Thermotherapy in Multicellular Tumor Spheroids. *Nanoscale* 5(1)143-6, 2012.
6. Hu XX, Hao XH, Wu Y, Zhang JC, Zhang XN, Wang PC, Zou GZ, Liang XJ. Multifunctional Hybrid Silica Nanoparticles for Controlled Doxorubicin Loading and release With Thermal and pH Dual Response. *J Material Chem B* (1)1109-1118, 2013. PMC3609667
7. Zhang FY, Shan L, Liu YY, Neville D, Woo JH, Chen Y, Korotcov A, Lin S, Huang S, Sridhar R, Liang W, Wang PC. An Anti-PSMA Bivalent Immunotoxin Exhibits Specificity and Efficacy for Prostate Cancer Imaging and Therapy. *Adv. Healthcare Materials*, 2(5)736-44, 2013, PMID 23184611.
8. Kumar A, Chen F, Mozhi A, Zhang X, Zhao YY, Xue XD, Hao YL, Zhang ZN, Wang PC, Liang XJ. Innovative pharmaceutical development based on unique properties of nanoscale delivery formulation. *Nanoscale* (5)8307-25, 2103.

Appendix 5. Reprints of Abstracts

1. Huang R, Gao RM, Drain CM, Wang PC, Gu XB, Imidazole-modified porphyrin ring (TIEBAP) for photodynamic therapy in cisplatin-resistant oral carcinoma cells in vitro and in vivo. 13th International RCMI Symposium on Health Disparity. San Juan, Puerto Rico, Dec 10-13, 2012.
2. Korotcov AV, Ishibashi N, Korotcova L, Chen Y, Lin S, Jonas RA, Wang PC. Cerebral white matter response to cardiopulmonary bypass in piglets. 13th International RCMI Symposium on Health Disparity. San Juan, Puerto Rico, Dec 10-13, 2012.
3. Lin S, Korotcov AV, Wu CS, Oh L, Wang PC. In vivo magnetic resonance imaging of multiple sclerosis mice. 13th International RCMI Symposium on Health Disparity. San Juan, Puerto Rico, Dec 10-13, 2012.
4. Wang PC. Introduction of Molecular Imaging laboratory at Howard University. 13th International RCMI Symposium on Health Disparity. San Juan, Puerto Rico, Dec 10-13, 2012.
5. Wright D, Lin S, Lin PC, Wu CS, Zhang D, Duerinckx A, Wang PC, Lee DL. Renal oxygenation levels are decreased in Peroxisome Proliferator Activated Receptor - α knockout mice during Angiotensin II hypertension. College of Medicine Research Day, Howard University, Washington DC, April 3, 2013.
6. Wright D, Lin S, Lin PC, Wu CS, Zhang D, Duerinckx A, Wang PC, Lee DL. Renal oxygenation levels are decreased in Peroxisome Proliferator Activated Receptor - α knockout mice during Angiotensin II hypertension. DB Johnson Distinguished Lecture, Howard University, Washington DC, April 3, 2013.
7. Zhang FY, Shan L, Liu YY, Neville D, Woo JH, Chen Y, Korotcov A, Lin S, Huang S, Sridhar R, Liang W, Wang PC. An Anti-PSMA Bivalent Immunotoxin Exhibits Specificity and Efficacy for Prostate Cancer Imaging and Therapy, ChinaNano 2013, Beijing, China, Sep 4-7, 2013.

Appendix 6. Dr. Ping-Chang Lin's curriculum vita

BIOGRAPHICAL SKETCH

Provide the following information for the Senior/key personnel and other significant contributors in the order listed on Form Page 2.
Follow this format for each person. **DO NOT EXCEED FOUR PAGES.**

NAME Lin, Ping-Chang	POSITION TITLE Research Assistant Professor of Radiology		
eRA COMMONS USER NAME (credential, e.g., agency login) pcclin			
EDUCATION/TRAINING <i>(Begin with baccalaureate or other initial professional education, such as nursing, include postdoctoral training and residency training if applicable.)</i>			
INSTITUTION AND LOCATION	DEGREE <i>(if applicable)</i>	MM/YY	FIELD OF STUDY
National Tsing Hua University, Hsinchu, Taiwan	B.S.	06/92	Physics
National Chiao Tung University, Hsinchu, Taiwan	M.S.	06/96	Electrophysics
University of California, Davis, CA	Ph.D.	09/06	Biophysics
National Institute on Aging, NIH, MD	Post-doc	08/11	Biomedical Science

NOTE: The Biographical Sketch may not exceed four pages. Follow the formats and instructions below.

A. Personal Statement

As an assistant professor Department of Radiology, Howard University, I have the expertise and motivation necessary to successfully carry out this project based on my broad background in magnetic resonance knowledge/ techniques and physiology, with specific training such as small animal handling, restraining and anesthesia in key research areas. Additionally, at the Molecular Imaging Laboratory, one of the the RCMI core facilities, I am responsible for the establishment of all research protocols for the Bruker MRI/NMR 400MHz scanner, the GE 3T MRI clinical scanner, and am also responsible for training new personnel, managing research assistants and coordinating diverse research projects while the RCMI Imaging Core Facility is involved in.

During my Ph.D. study at UC Davis, my research was to assess the physiological function of myoglobin by implementing nuclear magnetic resonance (NMR) spectroscopy. As a postdoctoral fellow at National Institutes of Health, in addition to conducting statistical approaches for investigation of cartilage degradation and neocartilage growth using magnetic resonance imaging (MRI) and Fourier transform infrared imaging, I expanded my research to include the study of brain volume and function in the heterozygous mice of haploinsufficient XRCC1 (the X-ray cross-complementing protein I) using magnetic resonance modalities (MRI and MRS). Furthermore, I implemented MRI techniques to investigate the study of taste perception and pancreatic function in the condition of brain-derived neurotrophic factor (BDNF) deficiency and the study of Cockayne syndrome, a DNA repair disorder. Recently, I participated in quantification of cerebral ketone body contents in streptozotocin-induced diabetic rat brains after ketoacidosis development using localized ¹H MRS, evaluation of efficacy of the HAV peptides in enhancing delivery of paracellular marker or drug molecules through the blood-brain barrier into rat brains using MRI T₁ mapping, and quantification of MR images of the abdominal adipose tissue in the study of obese pregnancy in human subjects. Currently my research focus is on investigating the pharmacokinetics of a novel targeted nanocomplex (Tf-Lip-CA) and its applications to non-invasively monitor tumor progression and tumor microenvironment using DCE-MRI. Specifically, we plan to emphasize the efficiency of targeting tumors under different microenvironments.

Briefly, based on my previous experience, I am aware of the importance of frequent communication among project members and will continue to have good and frequent communication to foster multidisciplinary research collaborations in the RCMI grant.

B. Positions and Honors

Positions and Employment

2007-11 Visiting Fellow, Division of Intramural Research, National Institute on Aging, NIH, Baltimore, MD
2011-12 Sr. Research Associate, Hoglund Brain Imaging Center, University of Kansas Medical Center, KS
2012- Res. Assistant Professor, Department of Radiology, College of Medicine, Howard University, DC

Other Experience and Professional Memberships

1999-2011 Member, AAAS
2007 Member, International Society for Magnetic Resonance in Medicine
2009 Journal Reviewer, PLoS ONE
2010 Journal Reviewer, Journal of Gerontology: Medical Sciences
2010-11 Abstract Judge, for 201 and 2012 NIH Fellows Award for Research Excellence
2011-12 Journal Reviewer, NIH Risk, Tissue Engineering, Part A

Honors

1997 The Graduate Students' Exquisite Thesis Award (The physical Society of Taiwan)
2003 Earle C. Anthony Fellowship (University of California Davis, CA)
2009 NIH 2010 the Fellows Award for Research Excellence (National Institutes of Health, MD)

C. Selected Peer-reviewed Publications

1. Hanifi, A., Bi, X., Yang, X., Kavukcuoglu, B., **Lin, P. -C.**, DiCarlo, E., Spencer, R. G., Bostrom, M., and Pleshko, N. "Infrared fiber optic probe evaluation of degenerative cartilage correlates to histological grading" *Am J Sports Med.* **2012**, 40(12), 2853-61
2. Scheibye-Knudsen, M., Ramamoorthy, M., Sykora, P., Maynard, S., **Lin, P. -C.**, Minor, R. K., Wilson, D. M. III, Cooper, M., Spencer, R. G., de Cabo, R., Croteau, D. L., and Bohr, V. A. "Cockayne syndrome group b protein prevents the accumulation of damaged mitochondria by promoting mitochondrial autophagy" *J Exp Med.* **2012**, 209(4), 855-69
3. Irrechukwu O.N., Reiter D.A., **Lin P.-C.**, Roque R.A., Fishbein K.W. and Spencer R.G. "Characterization of engineered cartilage constructs using multiexponential T₂ relaxation analysis and support vector regression" *Tissue Eng. Part C* **2012**, 18(6), 433-43
4. Reiter, D. A., Irrechukwu, O., **Lin, P. -C.**, Moghadam, S., Von Thaer, S., Pleshko, N., and Spencer, R.G. "Improved MR-based characterization of engineered cartilage using multiexponential T₂ relaxation and multivariate analysis" *NMR Biomed.* **2012**, 25(3), 476-88
5. **Lin, P. -C.**, Irrechukwu, O., Roque R. A., Hancock, B., Fishbein, K. W., and Spencer., R. G. "Multivariate analysis of cartilage degradation using the support vector machine algorithm" *Magn Reson Med.* **2012**, 67(6), 1815-26
6. McNeill, D. R., **Lin, P. -C.**, Miller, M. G., Pistell, P., de Souza-Pinto, N., Fishbein, K. W., Spencer, R. G., Liu, Y., Pettan-Brewer, C., Ladiges, W. C., and Wilson, D. M. III. "XRCC1 haploinsufficiency in mice has little effect on aging, but adversely modifies exposure-dependent susceptibility" *Nucl Acids Res.* **2011**, 39 (18), 7992-8004

7. Reiter, D. A., Roque, R. A., **Lin, P. -C.**, Doty, S. B., Pleshko, N., and Spencer, R. G. "Improved specificity of cartilage matrix evaluation using multiexponential transverse relaxation analysis applied to pathomimetically-degraded cartilage" *NMR Biomed.* **2011**, 24(10), 1286-94
8. Reiter, D. A., Roque, R. A., **Lin, P. -C.**, Irrechukwu, O. N., Doty, S. B., Longo, D. L., Pleshko, N., Spencer, R. G. "Mapping proteoglycan-bound water in cartilage: improved specificity of matrix assessment using multiexponential transverse relaxation analysis" *Magn Reson Med.* **2011**, 65 (2), 377-84
9. Irrechukwu, O. N., **Lin, P. -C.**, Fritton, K., Doty, S., Pleshko, N., and Spencer, R. G. "Magnetic resonance studies of macromolecular content in engineered cartilage treated with pulsed low-intensity ultrasound" *Tissue Eng. Part A* **2011**, 17 (3-4), 407-15
10. Baykal, D., Irrechukwu, O., **Lin, P. -C.**, Fritton, K., Spencer, R., and Pleshko, N. "Non-destructive assessment of engineered cartilage constructs using near infrared spectroscopy" *Appl. Spectrosc.* **2010**, 64 (10), 1160-1166
11. **Lin, P. -C.**, Reiter, D. A., and Spencer, R. G. "Classification of degraded cartilage through multiparametric MRI analysis" *J Magn Reson.* **2009**, 201 (1), 61-71
12. **Lin, P. -C.**, Reiter, D. A., and Spencer, R. G. "Sensitivity and specificity of univariate MRI analysis of experimentally degraded cartilage" *Magn Reson Med.* **2009**, 62 (5), 1311-8
13. Reiter, D. A., **Lin, P. -C.**, Fishbein, K. W., and Spencer, R. G. "Multicomponent T₂ relaxation analysis in cartilage" *Magn Reson Med.* **2009**, 61 (4), 803-9
14. Ponganis, P. J., Kreutzer, U., Stockard, T. K., **Lin, P. -C.**, Sailasuta, N., Tran, T. K., Hurd, R., and Jue, T. "Blood flow and metabolic regulation in seal muscle during apnea" *J. Exp. Biol.* **2008**, 211 (Pt 20), 3323-32
15. Masuda, K., Truscott, K., **Lin, P. -C.**, Kreutzer, U., Chung, Y., Sriram, R., and Jue, T. "Determination of myoglobin concentration in blood-perfused tissue", *Eur J. Appl. Physiol.* **2008**, 104 (1), 41-48
16. **Lin, P. -C.**, Kreutzer, U., and Jue, T. "Anisotropy and temperature dependence of myoglobin translational diffusion in myocardium: implication on oxygen transport and cellular architecture", *Biophysical J.* **2007**, 92 (7), 2608-20
17. **Lin, P. -C.**, Kreutzer, U., and Jue, T. "Myoglobin translational diffusion in myocardium and its implication on intracellular oxygen transport", *J. Physiol.* **2007**, 578 (Pt 2), 595-603

D. Research Support

Ongoing Research Support

CTSA TTR Pilot Award (GHUCCTS)

Lin, P.-C. (PI)

11/01/12-10/31/13

Dynamic contrast enhanced MRI of tumor using targeted nanoparticles

Using dynamic contrast enhanced MRI to study the pharmacokinetics of a novel targeted nanoprobe and its applications to monitor tumor progression and tumor microenvironment non-invasively.

Chapter Eleven

Design Principles of Nanoparticles as Contrast Agents for Magnetic Resonance Imaging

Liang Shan,^{†,‡} Xinbin Gu[§], Paul Wang^{*,†}

[†]*Molecular Imaging Laboratory, Department of Radiology, Howard University, USA*

[‡]*Molecular Imaging and Contrast Agent Database (MICAD), National Institutes of Health, USA*

[§]*Department of Oral Diagnostic Service, Howard University, USA*

Molecular imaging is an emerging field that introduces molecular agents into traditional imaging techniques, enabling visualization, characterization and measurement of biological processes at the molecular and cellular levels in humans and other living systems. The promise of molecular imaging lies in its potential for selective potency by targeting biomarkers or molecular targets and the imaging agents serve as reporters for the selectivity of targeting. Development of an efficient molecular imaging agent depends on well-controlled high-quality experiment design involving target selection, agent synthesis, *in vitro* characterization, and *in vivo* animal characterization before it is applied in humans. According to the analysis from the Molecular Imaging and Contrast Agent Database (MICAD, <http://www.ncbi.nlm.nih.gov/books/NBK5330/>), more than 6000 molecular imaging agents with sufficient preclinical evaluation have been reported to date in the literature and this number increases by 250–300 novel agents each year. The majority of these agents are radionuclides, which are developed for positron emission tomography (PET) and single photon emission computed tomography (SPECT). Contrast agents for magnetic resonance imaging (MRI) account for only a small part. This is largely due to the fact that MRI is currently not a fully quantitative imaging technique and is less

*Corresponding author: pwang@howard.edu

276 | *Nanopharmaceutics: The Potential Application of Nanomaterials*

sensitive than PET and SPECT. However, because of the superior ability to simultaneously extract molecular and anatomic information, molecular MRI is attracting significant interest and various targeted nanoparticle contrast agents have been synthesized for MRI. The first and one of the most critical steps in developing a targeted nanoparticle contrast agent is target selection, which plays the central role and forms the basis for success of molecular imaging. This chapter discusses the design principles of targeted contrast agents in the emerging frontiers of molecular MRI.

Keywords: MRI (magnetic resonance imaging), nanoparticle, molecular imaging.

11.1. INTRODUCTION

A molecular imaging contrast agent is typically composed of one or more labels for signaling the target distribution and density, and ligands for interacting with the targets.¹⁻³ Successful imaging needs certain parameters to be met for an agent. First, the ligand for targeting should be biocompatible and safe in living subjects and its binding affinity with targets is not negatively influenced by the presence of imaging labels and/or other components. Second, the agent as an intact unit should be easily delivered, is small enough to extravasate if given systemically, and is able to accumulate at the site of interest at a concentration sufficient to evoke visible contrast in imaging. One critical issue for agent design is selection of the targets.⁴⁻⁶ Most sensitive targets have been established in the clinically diagnosed diseases and often at advanced stages. Few targets are sensitive to cancer and other lesions at their early stages. Limited amount of target products for ligand binding is another major reason for failure to image early lesions. These issues require imaging agents to be highly specific, particularly considering of the limited sensitivity of magnetic resonance imaging (MRI). MRI detects the interaction of nuclei with each other and with surrounding molecules in the tissue of interest. Although it offers good depth penetration, high spatial resolution, and superior ability to extract molecular and anatomic information simultaneously, MRI is much less sensitive and is not a fully quantitative method with respect to other imaging technologies.^{7,8} Gadolinium (Gd^{3+}) is only reliably detected at the level of 10^{-4} M, although iron oxide nanoparticles can

be detected at 10^{-8} M range.⁹⁻¹² Similar to the agents for other imaging modalities, the majority of MRI contrast agents have been designed by targeting cell surface receptors.^{1,5,13,14} Cell surface receptors are easily accessed and provide a large number of available targets for ligand binding (~100 million per cell). Furthermore, surface receptors undergo repeated endocytosis and recycles, which is critical for designing MRI agents. With representative targets as examples, the principles for active and inverse active targeting, cell tracking, and hyperpolarized carbon-13 magnetic resonance spectroscopic imaging (¹³C MRSI) are discussed in this chapter. The targets discussed here include epidermal growth factor (EGF) family of tyrosine kinase (TK) receptors, $\alpha_v\beta_3$ integrin, vascular endothelial growth factor (VEGF) family, transferrin receptors (TfR), gastrin-releasing peptide receptors (GRPR), asialoglycoprotein receptors (ASGPR), and metabolic enzymes.

11.2. ACTIVE TARGETING TO RECEPTORS ON TUMOR CELL SURFACE

11.2.1. EGF Family of TK Receptors

The EGF family of TK receptors is a group of four structurally related receptor TKs: EGFR (ErbB1), HER2 (ErbB2), ErbB3, and ErbB4.^{13,15,16} All members consist of an extracellular domain, a transmembrane domain and a cytoplasmic TK domain. Under physiological conditions, EGFR is activated upon binding with EGF or transforming growth factor α . To date, HER2 has no known direct activating ligands, but is thought to be activated constitutively or following heterodimerization with other family members.

Mutation, amplification and misregulation of the EGF family are implicated in about 30% of all epithelial cancers.^{17,18} They have been attracting significant attention for developing targeted therapy and imaging with monoclonal antibodies (mAbs), antibody fragments, peptides, and small molecules. Trastuzumab (trade name: herceptin) is the first mAb that is approved by the United States Food and Drug Administration for treatment of HER2-positive breast cancers.¹³ Trastuzumab is a humanized IgG1 against the extracellular domain of HER2 with an affinity constant of 0.1 nM. Besides the successful use in cancer therapy, this antibody has also been applied for tumor characterization with imaging techniques. Lee *et al.* coupled trastuzumab with magnetism-engineered iron

oxide.¹⁹ The generated nanoparticles (~6 mAbs/nanoparticle) accumulated specifically in the HER2-positive NIH3T6.7 tumors with R2 increase for 25% at 1 h and 34% at 2 h after intravenous injection. Yang *et al.* conjugated anti-HER2 mAbs on the surface of poly(amino acid)-coated iron oxide nanoparticles and have shown that the targeted nanoparticles enhanced the signal intensity in imaging and presented excellent detection ability for breast cancer.²⁰

In general, the targeting antibodies should exhibit rapid tissue penetration, high target retention, and rapid blood clearance. Intact mAbs (~150 kDa) suffer from low blood clearance and incomplete tumor penetration.²¹ These disadvantages of mAbs are partially overcome by using recombinant single chain variable fragments (scFv).²² Monovalent scFv (25–30 kDa) represents the smallest functional component of an antibody, and is efficient in tumor penetration. Usefulness of the HER2 and EGFR scFv and iron oxide conjugates as MRI contrast agents has been demonstrated in mouse models of cancer. However, scFv fragments are usually cleared rapidly from blood and have poor binding affinity and tumor retention. Bivalent antibodies such as diabodies (55–60 kDa) and minibodies (~80 kDa) possess more ideal tumor-targeting characteristics such as compact size and high binding affinity.^{21–23} Diabodies are dimeric molecules consisting of two scFv fragments connected with a short linker. Minibodies are formed by fusion of scFv fragments with IgG1 CH3 domain. Improved affinity of bivalent antibodies relies on binding and rebinding as well as simultaneous binding to different molecules of antigens. Affibodies represent a group of small high affinity proteins (~6 kDa) which behave as antibodies.^{15,22,24} They are engineered to bind specifically to a large number of target proteins or peptides. Kinoshita *et al.* applied a combined strategy for imaging HER2-positive tumors with streptavidin-functionalized superparamagnetic iron oxide (SPIO) particles and biotinylated HER2-specific affibody molecules.²⁵ In this system, affibody molecules bind with HER2 on tumor cells, while SPIO binds with affibodies through interaction of streptavidin and biotin. One disadvantage for this strategy is the difficulty to optimize the pharmacokinetics of both components regardless of whether they are administered together or separately.

One specific mutation of EGFR, EGFRvIII, is frequently detected in a number of solid tumors including glioblastoma multiforme, breast adenocarcinoma, medulloblastoma, and ovarian adenocarcinoma, but this mutation has rarely been observed in normal tissue.¹⁸ EGFRvIII

results from an in-frame deletion of exons 2–7 of the wild type EGFR and creates a highly immunogenic tumor specific antigen. Conjugates of SPIO or Gd^{3+} with antibodies that selectively bind with EGFRvIII mutant protein provide selective MRI contrast enhancement of the tumor cells with EGFRvIII mutation.¹⁵ MRI with targeted contrast agents provides a means to detect the tumors with specific molecular alterations, which is critical for personalized treatment.

11.2.2. Vascular Surface Receptors

Angiogenesis is a process of neovascular development and growth from pre-existing vessels.²⁶ Unlike the normal blood vessel system, the neovasculature is chaotic and irregular in tumors. A large set of vascular surface biomarkers have been established such as the VEGF family, integrins, matrix metalloproteinases, endoglin, and E-selectin.^{6,27,28} The vessel biomarkers have the advantage of fewer kinetic compartments that must be crossed for an intravenously administered agent to reach its target. Success of the antiangiogenic treatment and expectation of an increasing number of the antiangiogenic agents to enter clinic in the near future spur the strong demand for imaging to determine the optimal doses of antiangiogenic agents and to evaluate the tumor response. Because MRI is sensitive to blood volume and blood flow changes resulted from antiangiogenic therapy, dynamic contrast-enhanced MRI has been used to study the vascular volume fraction and permeability. Different from traditional MRI, MRI with a vessel biomarker-targeted agent reflects the differential rate of new vessel formation. VEGF family and integrin $\alpha_v\beta_3$ are the most intensively investigated targets for imaging and antiangiogenic therapy.²⁹

The VEGF family consists of six growth factors (VEGF-A, -B, -C, -D, -E, and placental growth factor) and three high-affinity TK receptors (VEGF receptors 1–3 (VEGFR1, 2, and 3)).^{27,30} This family plays a central role in the regulation of angiogenesis and all members, in particular the VEGFR2, are expressed exclusively on endothelial cells of tumor neovasculature. Antibody- and peptide-conjugated Gd^{3+} or SPIO nanoparticles have been shown to enable assessment of the heterogeneous characteristics of VEGFR2 expression associated with angiogenesis.³⁰ Integrins are transmembrane glycoproteins with two noncovalently bound α and β subunits. Integrins comprise a large family of cell adhesion molecules, and among all 24 integrins discovered

to date, the integrin $\alpha_v\beta_3$ is most extensively studied.²⁹ Integrin $\alpha_v\beta_3$ is minimally expressed in normal blood vessels but is significantly overexpressed in newly sprouting vasculature in tumors.³¹ Various imaging agents targeting integrin $\alpha_v\beta_3$ have been developed with antibodies, peptides, and small molecules. For example, Gutheil *et al.* have reported that the Vitaxin-2-conjugated, Gd^{3+} -encapsulated nanoparticles could provide enhanced and detailed imaging of angiogenic “hot spots” that are not seen with standard MRI in a rabbit carcinoma model.³² Vitaxin is a humanized antibody against integrin $\alpha_v\beta_3$. Compared with intact mAbs, small peptides have been more widely investigated for imaging tumor neovasculature and the representative peptides include arginine-glycine-aspartic acid (RGD), asparagine-glycine-arginine, histidine-glycine-phenylalanine, and arginine-arginine-leucine.^{33,34} The RGD tripeptide sequence is an adhesive protein recognition site, presenting in the extracellular matrix and in blood. Integrin $\alpha_v\beta_3$ binds extracellular matrix proteins through the exposed RGD tripeptide sequence. Both linear and cyclic RGD peptide-based agents have been proven to be valuable in imaging neovasculature. In general, RGD peptides are less selective (binding with 8 of the 24 integrins), degrade rapidly *in vivo* and have a relatively low binding affinity. Cyclic peptides are superior to linear peptides for their pharmacokinetics because cyclic peptides are trapped in the active conformation and thus more resistant to proteolysis.³⁵ The pharmacokinetic behaviors of RGD peptides can be further improved with introduction of sugar moieties or by coupling with a chelating agent or polyethylene glycol.³⁶ Because of the low sensitivity, RGD- Gd^{3+} conjugates appear less useful in vessel imaging than RGD-SPIO conjugates. The later enables identification of the heterogeneous distribution of integrin $\alpha_v\beta_3$ -positive tumor vessels, showing an irregular signal intensity decrease in T2-weighted images. Recently, several classes of peptidomimetic antagonists have been synthesized, which consist of a rigid core scaffold bearing basic and acidic groups that mimic the guanidine and carboxylate groups of the RGD sequence.^{37,38} Peptidomimetic antagonist-conjugated magnetic nanoparticles have been demonstrated to be able to show very small regions ($\sim 30\text{ }\mu\text{m}^3$) of angiogenesis, which may enable phenotyping and staging of early tumors in a clinical setting. Improving the binding affinity and increasing the circulation time of peptide- and small molecule-based agents are still the key points for successful imaging of angiogenesis.

11.2.3. TfR

TfR is a cell-surface internalizing receptor, which is regulated by the iron concentration inside the cells. This receptor is normally expressed in a limited number of tissues at a low level, but is overexpressed in a variety of solid tumors and hematologic malignancies.^{39,40} The TfR level on breast cancer cells reaches up to 5-fold higher than its level on normal ductal cells. Transferrin (Tf) is the endogenous ligand of TfR, which binds with Fe^{3+} and delivers it to vertebrate cells through TfR-mediated endocytosis. Conjugates of human Tf with SPIO or Gd^{3+} have been tested for a long time in molecular imaging.¹⁰ In our laboratory, we have developed a series of TfR-targeted probes using Tf and anti-TfR scFv fragments as ligands.⁴⁰ TfR-mediated endocytosis of SPIO or Gd^{3+} allows *in vivo* detection of small tumors with MRI.

Gene reporters have recently been integrated into molecular imaging.^{41,42} The ability to image transgene localization and expression *in vivo* and in real-time has been changing the way of gene transfer studies. Imaging with gene reporters makes it possible to answer practical questions of a gene therapy paradigm in clinical application.⁴³ This technology eliminates the need for animal- and labor-intensive studies. One example is the application of Tf-TfR system.⁴² Moore *et al.* transfected a mutant form of human TfR into the rat 9L gliosarcoma cell line causing the cells to constitutively overexpress the engineered human TfR.^{44,45} Due to the absence of the iron-regulatory region and the mRNA destabilization motifs in the 3' untranslated region, the engineered TfR lacks the feedback of down-regulation in response to iron uptake. The engineered TfR can be probed with human holo-Tf that is covalently conjugated with monocrystalline iron-oxide nanoparticles. The MRI signal intensity is correlated with the expression level of engineered human TfR. This strategy allows us to quantify and characterize the expression of engineered human TfR with MRI.⁴⁴ Furthermore, a gene of interest can be fused with engineered TfR and its expression *in vivo* can be quantified and monitored with detection of TfR as a marker gene.

11.3. INVERSE ACTIVE TARGETING TO RECEPTORS ON NORMAL CELLS

Most target receptors are overexpressed on tumor cells and targeting these receptors has been shown to be useful for tumor detection, staging,

and evaluation of treatment response. This strategy, however, does not work well in some situations as many of the receptors are also expressed by normal cells and some receptors are under-expressed on tumor cells. An inverse strategy, targeting the receptors expressed on normal cells, has been applied by some investigators for designing imaging agents. One representative receptor is the GRPR, a glycosylated G-protein-coupled receptor.^{46,47} GRPR normally expresses on non-neuroendocrine cells of the breast and pancreas, and on neuroendocrine cells of the brain, gastrointestinal tract, lung, and prostate. GRPR has been found to be overexpressed in a large number of tumors, but rarely expressed in pancreas ductal adenocarcinoma (PDAC).⁴⁸ This offers a promising approach to design bombesin (BN)-based agents to detect early PDAC by targeting GRPR on normal pancreatic cells. BN peptide is an analogue of human gastrin-releasing peptide (GRP) that binds with GRPR. GRP and BN share an identical C-terminal region (-Trp-Ala-Val-Gly-His-Leu-Met-NH₂), which is necessary for receptor binding and signal transduction.⁴⁹ BN derivatives have been designed based on either truncated or full-length BN. Conjugates of BN analogues with iron oxide have been shown to be able to decrease the T2 of normal pancreas, thus enhance the ability to visualize tumors in animal models of pancreatic cancer.⁴⁸

Another representative receptor studied with the inverse strategy is ASGPR which is expressed on normal hepatocytes and plays a major role in hepatic clearance of galactosyl moiety-possessing serum ASGP.⁵⁰ Upon binding with ASGPR, ASGP is endocytosed, degraded in the lysosomes, and then excreted into the bile, while ASGPR is recycled to the cell surface. ASGPR expression is absent or at a low level on some hepatocellular carcinomas and metastatic lesions. Targeting the normal cells instead of the tumor cells enhances the visualization of tumors in liver and provides a means for differential diagnosis. An example with this strategy is the agent developed by Yoshinori *et al.* who have conjugated the hydrophilic polysaccharide chitosan with Gd-DTPA and then functionalized the conjugate with lactobionic acid.⁵¹ Lactobionic acid includes a galactose that interacts with ASGPR. This contrast agent exhibits marked T1-enhancement of the normal hepatocytes compared to the signal strength of the liver cancer cells in a rat model of tumors.

Because of the findings that both the number of ASGPR and its function are significantly reduced in the settings of various liver diseases and after liver resection, the blood clearance and binding with ASGPR for galactosylated ligands are considered to be an indicator of liver functional

reserve.^{52,53} Lee *et al.* synthesized a dual probe, ^{99m}Tc-labeled DTPA-SPIO-LBA, by functionalizing SPIO nanoparticles with dopamine, followed by conjugation with lactobionic acid.⁵⁴ This dual probe has been confirmed for its targeting specificity to normal hepatocytes with both nuclear imaging and MRI. Li *et al.* conjugated aminated carboxymethylarabinogalactan with Gd-DTPA by ethylenediamine or hexylamine for imaging hepatocytes via ASGPR.⁵⁵ These agents showed specific binding with ASGPR and specific homing in normal hepatocytes. In general, radiolabeled galactosylated ligands have been validated for their usefulness in liver function evaluation, but to date, MRI agents appear less useful because of the difficulty in precise quantification of the ASGPR with MRI.⁵⁶

11.4. CELL TRACKING

Personalized diagnosis and treatment with allogenic or autologous cells have been extensively investigated over the past decade.⁵⁷ For examples, cytotoxic T cells and engineered dendritic cells have been applied for the treatment of hematopoietic and solid tumors.⁵⁸ Genetically modified cells have been used to treat genetic disorders.⁵⁹ Stem cells are under intensive study in the regenerative medicine.⁶⁰ With promising results from these studies, some critical issues remain to be solved such as how to monitor the migration, homing, survival, and function of these cells *in vivo*.⁶¹ The fact that cells labeled with SPIO can be visualized with MRI creates the opportunity to answer these questions. SPIO particles provide a strong change in signal per unit of metal in T2-weighted images. The advantages of using MRI for cell tracking include its high resolution, lack of exposure to ionizing radiation, and its ability to follow the cells *in vivo* for months.^{62,63} Because iron participates in cell metabolism, SPIO particles are well tolerated by living organisms. Cell labeling with SPIO nanoparticles does not seem to affect the proliferation and differentiation capability of the labeled cells, although a few studies have reported that the stem cells labeled with SPIO lose part of their differentiation capacity in a SPIO concentration-dependent manner.^{63,64}

Labeling cells of interest can be achieved in different ways.^{61,62} Cells can be labeled *in situ* by directly injecting the SPIO-based agents into the tissue area of interest and target cell migration can be monitored following phagocytosis. Typically, cells are labeled *in vitro* by incorporating SPIO into the cells.^{62,63} For efficient cell labeling, SPIO particles need to be coated with organic polymers or others. Surface coating also increases the

stability of SPIO, and allows further chemical modification of the particles with ligands. Cell uptake of the SPIO particles depends on the surface modifications as well as cell types. De Vries *et al.* have first described the use of MRI to monitor the fate of transplanted cells.⁶⁵ In that study, autologous dendritic cells loaded with tumor-derived antigenic peptides have been labeled with SPIO. Zhu *et al.* tested the feasibility of tracking SPIO-labeled neural stem cells in patients with brain trauma and Toso *et al.* investigated the MRI-based monitoring of pancreatic islet grafts labeled with SPIO in patients with type 1 diabetes.^{66,67} All these studies have shown that migration and homing of the labeled cells could be monitored *in vivo* over days to months. A well studied example is the labeling and tracking of mesenchymal stem cells (MSCs). MSCs are a heterogeneous group of pluripotent stromal cells that can be isolated from various adult tissues, although the bone marrow remains the principal source for most studies.⁶⁸ These cells have the potential to differentiate into cells of diverse lineages, such as adipocytes, chondrocytes, osteocytes, myoblasts, cardiomyocytes, neurons, and astrocytes.⁶⁰ Therefore, MSCs are one of the major sources in regenerative medicine. Evidence has shown that MSCs can be efficiently and safely labeled *in vitro* with SPIO and as few as 1,000 labeled MSCs can be visualized with MRI *in vivo*.^{61,62} Currently, there are still a lot of challenges to turn cell tracking into a robust technique either in pre-clinical settings or in clinical applications. Most studies are focusing on the ability to visualize the labeled cells with MRI. The question is that the MRI signal cannot indicate whether cells are dead or alive, and whether the signal source comes from labeled cells or from reticuloendothelial system. It is more challenging to quantify the number of labeled cells *in vivo*, and to distinguish viable iron-labeled cells from other sources of iron in tissues. Development of standardized protocols will be crucial to enable comparison between different studies and facilitate translation to clinical application.

11.5. HYPERPOLARIZED ¹³C MRSI

MRSI is a technique allowing non-invasive detection of multiple small metabolites within intracellular or extracellular spaces *in vivo*.^{69,70} MRSI is theoretically applicable to any spin-possessing nuclei; however proton (¹H) and ¹³C are more applicable in reality. Because of the imaging sensitivity and hardware issues, most clinical studies to date are based on a combination of MRI and ¹H-based MRSI (¹H MRSI). The use of ¹³C-based

MRSI is limited because of the low natural abundance of ^{13}C (1.1%) and its low magnetogyric ratio.^{71,72} Several techniques have been developed to enhance the polarization of ^{13}C nuclear spins, including dynamic nuclear polarization (DNP). Electron spins have a ~660 times stronger magnetic moment than the ^1H spins.⁷³ DNP transfers the high electron spins to nuclear spins via microwave irradiation. Nearly 100% nuclear polarization for ^1H and 50% for ^{13}C can be achieved in various organic molecules when DNP is performed in a strong magnetic field and at cryogenic temperatures. However, hyperpolarization of ^1H *in vitro* is less interesting for medical applications, because most of the hyperpolarization would have vanished before the small molecules reach the target organs. In contrast, the chemical shift range for ^{13}C (~250 ppm) is much larger than that for ^1H (~15 ppm), allowing for improved resolution and quantification of each metabolite.⁷¹ Furthermore, the T1 relaxation time of ^{13}C in small molecules (>10 s in a magnetic field of 0.1–3.0 T) is much longer than that of ^1H (0.1–2.0 s). Replacing the ^{12}C (98.9% natural abundance) with ^{13}C at a specific carbon or carbons in a substrate does not affect the substrate's biochemistry. The hyperpolarized solid molecules can be rapidly dissolved in an injectable liquid with small polarization loss, allowing the generation of hyperpolarized ^{13}C -labeled tracers outside the subject and the MRI scanner.⁷⁴ In real practice with ^{13}C MRSI, body tissues are virtually invisible and only regions where the hyperpolarized ^{13}C -labeled substance is present will appear in the generated images. Thus, ^{13}C -labeled substrates provide more than 10,000-fold enhancement of the ^{13}C MRSI signals from the substrate and its subsequent metabolic products.⁷³ The intensity of the ^{13}C signal generated from the injected hyperpolarized ^{13}C -labeled molecules is linearly proportional to its concentration, allowing quantification of the metabolic fluxes *in vivo*. Vascular structure and perfusion can also be imaged without background signal from surrounding tissues.⁷⁵

Pyruvate is the first substrate hyperpolarized and applied successfully to evaluate the metabolic abnormalities in cancer and other diseases.⁷⁴ Pyruvate is normally produced by the glycolysis of glucose and oxidation of lactate, and then converted to acetyl-coenzyme A, CO_2 , and oxaloacetate in mitochondria, and alanine in cytoplasm. The chemical shift values between pyruvate and its metabolites are large enough to be resolved with MRSI. Typically, 20–30% of the carbons in pyruvate can be hyperpolarized with DNP technique. Studies with hyperpolarized ^{13}C -labeled pyruvate in healthy rats showed that pyruvate converts to its metabolites within a minute of injection.⁷⁶ In animal models of human

tumors, the lactate levels are significantly higher in the tumors than in the normal tissues.⁷⁷ The small molecule, α -keto isocaproate (KIC), is another substrate which has been used for evaluation of abnormal metabolism.⁷⁸ KIC is metabolized to leucine by branched chain amino acid transferase (BCAT). BCAT is highly expressed during oncogenesis and its activity can be used as a marker for grading and genetic characterization of tumors. Karlsson *et al.* generated hyperpolarized α -keto[1-¹³C]isocaproate ([1-¹³C] KIC) with polarization of $32 \pm 3\%$ at the time of administration to animals.⁷⁸ The hyperpolarized [1-¹³C]KIC yielded an unprecedented MRI contrast between EL4 murine lymphoma (high BCAT activity) and surrounding healthy tissue, but yielded no contrast between R3230AC rat mammary adenocarcinoma (low BCAT activity) and its surrounding tissue. The signal intensities of the [1-¹³C]KIC and its metabolite [1-¹³C]leucine detected in the two tumor models are well correlated with the BCAT activity, indicating the potential in assessing tissue BCAT activity *in vivo*.⁷⁸ Hyperpolarized [1,4-¹³C₂]fumarate is a ¹³C MRSI agent generated by Gallagher *et al.* for evaluation of early tumor response to treatment.⁷⁹ Fumarate, a tricarboxylic acid cycle intermediate, is catalyzed to malate by fumarase. The investigators showed that [1,4-¹³C₂]malate production from [1,4-¹³C₂]fumarate is increased in drug-treated lymphoma cells and tumors, and that this increase is caused by tumor cell necrosis. The formation of hyperpolarized [1,4-¹³C₂]malate from [1,4-¹³C₂]fumarate appears to be a sensitive marker of tumor cell death *in vivo* and could be used to detect the early response of tumors to treatment.

Extracellular acidosis is a hallmark of the tumor microenvironment at both early and advanced stages of tumor development.^{80,81} The extracellular pH (pH_e) can be as low as 6.0, while the intracellular pH (pH_i) maintains at 7.2–7.4. Extracellular acidosis results in a pH gradient across the tumor cell membrane and a peritumoral acid gradient.⁸² Hypoxia in tumors is believed to be the main mechanism. Extracellular acidosis affects many aspects of tumor physiology and therapeutic agent delivery. Measurement of tissue pH is of great value in diagnosis and treatment. It has been known that HCO₃⁻ is the primary extracellular buffer that maintains pH through interconversion with CO₂ by carbonic anhydrase. In theory, tissue pH should be able to be determined with ¹³C MRSI by measuring the concentration ratio of H¹³CO₃⁻ to ¹³CO₂ on the basis of the Henderson–Hasselbalch equation.⁸¹ Gallagher *et al.* tested the feasibility of measuring tissue pH with hyperpolarized H¹³CO₃⁻.⁸¹ In mice bearing murine lymphoma tumors, spectra of H¹³CO₃⁻ and ¹³CO₂ from tumor slices

(5 mm thick) revealed a calculated pH of 6.71 ± 0.14 , compared with that of surrounding tissue of 7.09 ± 0.10 . Administration of sodium bicarbonate in drinking water to animals led to increase of the measured tumor pH, while gavage with ammonium chloride decreased the tumor pH. The pH_i , as estimated from the chemical shift of intracellular inorganic phosphate resonance, remains unchanged regardless of the treatments. These results suggest that MRSI with hyperpolarized $\text{H}^{13}\text{CO}_3^-$ can measure the pH_e . In another study with hyperpolarized $[1-^{13}\text{C}]$ pyruvate, Schroeder *et al.* measured the pH in diseased and healthy cardiomyocytes by detection of hyperpolarized $[1-^{13}\text{C}]$ pyruvate-derived $\text{H}^{13}\text{CO}_3^-$ and $^{13}\text{CO}_2$.⁸³ Their results, however, showed that hyperpolarized $[1-^{13}\text{C}]$ pyruvate appears to measure the pH_i , rather than pH_e . Compared with other methods, ^{13}C MRSI with DNP provides a more precise means to evaluate tissue pH.⁸⁴

11.6. CONCLUSION

Molecular imaging as an important emerging diagnostic tool is based on the concept that targeted delivery of contrast agents can specifically increase the signal-to-noise ratio by targeting the difference in molecular profiles between diseased and normal tissues. Progress in molecular imaging is yielding important clinical benefits and at the same time, is resulting in new application fields. Multimodal imaging is a rapidly growing field.⁸⁵ The idea of using multiple imaging modalities in a single imaging session comes from the fact that modalities with high sensitivity have relatively poor resolution, while those with high resolution have relatively poor sensitivity.⁸⁶ Multimodal imaging would take the advantages of each modality and allow better characterization of diseases and disease processes. To date, the most successful hybrid system is derived from the fusion of PET and computed tomography (CT).^{87,88} PET is highly sensitive and allows three-dimensional images that show the tracer's concentration and location, while CT provides high-resolution imaging of the anatomical structures. Because of the limited soft-tissue contrast and high X-ray radiation that accompany CT imaging, considerable effort has been invested in recent years toward development of PET/MRI hybrid systems in an attempt to generate combined functional and morphological images with excellent soft tissue contrast, good spatial resolution of the anatomy, and accurate temporal and spatial image fusion.⁸⁸ Development of hybrid imaging technology has triggered great effort in probe development to boost the benefits of hybrid instrument

technology.^{86,89,90} The design principle for multimodal agents is similar to that for single modal agents. The difference is multiple reporters attached to each agent. Thus, there is the additional challenge to incorporate enough reporters without negatively influencing each other, in particular considering the relatively low sensitivity of MRI. Although multimodality imaging is still at its infancy, it is safe to predict that multimodality imaging techniques will play a leading role in clinical applications. Another new field is the use of molecular imaging in drug discovery and development.^{13,91} Molecular imaging can aid in many steps of the drug development process, such as providing whole body readout in an intact system, decreasing the workload, and facilitating development of personalized medicine.^{92,93} Microdose studies with imaging probes provide an opportunity for early assessment of the safety profile and pharmacokinetics of new drugs in healthy volunteers.^{94,95} The Food and Drug Administration has recently developed exploratory investigational new drug mechanism to allow faster first-in-human studies. In the foreseeable future, molecular imaging will be routinely applied in many steps of the drug development. On the other hand, despite the strong potentials of molecular imaging in various aspects of medicine, most of the research efforts have so far been limited to agent synthesis, optimization for enhanced efficacy, and improvement of agents *in vivo* kinetics. Translation from bench to bedside is slow for the targeted molecular imaging probes. Only a very small number of targeted imaging agents have so far been approved for clinical use. Simplifying the complexity of the synthesized nanoparticles and establishing standardized criteria and protocols for assessing and comparing potential agents are critical challenges that must be overcome for the field to move forward.

ACKNOWLEDGEMENT

This work was supported in part by the US DOD W81XWH-10-1-0767 grant and the NIH/NCRR/RCMI 2 G12 RR003048 grant.

REFERENCES

1. Alford R, Ogawa M, Choyke PL, Kobayashi H, *Mol Biosyst*, **5**, 1279 (2009).
2. Arbab AS, Janic B, Haller J, Pawelczyk E, Liu W, Frank JA, *Curr Med Imaging Rev*, **5**, 19 (2009).

3. Burtea C, Laurent S, Vander Elst L, Muller RN, *Handb Exp Pharmacol*, **135** (2008).
4. Cormode DP, Skajaa T, Fayad ZA, Mulder WJ, *Arterioscler Thromb Vasc Biol*, **29**, 992 (2009).
5. Van Beers BE, Vilgrain V, *Abdom Imaging*, **34**, 663 (2009).
6. Elias DR, Thorek DL, Chen AK, Czupryna J, Tsourkas A, *Cancer Biomark*, **4**, 287 (2008).
7. Blamire AM, *Br J Radiol*, **81**, 601 (2008).
8. Valliant JF, *J Nucl Med*, **51**, 1258 (2010).
9. Laurent S, Boutry S, Mahieu I, Vander Elst L, Muller RN, *Curr Med Chem*, **16**, 4712 (2009).
10. Islam T, Josephson L, *Cancer Biomark*, **5**, 99 (2009).
11. Hermann P, Kotek J, Kubicek V, Lukes I, *Dalton Trans*, **23**, 3027 (2008).
12. Hofmann-Antenbrink M, Hofmann H, Montet X, *Swiss Med Weekly*, **140**, w13081 (2010).
13. Capala J, Bouchelouche K, *Curr Opin Oncol*, **22**, 559 (2010).
14. Glunde K, Jacobs MA, Pathak AP, Artemov D, Bhujwalla ZM, *NMR Biomed*, **22**, 92 (2009).
15. Lyakhov I, Zielinski R, Kuban M, Kramer-Marek G, Fisher R, Chertov, O.; Bindu L, Capala J, *Chem Bio Chem*, **11**, 345 (2010).
16. Sorkin A, Goh LK, *Exp Cell Res*, **314**, 3093 (2008).
17. Harari PM, Allen GW, Bonner JA, *J Clin Oncol*, **25**, 4057 (2007).
18. Irmer D, Funk JO, Blaukat A, *Oncogene*, **26**, 5693 (2007).
19. Lee JH, Huh YM, Jun YW, Seo JW, Jang JT, Song HT, Kim S, Cho EJ, Yoon HG, Suh JS, Cheon J, *Nat Med*, **13**, 95 (2007).
20. Yang HM, Park CW, Woo MA, Kim MI, Jo YM, Park HG, Kim JD, *Biomacromolecules*, **11**, 2866 (2010).
21. Kortt AA, Dolezal O, Power BE, Hudson PJ, *Biomol Eng*, **18**, 95 (2001).
22. Gronwall C, Stahl S, *J Biotechnol*, **140**, 254 (2009).
23. Chames P, Baty D, *Curr Opin Drug Discov Devel*, **12**, 276 (2009).
24. Olafsen T, Wu AM, *Semin Nucl Med*, **40**, 167 (2010).
25. Kinoshita M, Yoshioka Y, Okita Y, Hashimoto N, Yoshimine T, *Contrast Media Mol Imaging*, **5**, 18 (2010).
26. Turkbey B, Kobayashi H, Ogawa M, Bernardo M, Choyke PL, *AJR Am J Roentgenol*, **193**, 304 (2009).
27. Murukesh N, Dive C, Jayson GC, *Br J Cancer*, **102**, 8 (2010).
28. Cai W, Niu G, Chen X, *Curr Pharm Des*, **14**, 2943 (2008).
29. Beer AJ, Schwaiger M, *Cancer Metastasis Rev*, **27**, 631 (2008).

30. Jun HY, Yin HH, Kim SH, Park SH, Kim HS, Yoon KH, *Korean J Radiol*, **11**, 449 (2010).
31. Beer AJ, Niemeyer M, Carlsen J, Sarbia M, Nahrig J, Watzlowik P, Wester HJ, Harbeck N, Schwaiger M, *J Nucl Med*, **49**, 255 (2008).
32. Gutheil JC, Campbell TN, Pierce PR, Watkins JD, Huse WD, Bodkin DJ, Cheresch DA, *Clin Cancer Res*, **6**, 3056 (2000).
33. Dijkgraaf I, Beer AJ, Wester HJ, *Front Biosci*, **14**, 887 (2009).
34. Lim EH, Danthi N, Bednarski M, Li KC, *Nanomedicine*, **1**, 110 (2005).
35. Liu S, *Mol Pharm*, **3**, 472 (2006).
36. Dijkgraaf I, Kruijtz JA, Liu S, Soede AC, Oyen WJ, Corstens FH, Liskamp RM, Boerman OC, *Eur J Nucl Med Mol Imaging*, **34**, 267 (2007).
37. Coleman PJ, Brashear KM, Askew BC, Hutchinson JH, McVean CA, Duong le T, Feuston BP, Fernandez-Metzler C, Gentile MA, Hartman GD, Kimmel DB, Leu CT, Lipfert L, Merkle K, Pennypacker B, Prueksaritanont T, Rodan GA, Wesolowski GA, Rodan SB, Duggan ME, *J Med Chem*, **47**, 4829 (2004).
38. Wang J, Breslin MJ, Coleman PJ, Duggan ME, Hunt CA, Hutchinson JH, Leu CT, Rodan SB, Rodan GA, Duong le T, Hartman GD, *Bioorg Med Chem Lett*, **14**, 1049 (2004).
39. Weaver M, Laske DW, *J Neurooncol*, **65**, 3 (2003).
40. Shan L, Wang S, Sridhar R, Bhujwalla ZM, Wang PC, *Mol Imaging*, **6**, 85 (2007).
41. Cohen B, Ziv K, Plaks V, Harmelin A, Neeman M, *Wiley Interdiscip Rev Nanomed Nanobiotechnol*, **1**, 181 (2009).
42. Gilad AA, Ziv K, McMahon MT, van Zijl PC, Neeman M, Bulte JW, *J Nucl Med*, **49**, 1905 (2008).
43. Waerzeggers Y, Monfared P, Viel T, Winkeler A, Voges J, Jacobs AH, *Methods*, **48**, 146 (2009).
44. Moore A, Josephson L, Bhorade RM, Basilion JP, Weissleder R, *Radiology*, **221**, 244 (2001).
45. Moore A, Basilion JP, Chiocca EA, Weissleder R, *Biochim Biophys Acta*, **1402**, 239 (1998).
46. Weber HC, *Curr Opin Endocrinol Diabetes Obes*, **16**, 66 (2009).
47. Maina T, Nock BA, Zhang H, Nikolopoulou A, Waser B, Reubi JC, Maecke HR, *J Nucl Med*, **46**, 823 (2005).
48. Montet X, Weissleder R, Josephson L, *Bioconjug Chem*, **17**, 905 (2006).
49. Ischia J, Patel O, Shulkes A, Baldwin GS, *Biofactors*, **35**, 69 (2009).
50. Sugahara K, Togashi H, Takahashi K, Onodera Y, Sanjo M, Misawa K, Suzuki A, Adachi T, Ito J, Okumoto K, Hattori E, Takeda T, Watanabe H, Saito K, Saito T, Sugai Y, Kawata S, *Hepatology*, **38**, 1401 (2003).

51. Yoshinori M, Masaharu M, Yuri H, Sayoko N, Nao S, Makoto H, *Magn Reson Imaging*, **28**, 708 (2010).
52. Huang G, Diakur J, Xu Z, Wiebe LI, *Int J Pharm*, **360**, 197 (2008).
53. Chaumet-Riffaud P, Martinez-Duncker I, Marty AL, Richard C, Prigent A, Moati F, Sarda-Mantel L, Scherman D, Bessodes M, Mignent N, *Bioconjug Chem*, **21**, 589 (2010).
54. Lee CM, Jeong HJ, Kim EM, Kim DW, Lim ST, Kim HT, Park IK, Jeong YY, Kim JW, Sohn MH, *Magn Reson Med*, **62**, 1440 (2009).
55. Li W, Li Z, Jing F, Deng Y, Wei L, Liao P, Yang X, Li X, Pei F, Wang X, Lei H, *Carbohydr Res*, **343**, 685 (2008).
56. Kokudo N, Vera DR, Makuuchi M, *Nucl Med Biol*, **30**, 845 (2003).
57. Hong H, Yang Y, Zhang Y, Cai W, *Curr Top Med Chem*, **10**, 1237 (2010).
58. Cesco-Gaspere M, Morris E, Stauss HJ, *Clin Exp Med*, **9**, 81 (2009).
59. Bachoud-Levi AC, *Lancet Neurol*, **8**, 979 (2009).
60. Sadan O, Melamed E, Offen D, *Expert Opin Biol Ther*, **9**, 1487 (2009).
61. Hoehn M, Wiedermann D, Justicia C, Ramos-Cabrer P, Kruttwig K, Farr T, Himmelreich U, *J Physiol*, **584**, 25 (2007).
62. Himmelreich U, Dresselaers T, *Methods*, **48**, 112 (2009).
63. Arbab AS, Liu W, Frank JA, *Expert Rev Med Devices*, **3**, 427 (2006).
64. Arbab AS, Bashaw LA, Miller BR, Jordan EK, Lewis BK, Kalish H, Frank JA, *Radiology*, **229**, 838 (2003).
65. de Vries IJ, Lesterhuis WJ, Barentsz JO, Verdijk P, van Krieken JH, Boerman OC, Oyen WJ, Bonenkamp JJ, Boezeman JB, Adema GJ, Bulte JW, Scheenen TW, Punt CJ, Heerschap A, Figdor CG, *Nat Biotechnol*, **23**, 1407 (2005).
66. Zhu J, Zhou L, XingWu F, *N Engl J Med*, **355**, 2376 (2006).
67. Toso C, Vallee JP, Morel P, Ris F, Demuylder-Mischler S, Lepetit-Coiffe M, Marangon N, Saudek F, James Shapiro AM, Bosco D, Berney T, *Am J Transplant*, **8**, 701 (2008).
68. Mathiasen AB, Haack-Sorensen M, Kastrup J, *Future Cardiol*, **5**, 605 (2009).
69. Pinker K, Stadlbauer A, Bogner W, Gruber S, Helbich TH, *Eur J Radiol*, doi:10.1016/j.ejrad.2010.04.028 (2010).
70. Prost RW, *Med Phys*, **35**, 4530 (2008).
71. Kurhanewicz J, Bok R, Nelson SJ, Vigneron DB, *J Nucl Med*, **49**, 341 (2008).
72. Mansson S, Johansson E, Magnusson P, Chai CM, Hansson G, Petersson JS, Stahlberg F, Golman K, *Eur Radiol*, **16**, 57 (2006).
73. Ardenkjaer-Larsen JH, Fridlund B, Gram A, Hansson G, Hansson L, Lerche MH, Servin R, Thaning M, Golman K, *Proc Natl Acad Sci USA*, **100**, 10158 (2003).

292 | Nanopharmaceutics: The Potential Application of Nanomaterials

74. Albers MJ, Bok R, Chen AP, Cunningham CH, Zierhut ML, Zhang VY, Kohler SJ, Tropp J, Hurd RE, Yen YF, Nelson SJ, Vigneron DB, Kurhanewicz J, *Cancer Res*, **68**, 8607 (2008).
75. Olsson LE, Chai CM, Axelsson O, Karlsson M, Golman K, Petersson JS, *Magn Reson Med*, **55**, 731 (2006).
76. Golman K, Zandt RI, Lerche M, Pehrson R, Ardenkjaer-Larsen JH, *Cancer Res*, **66**, 10855 (2006).
77. Day SE, Kettunen MI, Gallagher FA, Hu DE, Lerche M, Wolber J, Golman K, Ardenkjaer-Larsen JH, Brindle KM, *Nat Med*, **13**, 1382 (2007).
78. Karlsson M, Jensen PR, Zandt RI, Gisselsson A, Hansson G, Duus JO, Meier S, Lerche MH, *Int J Cancer*, **127**, 729 (2009).
79. Gallagher FA, Kettunen MI, Hu DE, Jensen PR, Zandt RI, Karlsson M, Gisselsson A, Nelson SK, Witney TH, Bohndiek SE, Hansson G, Peitersen T, Lerche MH, Brindle KM, *Proc Natl Acad Sci USA*, **106**, 19801 (2009).
80. Fukumura D, Jain RK, *J Cell Biochem*. **101**, 937 (2007).
81. Gallagher FA, Kettunen MI, Day SE, Hu DE, Ardenkjaer-Larsen JH, Zandt R, Jensen PR, Karlsson M, Golman K, Lerche MH, Brindle KM, *Nature*, **453**, 940 (2008).
82. Lunt SJ, Chaudary N, Hill RP, *Clin Exp Metastasis*, **26**, 19 (2009).
83. Schroeder MA, Swietach P, Atherton HJ, Gallagher FA, Lee P, Radda GK, Clarke K, Tyler DJ, *Cardiovasc Res*, **1**, 86(1), 82 (2010).
84. Penet MF, Glunde K, Jacobs MA, Pathak AP, Bhujwalla ZM, *J Nucl Med*, **49**, 687 (2008).
85. Cherry SR, *Annu Rev Biomed Eng*, **8**, 35 (2006).
86. Jennings LE, Long NJ, *Chem Commun (Camb)*, **24**, 3511 (2009).
87. Cherry SR, *Semin Nucl Med*, **39**, 348 (2009).
88. Boss A, Bisdas S, Kolb A, Hofmann M, Ernemann U, Claussen CD, Pfannenberger C, Pichler BJ, Reimold M, Stegger L, *J Nucl Med*, **51**, 1198 (2010).
89. Lee S, Chen X, *Mol Imaging*, **8**, 87 (2009).
90. Louie A, *Chem Rev*, **110**, 3146 (2010).
91. Hargreaves RJ, *Clin Pharmacol Ther*, **83**, 349 (2008).
92. Fox GB, Chin CL, Luo F, Day M, Cox BF, *Mol Interv*, **9**, 302 (2009).
93. Lee CM, Farde L, *Trends Pharmacol Sci*, **27**, 310 (2006).
94. Bauer M, Wagner CC, Langer O, *Drugs R D*, **9**, 73 (2008).
95. Komoda F, Suzuki A, Yanagisawa K, Inoue T, *Ann Nucl Med*, **23**, 829 (2009).

Essential Elements to Consider for MRI Cell Tracking Studies with Iron Oxide-based Labeling Agents

Paul C. Wang^{1*}, Liang Shan²

¹Molecular Imaging Laboratory, Department of Radiology, Howard University, Washington DC and ²Molecular Imaging and Contrast Agents Database, National Center for Biotechnology Information, National Library of Medicine, MD

Journal of Basic & Clinical Medicine 2012, 1(1):1-6

Abstract

Personalized diagnosis and treatment with allogenic or autologous cells have been intensively investigated over the past decade. Despite the promising findings in preclinical studies, the clinical results to date have been largely disappointing. Some critical issues remain to be solved, such as how to monitor the migration, homing, survival, and function of the transplanted cells *in vivo*. In the past years, imaging techniques have been introduced to solve these issues based on a concept that cells can be transformed to a cellular imaging agent following labeling of the cells with an imaging agent. For this purpose, magnetic resonance imaging (MRI) is so far the first choice imaging modality and iron oxide-based nanoparticles are the most frequently applied labeling agents. However, most MRI cell tracking studies are currently still limited in *in vivo* visualization of the labeled cells, some critical elements for cell tracking studies are often incompletely characterized, which makes it difficult to validate and meta-analyze the data generated from different studies. Incomplete information on preclinical studies also slows the transition of the findings to clinical practice. A robust protocol of MRI cell tracking studies is apparently critical to deal with these issues. In this review, we first briefly discuss the limitations of MRI cell tracking based on iron oxide nanoparticles and then recommend a minimum set of essential elements that should be considered in MRI cell tracking studies at preclinical stage.

Keywords: Contrast agents, characterization, cell tracking, magnetic resonance imaging

Introduction

How to monitor the migration and homing of transplanted cells as well as their engraftment efficiency and functional capability remains a critical issue to be solved in the field of cellular therapy (1, 2). Because magnetic resonance imaging (MRI) offers a good depth penetration and high spatial resolution, and exhibits a superior ability to extract molecular and anatomic information simultaneously, it has been actively investigated in past years and so far the first choice for tracking implanted cells (3, 4). Fundamentally, MRI cell tracking includes three components: labeling agents, labeling of cells of interest, and MRI tracking. The labeling agents are synthesized with procedures similar to those developed for organ imaging, with more attention in their cellular

internalization, intracellular retention, and cytotoxicity. Cell labeling can be achieved through three ways: 1) *in vivo* labeling by systemic application of a contrast agent with subsequent phagocytosis of the agent by the cells of interest; 2) *in situ* labeling by injection of a contrast agent into the tissue area of interest to label the local cells; and 3) *ex vivo* labeling by incorporation of a contrast agent into a population of purified cells *in vitro* (4, 5). To date, *ex vivo* cell labeling is the approach that has been most frequently applied for cell tracking purpose. With *ex vivo* labeling, excess contrast agents and dead cells can be removed simply; the labeled cells can be thoroughly characterized before transplantation; and non-specific labeling of irrelevant cells can be well controlled by purifying the relevant cell population before labeling (2, 6). Regarding contrast agents, although diverse contrast agents (superparamagnetic, paramagnetic, ferrimagnetic, and ferromagnetic) have been developed, superparamagnetic iron oxide nanoparticles (SPION) are probably the agents that have been most extensively explored so far.

MRI cell tracking studies in animals first started in the early 1990s, however, the first study in humans was performed delayed to 2005 (7-10). In this study, autologous dendritic cells were labeled with SPION and ¹¹¹In-oxiquinolone *ex vivo*. Migration of the cells after intranodal injection was tracked in patients with melanoma with 3T MRI and scintigraphy. With promising results from this study and others reported later, a huge challenge to turn MRI cell tracking into a robust technique for clinical application is the difficulty to study all the relevant features of the labeling contrast agents and the labeled cells *in vivo* (11, 12). None of the labeling agents to date has been approved by the U.S. Food and Drug Administration (FDA) for use specific to label cells in clinical practice. Most clinical investigations on cell tracking are based on the market-available SPION contrast agents, initially developed for enhancing the contrast of diseased lesions. There is a strong need to develop more sensitive and less toxic labeling agents as well as a robust protocol of cell tracking study. The critical elements in cell tracking studies should be characterized as completely as possible for allowing validate meta-analysis between studies and establishing a robust protocol (2). In this review, we will briefly discuss the limitations of MRI cell tracking with iron oxide-based agents and recommend a minimum set of essential elements that should be considered in MRI cell tracking studies (Table 1).

I. Limitations of MRI cell tracking

There are several limitations for MRI cell tracking, especially when long-term tracking of the cells is necessary (6, 11). These limitations are either technical or physiology-pathology-related.

Accepted in September 26, 2012

*Correspondence author, Tel: 202-865-3711; Fax: 202-865-3722

E-mail address: pwang@howard.edu

These limitations can be summarized into four major aspects, which should be considered in designing studies of MRI cell tracking.

1. *Live vs. dead cells*

The signal intensity in MRI depends primarily on the local values of longitudinal and transverse relaxation rates of water protons (13, 14). SPION agents are not detectable themselves, but are detected by their effects on surrounding water protons. When the transplanted cells of interest die, the SPION agents may remain in or around dead cells until the agents are cleared away. These agents produce signal that is detected by MRI. Therefore, the MRI signal cannot indicate whether cells are dead or alive.

2. *False positivity*

Except for the cell death, several other situations can also lead to false-positivity of MRI cell tracking (3, 4). First, endogenous host cells such as macrophages can phagocytize dying or dead SPION-labeled cells and these cells may actively move away from the site of cell implantation. These host cells can be mistaken to be the transplanted cells. Second, certain physiological and pathological conditions can result in hypointense signal, which can be confused with the presence of SPION agents (11). For example, macrophages loaded with hemosiderin from hemorrhage are often present in infarcted myocardium and these cells are indistinguishable from labeled cells of interest. Third, tissues with high iron content such as bone marrow and hemorrhage can lead to misinterpretation of MRI signal.

3. *Dilution of the labeling agents among daughter cells*

Immature cells such as stem cells continue to divide after transplantation. In such cases, the labeled contrast agents are diluted among daughter cells, which results in the loss of MR signal over time (12, 15). This issue is more prominent for rapidly dividing cells and stem cells. Stem cells may divide asymmetrically, leading to an unequal distribution of the labeled agents among daughter cells (16). The unequal distribution not only leaves some cells having less contrast agents and undetectable quickly, but also makes the quantification of cell number less precisely.

4. *Quantification of cell numbers*

Although MRI visualizes cells *in vivo*, cell number quantification is challenging. Cells may be quantified by counting areas of hypointensity against a homogeneous background (e.g., in phantoms) in *in vitro* experiments. However, quantification of absolute cell number *in vivo* can be extremely difficult because of the agent dilution during cell division, agent transfer to other cells or extracellular space, and irons of other sources (14, 17). In addition, MRI quantification of iron concentration is still not reliable, although various mathematical methods have been suggested. There is no clear correlation between the SPION signal and the absolute number of live cells.

II. Essential elements that need to be considered in MRI cell tracking studies

1. *Physicochemical and magnetic properties of the labeling agents*

The fundamentals of labeling agent development are similar to those of contrast agents developed for organ imaging (18, 19). As mentioned above, most labeling agents that have been developed so far are iron oxide (IO, mainly Fe_3O_4)-based. Although most of these nanoparticles are readily taken up by cells

when added to the culture medium, they are often further functionalized with target-specific ligands or internalization-enhancing agents to achieve optimal internalization. A detailed guideline regarding the characterization of MRI contrast agents has been previously proposed by Shan et al. and this guideline is also suitable for characterization of an agent developed for MRI cell labeling (20). All newly developed labeling agents should be thoroughly characterized for their physicochemical properties (chemical yield, chemical purity, structure/composition, size, and shape) and magnetic properties (relaxation time and relaxivity) before cell labeling.

2. *Cell information and labeling condition*

Efficient cell labeling is generally based on receptor-mediated endocytosis, cell phagocytosis, or permeability change of the cell membrane. Besides the characteristics of labeling agents, the labeling efficiency is also dependent on the cell types, cell state, and labeling condition. Some cell types allow for efficient uptake of the nanoparticles (NPs) by mere incubation with the NPs over a 24–48-h period. However, some cell types require additional enhancing methods to take up the labeling agents (6). Even for same type of cells, their growth status is an important determinant for labeling efficiency. Cells at different growth state can exhibit extremely different phagocytotic activities and express different amount of receptors and membrane transport proteins (21, 22). Transient changes of cell membrane permeability with the use of electroporation or ultrasound pulses allow for NP agents to pass through the membrane and into the cytosol, which may be less influenced by the cell types and cell growth status, compared to other labeling mechanisms. Therefore, the cell information includes the cell source, cell type, activation status, culture condition, antigen loading, etc. The cell labeling condition should include the medium, cell density or number, labeling agent concentration, and incubation time.

3. *Cell labeling evaluation: labeling efficiency, intracellular localization, label retention, detection limit, and cytotoxicity*

Labeling efficiency: Stable labeling of cells with a contrast agent is usually achieved through endocytosis, phagocytosis, lipofection, electroporation, or combined (3). Efficient labeling is necessary to maximize the signal that is generated from the label, while long retention within cells is critical to ensure that the label agent is not rapidly lost with time nor transferred to other cells. High stable labeling agents prevent their degradation within cells with time, allowing long-term visualization of the cells. However, agent synthesis is complicated and the materials used for synthesis are quietly diverse, which result in the development of diverse labeling agents that possess physicochemical and biological properties significantly different from the parent compounds and from each other. Furthermore, many other factors such as the cell type, cell growth status, agent concentration, and exposure time also influence agent internalization. All these make the labeling efficiency difficult to predict and the labeling efficiency should be determined individually (19).

Cell labeling efficiency is usually expressed as the percentage of labeled cells in total culture cells and the amount of iron per cell. We have noticed that only the percentage of labeled cells has been reported in many publications. For *in vivo* cell tracking, the amount of Fe per cell appears more important than the percentage of labeled cells because of the close relationship between Fe concentration and signal intensity in MRI. We strongly recommend investigators to report the labeling efficiency with both the percentage of labeled cells and the amount of Fe per cell (e.g., 10 pg Fe/cell) for IO-based agents. A particular concern for IO-

based agents is their aggregation and sedimentation, which often take place in medium when long incubation times are necessary. The aggregates can be on the culture dish surface or on the cell surface, which may be difficult to wash away. In such cases, quantification with techniques such as inductively coupled plasma

cells begin to divide, migrate, or die. The labeling agents can be taken up by and/or integrated into the host cells. The labeling agents can also remain in the extracellular matrix for a relatively long time or are cleared through unknown pathways. It may be difficult to clearly answer this issue through *in vitro* studies alone.

Table 1 Essential elements to consider for MRI cell tracking studies

Elements	Brief description
Labeling agent	Physicochemical and magnetic properties
Cell information	Cell source, cell type, activation status, culture condition, antigen loading, etc.
Labeling condition	Medium, cell density/number, labeling agent concentration and incubation time
Cell labeling evaluation	
Labeling efficiency	% of labeled cells in total and Fe/cell
Intracellular localization	Lysosomes, cytoplasm, nuclei, etc.
<i>In vitro</i> characterization	
Label retention	Especially in dividing or long-lived cells
Detection limit	Cells/voxel at a given field strength
Cytotoxicity	Mainly the adverse effect on cell function,
<i>In vivo</i> analysis	
Cell implantation	Cell number, route, and control
Monitorable period	Period from implantation to the time undetectable
Label clearance	Clearance of label from both living and dead cells
Imaging protocol	Detail imaging parameters
Outcome evaluation	
Functional outcome	Influence on cell function <i>in vivo</i>
Side effects	Acute and long-term effect on host
Validation	e.g. histology, flow cytometry on biopsy samples

atomic emission spectroscopy, R2 relaxometry, and colorimetric assays can be misleading (23). It is, therefore, important to eliminate any unbound NPs for accurate quantification. Density gradient centrifugation and flow cytometry are potentially useful to exclude extracellular aggregates.

Intracellular localization: Intracellular location of the labeling agent is associated with both the strength of local contrast enhancement and cytotoxicity. Studies with Prussian blue staining and light and/or electron microscopy have shown that inorganic NPs often accumulate in well-defined endosomal compartments resembling lysosomes within the cytoplasm. On the one hand, accumulation in the lysosomes may limit the exposure of sensitive cell organelles to the NPs and prevent protein adsorption to particle surface. Adsorption of proteins on surfaces can be irreversible and may lead to protein conformation changes, altering the biological stability and activity of the proteins. On the other hand, localization into lysosomes poses a potential drawback for long-term tracking, because lysosomes may degrade the NPs quickly. Importantly, observation of either the intact agent or any parts of the agent in the cell nuclei should be documented seriously because of potential damage of the labeling agent to cell genome.

4. *In vitro* characterization: Label retention, detection threshold, and cytotoxicity

Label retention: This is an important issue that must be considered, especially in longer-lived, rapidly dividing and migratory cells (12). In general, label retention time in cells is not a problem soon after transplant, but the issue arises when labeled

However, it is possible to define the pathways and timelines of agent clearance within cells. The retention information provides an important reference for predicting the time frame available for detection and the fate of labeling agents *in vivo*.

Detection threshold: *In vitro* detection threshold refers to the minimum number of cells detectable with MRI following labeling. This value forms the baseline for *in vivo* transplantation and cell number quantification (15). In the literature, detection threshold has been mostly determined by embedding the labeled cells in a phantom such as agarose. The data are usually expressed as cells/voxel at a given field strength. Theoretically, the *in vitro* detection threshold is much lower than the *in vivo* detection limit because of the cell distribution, division, migration, and death after transplantation (24). Several fold more cells than the detection threshold should be transplanted for *in vivo* tracking. Evidence has shown that the *in vitro* detection threshold for SPION-labeled human dendritic cells can be lower to ~125 cells/voxel at 7 T (~2000 cells/voxel for ^{19}F - or Gd-labeled cells) (25).

Cytotoxicity: Theoretically, the labeling agents and the labeling procedure should be non-toxic to labeled cells. Indeed, SPION seems no effect on the capability of cell proliferation and differentiation, although a few studies have reported that the stem cells labeled with SPION lose part of their differentiation capacity in a SPION concentration-dependent manner (26). However, NP imaging agents have been synthesized with various strategies and diverse nanomaterials. Each component of an NP agent can pose individual toxicity risks, and an intact agent might have toxic risks that differ from the toxicities of each component (27-29). The

potential cytotoxic effects need to be addressed individually for each NP agent and cell type used. Given the large number of possible interactions between NPs and cells, the cytotoxic evaluation is not straightforward (30). A particular concern may be the induction of reactive oxygen species mainly by a reaction of hydrogen peroxide with iron-oxide moieties in lysosomes (31). Reactive oxygen species could also be generated as a cell response to the presence of a high load of NPs. To assess cytotoxicity, it is necessary to perform a multitude of cytotoxicity assays and to test a range of cell types for each type of NPs with multiple doses (30, 32). Immediate toxic effects can be tested with studies of cell growth, viability, apoptosis, phenotype, activation, differentiation, etc.

5. *In vivo cell tracking: cell implantation, monitorable period, and label clearance*

Cell implantation (number of cells, route of implantation, and control): The goal of cell tracking is to track the cells qualitatively and quantitatively and long enough for evaluating the cell outcome. To reach the goal, precise control of all variables is necessary. Except for the information on experimental animals, the total implanted cell number and implantation route are also critical for the evaluation of cell tracking results (33). The former includes the cell number of each implantation and the times of implantation carried out. For the administration route, cells can be implanted through intravenous, subcutaneous, intraperitoneal, or intranodal injection. In addition, non-labeled cells as the control should also be included to establish a baseline for the experiment.

Monitorable period: The detection threshold for labeled cells is affected by several factors including field strength, pulse sequence, type of particles, signal-to-noise ratio, and voxel size. In typical settings for SPION- and ^{19}F -labeled cells, the minimum detection limit in animals is in the order of 10^4 - 10^5 cells/voxel for clinical MRI systems and 10^3 - 10^4 cells/voxel for high-field animal scanners (15, 25). In the case of cell vaccination, a typical study utilizes an intranodal or intradermal injection of ~ 10 million dendritic cells, with $3 \times 10^4 - 2 \times 10^5$ cells migrating to secondary lymph nodes. Although these data indicate that MRI is sensitive enough for cell tracking in clinical practice, however, mature dendritic cells will not divide further. For actively dividing cells such as T cells, SPION may be quickly divided among daughter cells to undetectable levels within a short period. The situation worsens in the case of stem cells that exhibit asymmetric cell division. Studies have shown that the cell number can be quantified for up to 3 weeks in actively dividing T cells in mice and the underestimation of cell numbers due to cell division is within tolerable limits. This error may be reduced if the cell division rate is known. Regardless the cell number determination, most studies indicate that the labeled cells could be visualized for up to 2-3 months in animal models (34).

Label clearance: Some important issues remain to be solved concerning the clearance of contrast agents from cells (35). These issues include whether the agents remain in the cells or leak to extracellular space following cell death, whether the released agents are incorporated into macrophages or other host cells, and how tissues clear the agents. There is no consensus on how these issues should be solved with imaging techniques. Pathological examination and flow cytometry of surgical specimens may help answer some questions, but these procedures are invasive.

6. *Imaging protocol*

Imaging sequence selection and parameter setting can influence the image contrast or sensitivity of cell detection (4). T2 and T2* relaxation times are shorter at high field strength,

increasing the ability to visualize cells labeled with IO particles. Protocols for the acquisition of MR data for cell tracking are similar to those for routine MRI/MRS (14). IO-based agents cause a hypointense contrast that can be confused with the susceptibility-induced field inhomogeneities *in vivo*, namely dark areas arising from airspaces, blood vessels, hemorrhages, and tissue interfaces. Modified acquisition protocols have been reported to convert IO-related hypointense to hyperintense spots ('bright contrast') through suppression of background tissue, which may help increase the robustness of cell detection with MRI (36, 37). Because the normal anatomic background of the image is lost with these bright contrast techniques, the bright contrast image needs to be overlaid with a standard MRI image.

7. *Outcome evaluation*

The outcome here refers to the outcome of animal models, functional outcome of implanted cells, and side effects of labeling agents on host. The function of implanted cells is dependent on the cell types and experimental purposes. Evaluation of the cell function is usually performed with a series of methods (38).

Different from the cytotoxicity of agents on cells *in vitro*, side effects are more referred to the negative effect on host and can be short-term and long-term. Because iron participates in cell metabolism, IO particles are well tolerated by living organisms. Iron presents in human body at a dose of ~ 4 g in the average adult, of which 80% is incorporated in cells of the haematopoietic system and another 10-15% is present in muscle fibers and other tissues. The total dose that would be introduced into the human body in MRI cell tracking would be ~ 1 mg, or 0.025% of total body iron, based on the calculation for a dose of 1×10^8 cells and 10 pg Fe/cell (11). This amount of iron introduced by cell tracking purpose is far less than the iron amount causing toxicity to human body. However, the coating and functionalizing materials may cause problems and close observation is recommended.

In conclusion, the feasibility of MRI cell tracking with IO-based agents as labels has been well demonstrated in animal experiments. Clinical trials of MRI cell tracking are also ongoing. Different to animal studies, some general requirements for clinical cell tracking should be met for the labeling agents. The labeling agents must be shown to be non-toxic to cells in culture and to animals. The labeled cells should be more extensively characterized to determine any effects of the labeling procedure on cell functionality. The labeling agents should be able to be synthesized in a reproducible manner in a GMP facility with compounds that are or can be approved for human use. Any design strategies for agent synthesis, cell labeling and *in vivo* MRI tracking would necessarily need to take the approval of regulatory agencies into consideration. A robust protocol for any MRI cell tracking studies is critical to obtain approval by the regulatory agencies to move to clinical trials or practice.

References

- Rodriguez-Porcel M, Kronenberg MW, Henry TD, Traverse JH, Pepine CJ, Ellis SG, Willerson JT, Moye LA, Simari RD. Cell tracking and the development of cell-based therapies: a view from the Cardiovascular Cell Therapy Research Network. *JACC Cardiovasc Imaging* 2012;5:559-65.
- Srinivas M, Aarntzen EH, Bulte JW, Oyen WJ, Heerschap A, de Vries IJ, Figdor CG. Imaging of cellular therapies. *Adv Drug Deliv Rev* 2010;62:1080-93.

3. Arbab AS, Liu W, Frank JA. Cellular magnetic resonance imaging: current status and future prospects. *Expert Rev Med Devices* 2006;3:427-39.
4. Delikatny EJ, Poptani H. MR techniques for in vivo molecular and cellular imaging. *Radiol Clin North Am* 2005;43:205-20.
5. Vreys R, Soenen SJ, De Cuyper M, Van der Linden A. Background migration of USPIO/MLs is a major drawback for in situ labeling of endogenous neural progenitor cells. *Contrast Media Mol Imaging* 2011;6:1-6.
6. Kircher MF, Gambhir SS, Grimm J. Noninvasive cell-tracking methods. *Nat Rev Clin Oncol* 2011;8:677-88.
7. de Vries IJ, Lesterhuis WJ, Barentsz JO, Verdijk P, van Krieken JH, Boerman OC, Adema GJ, Bulte JW, Scheenen TW, Punt CJ, Heerschap A, Figdor CG. Magnetic resonance tracking of dendritic cells in melanoma patients for monitoring of cellular therapy. *Nat Biotechnol* 2005;23:1407-13.
8. Bulte JW, Ma LD, Magin RL, Kamman RL, Hulstaert CE, Go KG, The TH, de Leij L. Selective MR imaging of labeled human peripheral blood mononuclear cells by liposome mediated incorporation of dextran-magnetite particles. *Magn Reson Med* 1993;29:32-7.
9. Hawrylak N, Ghosh P, Broadus J, Schlueter C, Greenough WT, Lauterbur PC. Nuclear magnetic resonance (NMR) imaging of iron oxide-labeled neural transplants. *Exp Neurol* 1993;121:181-92.
10. Yeh TC, Zhang W, Ildstad ST, Ho C. Intracellular labeling of T-cells with superparamagnetic contrast agents. *Magn Reson Med* 1993;30:617-25.
11. Bulte JW. In vivo MRI cell tracking: clinical studies. *AJR Am J Roentgenol* 2009;193:314-25.
12. Taylor A, Wilson KM, Murray P, Fernig DG, Levy R. Long-term tracking of cells using inorganic nanoparticles as contrast agents: are we there yet? *Chem Soc Rev* 2012;41:2707-17.
13. Gossuin Y, Gillis P, Hocq A, Vuong QL, Roch A. Magnetic resonance relaxation properties of superparamagnetic particles. *Wiley Interdiscip Rev Nanomed Nanobiotechnol* 2009;1:299-310.
14. Shah B, Anderson SW, Scalera J, Jara H, Soto JA. Quantitative MR imaging: physical principles and sequence design in abdominal imaging. *Radiographics* 2011;31:867-80.
15. Stroh A, Faber C, Neuberger T, Lorenz P, Sieland K, Jakob PM, Webb A, Pilgrimm H, Schober R, Pohl EE, Zimmer C. In vivo detection limits of magnetically labeled embryonic stem cells in the rat brain using high-field (17.6 T) magnetic resonance imaging. *Neuroimage* 2005;24:635-45.
16. Walczak P, Kedziorek DA, Gilad AA, Barnett BP, Bulte JW. Applicability and limitations of MR tracking of neural stem cells with asymmetric cell division and rapid turnover: the case of the shiverer dysmyelinated mouse brain. *Magn Reson Med* 2007;58:261-9.
17. Langley J, Liu W, Jordan EK, Frank JA, Zhao Q. Quantification of SPIO nanoparticles in vivo using the finite perturber method. *Magn Reson Med* 2011;65:1461-9.
18. Laurent S, Boutry S, Mahieu I, Vander Elst L, Muller RN. Iron oxide based MR contrast agents: from chemistry to cell labeling. *Curr Med Chem* 2009;16:4712-27.
19. Di Marco M, Sadun C, Port M, Guilbert I, Couvreur P, Dubernet C. Physicochemical characterization of ultrasmall superparamagnetic iron oxide particles (USPIO) for biomedical application as MRI contrast agents. *Int J Nanomedicine* 2007;2:609-22.
20. Shan L, Chopra A, Eckelman WC, Leung K, Menkens A. characterization of nanoparticle-based contrast agents for molecular magnetic resonance imaging. *J Nanopart Res* 2012;14:1122-33.
21. Chopra A, Shan L, Eckelman WC, Leung K, Menkens AE. Important parameters to consider for the characterization of PET and SPECT imaging probes. *Nucl Med Biol* 2011;38:1079-84.
22. Leung K, Chopra A, Shan L, Eckelman WC, Menkens AE. Essential parameters to consider for the characterization of optical imaging probes. *Nanomedicine (Lond)* 2012;7:1101-7.
23. Boutry S, Forge D, Burtea C, Mahieu I, Murariu O, Laurent S, Vander Elst L, Muller RN. How to quantify iron in an aqueous or biological matrix: a technical note. *Contrast Media Mol Imaging* 2009;4:299-304.
24. Verdijk P, Scheenen TW, Lesterhuis WJ, Gambarota G, Veltien AA, Walczak P, Scharenborg NM, Bulte JW, Punt CJ, Heerschap A, Figdor CG, de Vries IJ. Sensitivity of magnetic resonance imaging of dendritic cells for in vivo tracking of cellular cancer vaccines. *Int J Cancer* 2007;120:978-84.
25. Bonetto F, Srinivas M, Heerschap A, Mailliard R, Ahrens ET, Figdor CG, de Vries IJ. A novel (19)F agent for detection and quantification of human dendritic cells using magnetic resonance imaging. *Int J Cancer* 2011;129:365-73.
26. Siglienti I, Bendszus M, Kleinschnitz C, Stoll G. Cytokine profile of iron-laden macrophages: implications for cellular magnetic resonance imaging. *J Neuroimmunol* 2006;173:166-73.
27. Schrand AM, Rahman MF, Hussain SM, Schlager JJ, Smith DA, Syed AF. Metal-based nanoparticles and their toxicity assessment. *Wiley Interdiscip Rev Nanomed Nanobiotechnol* 2010;2:544-68.
28. Sayes CM, Warheit DB. Characterization of nanomaterials for toxicity assessment. *Wiley Interdiscip Rev Nanomed Nanobiotechnol* 2009;1:660-70.
29. Brown SC, Palazuelos M, Sharma P, Powers KW, Roberts SM, Grobmyer SR, Moudgil BM. Nanoparticle characterization for cancer nanotechnology and other biological applications. *Methods Mol Biol* 2010;624:39-65.
30. Soenen SJ, De Cuyper M. How to assess cytotoxicity of (iron oxide-based) nanoparticles: a technical note using cationic magnetoliposomes. *Contrast Media Mol Imaging* 2011;6:153-64.
31. Emerit J, Beaumont C, Trivin F. Iron metabolism, free radicals, and oxidative injury. *Biomed Pharmacother* 2001;55:333-9.
32. Soenen SJ, Himmelreich U, Nuytten N, De Cuyper M. Cytotoxic effects of iron oxide nanoparticles and implications for safety in cell labelling. *Biomaterials* 2011;32:195-205.
33. Eckelman WC, Kilbourn MR, Joyal JL, Labiris R, Valliant JF. Justifying the number of animals for each experiment. *Nucl Med Biol* 2007;34:229-32.
34. Wang HH, Wang YX, Leung KC, Au DW, Xuan S, Chak CP, Lee SK, Sheng H, Zhang G, Qin L, Griffith JF, Ahuja AT. Durable mesenchymal stem cell labelling by using polyhedral superparamagnetic iron oxide nanoparticles. *Chemistry* 2009;15:12417-25.

35. Berman SC, Galpoththawela C, Gilad AA, Bulte JW, Walczak P. Long-term MR cell tracking of neural stem cells grafted in immunocompetent versus immunodeficient mice reveals distinct differences in contrast between live and dead cells. *Magn Reson Med* 2011;65:564-74.
36. Cunningham CH, Arai T, Yang PC, McConnell MV, Pauly JM, Conolly SM. Positive contrast magnetic resonance imaging of cells labeled with magnetic nanoparticles. *Magn Reson Med* 2005;53:999-1005.
37. Stuber M, Gilson WD, Schar M, Kedziorek DA, Hofmann LV, Shah S, Vonken EJ, Bulte JW, Kraitchman DL. Positive contrast visualization of iron oxide-labeled stem cells using inversion-recovery with ON-resonant water suppression (IRON). *Magn Reson Med* 2007;58:1072-7.
38. Darkazalli A, Levenson CW. Tracking stem cell migration and survival in brain injury: Current approaches and future prospects. *Histol Histopathol* 2012;27:1255-61.

Evaluation of Tumor Cell Response to Hyperthermia with Bioluminescent Imaging

Renshu Zhang¹, Yanfei Zhou¹, Paul C. Wang², Rajagopalan Sridhar^{1*}

¹Department of Radiation Oncology and ²Department of Radiology, Howard University, Washington, DC.

Journal of Basic & Clinical Medicine 2012, 1(1):16-19

Abstract

Background: Hyperthermia is used in combination with radiotherapy and/or chemotherapy in the treatment of various types of cancer. Currently, the tumor cell response to hyperthermia is determined largely based on the size reduction of tumor mass, which is insensitive.

Methods: We tested the feasibility of bioluminescent imaging (BLI) in evaluation of the tumor cell response to hyperthermia by exposing luciferase-expressing MDA-MB-231-luc human breast cancer cells to high temperature (43 °C) for 10 minutes to 2 hours. The tumor cells were imaged and the light signal generated by the tumor cells was quantified with BLI. To validate its usefulness, the light signal intensity was comparatively analyzed with the tumor cell clonogenicity and cell viability, which were measured with classic clonogenic and MTT assays.

Results: The light signal intensity determined by BLI was closely correlated with the absolute number of viable cells as well as the cell viability measured with the traditional MTT assay under normal culture condition. Relative to the clonogenicity of tumor cells after exposure to hyperthermia, however, BLI underestimated, while MTT assay overestimated the cell viability. Difference in the interpretation of tumor cell clonogenic ability following hyperthermia with BLI, MTT dye, and clonogenic assay may be due to the different mechanisms of the three measurements as well as the fact that hyperthermia can induce cell damage at levels of both transient and permanent.

Conclusions: BLI is sensitive, convenient, and potentially valuable in the evaluation and monitoring of tumor cell response to treatments including hyperthermia.

Keywords: Hyperthermia, tumor cell response, bioluminescent imaging, breast cancer

Introduction

Hyperthermia, also called thermal therapy or thermotherapy, is used in the treatment of various types of cancer in combination with other therapies (1,2). Hyperthermia has been shown to increase the sensitivity of some cancer cells to radiation and enhance the efficacy of anticancer drugs (3). To date, the anti-tumor efficacy of hyperthermia *in vivo* is largely based on the reduction of tumor size, which is insensitive, especially at the early stage of treatment. In *in vitro* studies, the tumor cell response to hyperthermia is mainly evaluated with cell viability and clonogenic assays, which differ widely in their mechanisms and applications

(4). Some assays are based on the cellular uptake of vital dyes and/or intracellular enzyme activity such as neutral red, alamar blue, 3-(4,5-dimethylthiazol-2-yl)-2,5-diphenyltetrazolium bromide (MTT), and 2,3-bis(2-methoxy-4-nitro-5-sulphophenyl)-5-[(phenylamino)carbonyl]-2H-tetrazolium (5-7). Some other assays depend on the uptake of DNA precursors such as radiolabeled thymidine (8). In general, dye uptake-based assays such as MTT are suitable for estimating cell proliferation and evaluating the rapid cellular response to treatments (9). Considering that tumor growth and recurrence depend on the surviving clonogens, clonogenic measurements are more useful than dye-based cell viability assays when investigating therapeutic efficacy (10-12). Irrespective of the mechanisms of these assays, their application is limited to *in vitro* evaluation of the cellular viability or clonogenicity. A rapid, sensitive and noninvasive technique is desired for determination of the tumor response to therapy both *in vitro* and in living subjects.

Luciferase gene is widely used as a reporter in biochemical assays and gene expression analysis (13, 14). Luciferase catalyzes the conversion of its substrate D-luciferin to oxyluciferin in the presence of oxygen, Mg²⁺, and ATP, which is accompanied by release of photons. Luciferase-based bioluminescent imaging (BLI) is becoming more and more attractive because of its capability for rapid and noninvasive monitoring of subtle changes in tumors (15-18). Because the light intensity depends on the level and activity of both luciferase and ATP, we hypothesized that the light intensity could reflex the cell viability and cell response to treatment. In the present study, we tested the hypothesis using BLI to evaluate the cytotoxicity of hyperthermia (43 °C) to human breast cancer MDA-MB-231-luc cells. MDA-MB-231-luc cells are stably transfected with the firefly luciferase gene, express high level of luciferase, and produce strong light when they are incubated with the luciferase substrate D-luciferin. The results showed that the light intensity measured with BLI was closely correlated with the absolute cell number as well as the cell viability measured with the traditional MTT assays under normal culture conditions, indicating the usefulness of BLI in cell viability evaluation. After exposure of the cells to hyperthermia, the light intensity decreased rapidly and significantly. Relative to the clonogenicity determined with colony formation assay, BLI tended to underestimate and MTT assay tended to overestimate the cell viability.

Materials and Methods

Cell line and hyperthermia treatment

MDA-MB-231-luc human breast cancer cell line was used in this study (Caliper, Alameda, CA). Cells were routinely maintained as monolayers in RPMI1640 medium and kept at 37 °C in humidified atmosphere containing 5% CO₂. The medium was supplemented with 10% heat-inactivated fetal bovine serum (FBS),

Accepted in September 28, 2012

*Correspondence author, Tel: 202-865-4968; Fax: 202-865-3722

E-mail address: rajsridhar2003@yahoo.com

penicillin (50 units/ml), and streptomycin (50 µg/ml) (Invitrogen, Carlsbad, CA). To test the relationship between light signal intensity and viable cell number, cells were seeded in sterile 96-well plates at various cell densities (25 to 5×10^3 cells/well) and allowed to grow overnight before measurements. For hyperthermia treatment, cells (1×10^4 cells/well) were seeded in sterile 96-well plates, grow overnight, and was then subjected to hyperthermia by sealing the plates with parafilm, enclosing in a Ziploc bag, and immersing into a water bath of 43 ± 0.1 °C for 10 to 120 minutes (min). Controls were similarly sealed in Ziploc bags but immersed in a 37°C water bath. After heating, plates were ready for BLI, MTT assay, and clonogenic measurement.

Bioluminescent imaging

Luciferase-based BLI was performed with a highly sensitive, cooled CCD camera, which is mounted in a light-tight specimen box (Caliper IVIS spectrum optical imaging system). After heating, the old medium was removed from each well and 100 µl of D-luciferin solution (150 µg/ml in RPMI medium) (Caliper) were added. The plate was placed on the stage of specimen box, which was maintained at 37 °C. Images were captured at 5 min after addition of D-luciferin. The imaging time was set to 1 min. The light emitted from each well was detected, integrated, digitized, and displayed with the acquisition and analysis software (Caliper). The bioluminescent signal from each well was measured and expressed as total flux (photons per second, p/s). At least 5 replicates were performed in all experiments and each experiment was repeated at least 3 times.

MTT and clonogenic assays

MTT assay was used to measure the tumor cell viability, which is based on the reduction of tetrazolium dye MTT (Sigma, St. Louis, MO) by viable cells. After exposure to 43 °C, the old medium was replaced with MTT solution (100 µl; 0.5 mg/ml phenol red-free RPMI1640). Three hours after incubation at 37 °C, the absorbance was determined at the wavelength of 560 nm with a multiwell spectrophotometer (BIO-RAD, Hercules, CA). For the clonogenic assay, cells were trypsinized and pipetted to single cell suspension. All cells were plated on 100-mm tissue culture dishes with fresh medium and kept at 37 °C, 5% CO₂ incubator for 10-14 days. Colonies with more than 50 cells were counted.

Statistical analysis

All correlation analyses were performed with the statistical software Origin 7.0 (OriginLab, Northampton, MA).

Results

Correlation between imaging-based light intensity and cell viability

BLI showed that the light signal intensity increased with increased cell number (Fig. 1A). A close correlation between the bioluminescent signal intensity and absolute cell number was obtained over the range from 25 to 5×10^3 cells per well ($R = 0.99$, $P < 0.0001$). As few as 125 cells could be detected clearly (Fig. 1B). Similar correlative results were also obtained with MTT assay between the absorbance at 560 nm and cell number ($R = 0.99$, $P < 0.0001$) (Fig. 1C). The bioluminescent signal intensity was also closely correlated with the formazan absorbance at 560 nm obtained with MTT assay ($R = 0.98$, $P < 0.0001$) (Fig. 1D).

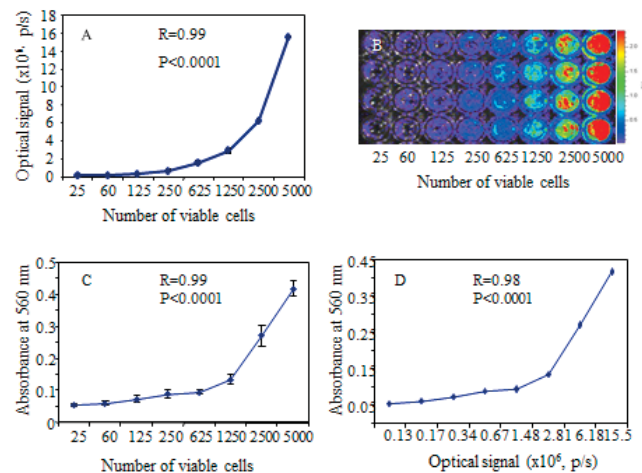


Figure 1. Comparison of MTT assay and BLI for measurement of cell viability under normal culture condition. 1A: correlation between absolute cell number and light signal intensity; 1B: a representative bioluminescent image of cells at various intensities; 1C: correlation of the absorbance at 560 nm and absolute cell number; and 1D: close correlation between MTT assay absorbance and bioluminescent signal intensity.

Evaluation of tumor cell response to hyperthermia

To test the cell response to hyperthermia, cells were subjected to hyperthermia (43 °C) for 10 to 120 min. At 10 min after exposure to hyperthermia, the light signal intensity from the treated cells decreased to 77% of the intensity from the control cells (untreated). A dramatic decrease of the light intensity was then detected at 20 min, showing only 22% of the control intensity (Fig. 2). With prolonged exposure to hyperthermia, the light signal intensity from the treated cells decreased further, showing only 9%, 3.6%, and 2% of the control light intensity at 30, 60, and 120 min, respectively. The corresponding cell viability measured with MTT assay was 95%, 90%, 90%, 83%, and 68% of the controls, and the colony number measured with clonogenic assay was 94%, 99%, 85%, 62%, and 7% of the controls at 10, 20, 30, 60, and 120 min, respectively, after exposure to hyperthermia (Fig. 2). These results suggested that BLI might underestimate, while MTT assay might overestimate the cell viability of tumor cells relative to the cell colony forming ability following exposure to hyperthermia.

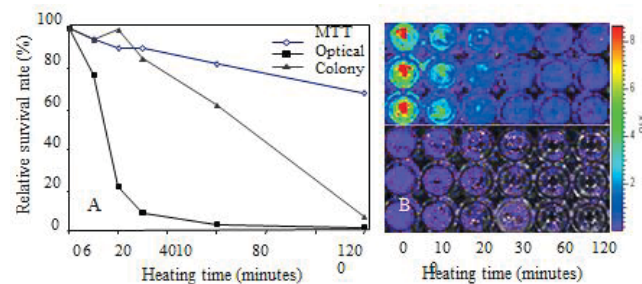


Figure 2. Evaluation of tumor cell response to hyperthermia at 43°C for different durations from 10 to 120 min, indicating BLI may underestimate and MTT may overestimate the cell viability with respect to the clonogenic potential as estimated by clonogenic assay (2A). 2B shows the bioluminescent images of cells with (lower panel) and without (upper panel) heat treatment. The relative survival rate is reported as percentage relative to 100% survival for untreated controls.

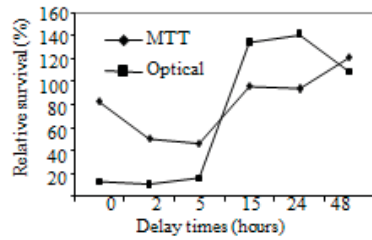


Figure 3. Delayed assessment of the cell viability following 1 hour treatment at 43 °C with BLI and MTT assay, indicating continued cell damage within the initial 5 hours followed by recovery of cells from damage.

Evaluation of the tumor damage recovery following hyperthermia

Heating can cause cell damages at different levels. Damages may be transient or permanent. Cells may lose enzyme activity as well as clonogenic potential, or may lose just one of these two properties. With this in mind, delayed assessment of the cell viability was performed at 3, 5, 15, 24, 48, and 72 hours after the cells returned to normal culture condition following 1 hour heating at 43 °C. Delayed assessment permits a recovery of the cells from transient but not from permanent damage. Immediate assessment of the cell viability after 1 hour exposure to hyperthermia showed a significantly low level of the light intensity relative to the controls not subjected to hyperthermia. The low level of signal intensity remained for more than 5 hours and a complete recovery of the light signal intensity was observed at ~15 hours (Fig. 3). Similar tendency was also observed for the cell viability measured with MTT assay, showing continued decrease of the cell viability for 5 hours followed by gradual recovery (Fig. 3). The light signal intensity at both 24 and 48 hours was higher than that of the controls, which might be due to the rapid cell proliferation following recovery from hyperthermia damage. MDA-MB-231-luc cells are known to have a cell cycle time of about 23 hours (19).

Discussion

Bioluminescent signal is a measurement of the luciferase expression level and activity, oxygen, and ATP content of the viable cells (20). Because the light signal intensity reflects the metabolic activity of viable cells, we hypothesized that BLI would be useful to evaluate tumor response to treatments including hyperthermia under the contextual influences of whole biological systems. To test this hypothesis, we first evaluated the feasibility with BLI to determine viable cell number using luciferase-expressing breast cancer cells under normal culture condition. As expected, the absolute number of viable cells was closely correlated with the bioluminescent signal intensity. Measurement with BLI was extremely sensitive. As low as 125 cells could be detected and fewer than 100 cell difference could be identified. The close correlation between the light signal intensity and the cell viability estimated with traditional MTT assay further indicate that the BLI-based light signal intensity could be used as an indicator of the cell viability.

The results that rapid and dramatic decrease of the light signal intensity after exposure to hyperthermia suggest that hyperthermia has a significant effect on the light generation. The significant loss of bioluminescent signal was less consistent with the loss of clonogenic potential of tumor cells. Immediate assessment with

BLI appeared to underestimate the clonogenic potential of cells. This result may be partially explained by the shape decrease of ATP content but not clonogenic potential of the cells because hyperthermia has been shown to damage mitochondria (21). Hyperthermia may also down-regulate the luciferase expression and/or inactivate its activity. Further studies are necessary to determine the level and activity of ATP and luciferase after hyperthermia. Considering the effect of transient damage on light generation, delayed assessment after cells returned to normal temperature was designed to allow the cell recovery from transient damage. Indeed, relative to the control, continued low cell signals from BLI were observed for the initial 5 hours and the signal intensity then recovered gradually to the control levels. Similar results were also obtained with MTT assay. It appeared that transient damage to cells by hyperthermia significantly influenced the light production.

The difference in the interpretation of clonogenic ability following hyperthermia with BLI, MTT and clonogenic assay may be partially explained by the damages at different levels. Clonogenic ability is largely affected by the permanent cell damage. Whereas BLI and MTT assay reflect both transient and permanent damages. Compared to MTT assay, BLI is rapid, convenient and more sensitive [16, 17, 22]. Importantly, BLI can be repeated for the same cells at different times. Our study with cells in culture provides the insight towards noninvasive monitoring of tumor response to hyperthermia or other treatments *in vivo* with BLI.

Acknowledgement

This work was supported in part by DoD USAMRMC W81XWH-10-1-0767, NIH National Center for Research Resources 3 G12 RR003048, and National Institute on Minority Health and Health Disparities 8 G12 MD007597 grants.

References

1. van der Zee J. Heating the patient: a promising approach? *Ann Oncol* 2002;13:1173-84.
2. Wust P, Hildebrandt B, Sreenivasa G, Rau B, Gellermann J, Riess H, Felix R, Schlag PM. Hyperthermia in combined treatment of cancer. *Lancet Oncol* 2002;3:487-97.
3. Dahl O, Dalene R, Schem BC, Mella O. Status of clinical hyperthermia. *Acta Oncol* 1999;38:863-73.
4. Bellamy WT. Prediction of response to drug therapy of cancer, a review of *in vitro* assays. *Drugs* 1992;44:690-708.
5. O'Brien J, Wilson I, Orton T, Pognan F. Investigation of the alamar blue (resazurin) fluorescent dye for the assessment of mammalian cell cytotoxicity. *Eur J Biochem* 2000;267:5421-6.
6. Berridge MV, Herst PM, Tan AS. Tetrazolium dyes as tools in cell biology: new insights into their cellular reduction. *Biotechnol. Annu Rev* 2005;11:127-52.
7. Lechpammer S, Asea A, Mallick R, Zhong R, Sherman MY, Calderwood SK. Development of an XTT tetrazolium salt-based assay for detection of specific hyperthermia sensitizers in a high-flux screening programme. *Int J Hyperthermia* 2002;18:203-15.
8. Senekowitsch-Schmidtke R, Ruth F, Bernatz S. Radiolabeled thymidine: a sensitive tracer for early tumor

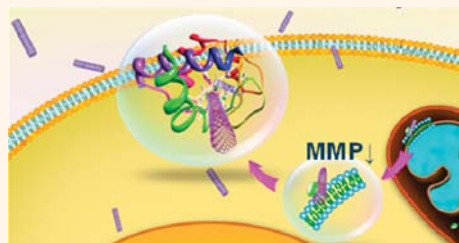
- response and recurrence after irradiation. *J Nucl Med* 1999;40:1702-5.
9. Hamid R, Rotshteyn Y, Rabadi L, Parikh R, Bullock P. Comparison of alamar blue and MTT assays for high through-put screening. *Toxicol In Vitro* 2004;18:703-10.
10. Miret S, De Groene EM, Klaffke W. Comparison of in vitro assays of cellular toxicity in the human hepatic cell line HepG2. *J Biomol Screen* 2006;1:184-93.
11. Kawada K, Yonei T, Ueoka H, Kiura K, Tabata M, Takigawa N, Harada M, Tanimoto M. Comparison of chemosensitivity tests: clonogenic assay versus MTT assay. *Acta Med Okayama* 2002;56:129-34.
12. Tomasovic SP, Barta M, Klostergaard J. Neutral red uptake and clonogenic survival assays of the hyperthermic sensitization of tumor cells to tumor necrosis factor. *Radiat Res* 1989;119:325-37.
13. Bloquel C, Trollet C, Pradines E, Seguin J, Scherman D, Bureau MF. Optical imaging of luminescence for in vivo quantification of gene electrotransfer in mouse muscle and knee. *BMC Biotechnol* 2006;6:16.
14. Shinde R, Perkins J, Contag CH. Luciferin derivatives for enhanced in vitro and in vivo bioluminescence assays. *Biochem* 2006;45:11103-12.
15. Massoud TF, Gambhir SS. Molecular imaging in living subjects: seeing fundamental biological processes in a new light. *Genes Develop* 2003;17:545-80.
16. Greer III LF, Szalay AA. Imaging of light emission from the expression of luciferases in living cells and organisms: a review. *Luminescence* 2002;17:43-74.
17. Jenkins DE, Hornig YS, Oei Y, Dusich J, Purchio T. Bioluminescent human breast cancer cell lines that permit rapid and sensitive in vivo detection of mammary tumors and multiple metastases in immune deficient mice. *Breast Cancer Res* 2005;7:R444-54.
18. Nogawa M, Yuasa T, Kimura S, Kuroda J, Sato K, Segawa H, Yokota A, Maekawa T. Monitoring luciferase-labeled cancer cell growth and metastasis in different in vivo models. *Cancer Lett* 2005;217:243-53.
19. Zhang RD, Fidler IJ, Price JE. Relative malignant potential of human breast carcinoma cell lines established from pleural effusions and brain metastasis. *Invasion Meta* 1991;11:204-15.
20. Paulmurugan R, Massoud TF, Huang J, Gambhir SS. Molecular Imaging of drug-modulated protein-protein interactions in living subjects. *Cancer Res* 2004;64:2113-9.
21. Miyazaki N, Kurihara K, Nakano H, Shinohara K. Role of ATP in the sensitivity to heat and the induction of apoptosis in mammalian cells. *Int J Hyperthermia* 2002;18:316-31.
22. Shan L, Wang S, Korotcov A, Sridhar R, Wang PC. Bioluminescent animal models of human breast cancer for tumor biomass evaluation and metastasis detection. *Ethn Dis* 2008;18(2 Suppl 2):S2-65-9.

Single-Walled Carbon Nanotubes Alter Cytochrome *c* Electron Transfer and Modulate Mitochondrial Function

Xiaowei Ma,^{†,‡} Li-Hua Zhang,^{†,*,‡} Li-Rong Wang,^{†,‡} Xue Xue,[†] Ji-Hong Sun,^{†,*} Yan Wu,[†] Guozhang Zou,[†] Xia Wu,^{†,*} Paul C. Wang,[§] Wayne G. Wamer,^{||} Jun-Jie Yin,^{||} Kaiyuan Zheng,[†] and Xing-Jie Liang^{†,*}

[†]Laboratory of Nanomedicine and Nanosafety, Division of Nanomedicine and Nanobiology, National Center for Nanoscience and Technology, China, and CAS Key Laboratory for Biomedical Effects of Nanomaterials and Nanosafety, Chinese Academy of Sciences, Beijing 100190, China, [‡]Department of Chemistry & Chemical Engineering, College of Environment and Energy Engineering, Beijing University of Technology, Beijing 100124, China, [§]Molecular Imaging Laboratory, Department of Radiology, Howard University, Washington, D.C. 20060, United States, and ^{||}Center for Food Safety and Applied Nutrition, Food and Drug Administration, College Park, Maryland 20740, United States. [‡]These authors contributed equally to this work.

ABSTRACT Single-walled carbon nanotubes (SWCNTs) are broadly used for various biomedical applications such as drug delivery, *in vivo* imaging, and cancer photothermal therapy due to their unique physicochemical properties. However, once they enter the cells, the effects of SWCNTs on the intracellular organelles and macromolecules are not comprehensively understood. Cytochrome *c* (Cyt *c*), as a key component of the electron transport chain in mitochondria, plays an essential role in cellular energy consumption, growth, and differentiation. In this study, we found the mitochondrial membrane potential and mitochondrial oxygen uptake were greatly decreased in human epithelial KB cells treated with SWCNTs, which accompanies the reduction of Cyt *c*. SWCNTs deoxidized Cyt *c* in a pH-dependent manner, as evidenced by the appearance of a 550 nm characteristic absorption peak, the intensity of which increased as the pH increased. Circular dichroism measurement confirmed the pH-dependent conformational change, which facilitated closer association of SWCNTs with the heme pocket of Cyt *c* and thus expedited the reduction of Cyt *c*. The electron transfer of Cyt *c* is also disturbed by SWCNTs, as measured with electron spin resonance spectroscopy. In conclusion, the redox activity of Cyt *c* was affected by SWCNTs treatment due to attenuated electron transfer and conformational change of Cyt *c*, which consequently changed mitochondrial respiration of SWCNTs-treated cells. This work is significant to SWCNTs research because it provides a novel understanding of SWCNTs' disruption of mitochondria function and has important implications for biomedical applications of SWCNTs.



KEYWORDS: single-walled carbon nanotubes · carboxy · cytochrome *c* · electron transfer · mitochondrial function · redox activity

Carbon nanomaterials with tunable surface properties and good biocompatibility have great potential for biological and medical applications.^{1,2} As a unique quasi one-dimensional material, SWCNTs have been explored as novel delivery vehicles for drugs, peptides, proteins, plasmid DNA, and small interfering RNA.³ The interactions between biological macromolecules and carbon nanomaterials have been reported to cause changes in the structure and function of proteins.^{2,4–10} When the functionalized carbon nanotubes recognize and bind to the catalytic site of α -chymotrypsin, its enzymatic activity was inhibited completely.⁶ Karajanagi *et al.* demonstrated that activities of α -chymotrypsin (CT) and soybean peroxidase (SBP) were

differently affected by their interaction with SWCNTs. It was found that SBP retained its native three-dimensional conformation and up to 30% of its native activity after interaction with SWCNTs. In contrast, α -CT unfolded on the SWCNT surface and retained only 1% of its original activity.⁵ Proteins can bind with SWCNTs through covalent or noncovalent interactions due to their large surface areas. SWCNTs tend to strongly bind proteins through charge complementarities, π – π stacking, and other nonspecific interactions.^{11–13} Carboxylated SWCNTs might interact with proteins located on the cell membrane or in the cytoplasm of multipotent mesenchymal stem cells, which have a further impact on subsequent cellular signaling pathways.¹⁴ Recent studies have

* Address correspondence to
jhsun@bjut.edu.cn or
liangxj@nanoctr.cn.

Received for review March 31, 2012
and accepted November 21, 2012.

Published online November 21, 2012
10.1021/nn302457v

© 2012 American Chemical Society

shown that bacterial membrane rhodopsin proteins (bR) can be adsorbed onto SWCNTs through hydrophobic interactions between the bR α -helices and the sidewall of the nanotube. This noncovalent functionalization caused bR proteins to undergo significant secondary structural changes.¹⁵ These results suggest that an understanding of the effects of SWCNTs on protein conformation and function may be essential for developing novel biological and medical applications for SWCNTs.

Cytochrome *c* (Cyt *c*) is a key component of the mitochondrial respiratory chain that exists in the cytosol between the inner and outer membranes of mitochondria. The heme group of Cyt *c* allows it to undergo redox reactions. Cyt *c* plays an important role in the biological respiratory chain, whose function is to receive electrons from cytochrome *c* reductase and deliver them to cytochrome *c* oxidase. The activity of Cyt *c* is essential for mitochondrial function and is further associated with a variety of processes including cellular differentiation, apoptosis, control of the cell cycle, and cell growth.¹⁶ Mitochondrial dysfunction leads to cell apoptosis and is closely linked with several diseases.^{17,18} Cyt *c* is also involved in initiation of apoptosis by abnormal accumulation in cytoplasm, which initiates signal pathways leading to cell dysfunction.^{19,20} The release of Cyt *c* from mitochondria into the cytoplasm has been shown to induce or activate apoptosis through interactions with cytoplasmic proteins such as apaf-1, Bcl-2, TIB, and caspase.²¹ In addition, dysfunction of Cyt *c* can modulate the mitochondrial membrane potential (MMP) and cause mitochondrial respiratory chain malfunction.²² SWCNTs have been demonstrated to promote the reduction/oxidation of cytochrome *c*.²³ In another study, SWCNTs were used as transporters to shuttle Cyt *c* through the plasma membrane and into the cytoplasm to regulate the activities of cells.²⁴

SWCNTs were found to localize exclusively in the mitochondria of both tumor and normal cells.²⁵ To date, reports on whether SWCNTs themselves could affect the function and activity of Cyt *c* and the resulting effects on cellular functions are limited. Technically, it is very difficult to avoid aggregation of pristine SWCNTs when they are suspended in physiologically relevant solvents. This problem has hindered the progress of our understanding of the interactions between Cyt *c* and SWCNTs. In this study, we modified SWCNTs with carboxy groups to avoid their aggregation. The redox properties of Cyt *c* were examined following incubation with suspensions of SWCNTs in physiological buffer. For the first time, we demonstrate that the redox potential of Cyt *c* is altered by interacting with SWCNTs. In addition, the SWCNT treatment caused MMP change, and mitochondrial respiration inhibition in KB cells was measured. The results provide evidence that SWCNTs can cause MMP change and

decrease the level of mitochondrial oxygen uptake in cells, which are the results of the redox activity change and impaired electron transfer of Cyt *c*. While the exact mechanism needs to be further explored, our studies of the interactions between SWCNTs and Cyt *c* provide some clues about how SWCNTs may interact with Cyt *c* and affect cellular functions.

RESULTS AND DISCUSSION

SWCNTs have been widely used to shuttle biomolecules including proteins, DNA, and siRNA into cells.^{26–28} Whether the structure and function of these “passenger” molecules as well as cellular components can be affected by SWCNTs and how SWCNTs affect cellular activities need to be addressed. Because pristine SWCNTs have low solubility in water, we modified SWCNTs with carboxy groups and dispersed them in PB containing 0.5 wt % sodium cholate. The derived suspensions of individual SWCNTs have enhanced stability (Figure 1a, b). While pristine SWCNTs rapidly aggregated and precipitated out, carboxy-SWCNTs exhibited high suspension stability. We also tested the stability of carboxy-SWCNTs in complete DMEM media. As is shown in Figure S1, carboxy-SWCNTs exhibited high suspension stability in complete DMEM media. These stable suspensions of SWCNTs were used in studies on Cyt *c* to clarify how SWCNTs affect cellular activities and interact with Cyt *c*.

Cellular Uptake of SWCNTs and Mitochondrial Morphology Change. In order to monitor the entry of SWCNTs into cells under selected conditions, we employed the micro-Raman technique of the G-band of SWCNTs in KB cells with an approximately 2 mm spatial resolution. In Raman mapping images, the color change represents the content of carbon nanotubes in the cells. With the increase of SWCNTs content, the color of the Raman mapping images changes from black to orange. Figure 1c and d show the Raman mapping images of KB cells incubated with or without 60 $\mu\text{g/mL}$ SWCNTs for 24 h. As expected, a strong Raman signal was observed at about 1580 cm^{-1} in KB cells after incubation with SWCNTs. In contrast, almost no obvious Raman signals were observed for control cells. The presence of SWCNTs is seen as an orange area in the cells by a Raman intensity ratio map. Raman mapping clearly indicates that SWCNTs entered and accumulated in KB cells with intensive near-infrared excited Raman signals.

It is known that SWCNTs exhibit a strong resonance Raman shift at about 1580 cm^{-1} , a specific characteristic graphitic stretching mode, which can be used to measure the quantity of SWCNTs. Therefore, we further examined the G band intensity of 1580 cm^{-1} in the isolated mitochondria of KB cells treated with SWCNTs from 0 to 60 $\mu\text{g/mL}$ for 24 h. It was found that the mitochondrial targeting of SWCNTs is dose-dependent, with higher Raman intensities observed for SWCNT signals in the mitochondria isolated from cells treated with a higher SWCNT concentration (Figure 2A).

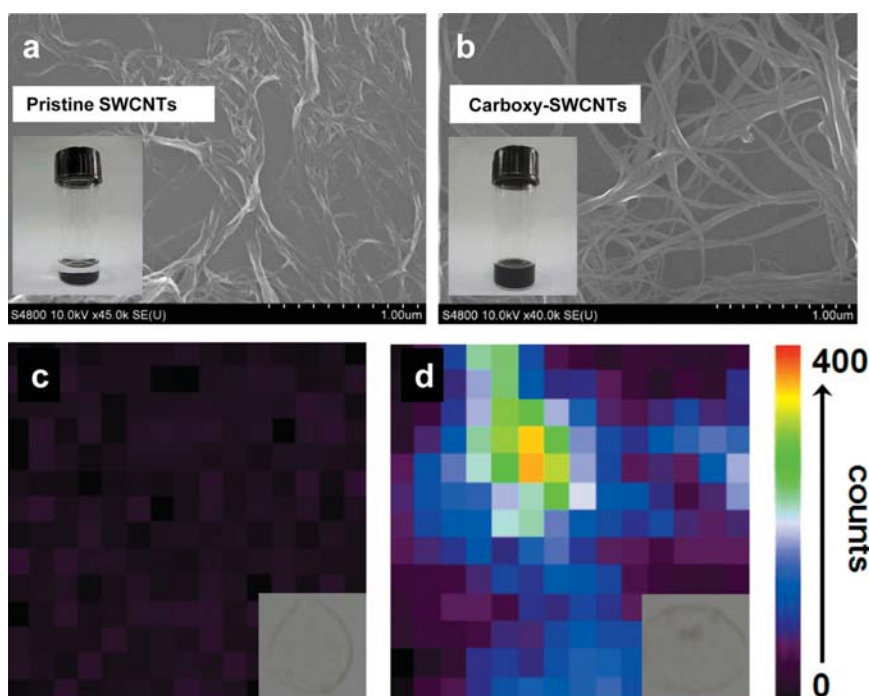


Figure 1. Characterization and cellular penetration of SWCNTs. TEM images and dispersion images of (a) pristine SWCNTs and (b) carboxy-SWCNTs. Raman mapping images of carboxy-SWCNT penetration into KB cells. G-mode (1580 cm^{-1}) Raman intensity images of SWCNTs in single KB cell (c) incubated in PB buffer as control for 24 h and (d) incubated with $60\text{ }\mu\text{g/mL}$ carboxyl-SWCNTs for 24 h. Inset: Regular optical microscope images of a KB cell. Scale is $10 \times 10\text{ }\mu\text{m}$.

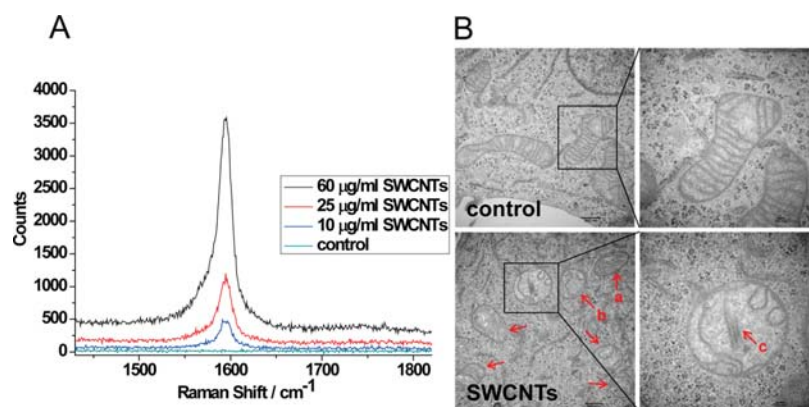


Figure 2. Entering of SWCNTs to the mitochondria and mitochondria structure change. (A) Raman spectra of isolated mitochondria of cells treated with different concentrations of SWCNTs from 0 to $60\text{ }\mu\text{g/mL}$ for 24 h. Curves represent G band (1580 cm^{-1}) Raman spectra of SWCNTs in mitochondria, extracted with a mitochondria isolation kit, measured with equal quantities. (B) Morphology of mitochondria of SWCNT-treated cells examined by transmission electron microscopy. Swelling of mitochondria is indicated by arrows. Arrow a: Mild mitochondrial damage; the cristae are smaller. Arrow b: Severe mitochondrial damage; the cristae are nearly completely destroyed or disappeared. Arrow c: SWCNTs located in a mitochondrion. Scale bar: 500 and 100 nm.

To verify the entering of SWCNTs to the mitochondria, we carried out transmission electron microscopy to observe the mitochondria in KB cells treated with $60\text{ }\mu\text{g/mL}$ of SWCNTs for 24 h. TEM images show that SWCNTs appeared in mitochondria (Figure 2B, arrow c), and the mitochondrial structure was greatly affected. The mitochondria became swollen and round, with the cristae appearing irregular and disordered. Some mitochondria became vacuolus, and the cristae were nearly completely destroyed or disappeared (Figure 2B). The morphology of

mitochondria of KB cells treated with 20, 40, and $80\text{ }\mu\text{g/mL}$ of SWCNTs for 24 h is shown in Figure S2.

SWCNT Treatment Decreases the Level of Mitochondrial Oxygen Uptake. To measure whether SWCNTs can affect mitochondrial respiration, oxygen uptake was measured in KB cells in culture using a sensitive self-referencing oxygen electrode.²⁹ The oxygen consumption measurement is based on the translational movement of an oxygen-selective microelectrode at a known frequency through the gradient of the oxygen concentration

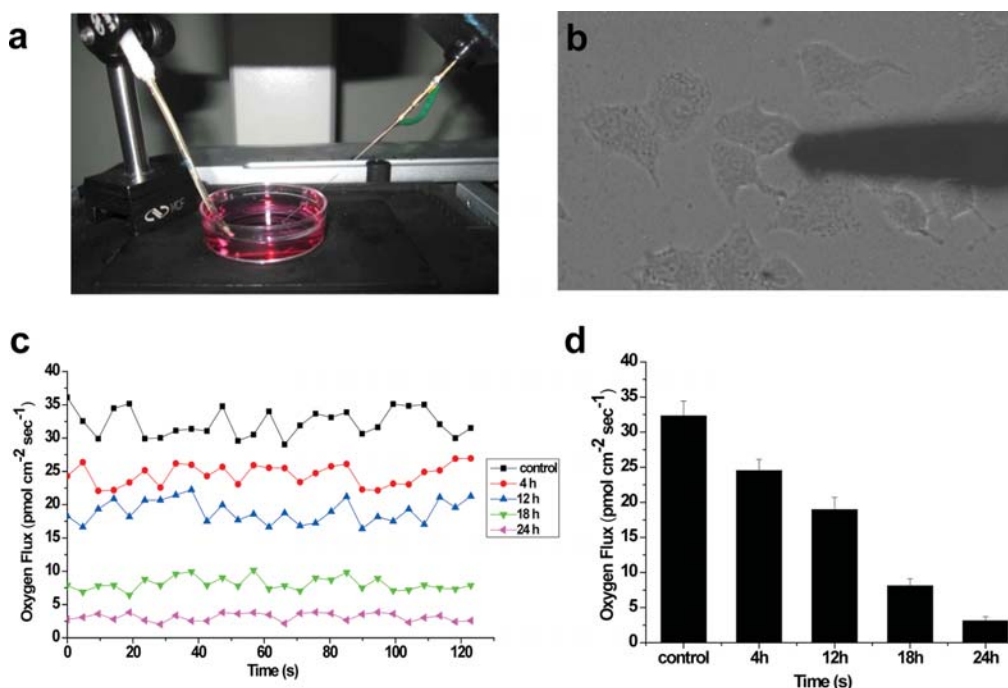


Figure 3. SWCNTs alter O₂ consumption by KB cells. (a) The self-reference electrode. The system is set up on top of a spinning disk confocal microscope. (b) Self-referencing electrode positioned next to a single KB cell. (c) Representative traces of oxygen flux levels of single KB cells. (d) Group data for basal respiration levels of single KB cells (control) or KB cells treated with 60 μ g/mL SWCNTs from 4 to 24 h. At least three independent cultures were used for each study.

around the cell. The differential current of the electrode was converted into a directional measurement of oxygen flux using the Fick equation. Mitochondria require oxygen to produce ATP in sufficient quantities to drive energy-requiring reactions in eukaryotic organisms. The oxygen flux detected reliably correlates with the metabolic state of the cell. Normal mitochondria have high oxygen flux, and a lower level of oxygen flux is a result of malfunctioning mitochondria. As is shown in Figure 3c and d, oxygen consumption in KB cells declined after SWCNT treatment in a time-dependent manner. After 24 h of SWCNT treatment, the oxygen flux of cells is only about 9.7% of that in the control group. The result clearly shows that mitochondrial oxygen consumption of cells is significantly decreased by SWCNT treatment.

Effects of SWCNTs on Mitochondrial Membrane Potential.

Mitochondria, one of the most important organelles in eukaryotic cells, furnish cellular energy through respiration and regulate cellular metabolism as a cellular power plant to maintain the growth, differentiation, and proliferation of cells. The effect of SWCNTs on mitochondrial function was investigated by examining their effects on the MMP, an indicator of mitochondrial activity. We used the MTT assay to evaluate the effect of different concentrations of SWCNTs on cell viability. Our results show that the viability of KB cells decreased after exposure to SWCNTs dispersion for 24 h at high concentrations, while the viability was not significantly affected by PB buffer containing sodium cholate with

the same concentration (Figure S3). Sodium cholate is a surfactant of low biological toxicity broadly used to disperse SWCNTs.³⁰ Cells treated with 60 μ g/mL SWCNTs, which would result in 70% cell viability after 24 h of exposure, were used to investigate the effects of SWCNTs to mitochondria.

The effect of SWCNTs on the MMP of KB cells was first measured by flow cytometry with JC-1 staining. JC-1 existed either as a green fluorescent monomer at depolarized membrane potentials or as a red fluorescent J-aggregate at hyperpolarized membrane potentials. Changed MMPs were indicated by a fluorescence emission shift from J-aggregates with red fluorescence (\sim 590 nm) to J-monomers with green fluorescence (\sim 529 nm). The higher mitochondrial membrane potentials were defined by the higher ratio of red fluorescent intensity and green fluorescent intensity.³¹ Flow cytometry results are expressed as a decrease or increase of fluorescence intensity, indicating a change of MMP among cell populations (Figure 4). Cells incubated with 60 μ g/mL SWCNTs showed a decrease of the red fluorescence intensity in a time-dependent manner. Carbonyl cyanide 3-chlorophenyl hydrazone (CCCP), an uncoupled agent that depolarizes mitochondrial membranes, was used as a positive control. The CCCP-treated group showed a dramatic decrease of red fluorescence intensity (Figure 4b). Cells in the R₂ region have normal MMP, while those in the R₃ region have reduced MMP. The percentages appearing in each panel of Figure 4 are the percentages of cells in

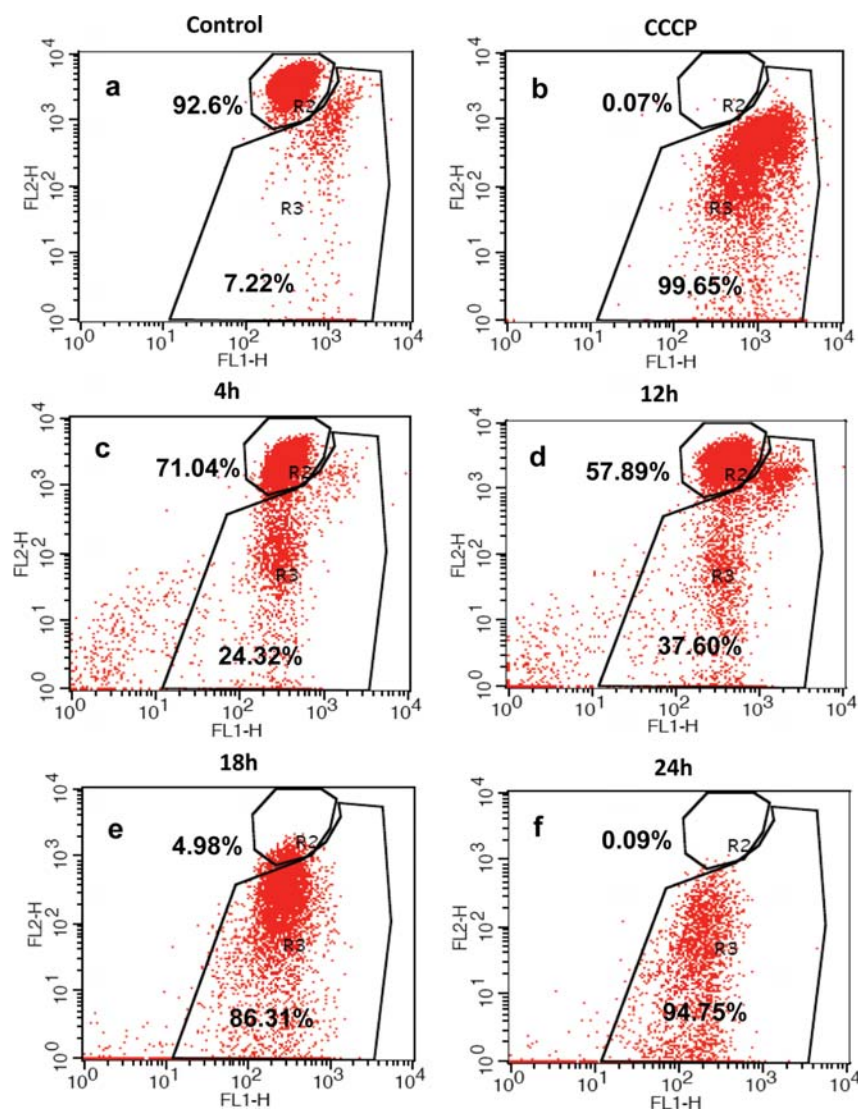


Figure 4. SWCNT treatment significantly triggered MMP decrease. Changes of MMP in KB cells were examined by flow cytometry. (a) KB cells were cultured in DMEM media as control. (b) KB cells treated with CCCP were used as a positive control. (c–f) Cells were treated with 60 $\mu\text{g}/\text{mL}$ of SWCNTs for 4, 12, 18, and 24 h. The numbers indicate the percentage of KB cells with undepolarized (R_2) or depolarized (R_3) membrane potential.

the R_2 and R_3 regions. The results show that the longer KB cells are incubated with SWCNTs, the more cells exhibit a depolarized MMP. When cells were incubated with SWCNTs for 24 h, the MMP of 94.75% of cells was depolarized (Figure 4f).

To confirm the results obtained from flow cytometry, we examined the change of fluorescence in mitochondria by confocal microscopy. The MMP of KB cells in the presence or absence of SWCNTs was measured by confocal microscopy after staining with JC-1 (Figure 5). Control cells had both red and green fluorescence, coexisting in the same cell (Figure 5, top panels). Superimposition of the green and red fluorescent images revealed a large degree of overlap and displayed an orange color. Treatment with the positive control, CCCP, dramatically decreased the red fluorescence (Figure 5, middle panels) and caused a visible increase

of the green fluorescence intensity. The shift in membrane potential was observed by disappearance of fluorescent red-stained mitochondria and an increase in fluorescent green-stained mitochondria. Following treatment with SWCNTs, formation of red fluorescent J-aggregates decreased, and the ratio of red fluorescence intensity to green fluorescence intensity decreased gradually (Figure 5, bottom panels), indicating increased depolarization of mitochondria with prolonged exposure to SWCNTs. These results are consistent with the results obtained using flow cytometry.

SWCNT Treatment Increases the ROS Level in Cells. It has been reported that Cyt c plays an important role in ROS clearance.^{32,33} The intracellular ROS level of cells treated with SWCNTs was measured after treating the KB cells with 60 $\mu\text{g}/\text{mL}$ SWCNTs for 24 h. As shown in Figure S4, compared with the control group, an enhanced ROS level

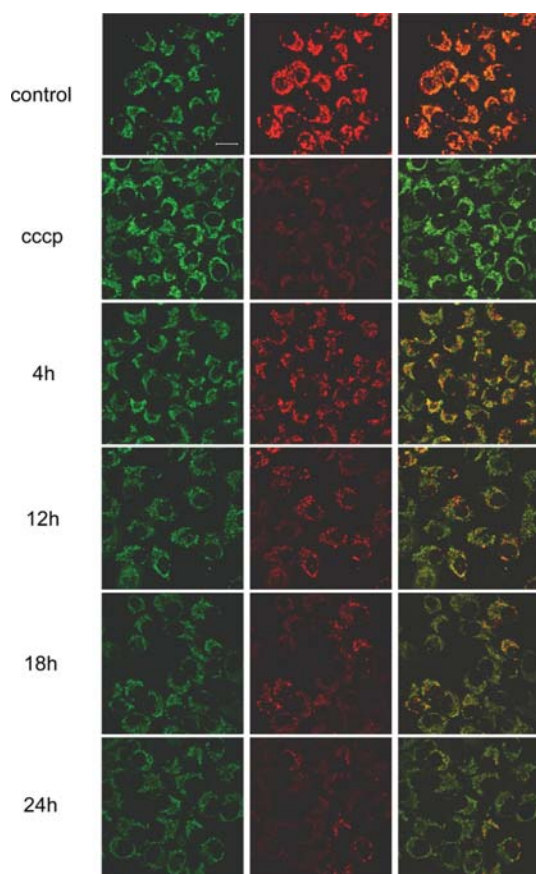


Figure 5. Mitochondrial depolarization imaged by confocal microscopy. MMP of cells stained with JC-1 dye was measured with confocal microscopy. Left and middle images showed the fluorescence of green fluorescent J-monomer and red fluorescent J-aggregate, respectively. The right images showed the overlay of two images. The results were consistent with FACS quantitative measurements. Scale bar: 20 μm .

was detected in SWCNTs-treated cells, which is direct evidence of mitochondrial electron transport disruption and blocked respiratory chain activity.

Interaction of SWCNTs with Cyt c. Normal mitochondrial function requires the balanced interaction between many critical mitochondrial proteins. Minor changes of these proteins could result in dramatic effects on cellular metabolism. Cyt c plays an important role in mitochondrial electron transport and cell metabolism. Its role in maintaining a normal MMP is well established.³⁴ Cyt c is a well-characterized, small, heme-containing redox protein with a molecular weight of 12.384 g/mol. The heme edge of Cyt c is surrounded by an array of lysine and arginine residues. Cyt c transfers electrons by undergoing oxidation and reduction of the iron cation (which can be alternately 2+ or 3+) in Cyt c's heme moiety. Oxidized Cyt c has absorption peaks at 408 and 530 nm, while reduced Cyt c has three peaks, at 415, 520, and 550 nm.³⁵ The additional peak at 550 nm can, therefore, be monitored spectroscopically to quantitate the amount of reduced Cyt c. We determined that Cyt c could bind onto SWCNTs (Figure S5). The extent of binding depended on

the concentrations of both Cyt c and SWCNTs. The amount of Cyt c binding with SWCNTs was quantified with UV–visible spectra at 408 nm. When the concentration of Cyt c was changed, the amount of Cyt c bound to 100 $\mu\text{g/mL}$ SWCNTs showed a linear increase and reached a maximum at 150 $\mu\text{g/mL}$ (Figure S5). The adsorption of Cyt c onto SWCNTs is shown in Figure S6.

Systematic spectroscopic studies were conducted to explore the interaction between Cyt c and SWCNTs. First, it was found that a new absorption peak at 550 nm, the characteristic peak of reduced Cyt c, appeared in the presence of SWCNTs (Figure 6a), similar to the positive control of ascorbic acid, which reduces Cyt c rapidly and thoroughly (Figure S7). This result clearly demonstrates that Cyt c undergoes reduction in the presence of SWCNTs. Next, the effect of pH on the interaction between SWCNTs and Cyt c was investigated. A solution with Cyt c was used as a control. Reduction of Cyt c was facilitated when the pH increased from 7.0 to 9.0, consistent with an increase in the absorbance at 550 nm (Figure 6b). In order to prove this phenomenon was caused only by SWCNTs, the effects of sodium cholate and ionic strength, the other two components in this system, on Cyt c reduction were evaluated at pH 7.0. There was no peak at 550 nm when the concentration of sodium cholate increased from 0.25 wt % to 2.0 wt %, indicating that sodium cholate had little effect on the reduction (Figure S8a). The effect of PB on the interaction between SWCNTs and Cyt c was also investigated. The change of PB concentration from 10 mM to 50 mM had no significant effect on the interaction of SWCNTs with Cyt c (Figure S8b). Taken together, these results demonstrate that the reduction of Cyt c is caused only by SWCNTs and that this reduction is enhanced by an increase of pH.

To find out whether the nonspecific adsorption of serum proteins onto the SWCNT surface will affect their interaction with Cyt c, we also carried out the experiment in complete DMEM media. It was found that Cyt c can still be reduced by SWCNTs in complete DMEM media (Figure S9).

Mechanism of the Interaction of SWCNTs with Cyt c. To analyze the underlying mechanism of the interaction between Cyt c and SWCNTs, we further examined the structural change of Cyt c at different pH's. It has been reported that the structure of Cyt c changes in alkaline solutions. This conformational change is thought to increase the exposure of Cyt c's heme group to the solvent.^{36,37} In this study, the reduction of Cyt c by SWCNTs was enhanced under alkaline conditions. This observation raises the possibility that, at alkaline pH, SWCNTs can more easily access the heme group of Cyt c, resulting in facilitated reduction of Cyt c.

To test this hypothesis, the effect of pH on the conformation change of Cyt c was measured using circular dichroism.³⁸ We found that the α -helical content of Cyt c decreased from 29.9% to 25.8% (pH 7.0

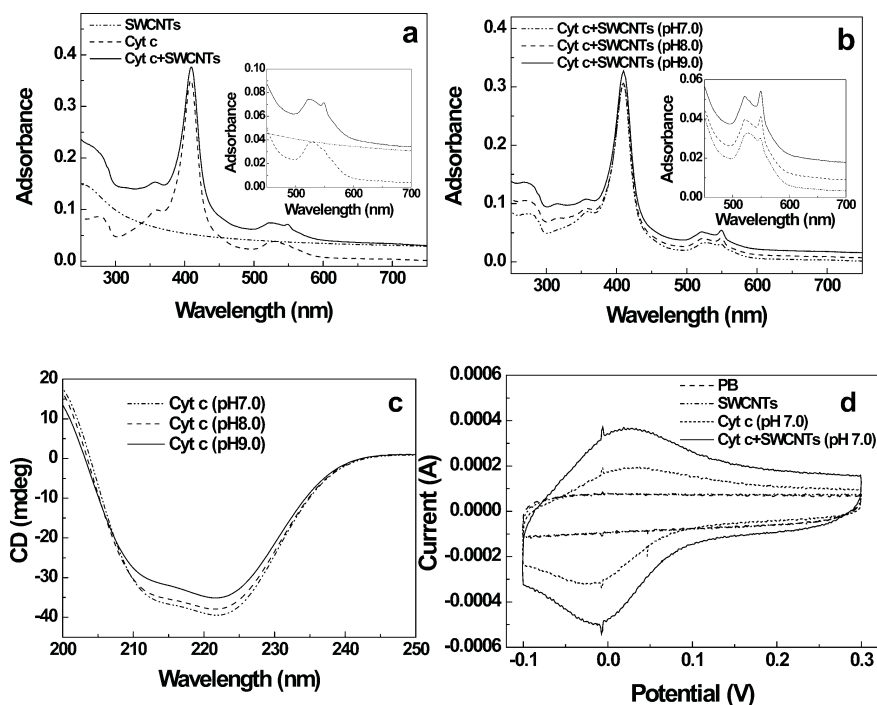


Figure 6. Interaction of SWCNTs with Cyt *c* was indicated with different measurements. (a) UV–vis spectra of Cyt *c*, SWCNTs, and SWCNT + Cyt *c*. The absorption spectrum was magnified in the inset graph as a characteristic peak of Cyt *c* at 550 nm. (b) UV–vis spectra of Cyt *c* under interaction with SWCNTs at different pH's from 7.0 to 9.0. The adsorption spectrum was magnified in the inset graph as a characteristic peak of Cyt *c* at 550 nm. (c) CD spectra of Cyt *c* at different pH's from 7.0 to 9.0. (d) Cyclic voltammograms of Cyt *c* (150 μg/mL) measured with or without SWCNTs (100 μg/mL) and 10 mM PB at pH 7.0. Scan rate = 50 mV s⁻¹.

and pH 8.0, respectively) and to 23.1% (pH 9.0) when the pH was raised (Figure 6c). The distal loop region moved away from the heme moiety at alkaline pH to form a channel with a heme group.³⁶ As the pH increases, the heme group of Cyt *c* was exposed to the solvent to a greater extent, which makes SWCNTs more accessible to the heme group and thereby increases the percentage of Cyt *c* being reduced. The structure change of Cyt *c* opened a channel to the heme pocket through the α -helix and allowed SWCNTs an easier access to the heme group through this channel at higher pH. In addition to the CD measurement, the redox potential of Cyt *c* was determined using cyclic voltammetry (CV). The results of the CV measurements indicated that Cyt *c* had a pair of redox peaks and its redox potential was significantly enhanced in the presence of SWCNTs (Figure 6d). On the basis of CD results and CV results, the structure of Cyt *c* was changed, which increased the exposure of the heme moiety to the solvent, and then the reduction activity became more obvious in the presence of SWCNTs.

To better understand the effects of SWCNTs on the electron transfer of Cyt *c*, the ability of Cyt *c* to catalyze the oxidation of 5,5-dimethyl *N*-oxide pyrroline (DMPO) to 5,5-dimethyl-1-pyrrolidone-*N*-oxyl (DMPOX) was studied using the electron spin resonance (ESR) technique. In the presence of Cyt *c*, H₂O₂ caused the oxidation of DMPO to DMPOX, which gave the typical seven-line ESR

spectrum shown as an inset in Figure 7, and the intensity of the second line in the ESR spectrum of DMPOX was used to monitor the time dependence. Ascorbic acid, as a positive control, inhibited this oxidation in a concentration-dependent manner (Figure 7a). This inhibition was observed as a delay in the appearance of the ESR signal for DMPOX. Similarly, addition of SWCNTs also resulted in a similar concentration-dependent inhibition of oxidation (Figure 7b). As the SWCNT concentration increased, the phenomenon of the ESR signal delay for DMPOX became more obvious with the appearance time from about 150 to 350 s and lowered the intensity from 10.5 to 4.5 au, indicating the slower and smaller amount of electron being transferred. These results indicated that SWCNTs can affect the electron transfer and catalytic ability of Cyt *c* required for the oxidation of DMPO to DMPOX.

Mitochondria are the powerhouses of the living cell, generating energy for various cellular activities. The function and integrity of mitochondria may impact the viability, proliferation/division, and hypoxic tolerance of the cell, and mitochondrial dysfunction is implicated in the pathogenesis of many diseases. For this reason, the study of mitochondrial function has become central to a wide variety of clinical and basic science research. The majority of ATP generation is dependent on mitochondrial electron transport. Cyt *c*, as an integral mitochondrial protein, plays an important role in electron transport and cell respiration.³⁴ Cytochrome *c*

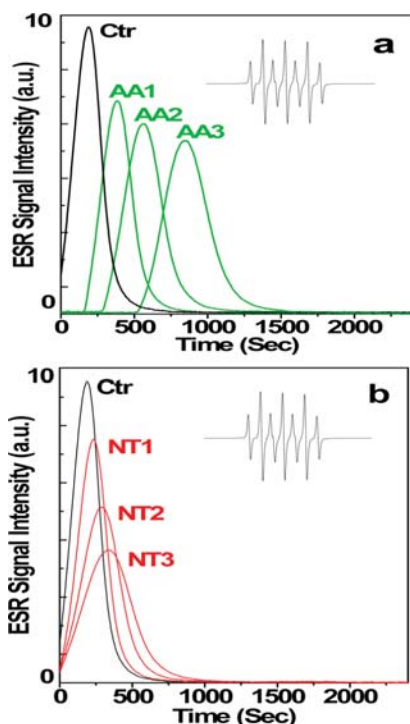


Figure 7. Time-dependent ESR signal of DMPOX measured during oxidation of the spin trap DMPO by Cyt *c*/H₂O₂ at ambient temperature. The intensity of the second line in the ESR spectrum of DMPOX was used to monitor the time dependence. (a) Time dependence of the ESR signal for solutions containing 50 mM DMPO, 0.1 mM Cyt *c*, and 0.5 mM H₂O₂ without (Ctr: control) or with ascorbic acid (AA1: 0.01 mM ascorbic acid; AA2: 0.05 mM ascorbic acid; AA3: 0.1 mM ascorbic acid) measured at pH 7.0. (b) Time dependence of the ESR signal with 10 μg/mL SWCNTs (NT1: 2.5 μL; NT2: 5 μL; NT3: 7.5 μL), substituted for ascorbic acid, measured at pH 7.0. The typical seven-line ESR spectrum of DMPOX is given as the inset after oxidation of DMPO in the presence of Cyt *c* and H₂O₂.

oxidase is the terminal enzyme of the mitochondrial respiratory chain and is responsible for 90% of cellular oxygen consumption in mammals. In mitochondria, cytochrome *c* plays an essential role in the generation of MMP. This potential is essential for various functions including the production of ATP via oxidative phosphorylation.

To successfully apply the new generation of nanomaterials as drug carriers in the treatment of diseases, it is essential to determine their pharmacological and toxicological profiles. SWCNTs are commonly used as carriers to forward different payloads into cells. However, as the basis of biomedical applications of SWCNTs, their interactions with intracellular molecules in cells have not been fully understood. The potential biomedical applications of nanotubes require a better understanding of their cellular dynamics for their better usage in the clinic. The toxicity of carbon nanotubes has been an important issue in carbon nanomaterial research. The potential cytotoxicity includes metabolic pathway disruption, redox regulation, cytoskeleton formation alteration, cell growth inhibition, etc. Yuan *et al.* found that two cytoskeleton-related proteins, profilin and filamin,

were upregulated by approximately 35% in oxidized SWCNT-treated cells. The upregulation of these cytoskeleton proteins suggested that the exposure of SWCNTs might alter the intracellular microfilament network.³⁹ Kagan *et al.* demonstrated that iron-rich SWCNTs caused a significant loss of intracellular low molecular weight thiols and accumulation of lipid hydroperoxides in murine macrophages.⁴⁰ It has been reported that mitochondria are the target organelles for the cytotoxicity of SWCNTs.⁴¹ Consistent with the reports of other investigators, we have found that treatment of cells with SWCNTs resulted in accumulation of the SWCNTs in the cells. At low concentrations, for short periods, SWCNTs inhibit cytochrome *c* oxidase to a lower extent, but a higher period of SWCNT exposure results in inhibition of respiration, leading to the development of “metabolic hypoxia”, a situation in which, although oxygen is available, the cell is unable to utilize it. We have further determined that this accumulation of SWCNTs was accompanied by a reduction in the MMP. Cytochrome *c* molecules can be successfully absorbed noncovalently on carbon nanotubes.⁴² The interaction most likely occurs via the protein side that is rich in Lys residues, since the primary amines strongly bind to carboxylate functionalities, and amines are also known to strongly interact with the carbon-nanotube sidewall.⁴³ The effect of SWCNTs on the electron-transfer reaction of cytochrome *c* has been previously studied in biosensor research. Wang *et al.* has found the activated SWCNT-modified electrode promotes the reduction/oxidation of cytochrome *c*.²³ Our results suggest that SWCNTs may directly interact with Cyt *c* to alter its oxidation state and redox potential, resulting in an alteration in Cyt *c*'s ability to facilitate electron transport. Disruption in electron transfer has many unfavorable consequences. It has been reported that disrupting electron transfer at cytochrome *c* oxidase may result in ionic readjustment and modulation of the Ca²⁺ flux between the mitochondria and the endoplasmic reticulum.⁴⁴

CONCLUSIONS

In this study, we investigated the effect of SWCNTs on mitochondria function and the interactions of SWCNTs with Cyt *c*, an important component of the electron transport chain in mitochondria. On the basis of the extracellular interactions of cytochrome *c* with carbon nanotubes, and the intracellular mitochondrial dysfunction induced by SWCNT treatment, we primarily conclude that the effects of SWCNTs on mitochondria should be a stepwise process: (1) SWCNTs enter the cells and localize in the mitochondria; (2) Cyt *c* is partially reduced when interacting with SWCNTs and the redox activity of Cyt *c* is affected; (3) the electron transfer of Cyt *c* is decreased and attenuated; (4) MMP is decreased; (5) the mitochondrial respiratory chain is disrupted and mitochondrial oxygen uptake is greatly reduced; (6) metabolic hypoxia is caused by SWCNTs

and the mitochondrial electron transport-dependent ATP generation is affected. Identification of pharmacological and toxicological profiles is of critical importance for the use of nanoparticles as drug carriers in nanomedicine and for the biosafety evaluation of environmental nanoparticles in nanotoxicology. The findings of this study will broaden and deepen our

understanding of the interaction of SWCNTs with Cyt c and the mechanism of mitochondria dysfunction caused by SWCNTs. When using SWCNTs to fulfill different applications such as live imaging, photothermal therapy, and pharmaceutical carriers in the future, their disruption of mitochondria function and cellular respiration should be considered.

METHODS

Materials. Pristine SWCNTs were purchased from Chengdu Organic Chemicals Company Ltd. of Chinese Academy of Sciences. Carbonyl cyanide 3-chlorophenyl hydrazone (CCCP) and sodium cholate were obtained from Alfa Aesar (Ward Hill, MA, USA). Oxidized Cyt c from horse heart, the spin trap, 5,5-dimethyl *N*-oxide pyrroline (DMPO), and L-ascorbic acid were purchased from Sigma (St. Louis, MO, USA). Mitochondria were isolated by a Mitochondria Isolation Kit (Pierce, Rockford, IL, USA) for cultured cells. All chemicals were of analytical grade and were used without further purification.

Preparation of Carboxyl-SWCNTs. In order to improve their dispersity and stability in solutions, pristine SWCNTs were treated by acid oxidation. Briefly, 0.1 g of pristine SWCNTs and 100 mL of a 3:1 (v/v) mixture of 98% H₂SO₄ and 68% HNO₃ were mixed and sonicated for 2 h. The resulting dark suspension was cooled to room temperature and diluted with distilled water. The diluted suspension was filtered through a 0.22 μ m polycarbonate membrane (Millipore, USA) and rinsed with distilled water until the pH was greater than 5. Finally, the purified carboxy-SWCNTs were dried at room temperature. Carboxyl-SWCNTs were suspended in phosphate buffer (30 mM, pH 7.0) with 0.5 wt % sodium cholate surfactant and sonicated for 2 h. The suspension was then centrifuged at 1500 rpm for 10 min to remove large bundles. The concentration of carboxyl-SWCNTs was determined by UV–visible spectroscopy.

MTT Assay. The cell viability of human epithelial carcinoma cells (KB cells, kindly provided by Dr. Michael M. Gottesman, CCR, NCI) treated with SWCNTs was determined using the MTT assay. Cells were stained with 100 μ L of sterilized MTT dye (3-(4,5-dimethylthiazol-2-yl)-2,5-diphenyltetrazolium bromide, 0.5 mg/mL, Sigma-Aldrich) for 4 h at 37 °C, and 100 μ L of DMSO was added. The spectrometric absorbance at 570 nm was measured on a microplate reader (M200, Tecan, Männedorf, Switzerland).

Micro-Raman Mapping. After 24 h of treatment with SWCNTs, KB cells were washed twice to remove free SWCNTs, and the media was replaced with PBS. The scanning area was selected by focusing on the cells using the microscope, and the micro-Raman laser was then focused on the dish (λ excitation = 785 nm) using the Renishaw micro-Raman spectroscopy system (Renishaw plc, Wotton-under-Edge, UK). A line scanning mode was applied to get a Raman spectrum at every point in the selected area (1 μ m \times 1 μ m for each point). The image was obtained by plotting the integrated area in the range 1580–1610 cm⁻¹ of the Raman spectra obtained in the cell-containing area.

Oxygen Flux Measurements. Oxygen consumption was recorded according to the self-referencing method.^{29,45} Briefly, a platinum electrode was placed 5 μ m from the cell and then moved rapidly back and forth over a 10 μ m distance between two points located 5 and 15 μ m away from the cell soma in the X–Y axes, so that the oxygen-sensing electrode was positioned repeatedly closer to and farther from the cell. This amperometric probe was polarized with –0.6 V, at which voltage the reduction of oxygen at the probe tip was diffusion-limiting, and therefore [O₂] in the solution could be assessed. As the O₂ concentration near the cell is smaller than in the far position, the difference in current between the near and the far position of the platinum electrode represents the gradient of the oxygen concentration around the cell, a reflection of O₂ consumption. We then converted the difference in current into oxygen flux. The oxygen flux level was measured every 4.73 s. Figure 3c is the

representative trace of the oxygen flux level of one single cell under each treatment. Figure 3d is the average oxygen flux value of all the measured values of all the cells under each treatment.

Flow Cytometry Measurements. The MMP was measured with 1.5 μ M JC-1 (5,5',6,6'-tetrachloro-1,1',3,3'-tetraethylbenzimidazolylcarbocyanine iodide) (Invitrogen, Rockville, MD, USA) by flow cytometry. KB cells were seeded in six-well plates and incubated for 24 h. Then cells were incubated in fresh DMEM media or in media containing SWCNTs for 4, 12, 18, and 24 h. As a known MMP disrupter, 100 μ M carbonyl cyanide 3-chlorophenyl hydrazone (CCCP, Alfa Aesar, Haverhill, MA, USA) was used as a positive control. After incubation, cells were trypsinized, collected by centrifugation, and then incubated with medium containing JC-1 dye for 20 min at 37 °C. Finally, the cells were washed and resuspended in 1 mL of PBS for fluorescent analysis using a FACScan flow cytometer. J-aggregate fluorescence was recorded by flow cytometry in fluorescence channel 2 (FL2) and monomer fluorescence in fluorescence channel 1 (FL1).

Confocal Microscopy Imaging. KB cells were seeded in polylysine-coated glass bottom dishes. After 24 h, the cells were treated with SWCNTs for 4, 12, 18, and 24 h. The cells were then stained with JC-1 dye as previously described for flow cytometry and examined by confocal microscopy (Ultraview VOX, Perkin-Elmer, Waltham, MA, USA).

Measurement of Interactions between Cyt c and Carboxyl-SWCNTs. Cyt c was incubated with selected concentrations of carboxyl-SWCNTs for 1 h at room temperature. After incubation, the suspension was centrifuged at 13 000 rpm for 30 min, and the supernatant was removed. The amount of Cyt c in the supernatant was measured using UV–visible spectroscopy (Lambda 950, Perkin-Elmer, USA). The UV absorption peak at 408 nm, attributable to the heme group in the Soret region of the Cyt c spectrum, was used to quantitate Cyt c.

UV–Visible Spectroscopy Assay. The reduction of oxidized Cyt c in the presence of SWCNTs was measured using the absorption of Cyt c at 550 nm characteristic for reduced Cyt c. Ascorbic acid, a known reducing agent, was used as a positive control. Briefly, oxidized Cyt c was dissolved in PB solution. The spectra were measured after SWCNTs (0.1 mg/mL) or ascorbic acid (5 mg/mL) was added. In addition, to measure the effect of the surfactant, sodium cholate, on the reduction of Cyt c by SWCNTs, UV–visible absorption spectra were obtained for solutions containing Cyt c (150 μ g/mL), SWCNTs (100 μ g/mL), and sodium cholate ranging from 0.25 to 2 wt %. To study the effect of pH on the interaction between SWCNTs and Cyt c, SWCNTs (100 μ g/mL) were incubated with oxidized Cyt c (150 μ g/mL) in PB with increasing pH from 7.0 to 9.0.

Circular Dichroism (CD) Measurement. CD spectra in the far-UV (200–250 nm), near-UV (250–350 nm), and the Soret (350–450 nm) spectral regions were recorded using a spectropolarimeter (J-720, Jasco). Spectra were obtained for samples containing 600 μ g/mL oxidized Cyt c in the absence or presence of SWCNTs (400 μ g/mL) at different pH. CD spectra were measured using quartz cells with a 1 mm path length. All spectra were corrected for background absorption. Each experiment was repeated three times with a bandwidth of 1.0 nm and scanning rate of 100 nm/min. All the measurements were performed at a constant temperature of 20 °C.

Cyclic Voltammetry Analysis. A three-electrode cell with indium tin oxides (ITO) as working electrode, Pt as counter electrode, and Hg/Hg₂Cl₂ as reference electrode was used for the

measurements by potentiostat with PHE200TM physical electrochemistry analysis (Gamry Instruments, Warminster, PA, USA). The working electrode area was identical among samples. The cyclic voltammograms were recorded immediately after inserting the reference electrode into the potentiostat analyte solution (Princeton Applied Research, Oak Ridge, TN, USA). The potential cycling was started at 0.3 V and allowed to proceed until -0.1 V, and the cycle was completed by stopping the scan at 0.3 V (scan rate 50 mV/s).

Electron Spin Resonance Measurements. Oxidation of the spin trap DMPO, to form DMPOX, was monitored by ESR to determine the effects of SWCNTs on Cyt *c*'s ability to catalyze oxidation of substrates by H_2O_2 . Conventional ESR spectra were obtained using a Bruker EMX ESR spectrometer (Billerica, MA, USA). ESR spectral measurements were obtained using the following settings: 10 mW microwave power, 1 G field modulation, and 100 G scan range. The time dependence of the ESR signal for solutions containing 50 mM DMPO, 0.1 mM Cyt *c*, and 0.5 mM H_2O_2 with or without ascorbic acid (from 0.01 to 0.1 mM) was measured. Similarly, the time dependence of the ESR signal with 10 $\mu\text{g}/\text{mL}$ SWCNTs (from 2.5 to 7.5 μL), substituted for ascorbic acid, was measured. The time dependence of the ESR signal intensity was obtained at a fixed field position (the peak position of the center line of ESR spectrum). Data collection began 1 min after sample mixing. For measurement of the time dependence of the ESR signal, a scan time of 30 min at the described fixed field position was used. All measurements were performed in triplicates at ambient temperature.

ROS Levels Detection. The cells treated with or without SWCNTs for 24 h were stained for 30 min with a 10 μM ROS probe DCFH-DA (Molecular Probes, Eugene, Oregon, USA) in PBS solution with 0.4% glucose. After the free probes were washed, the cells were observed using fluorescence microscopy.

Conflict of Interest: The authors declare no competing financial interest.

Supporting Information Available: Stability of carboxy-SWCNTs in physiological buffer and media; effect of SWCNTs and sodium cholate on the viability of KB cells; fluorescence microscopy images of ROS generation in SWCNT-treated KB cells; quantification of Cyt *c* adsorbed onto SWCNTs; UV-visible spectra of Cyt *c* in the absence and presence of ascorbic acid; UV-visible spectra of Cyt *c* interacting with SWCNTs in the presence of different concentrations of sodium cholate; UV-visible spectra of Cyt *c* interacting with SWCNTs at pH 7.0 with varied PB concentration; and UV-vis spectra of Cyt *c* interacting with SWCNTs in complete DMEM media. These materials are available free of charge via the Internet at <http://pubs.acs.org>.

Acknowledgment. This work was supported by grants from the Chinese Natural Science Foundation project (Nos. 30970784 and 81171455), National Key Basic Research Program of China (2009CB930200), Chinese Academy of Sciences (CAS) "Hundred Talents Program" (07165111ZX), and CAS Knowledge Innovation Program. This work was supported in part by NIH/NCRR 3 G12 RR003048, NIH/NIMHD 8 G12 MD007597, and USAMRMC W81XWH-10-1-0767 grants. This article is not an official U.S. Food and Drug Administration (FDA) guidance or policy statement. No official support or endorsement by the U.S. FDA is intended or should be inferred. This work was supported by a regulatory science grant under the FY11 FDA Nanotechnology CORES Program (J.J.Y. and W.G.W.).

REFERENCES AND NOTES

- Liu, Z.; Tabakman, S.; Welshe, K.; Dai, H. J. Carbon Nanotubes in Biology and Medicine: *In Vitro* and *In Vivo* Detection, Imaging and Drug Delivery. *Nano Res.* **2009**, *2*, 85–120.
- Prato, M.; Kostarelos, K.; Bianco, A. Functionalized Carbon Nanotubes in Drug Design and Discovery. *Acc. Chem. Res.* **2008**, *41*, 60–68.
- Zhou, F.; Xing, D.; Wu, B.; Wu, S.; Ou, Z.; Chen, W. R. New Insights of Transmembrane Mechanism and Subcellular Localization of Noncovalently Modified Single-Walled Carbon Nanotubes. *Nano Lett.* **2010**, *10*, 1677–1681.

- Bayraktar, H.; Ghosh, P. S.; Rotello, V. M.; Knapp, M. J. Disruption of Protein-Protein Interactions Using Nanoparticles: Inhibition of Cytochrome C Peroxidase. *Chem. Commun. (Cambridge, U.K.)* **2006**, 1390–1392.
- Karajanagi, S. S.; Vertegel, A. A.; Kane, R. S.; Dordick, J. S. Structure and Function of Enzymes Adsorbed onto Single-Walled Carbon Nanotubes. *Langmuir* **2004**, *20*, 11594–11599.
- Zhang, B.; Xing, Y.; Li, Z.; Zhou, H.; Mu, Q.; Yan, B. Functionalized Carbon Nanotubes Specifically Bind to Alpha-Chymotrypsin's Catalytic Site and Regulate Its Enzymatic Function. *Nano Lett.* **2009**, *9*, 2280–2284.
- Wijaya, I.; Gandhi, S.; Nie, T.; Wangoo, N.; Rodriguez, I.; Shekhawat, G.; Suri, C.; Mhaisalkar, S. Protein/Carbon Nanotubes Interaction: The Effect of Carboxylic Groups on Conformational and Conductance Changes. *Appl. Phys. Lett.* **2009**, *95*, 073704.
- Yi, C.; Fong, C.; Zhang, Q.; Lee, S.; Yang, M. The Structure and Function of Ribonuclease A upon Interacting with Carbon Nanotubes. *Nanotechnology* **2008**, *19*, 095102.
- Bayraktar, H.; You, C. C.; Rotello, V. M.; Knapp, M. J. Facial Control of Nanoparticle Binding to Cytochrome *c*. *J. Am. Chem. Soc.* **2007**, *129*, 2732–2733.
- Sandhanaraj, B.; Bayraktar, H.; Krishnamoorthy, K.; Knapp, M.; Thayumanavan, S. Recognition and Modulation of Cytochrome *c*'s Redox Properties Using an Amphiphilic Homopolymer. *Langmuir* **2007**, *23*, 3891–3897.
- Shang, W.; Nuffer, J. H.; Dordick, J. S.; Siegel, R. W. Unfolding of Ribonuclease A on Silica Nanoparticle Surfaces. *Nano Lett.* **2007**, *7*, 1991–1995.
- Cedervall, T.; Lynch, I.; Lindman, S.; Berggard, T.; Thulin, E.; Nilsson, H.; Dawson, K. A.; Linse, S. Understanding the Nanoparticle-Protein Corona using Methods to Quantify Exchange Rates and Affinities of Proteins for Nanoparticles. *Proc. Natl. Acad. Sci. U. S. A.* **2007**, *104*, 2050–2055.
- Yi, C.; Fong, C.; Chen, W.; Qi, S.; Tzang, C.; Lee, S.; Yang, M. Interactions between Carbon Nanotubes and DNA Polymerase and Restriction Endonucleases. *Nanotechnology* **2007**, *18*, 025102.
- Liu, D.; Yi, C.; Zhang, D.; Zhang, J.; Yang, M. Inhibition of Proliferation and Differentiation of Mesenchymal Stem Cells by Carboxylated Carbon Nanotubes. *ACS Nano* **2010**, *4*, 2185–2195.
- Bertoncini, P.; Chauvet, O. Conformational Structural Changes of Bacteriorhodopsin Adsorbed onto Single-Walled Carbon Nanotubes. *J. Phys. Chem. B* **2010**, *114*, 4345–4350.
- Li, K.; Li, Y.; Shelton, J. M.; Richardson, J. A.; Spencer, E.; Chen, Z. J.; Wang, X.; Williams, R. S. Cytochrome *c* Deficiency Causes Embryonic Lethality and Attenuates Stress-Induced Apoptosis. *Cell* **2000**, *101*, 389–399.
- Maloyan, A.; Sanbe, A.; Osinska, H.; Westfall, M.; Robinson, D.; Imahashi, K.; Murphy, E.; Robbins, J. Mitochondrial Dysfunction and Apoptosis Underlie the Pathogenic Process in Alpha-B-Crystallin Desmin-Related Cardiomyopathy. *Circulation* **2005**, *112*, 3451–3461.
- Irwin, W. A.; Bergamin, N.; Sabatelli, P.; Reggiani, C.; Megighian, A.; Merlini, L.; Braghetta, P.; Columbaro, M.; Volpin, D.; Bressan, G. M.; et al. Mitochondrial Dysfunction and Apoptosis in Myopathic Mice with Collagen VI Deficiency. *Nat. Genet.* **2003**, *35*, 367–371.
- Chandra, D.; Bratton, S. B.; Person, M. D.; Tian, Y.; Martin, A. G.; Ayres, M.; Fearnhead, H. O.; Gandhi, V.; Tang, D. G. Intracellular Nucleotides Act as Critical Prosurvival Factors by Binding to Cytochrome *c* and Inhibiting Apoptosome. *Cell* **2006**, *125*, 1333–1346.
- Hao, Z.; Duncan, G. S.; Chang, C. C.; Elia, A.; Fang, M.; Wakeham, A.; Okada, H.; Calzascia, T.; Jang, Y.; You-Ten, A.; et al. Specific Ablation of the Apoptotic Functions of Cytochrome C Reveals a Differential Requirement for Cytochrome *c* and Apaf-1 in Apoptosis. *Cell* **2005**, *121*, 579–591.
- Zhivotovsky, B.; Orrenius, S.; Brustugun, O.; Doskeland, S. Injected Cytochrome *c* Induces Apoptosis. *Nature* **1998**, *391*, 449–450.

22. Waterhouse, N. J.; Goldstein, J. C.; von Ahsen, O.; Schuler, M.; Newmeyer, D. D.; Green, D. R. Cytochrome C Maintains Mitochondrial Transmembrane Potential and ATP Generation after Outer Mitochondrial Membrane Permeabilization during the Apoptotic Process. *J. Cell Biol.* **2001**, *153*, 319–328.
23. Wang, J.; Li, M.; Shi, Z.; Li, N.; Gu, Z. Direct Electrochemistry of Cytochrome c at a Glassy Carbon Electrode Modified with Single-Wall Carbon Nanotubes. *Anal. Chem.* **2002**, *74*, 1993–1997.
24. Kam, N. W.; Dai, H. Carbon Nanotubes as Intracellular Protein Transporters: Generality and Biological Functionality. *J. Am. Chem. Soc.* **2005**, *127*, 6021–6026.
25. Zhou, F.; Wu, S.; Wu, B.; Chen, W. R.; Xing, D. Mitochondria-Targeting Single-Walled Carbon Nanotubes for Cancer Photothermal Therapy. *Small* **2011**, *7*, 2727–2735.
26. Kam, N. W.; Liu, Z.; Dai, H. Carbon Nanotubes as Intracellular Transporters for Proteins and DNA: An Investigation of the Uptake Mechanism and Pathway. *Angew. Chem., Int. Ed.* **2006**, *45*, 577–581.
27. Liu, Z.; Tabakman, S. M.; Chen, Z.; Dai, H. Preparation of Carbon Nanotube Bioconjugates for Biomedical Applications. *Nat. Protoc.* **2009**, *4*, 1372–1382.
28. Liu, Z.; Winters, M.; Holodniy, M.; Dai, H. siRNA Delivery into Human T Cells and Primary Cells with Carbon-Nanotube Transporters. *Angew. Chem., Int. Ed.* **2007**, *46*, 2023–2027.
29. Land, S. C.; Porterfield, D. M.; Sanger, R. H.; Smith, P. J. The Self-Referencing Oxygen-Selective Microelectrode: Detection of Transmembrane Oxygen Flux from Single Cells. *J. Exp. Biol.* **1999**, *202*, 211–218.
30. Blackburn, J. L.; McDonald, T. J.; Metzger, W. K.; Engtrakul, C.; Rumbles, G.; Heben, M. J. Protonation Effects on the Branching Ratio in Photoexcited Single-Walled Carbon Nanotube Dispersions. *Nano Lett.* **2008**, *8*, 1047–1054.
31. Mathur, A.; Hong, Y.; Kemp, B. K.; Barrientos, A. A.; Eruslimsky, J. D. Evaluation of Fluorescent Dyes for the Detection of Mitochondrial Membrane Potential Changes in Cultured Cardiomyocytes. *Cardiovasc. Res.* **2000**, *46*, 126–138.
32. Atlante, A.; Calissano, P.; Bobba, A.; Azzariti, A.; Marra, E.; Passarella, S. Cytochrome c Is Released from Mitochondria in a Reactive Oxygen Species (ROS)-Dependent Fashion and Can Operate as a ROS Scavenger and as a Respiratory Substrate in Cerebellar Neurons Undergoing Excitotoxic Death. *J. Biol. Chem.* **2000**, *275*, 37159–37166.
33. Skulachev, V. P. Cytochrome c in the Apoptotic and Antioxidant Cascades. *FEBS Lett.* **1998**, *423*, 275–280.
34. Dalmonte, M. E.; Forte, E.; Genova, M. L.; Giuffrè, A.; Sarti, P.; Lenaz, G. Control of Respiration by Cytochrome c Oxidase in Intact Cells: Role of the Membrane Potential. *J. Biol. Chem.* **2009**, *284*, 32331–32335.
35. Margoliash, E.; Frohwirt, N. Spectrum of Horse-Heart Cytochrome c. *Biochem. J.* **1959**, *71*, 570–572.
36. Assfalg, M.; Bertini, I.; Dolfi, A.; Turano, P.; Mauk, A. G.; Rosell, F. I.; Gray, H. B. Structural Model for an Alkaline Form of Ferricytochrome c. *J. Am. Chem. Soc.* **2003**, *125*, 2913–2922.
37. Sivakolundu, S.; Mabrouk, P. Cytochrome c Structure and Redox Function in Mixed Solvents Are Determined by the Dielectric Constant. *J. Am. Chem. Soc.* **2000**, *122*, 1513–1521.
38. Kerr, L. E.; Birse-Archbold, J. L.; Short, D. M.; McGregor, A. L.; Heron, I.; Macdonald, D. C.; Thompson, J.; Carlson, G. J.; Kelly, J. S.; McCulloch, J.; et al. Nucleophosmin is a Novel Bax Chaperone that Regulates Apoptotic Cell Death. *Oncogene* **2007**, *26*, 2554–2562.
39. Yuan, J.; Gao, H.; Sui, J.; Duan, H.; Chen, W. N.; Ching, C. B. Cytotoxicity Evaluation of Oxidized Single-Walled Carbon Nanotubes and Graphene Oxide on Human Hepatoma HepG2 cells: An iTRAQ-Coupled 2D LC-MS/MS Proteome Analysis. *Toxicol. Sci.* **2012**, *126*, 149–161.
40. Kagan, V. E.; Tyurina, Y. Y.; Tyurin, V. A.; Konduru, N. V.; Potapovich, A. I.; Osipov, A. N.; Kisin, E. R.; Schwegler-Berry, D.; Mercer, R.; Castranova, V.; et al. Direct and Indirect Effects of Single Walled Carbon Nanotubes on RAW 264.7 Macrophages: Role of Iron. *Toxicol. Lett.* **2006**, *165*, 88–100.
41. Yang, Z.; Zhang, Y.; Yang, Y.; Sun, L.; Han, D.; Li, H.; Wang, C. Pharmacological and Toxicological Target Organelles and Safe Use of Single-Walled Carbon Nanotubes as Drug Carriers in Treating Alzheimer Disease. *Nanomed. Nanotechnol. Biol. Med.* **2010**, *6*, 427–441.
42. Azamian, B. R.; Davis, J. J.; Coleman, K. S.; Bagshaw, C. B.; Green, M. L. H. Bioelectrochemical Single-Walled Carbon Nanotubes. *J. Am. Chem. Soc.* **2002**, *124*, 12664–12665.
43. Heering, H. A.; Williams, K. A.; de Vries, S.; Dekker, C. Specific Vectorial Immobilization of Oligonucleotide-Modified Yeast Cytochrome c on Carbon Nanotubes. *ChemPhysChem* **2006**, *7*, 1705–1709.
44. Xu, W.; Charles, I. G.; Moncada, S. Nitric Oxide: Orchestrating Hypoxia Regulation through Mitochondrial Respiration and the Endoplasmic Reticulum Stress Response. *Cell Res.* **2005**, *15*, 63–65.
45. Smith, P. J. S.; Sanger, R. H.; Messerli, M. A. Principles, Development and Applications of Self-Referencing Electrochemical Microelectrodes to the Determination of Fluxes at Cell Membranes. In *Electrochemical Methods for Neuroscience*; Michael, A. C., Borland, L. M., Eds.; CRC Press: Boca Raton, FL, 2007; pp 373–405.

Surface chemistry-mediated penetration and gold nanorod thermotherapy in multicellular tumor spheroid†

Cite this: *Nanoscale*, 2013, 5, 143

Received 16th July 2012
Accepted 23rd October 2012

DOI: 10.1039/c2nr31877f

www.rsc.org/nanoscale

Shubin Jin,^{‡ab} Xiaowei Ma,^{‡ab} Huili Ma,^{ab} Kaiyuan Zheng,^{ab} Juan Liu,^{ab} Shuai Hou,^c Jie Meng,^{ab} Paul C. Wang,^d Xiaochun Wu^{*c} and Xing-Jie Liang^{*ab}

We investigated the penetration and thermotherapy efficiency of different surface coated gold nanorods (Au NRs) in multicellular tumor spheroids. The current data show that negatively charged Au NRs, other than positively charged Au NRs, can penetrate deep into the tumor spheroids and achieve a significant thermal therapeutic benefit.

Gold nanorods (Au NRs) are well-developed nanomaterials that have various applications in biomedical research, such as cell imaging, drug and gene delivery and thermal therapy, because of their biocompatibility and unique optical properties.^{1–4} In thermal therapy, the localized surface plasmon resonance (LSPR) effect enables Au NRs to convert luminous energy into heat when activated by laser at a specific wavelength.⁵ The LSPR maximum can be tuned to the near-infrared (NIR, 700–900 nm)⁶ region by controlling the aspect ratio and size of the Au NRs.⁷ Thus, the laser powerfully penetrates through human tissues and can reach deep sites in the lesions. Additionally, it is harmless to cells without Au NRs.^{4,8}

The bio-distribution of Au NRs in tumor tissues is still unclear. Most tumor cells, unlike normal tissue cells, are not reached by vasculature: blood and lymphatic vessels.⁹ Many effective *in vitro* drugs fail to be used in clinical settings because of their poor distribution at the tumor site; therefore, they could only achieve an effective concentration in the cells close to the vasculatures.⁹ The ability of Au NRs to penetrate the tumor tissues and accumulate at

sites distant to the blood vessels is essential for the success of the thermal therapy.

Previous studies have reported that the surface chemistry is a key factor affecting the cellular uptake and tissue penetration of nanomaterials.^{10–13} In this study, the relationship between the surface chemistry and the penetration ability of Au NRs was investigated. We synthesized Au NRs with three different polymer coatings: cetyltrimethylammonium bromide (CTAB), polystyrene sulfonate (PSS) and poly(diallyldimethylammonium chloride) (PDDAC). All Au NRs have an aspect ratio of 4, while the LSPR maximum wavelength is 808 nm, which is the optimized wavelength for NIR thermal therapy. Dark-field (DF) imaging is commonly used for *in vitro* imaging of the Au NRs;¹⁴ however, the concentration of Au NRs near the solid tumor tissue is difficult to measure, and the solid tumor tissue is relatively large and complex. Therefore, it is difficult to observe the Au NR distribution in the solid tumor tissue using this technique.

Hence, we employed a multicellular tumor spheroid (MCTS) as a model to study the Au NR distribution. MCTSs are similar to solid tumor tissues in morphology, structure, function and gene expression,^{15–19} but they are smaller and easier to establish. The interactions between the cells and their extracellular matrix in 3D cell culture enable them to maintain the unique features of tissues, especially the adherent cell junctions. We could obtain a visual proof of the Au NR distribution through the MCTS sections. The concentration of the Au NRs is adjustable and can be controlled to be much higher than in an animal test. Thus, in comparison to the *in vivo* test, the only factor that determines the penetration of the Au NRs is the difference in surface coating. Hence, MCTS is an ideal model for the study of Au NR penetration. We predicted that different surface charges would affect the penetration and retention of the nanoparticles in tumors, resulting in different thermal therapeutic benefits.

Three types of Au NRs were synthesized following the protocol described in the Materials and methods section.[†] The mean size of the Au NRs was 55 × 14 (length × diameter/nm), which was measured and statistically analyzed according to the TEM images. The UV-Vis-NIR absorption spectra demonstrated that Au NRs with

^aLaboratory of Nanomedicine and Nanosafety, Division of Nanomedicine and Nanobiology, National Center for Nanoscience and Technology, Beijing, China. E-mail: liangxj@nanoctr.cn

^bCAS Key Laboratory for Biomedical Effects of Nanomaterials and Nanosafety, Chinese Academy of Sciences, Beijing 100190, P. R. China

^cCAS Key Laboratory of Standardization and Measurement for Nanotechnology, National Center for Nanoscience and Technology, Beijing 100190, P. R. China. E-mail: wuxc@nanoctr.cn

^dLaboratory of Molecular Imaging, Department of Radiology, Howard University, Washington, D.C. 20060, USA

[†] Electronic supplementary information (ESI) available: Materials and methods section. See DOI: 10.1039/c2nr31877f

[‡] These authors contributed equally to this work.

different surface coatings had similar absorption and the maximum absorption peaks were close to 808 nm, which was in the NIR region. The soft tissue has low absorption in this region and the laser penetration depth would be maximized.⁶ Zeta-potential results showed that the PDDAC-coated Au NRs and the CTAB-coated Au NRs were positively charged, whereas the PSS-coated Au NRs were negatively charged (Fig. 1).

A series of environmental scanning electron microscopy (ESEM) images with different magnifications demonstrated the structure of the spheroids. The MCF-7 cells formed tightly packed round spheroids (Fig. 2A). The surface cells of the MCTSs were similar to *in vivo* tumor tissues but showed different morphologies compared to the monolayer cells. The cells in the MCTSs appeared to be crowded, compact and had an irregular spindle shape, while monolayer cells were more stretched.

Transmission electron microscopy (TEM) was performed to observe the cells outside and inside the MCTSs. The representative images are shown in Fig. 2B, and the nucleus shape was still normal in the outer cells. In the inner cells, however, the nucleus swelled and became malformed. A large amount of protuberances and invaginations occurred, which indicated bad cell viability. It has been reported that the proliferating and non-proliferating tumor cell nuclei vary in shape, and tumor cells with low proliferative activity have a tendency towards a more irregular nuclear shape.²⁰ The outer and inner regions of the cylindroids have been shown to contain viable and apoptotic microenvironments, respectively.²¹ The cells in the periphery were predominantly proliferating, while the cells in the center were mostly apoptotic and necrotic. This suggested that the radial organization mimics the distribution of cells around blood vessels in tumor tissues *in vivo*. The outer region of the spheroid corresponded to the tumor tissue near the blood supply where cells can proliferate in the presence of sufficient oxygen and nutrients. The inner region of the spheroid was similar to the tumor tissue that was far away from the blood supply, where cells also grow with a decreased oxygen and nutrient level.^{22,23} The cells in the inner region of the MCTS may be more vulnerable to the thermal therapeutic treatment. Therefore, spheroids were selected

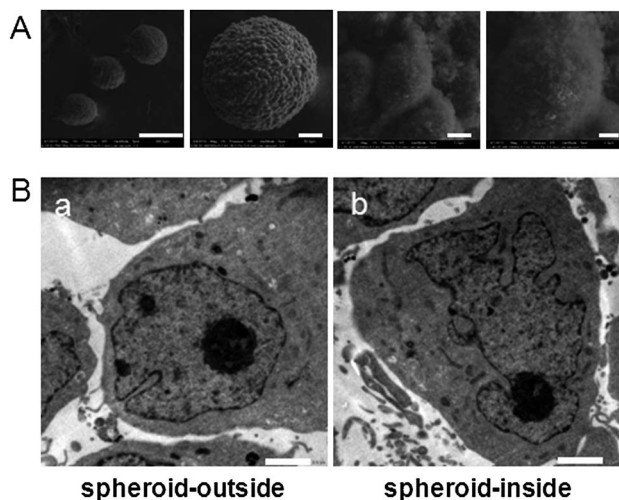


Fig. 2 (A) ESEM images of MCF-7S spheroids after 7 days of culturing taken under a series of magnifications (scale bar from left to right: 300 μ m, 50 μ m, 5 μ m, 2 μ m). (B) TEM images of cells on the outside (a) and inside (b) of the MCF-7 tumor spheroid (scale bar, 2.0 μ m).

as a suitable model for evaluating the relationship between the penetration behavior of the Au NRs in tumor tissue and the thermal therapeutic efficacy.

The viability of the MCTSs treated with 150 pM Au NRs with different surface modifications for 24 h was assessed by acid phosphatase (APH) assay. Conventional cell viability assays need to digest the MCTSs in order to disperse cells before the assays. This step would damage cells and cause inaccuracy in the results. Hence, the APH assay was employed to avoid the disadvantages. This assay could be run without any pretreatment of the MCTSs and is more accurate in reflecting the cellular viability in the 3D cell culture model.^{24,25} As shown in Fig. 3A, the viability of the MCTSs was not

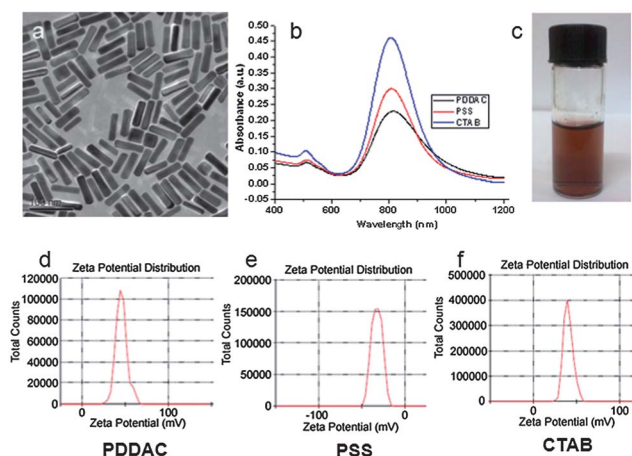


Fig. 1 Characterization of Au NRs. (a) TEM image of the CTAB-coated Au NRs. (b) UV-Vis-NIR absorption spectra of PDDAC-coated Au NRs, PSS-coated Au NRs and CTAB-coated Au NRs. (c) Suspension of Au NRs. Zeta potential distribution of PDDAC (d), PSS (e) and CTAB-coated Au NRs (f).

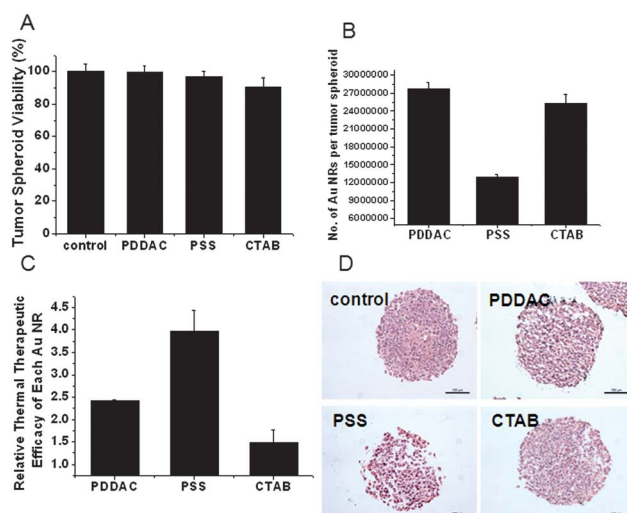


Fig. 3 NIR thermal therapy effect. (A) Tumor spheroid viability after treatment with different Au NRs at 150 pM for 24 h. (B) The number of Au NRs per tumor spheroid after 24 h of treatment. (C) Thermal therapy efficiency of different Au NRs calculated by the following formula: thermal therapy efficiency = viability loss/the number of Au NRs per MCTS. (D) HE staining. MCTSs were sectioned and stained after NIR laser radiation (scale bar, 100 μ m).

affected significantly after 24 h of Au NR treatment in different groups. Thus, the following experiments were conducted with 24 h Au NR treatment to rule out the impact of cellular toxicity on the thermal therapy test result.

A quantitative, inductively coupled plasma mass spectrometry (ICP-MS) measurement was conducted to estimate the amount of Au NRs internalized by the spheroids. The ICP-MS results showed that PDDAC-coated Au NRs had the greatest amount of retention (Fig. 3B). It has been reported that in a monolayer cell culture, the PDDAC-coated Au NRs had the greatest amount of cellular uptake, while the PSS-coated Au NRs had the least amount of cellular uptake. The uptake dosage of the PDDAC-coated Au NRs was more than 16-fold compared with the CTAB-coated Au NRs and 30-fold compared with the PSS-coated Au NRs.¹² The tendency of Au NR uptake in MCTSSs is consistent with that of a monolayer cell culture; however, the difference is not that obvious. The number of Au NRs per spheroid treated with the PDDAC-coated Au NRs was only twice that of the PSS-coated Au NR treated spheroids. The difference in the uptake of Au NRs between the PDDAC-coated and the CTAB-coated Au NR treated groups was minimal. In a monolayer cell culture, cationic surface coatings will enhance the uptake of nanoparticles greatly.²⁶ While in MCTSSs, this kind of surface coatings had effects only on the surface cells. Penetration is another key factor which is only present in MCTSSs. Consequently, the results obtained in different cell culture models varied.

Thermal therapy is one of the major applications of Au NRs in cancer treatment; therefore, the bio-distribution of the Au NRs in tumor tissue would affect the therapeutic efficiency. The MCTSSs were radiated under the NIR laser for 4 min after incubation with Au NRs for 24 h. The thermal therapy efficiency of each kind of Au NRs is shown in Fig. 3C and calculated according to the following formula:

$$\text{Thermal therapy efficiency} = \frac{\text{viability loss}}{\text{the number of Au NRs per MCTSS}}$$

After laser radiation, the Au NR-treated MCTSSs suffered great viability loss. The thermal therapy efficiency of the PSS-coated Au NRs was the highest, followed by the PDDAC-coated Au NRs. The CTAB-coated Au NRs had the lowest efficiency, which was less than 40% compared to that of the PSS-coated Au NRs.

Hematoxylin-eosin (HE) staining was employed to observe the morphological change of MCTSSs after thermal therapy. The HE staining result showed that radiation rarely had any effect on the control group, while the MCTSSs treated with Au NRs showed a variety of structural changes. In the PSS-coated Au NR group, a mass of inner cells were killed, and the skeleton was destroyed; hence, cavities appeared, the structure became loose, and the shape became irregular. The damage of inner cells was not obvious in the other two Au NR treated groups, and cavities could only be seen at the border of the MCTSSs (Fig. 3D).

To show the distribution of Au NRs in the MCTSSs directly, a DF microscope was used to examine the penetration of Au NRs in the tumor spheroids. The DF microscope illuminated the samples with oblique beam and collected the reflected and scattered light for imaging. Some metal materials, such as Au NRs, exhibit better

reflecting property. Therefore, the interference of the dye used in HE staining can be excluded. In the sections of the PDDAC-coated Au NR and the CTAB-coated Au NR treated MCTSSs, the reflected light of the Au NRs was around the spheroids (Fig. 4b and f), which demonstrates that most of the Au NRs were distributed in the outer region of the MCTSSs. The bright spots (Fig. 4d) in the inner region of the MCTSSs were Au NRs, which penetrated into the MCTSSs. The DF images showed that the PSS-coated Au NRs can penetrate into the MCTSSs and reach the inner regions of the cylindroids, while the other two Au NRs were distributed outside. The Au NRs used in the experiments were suspended in complete medium; therefore, they would interact with serum proteins. For physiological conditions, most serum proteins show slightly anionic property. For monolayer cells, the proteins would be adsorbed onto the Au NRs, mediating their cellular uptake.^{27,28} Because serum proteins are diverse, the Au NR probably contained a variety of serum proteins nonspecifically adsorbed onto its surface. The PDDAC and the CTAB are cationic polymers, thus they would adsorb more proteins with negative charges. To support this assumption, the zeta potentials of three Au NRs were measured after incubation with serum containing medium for 24 hours. The PDDAC-coated and CTAB-coated Au NRs were found to be negatively charged after incubation, while the PSS-coated Au NRs retained their negative charge (Fig. S1†). The proteins adsorbed by the negatively charged PSS Au NRs would be different from those of the other two Au NRs, and the presence and amount of these proteins on the surface of nanoparticles would affect their interaction with MCTSSs. The positively charged Au NRs adsorbed more proteins on their surface and increased more in size compared with the negatively charged Au NRs and this dictates the penetration behavior of Au NRs into the spheroids. Consequently, the PSS-coated Au NRs had better penetration ability and were more homogeneously distributed in the spheroids, whereas the cationic polymer-coated Au NRs were distributed in the outer region or adsorbed onto the surface of the spheroids. During radiation treatment, in the PSS-coated Au NR treated group, the inner cells around the Au NRs were killed, and the compact structures were broken. The PDDAC- or CTAB-coated Au NRs were located or

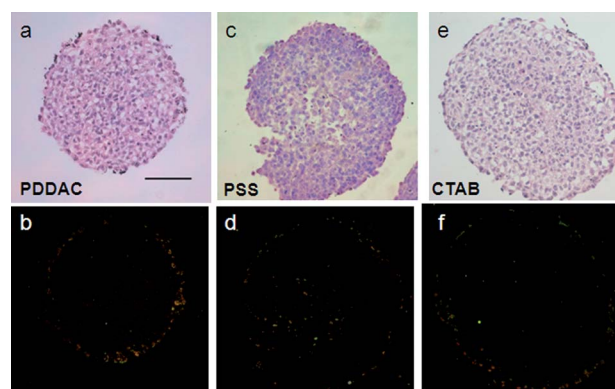


Fig. 4 Distribution of Au NRs in MCTSSs. HE staining of the tumor spheroid treated with different Au NRs for 24 h (a, c and e). DF images of the tumor spheroid treated with different Au NRs for 24 h (b, d and f). The bright spots in the DF images represent the existence of Au NRs. In (b) and (f), Au NRs are distributed mainly outside. In (d), Au NRs are distributed both outside and inside (scale bar, 100 μm).

adhered to the border of the MCTSs; therefore only parts of the MCTSs were destroyed by hyperthermia. Consequently, the thermal therapy efficiency was limited despite the higher amount of Au NRs per MCTS.

It has been reported that positively charged nanoparticles improve the delivery of the payloads to the cells, whereas the negatively charged nanoparticles diffuse more rapidly, thereby delivering drugs deeper into tissues.²⁹ In this study, a MCF-7 multicellular tumor spheroid, which mimicked the distribution of the cells around the blood vessels in tumor tissue *in vivo*, was used for the thermal therapeutic evaluation of Au NRs with different surface coatings. The cells in the outer region of the spheroid corresponded to the tumor tissue near the blood supply having sufficient oxygen and nutrients, while the cells in the inner region of the spheroid were similar to the tumor tissue far away from the blood supply with decreased oxygen and nutrients. Therefore, the cells in the inner region of the MCTS may be more vulnerable to the thermal therapeutic treatment.

After the laser radiation, the APH assay proved that in comparison to the other two cationic polyelectrolyte-coated Au NRs, the PSS-coated Au NRs had the highest hyperthermia efficacy. In the PSS group, the compact structure of the MCTSs was broken by the Au NR thermal therapy, and sections of the MCTSs appeared to be cracked. The DF images indicated an optimized spheroid distribution of the Au NRs in hyperthermia obtained by the negatively charged PSS Au NRs.

In conclusion, our results showed that surface charge can be used to control tissue penetration and thermal therapeutic efficacy. We believe that a relationship possibly exists between the adsorption of protein onto the surface of Au NRs and their tumor spheroid penetration efficiency. The difference in thermal therapy efficacy was due to the effective heat generated by the Au NRs with different surface coatings, which is affected by different Au NR distribution patterns in the tumor. This conclusion may help guide the design of the surface chemistry of Au NRs for tailoring the thermal therapy.

Acknowledgements

This work was supported by grants from the Chinese Natural Science Foundation project (no. 30970784), National Key Basic Research Program of China (2009CB930200), Chinese Academy of Sciences (CAS) "Hundred Talents Program" (07165111ZX) and CAS Knowledge Innovation Program. This work was also supported in part by NIH/NCRR/RCMI 2G12RR003048 and USAMRMC W81XWH-05-1-0291 grants.

Notes and references

- X. Huang, I. H. El-Sayed, W. Qian and M. A. El-Sayed, *J. Am. Chem. Soc.*, 2006, **128**, 2115–2120.
- A. C. Bonoio, S. D. Mahajan, H. Ding, I. Roy, K. T. Yong, R. Kumar, R. Hu, E. J. Bergey, S. A. Schwartz and P. N. Prasad, *Proc. Natl. Acad. Sci. U. S. A.*, 2009, **106**, 5546–5550.
- G. Von Maltzahn, J. H. Park, A. Agrawal, N. K. Bandaru, S. K. Das, M. J. Sailor and S. N. Bhatia, *Cancer Res.*, 2009, **69**, 3892–3900.
- R. Weissleder, *Nat. Biotechnol.*, 2001, **19**, 316–317.
- E. B. Dickerson, E. C. Dreaden, X. Huang, I. H. El-Sayed, H. Chu, S. Pushpanketh, J. F. McDonald and M. A. El-Sayed, *Cancer Lett.*, 2008, **269**, 57–66.
- Y. Xia, W. Li, C. M. Cobley, J. Chen, X. Xia, Q. Zhang, M. Yang, E. C. Cho and P. K. Brown, *Acc. Chem. Res.*, 2011, **44**, 914–924.
- P. K. Jain, X. Huang, I. H. El-Sayed and M. A. El-Sayed, *Acc. Chem. Res.*, 2008, **41**, 1578–1586.
- P. K. Jain, K. S. Lee, I. H. El-Sayed and M. A. El-Sayed, *J. Phys. Chem. B*, 2006, **110**, 7238–7248.
- A. I. Minchinton and I. F. Tannock, *Nat. Rev. Cancer*, 2006, **6**, 583–592.
- A. Verma and F. Stellacci, *Small*, 2010, **6**, 12–21.
- R. K. Jain and T. Stylianopoulos, *Nat. Rev. Clin. Oncol.*, 2010, **7**, 653–664.
- Y. Qiu, Y. Liu, L. Wang, L. Xu, R. Bai, Y. Ji, X. Wu, Y. Zhao, Y. Li and C. Chen, *Biomaterials*, 2010, **31**, 7606–7619.
- A. E. Nel, L. Mädler, D. Velegol, T. Xia, E. M. V. Hoek, P. Somasundaran, F. Klaessig, V. Castranova and M. Thompson, *Nat. Mater.*, 2009, **8**, 543–557.
- C. J. Murphy, A. M. Gole, J. W. Stone, P. N. Sisco, A. M. Alkilany, E. C. Goldsmith and S. C. Baxter, *Acc. Chem. Res.*, 2008, **41**, 1721–1730.
- K. Huang, H. Ma, J. Liu, S. Huo, A. Kumar, T. Wei, X. Zhang, S. Jin, Y. Gan and P. C. Wang, *ACS Nano*, 2012, **6**, 4483–4493.
- M. Pickl and C. Ries, *Oncogene*, 2008, **28**, 461–468.
- F. Hirschhaeuser, H. Menne, C. Dittfeld, J. West, W. Mueller-Klieser and L. A. Kunz-Schughart, *J. Biotechnol.*, 2010, **148**, 3–15.
- H. K. Kleinman, D. Philp and M. P. Hoffman, *Curr. Opin. Biotechnol.*, 2003, **14**, 526–532.
- S.-M. Ong, Z. Zhao, T. Arooz, D. Zhao, S. Zhang, T. Du, M. Wasser, D. van Noort and H. Yu, *Biomaterials*, 2010, **31**, 1180–1190.
- R. Nafe, S. Herminghaus, U. Pilatus, E. Hattingen, G. Marquardt, W. Schlote, H. Lanfermann and F. Zanella, *Neuropathology*, 2004, **24**, 172–182.
- J. P. Freyer and R. M. Sutherland, *Cancer Res.*, 1980, **40**, 3956–3965.
- C. Fischbach, R. Chen, T. Matsumoto, T. Schmelzle, J. S. Brugge, P. J. Polverini and D. J. Mooney, *Nat. Methods*, 2007, **4**, 855–860.
- H. M. Byrne, *Nat. Rev. Cancer*, 2010, **10**, 221–230.
- J. Friedrich, C. Seidel, R. Ebner and L. A. Kunz-Schughart, *Nat. Protoc.*, 2009, **4**, 309–324.
- J. Friedrich, W. Eder, J. Castaneda, M. Doss, E. Huber, R. Ebner and L. A. Kunz-Schughart, *J. Biomol. Screening*, 2007, **12**, 925–937.
- E. C. Cho, J. Xie, P. A. Wurm and Y. Xia, *Nano Lett.*, 2009, **9**, 1080–1084.
- A. M. Alkilany, P. K. Nagaria, C. R. Hexel, T. J. Shaw, C. J. Murphy and M. D. Wyatt, *Small*, 2009, **5**, 701–708.
- T. S. Hauck, A. A. Ghazani and W. C. Chan, *Small*, 2008, **4**, 153–159.
- B. Kim, G. Han, B. J. Toley, C. Kim, V. M. Rotello and N. S. Forbes, *Nat. Nanotechnol.*, 2010, **5**, 465–472.

Multifunctional hybrid silica nanoparticles for controlled doxorubicin loading and release with thermal and pH dual response†

Cite this: *J. Mater. Chem. B*, 2013, **1**, 1109

Xixue Hu,^{‡a} Xiaohong Hao,^{‡ab} Yan Wu,^a Jinchao Zhang,^{*b} Xiaoning Zhang,^c Paul C. Wang,^d Guozhang Zou^{*a} and Xing-Jie Liang^{*a}

Controlled drug loading and release into tumor cells to increase the intracellular drug concentration is a major challenge for cancer therapy due to resistance and inefficient cellular uptake. Here, a temperature and pH dual responsive PNIPAM/AA@SiO₂ core-shell particles with internal controlled release were designed and fabricated for efficient cancer treatment, which could recognize the intrinsic pH differences between cancers and normal tissues. Upon lowering the temperature, doxorubicin was loaded into the PNIPAM/AA@SiO₂ nanoparticles, whereas by increasing the acidity, previously loaded doxorubicin was quickly released. Comparing with common mesoporous silica particles (MSNs), these core-shell particles have a more uniform size and better dispersity. In addition, dried PNIPAM/AA@SiO₂ nanoparticles could be easily redispersed in distilled water. The *in vitro* cell culture experiments showed that not only were PNIPAM/AA@SiO₂ particles more biocompatible and less cytotoxic than MSN, but also DOX@PNIPAM/AA@SiO₂ had a higher drug release efficiency in the lysosomes and a stronger inhibitory effect on tumor cell growth than DOX@MSN. All these features indicated that PNIPAM/AA@SiO₂ particles have great potential in therapy applications.

Received 10th October 2012
Accepted 11th December 2012

DOI: 10.1039/c2tb00223j

www.rsc.org/MaterialsB

1 Introduction

Recently, various nanostructured materials have been developed for biomedical imaging, diagnostics and therapy, because they show improved pharmacokinetics and biodistribution and exciting efficacy for cancer treatments. However, the poor cellular internalization of nanoparticles and insufficient intracellular drug release always limits the amount of anticancer drugs that actually reach cancer cells, which hampers the efficacy of cancer chemotherapy. To conquer the challenges, stimuli-responsive nanoparticles have been regarded as one of the most promising carriers for drug delivery, which are sensitive to environmental stimuli such as temperature,^{1–4} ionic strength,⁵ ultraviolet light,⁶ or magnetic field.^{7–9}

It is well documented that pH values in different tissues and cellular compartments vary significantly. For example, the tumor extracellular environment is more acidic (pH 6.8)¹⁰ than blood and normal tissues (pH 7.4), and the pH values of late endosome and lysosome are even lower, at 5.0–5.5.¹¹ So a pH sensitive delivery system is of special interest for controlled drug delivery.^{12–14}

Mesoporous silica nanoparticles have been extensively explored as drug delivery systems due to their superior features such as high pore volume, large surface area, prominent biocompatibility, accessible surface functionalization, and effective protection for the payloads.^{15–18} With the aim to administer drug molecules specifically toward target tissues, pH sensitive molecules have been introduced to prepare hybrid nanoparticles with MSN.^{19,20} The pore surface and opening of MSNs have been functionalized with stimuli-responsive groups,^{21–24} inorganic nanoparticles,²⁵ and peptide²⁶ that worked as caps and gatekeepers.^{15,27} Controlled release of encapsulated drugs can be triggered in responding to internal or external stimuli such as pH, temperature, redox potential, light, and enzymatic reactions.

For example, the folate was linked by disulfide bonds to construct the gate-like structure on the outlet of the pores of MSNPs, the controlled release can be triggered in the presence of reductant dithiothreitol or glutathione (GSH).²⁸ MSNP coated by PEG-DA-peptide macromer possessing MMP substrate polypeptides can be responsive to endogenous proteases triggered,

^aCAS Key Laboratory for Biomedical Effects of Nanomaterials and nanosafety, National Center for Nanoscience and Technology, Beijing 100190, PR China. E-mail: zougz@nanoctr.cn; liangxj@nanoctr.cn; Fax: +86 10 62656765; Tel: +86 10 82545569

^bCollege of Chemistry & Environmental Science, Chemical Biology Key Laboratory of Hebei Province, Hebei University, Baoding, 071002, P. R. China. E-mail: jczhang6970@yahoo.com.cn

^cLaboratory of Pharmaceutics, School of Medicine, Tsinghua University, Beijing 100084, P. R. China

^dLaboratory of Molecular Imaging, Department of Radiology, Howard University, Washington, D.C. 20060, USA

† Electronic supplementary information (ESI) available. See DOI: 10.1039/c2tb00223j

‡ These authors contributed equally to this work.

localized drug release *in vitro* and *in vivo*.²⁹ Nanoparticles with pH responsive hydrazone bonds immobilized on a mesoporous silica nanocomposite allow pH-sensitive drug release.³⁰ Poly-valent mesoporous silica nanocarriers–aptamer bioconjugates were fabricated as controlled release drug delivery systems and were able to effectively target cancer cells.³¹

Despite the success of these approaches, they need to be improved because of the tedious multiple-step syntheses, necessity of suitable surfactants, very low surface grafting efficiency or encapsulation efficiency, *etc.*, and more importantly, slow release of the encapsulated drug and low releasing efficiency caused by strong adsorption of MSNP. Therefore, it is in our interest to explore a simple and facile method to prepare drug carriers that are capable of recognizing the intrinsic pH differences between tumor and normal tissues and possessing higher releasing efficiency and faster release behavior at low pH.

Herein, we propose a facile and efficient strategy to introduce the pH/thermo-responsive nanocarriers with dually responsive poly(*N*-isopropylacrylamide) (PNiPAM)-*co*-acrylic acid (AA) hydrogel core enclosed in silica shell *via* self-assembly approach. The PNiPAM/AA@silica particles not only possess pH/thermal responsive features, high dispersity and the unique features derived from a silica shell, but also have improved drug release efficiency in cells. The physicochemical and pH/thermo-sensitive properties of PNiPAM/AA@silica composite microspheres were tested. Doxorubicin hydrochloride (DOX), a classic anticancer drug, was chosen as a model drug to assess the drug loading and releasing behaviors of the carriers. The cytotoxicity of PNiPAM/AA@silica and DOX@PNiPAM/AA@silica to MCF-7 cells was measured. The drug release efficiency of DOX@PNiPAM/AA@SiO₂ in cells had been compared with that of DOX@MSN.

2 Materials and methods

2.1 Materials

Cetyl trimethylammonium bromide (CTAB), *N*-isopropylacrylamide (NiPAM), *N,N'*-methylene bis(arylamide) (MBA), 3-(trimethoxysilyl) propylmethacrylate (MPS), tetraethoxysilane (TEOS), 3-(4,5)-dimethylthiazoliazolo(-z-yl)-3,5-diphenyltetrazolium bromide (MTT) and trypsin were purchased from Sigma-Aldrich (St. Louis, USA). Lysotracker Green was purchased from Invitrogen. Acrylic acid (AA), sodium dodecyl sulfate (SDS) and ammonium persulfate (APS) were obtained from Shanghai Chemical Reagents Company (Shanghai, China). NiPAM was recrystallized from *n*-hexanes and dried under vacuum prior to use.

2.2 Synthesis of mesoporous silica nanoparticles

Mesoporous silica nanoparticles (MSNs) were synthesized as previously reported.^{32–34} Briefly, 200 mg of CTAB were dissolved in 96 mL of water, followed by the addition of 7 mL of 0.2 M NaOH aqueous solution. The solution was heated to 80 °C and kept at that temperature for 30 minutes before 1 mL of TEOS was added. The solution went from clear to opaque, indicative of a hydrolysis process. The reaction was kept at 80 °C for 2 h.

The resulting nanoparticles were centrifuged and washed with methanol. In order to remove the CTAB, the as-synthesized particles were suspended in 50 mL solution of methanol and 2.0 mL of 12 M hydrochloride acid. The solution was refluxed for 10 h and the MSNs were collected by centrifugation and washed with methanol.

2.3 Synthesis of PNiPAM/AA hydrogel nanoparticles

The PNiPAM/AA hydrogel particles were prepared by the precipitation polymerization of NiPAM, MBA and AA using APS as an initiator. More specifically, an appropriate amount of NiPAM, AA and MBA was dissolved in 120 mL of doubly distilled water containing 0.042 g of SDS. The dispersion was purged with nitrogen for 30 min under continuous mechanical stirring at 500 rpm (revolutions per minute) at room temperature. Then the solution was heated to 70 °C, and APS (0.053 g) dissolved in 3 mL of water was quickly injected to initiate the polymerization. The reaction mixture was stirred for 12 h at 70 °C under the nitrogen atmosphere. The obtained PNiPAM/AA nanoparticles were centrifuged and thoroughly washed with water and methanol to remove SDS and unreacted monomers.^{35–37} The purified PNiPAM/AA particles were redispersed in distilled water at a solid content of 0.5 wt% for subsequent use.

2.4 Synthesis of PNiPAM/AA@SiO₂ nanoparticles

The synthesis procedure was described as following: 10 mg of CTAB was dissolved in 5 mL of water, then a predetermined amount of above PNiPAM/AA particles and TEOS were added, and the mixture was ultrasonically treated for 30 minutes. Then the mixture was stirred at 37 °C for 24 h. The obtained PNiPAM/AA@SiO₂ nanoparticles were centrifuged and thoroughly washed with distilled water and then re-dispersed in water at a solid content of 1.0 wt% for further use.

2.5 Synthesis of FITC–PNiPAM/AA@SiO₂ nanoparticles

FITC-grafting PNiPAM/AA@SiO₂ nanoparticles were prepared with modified Stöber method.³⁸ A typical synthesis procedure was depicted as following: 5 mg of fluorescein isothiocyanate (FITC) was reacted with 25 mg 3-aminopropyl trimethoxysilane (APS) in 2 g absolute ethanol by stirring for 48 h at room temperature. Then 200 µL of the resulting solution was mixed with 200 mg PNiPAM/AA@SiO₂ and injected into the mixed solution of water (0.5 g) and ethanol (1.5 g). The mixed solution was magnetically stirred at room temperature for 48 h. The obtained particles were centrifuged and washed with ethanol and distilled water three times, respectively. The FITC-grafting PNiPAM/AA@SiO₂ nanoparticles were finally redispersed in water.

2.6 Drug loading into SiO₂ and PNiPAM/AA@SiO₂ nanoparticles

Doxorubicin was dissolved in distilled water to prepare 3 mg mL^{−1} solutions. 1.5 mL of the doxorubicin solution was pipetted into test tubes containing 3 mL of 10 mg mL^{−1} SiO₂ or 3 mL of 10 mg mL^{−1} PNiPAM/AA@SiO₂ solution. The mixed solution

was kept at 4 °C for 24 h, to reach maximum doxorubicin loading. Then the dispersion was centrifuged at 6000 rpm for 10 min to separate the loaded nanoparticles and carefully washed with distilled water twice. The amount of drugs loaded in the nanoparticles was determined by subtracting the amount of drug in the supernatant from that in the loading solution using a UV spectrophotometer with the detection wavelength of 485 nm.

2.7 *In vitro* drug release from the DOX@SiO₂ and DOX@PNiPAM/AA@SiO₂ nanoparticles

Nanoparticles loaded with doxorubicin were re-dispersed in 5 mL of PBS (pH 7.4 and 5.0) immediately after loading. The dispersion was then transferred into a dialysis bag (molecular weight cut off 7000 Da) and the bag was subsequently placed in a 50 mL centrifuge tube containing 25 mL of PBS. 5 mL of solution was sampled from the tube every half an hour during the first three hours, then sampled every hour in the following four hours. Finally, 5 mL of solution was taken out every day and the released drug was determined spectrophotometrically. The volume of the release medium in the flask was kept constant by adding equal volume of fresh medium back after each sampling. All drug release data were averaged with three measurements.

2.8 Cell culture

Human breast cancer cells (MCF-7) and human embryonic kidney (HEK293, normal cell) cells were maintained in Dulbecco's modified Eagle's medium (DMEM) and Minimum Essential Medium (MEM) supplemented with 10% (v/v) fetal bovine serum (FBS) in a humidified atmosphere containing 5% CO₂ at 37 °C.

2.9 The cytotoxicity assay

The cytotoxicity of DOX@PNiPAM/AA@SiO₂ against MCF-7 cells was determined by standard MTT assay. Briefly, the cells were seeded onto 96-well plates at a density of 5000 viable cells per well and incubated for 24 h to allow cell attachment. Then the cells were incubated with free DOX, DOX@SiO₂, DOX@PNiPAM/AA@SiO₂ with the doxorubicin concentrations ranging from 0.08 to 20 µg mL⁻¹, and blank PNiPAM/AA@SiO₂ from 0.4 to 200 µg mL⁻¹ respectively. After 48 h, fresh medium containing MTT (0.5 mg mL⁻¹) were replaced and the cells were incubated for additional 3.5 h. Upon removing MTT solution, the purple formazan crystals were dissolved with 100 µL DMSO, and the absorbance was recorded at 570 nm with a microplate reader (TECAN Zfinite M200, Austria). Untreated cells in medium were used as a control. Corresponding groups without cells were used as blanks. All experiments were carried out with four replicates.

2.10 Confocal microscopy assay

MCF-7 cells were incubated with DOX@PNiPAM/AA@SiO₂ or DOX@MSN for 1 or 4 h in Petri dishes, washed with PBS three times and subsequently labeled with fluorophore Lysotracker

Green in the culture medium at 37 °C for 30 min. After labeling, cells were washed with PBS buffer to remove the residual DOX or nanoparticles. The intracellular localizations of free DOX and released DOX from DOX@PNiPAM/AA@SiO₂ or DOX@MSN were directly visualized with a confocal laser scanning microscope (Carl Zeiss, Germany). Lysotracker Green was excited at 488 nm and their emission was recorded at 505–525 nm. Doxorubicin was excited at 488 nm and its emission was recorded at 560–600 nm. In the assay, all experiments were carried out under a light-sealed condition to avoid photobleaching.

2.11 Cellular uptake by flow cytometry

Flow cytometry (FCM) was used to determine the drug transfer capability of the PNiPAM/AA@SiO₂ nanoparticles into cells. MCF-7 cells were seeded onto a 6-well plate (5 × 10⁵ cells per well), and cultured for 24 h, then treated with DOX, DOX@PNiPAM/AA@SiO₂ or DOX@MSN at the same final concentration of 5 µg mL⁻¹ of equivalent DOX. The untreated cells were used as a blank control. After incubating for 1 h, 4 h or 12 h, the media were removed, and the cells were washed twice with PBS buffer to remove residual nanoparticles. Then the cells were harvested after being treated with 0.25% trypsin solution, washed with PBS buffer three times, and finally suspended in PBS. The signals of DOX fluorescence were recorded by FCM (Attune® acoustic focusing cytometer, Applied Biosystems, Life Technologies, Carlsbad, CA).

2.12 General analysis

The average hydrodynamic radius of MSN, PNiPAM/AA and PNiPAM/AA@SiO₂ nanoparticles at different temperatures and pH were determined by ZetaSizer Nano ZS (Malvern Instruments Ltd., Worcestershire, UK). All the measurements were performed with the nanoparticles suspended in distilled water at the concentration of 100 µg mL⁻¹.

TEM images were obtained using a Tecnai G2 20 S-TWIN transmission electron microscope (FEI Company) operating at 200 kV. Samples were deposited onto carbon coated copper grids, dried at room temperature and stained with uranyl acetate when necessary.

Infrared spectroscopy was carried out using a Spectrum One FT-IR spectrometer. The freeze-dried nanoparticles were grounded with KBr and pressed into a thin wafer. For each sample, 32 scans were recorded from 4000 to 400 cm⁻¹ with a resolution of 2 cm⁻¹.

Nitrogen adsorption-desorption isotherms were measured at -196 °C by ASAP 2020 (M+C) (Micromeritics, America). Before the samples were analyzed, they were degassed in a vacuum at 150 °C for 12 hours. Specific surface area was calculated using the multiple-point Brunauer-Emmett-Teller method. Pore volume was determined from the adsorption branch of nitrogen adsorption-desorption isotherm curve at a relative nitrogen pressure $P/P_0 = 0.992$ signal point. Pore diameter was calculated from the adsorption branch of the isotherms using the Barrett-Joyner-Halenda method.

3 Results and discussion

3.1 Synthesis physicochemical characterization of nanoparticles

In order to achieve an optimal controllable delivery system for doxorubicin, three types of particles (Mesoporous silica particles, PNIPAM/AA hydrogel particles and PNIPAM/AA@SiO₂ particles) were prepared. Mesoporous silica nanoparticles (MSNs) with highly ordered mesostructures and spherical morphology were synthesized, using CTAB as template. As shown in Fig. 1a, spherical particles of MSNs with regular morphology and diameter of approximately 100 nm were obtained. The mean particle size of MSNs in H₂O determined by dynamic light scattering was about 525.8 nm, and the zeta potential was −29.1 mV (Table 1). The 2D cylindrical pores with the diameter of 2–3 nm were arranged in parallel. Transmission electron microscopy (TEM) images of PNIPAM/AA hydrogel nanoparticles and PNIPAM/AA@SiO₂ nanoparticles are shown in Fig. 1b and c. The images show that the particles are homogeneous and well-dispersed. The hydrodynamic size of the NiPAM/AA@SiO₂ particles (247.3 nm) is smaller than that of NiPAM/AA hydrogel particles (306.2 nm), the reason for which might be that the size of PNIPAM/AA hydrogel cores decreased when NiPAM/AA@SiO₂ particles were fabricated at 37 °C. The zeta potential of the PNIPAM/AA@SiO₂ is similar to that of SiO₂, increasing from −14.5 mV of PNIPAM/AA particles to −22.9 mV, which further verifies that the PNIPAM/AA hydrogel particles are covered by SiO₂. As illustrated in Fig. 1c, many small SiO₂ fragments aggregated on the surface of PNIPAM/AA hydrogel particles. There are many visible gaps among the fragments, which are probably the channels connecting PNIPAM/AA cores and the outside facilitate drug loading and release. The result of nitrogen adsorption-desorption measurement indicates that PNIPAM/AA@SiO₂ and MSN have a specific surface area of 27.37 and 751.05 m² g^{−1}. Total pore volume and average pore diameter of PNIPAM/AA@SiO₂ and MSN are 0.12 cm³ g^{−1} and 17.97 nm for PNIPAM/AA@SiO₂ and 0.42 cm³ g^{−1} and 2.23 nm for MSN, respectively. It is well known that the morphology of mesoporous silica nanoparticles synthesized by the conventional methods may hamper its practical application, because it is unfavorable for large scale production. Most often, irregular or agglomerated particles are obtained, which limits the therapeutic efficacy of the particles. As an alternative, we used the PNIPAM/AA particles as templates, the size of the obtained PNIPAM/AA@SiO₂ nanoparticles was controlled by the size of cores and the dispersity was good, as

Table 1 Physicochemical characterization of the different nanoparticles

Particles type	Size in H ₂ O (nm)	Zeta potential in H ₂ O (mV)	PdI in H ₂ O
MSN	525.8	−29.1	0.253
PNIPAM/AA hydrogel particles	306.2	−14.5	0.006
PNIPAM/AA@SiO ₂ nanoparticles	247.3	−22.9	0.04

shown in Table 1. This type of particles not only possess the environmental responsive properties of PNIPAM/AA hydrogel, but can also be modified like SiO₂ particles. These features, in combination with its unique structural advantages, render the PNIPAM/AA@SiO₂ nanoparticles excellent candidates as drug carriers.

3.2 Fourier transforms infrared spectra (FTIR) characterization of particles

Fig. 2 provides the FTIR spectra of MSN, NiPAM/AA, and NiPAM/AA@SiO₂. In the framework region, the MSN FTIR spectrum shows strong absorption peaks at about 464 cm^{−1}, 808 cm^{−1} and 1091 cm^{−1} due to the vibrations of Si–O–Si and Si–O linkages, the hydroxyl absorption peak at 3700–2900 cm^{−1} resulted from hydrolyzed ethyl orthosilicate.^{39,40} The FT-IR spectra of the NiPAM/AA hydrogels demonstrates broad bands of N–H stretch and vibration at 3299.0 cm^{−1} and 1540.5 cm^{−1}, respectively. The strong peak at 1648.5 cm^{−1} originates from the C=O carbonyl

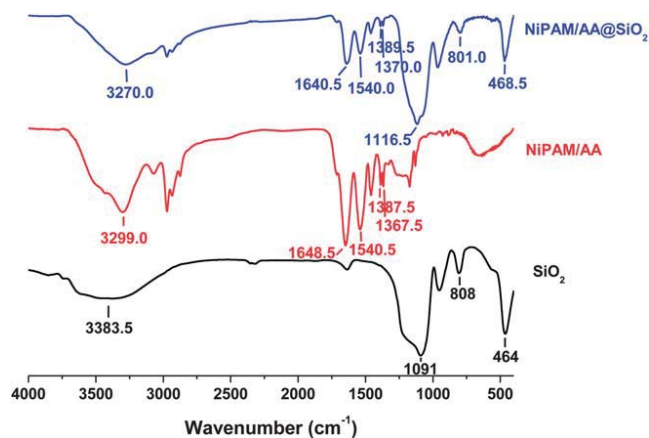


Fig. 2 FT-IR spectra of MSN, PNIPAM/AA and PNIPAM/AA@SiO₂ nanoparticles.

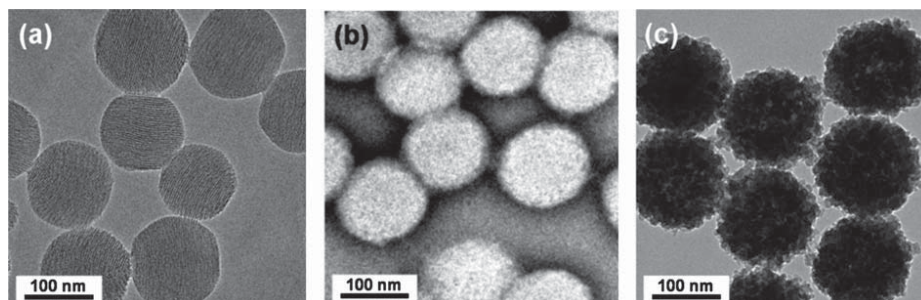


Fig. 1 TEM images of mesoporous SiO₂ (a), PNIPAM/AA nanoparticles (b) and PNIPAM/AA@SiO₂ nanoparticles (c).

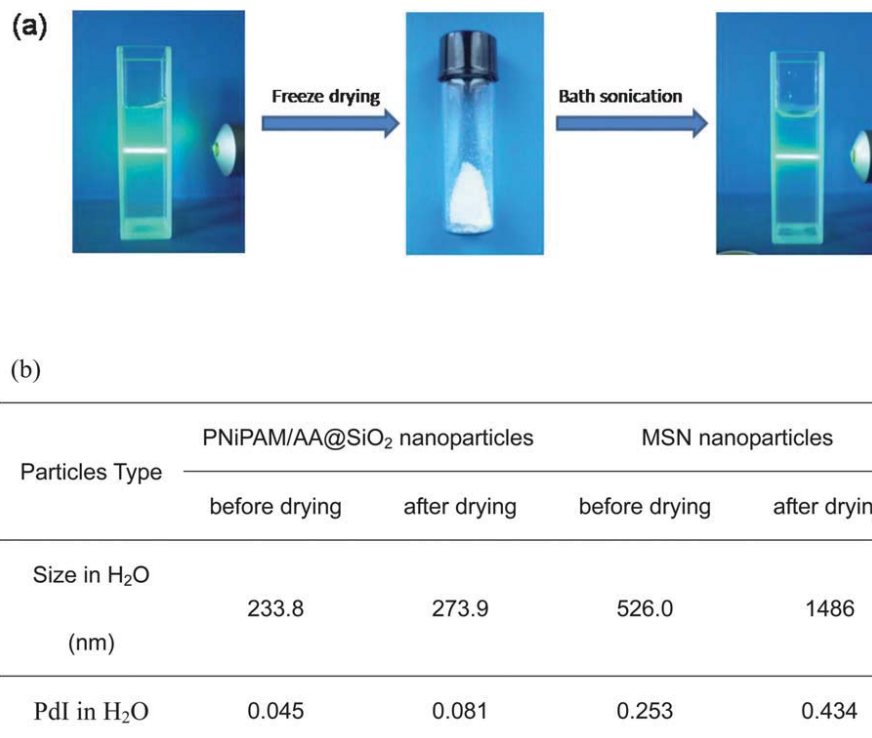


Fig. 3 (a) The photograph of colloidal solution of PNIPAM/AA@SiO₂ particles before and after drying; (b) change of size and polydispersity of PNIPAM/AA@SiO₂ and MSN in water before and after drying.

stretching vibration. Two typical bands of C–H vibration at 1387.5 and 1367.5 cm^{−1} belong to the divided bands of the symmetric –CH(CH₃)₂ group. In the spectra of the NiPAM/AA@SiO₂, the typical peaks are similar to those of MSN and NiPAM/AA. These findings indicate that NiPAM/AA@SiO₂ shell-core particles were successfully obtained.

3.3 Determination of dispersity and modification of PNIPAM/AA@SiO₂ nanoparticle powder

One of problems of various nanotherapeutic candidates is that particles tend to agglomerate. Good dispersity of therapeutic nanoparticles is essential.⁴¹ Here, the dispersity of PNIPAM/AA@SiO₂ nanoparticles was evaluated and compared with that

of MSN. Nanoparticles of PNIPAM/AA and MSN in ethanolic suspensions were dried using rotary evaporation and redispersed in distilled water (Fig. 3a). A well-suspended, optically transparent colloidal solution could be clearly seen after simply redispersing the powder in distilled water by ultrasonication for 5 min. The hydrodynamic size of the redispersed PNIPAM/AA@SiO₂ nanoparticles is ~274 nm in distilled water and slightly larger than as-synthesized PNIPAM/AA@SiO₂ nanoparticles (~234 nm). As shown in Fig. 3b, PNIPAM/AA@SiO₂ nanoparticles have much better dispersity than MSN.

In order to determine whether the prepared PNIPAM/AA@SiO₂ particles can be chemically modified similarly as MSN, FITC was grafted to the SiO₂ shell of the particles and

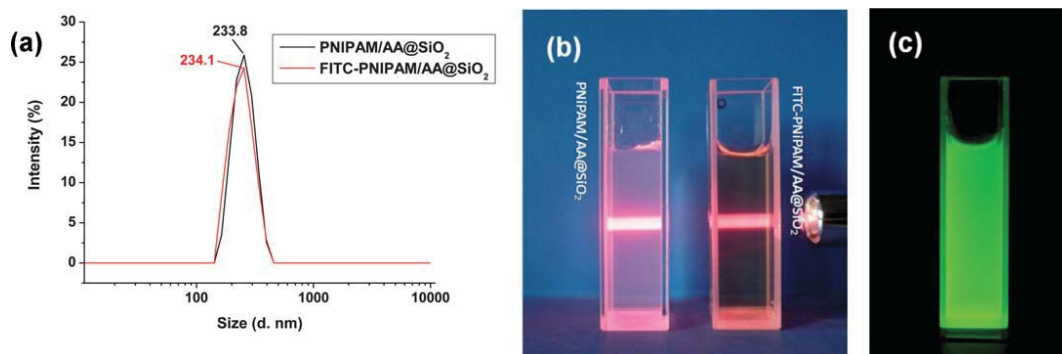


Fig. 4 (a) Hydrodynamic diameter distributions; (b) colloidal solutions of FITC–PNIPAM/AA@SiO₂ particles; (c) a photograph of aqueous solution of FITC–PNIPAM/AA@SiO₂ particles under illumination.

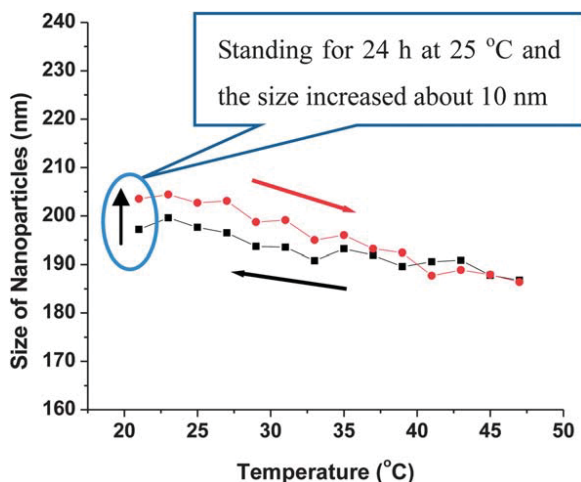


Fig. 5 The effect of temperature changing on hydrodynamic diameter of PNiPAM/AA@SiO₂ nanoparticles.

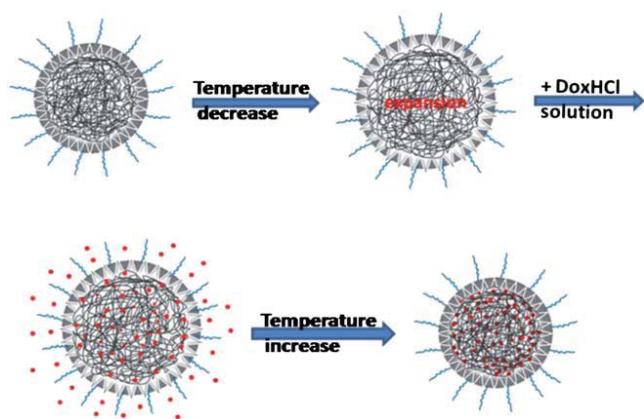


Fig. 6 A schematic diagram of the mechanism of drug loading of DOX@PNiPAM/AA@SiO₂ nanoparticles.

their hydrodynamic size was measured using DLS. The hydrodynamic size distribution of synthesized FITC-PNiPAM/AA@SiO₂ particles was almost identical to the unmodified PNiPAM/AA@SiO₂ particles, as shown in Fig. 4a. Yellowish and transparent colloidal solutions showing Tyndall light scattering

behavior further confirmed the dispersity of the FITC-PNiPAM/AA@SiO₂ particles (Fig. 4b). The fluorescence of FITC-PNiPAM/AA@SiO₂ particles under UV illumination was homogeneously distributed in water (Fig. 4c).

The above results indicate that PNiPAM/AA@SiO₂ nanoparticles obtained by the simple self-assembly method have a relatively better dispersity than MSN, nevertheless their surface could be modified just like MSN.

3.4 Thermal sensitive characterization of PNiPAM/AA@SiO₂ particles

Here, we further study the influence of temperature on the size of PNiPAM/AA@SiO₂ core-shell nanoparticles. As shown in Fig. 5, the particles, prepared at 37 °C, became slightly swollen when the temperature decreased from 47 °C to 21 °C. It is interesting that after the particles were stored for 24 hours at room temperature, the size of the particles increased by about 10 nm, and the size of the nanoparticles went back to the original size when the medium temperature was raised again 37 °C above. The reason for the size increment of the nanoparticles might be that the sustained expanding force of PNiPAM/AA cores at lower temperature for a long time acted on SiO₂ shells and the shells were broken open along the gap. When the temperature was raised, contraction force of the cores would draw the open shells back to original topography.

According to the results, PNiPAM/AA@SiO₂ nanoparticles will expand and the drug could be loaded into the nanoparticles when the medium temperature decreases. Then the medium temperature is returned to its preparation temperature and the drug is encapsulated into the nanoparticles, as shown in Fig. 6. In turn, the release of drug molecules from DOX@PNiPAM/AA@SiO₂ was accelerated when the temperature was decreased (Fig. S1†).

3.5 Effect of pH values on drug release

In order to determine whether lower pH can trigger drug release at body temperature, PNiPAM/AA@SiO₂ nanoparticles were fabricated at 37 °C and doxorubicin was loaded for 48 h at 4 °C and neutral pH. Drug loading contents and encapsulating efficiency of MSN and PNiPAM/AA@SiO₂ nanoparticles are 9.98%, 71.59% and 5.98%, 51.89%, respectively. *In vitro* release profiles

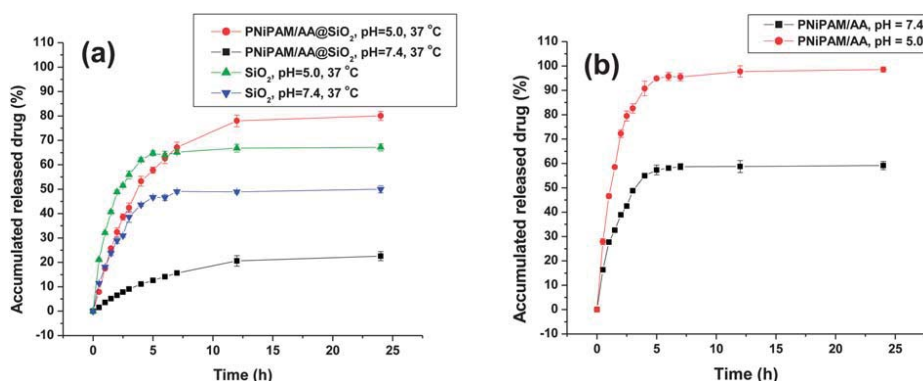


Fig. 7 DOX release profiles from DOX@MSN, DOX@PNiPAM/AA@SiO₂ (a) and PNiPAM/AA nanoparticles (b) under different pH.

of DOX from MSN, PNiPAM/AA and PNiPAM/AA@SiO₂ nanoparticles were examined in phosphate buffer at pH 7.4 and pH 5.0, respectively. As shown in Fig. 7, the drug release rate of both

particles was faster at low pH (pH 5.0) than at high pH (pH 7.4). There was a slight difference between the cumulative drug release from MSNs at pH 7.4 and pH 5.0, which was respectively

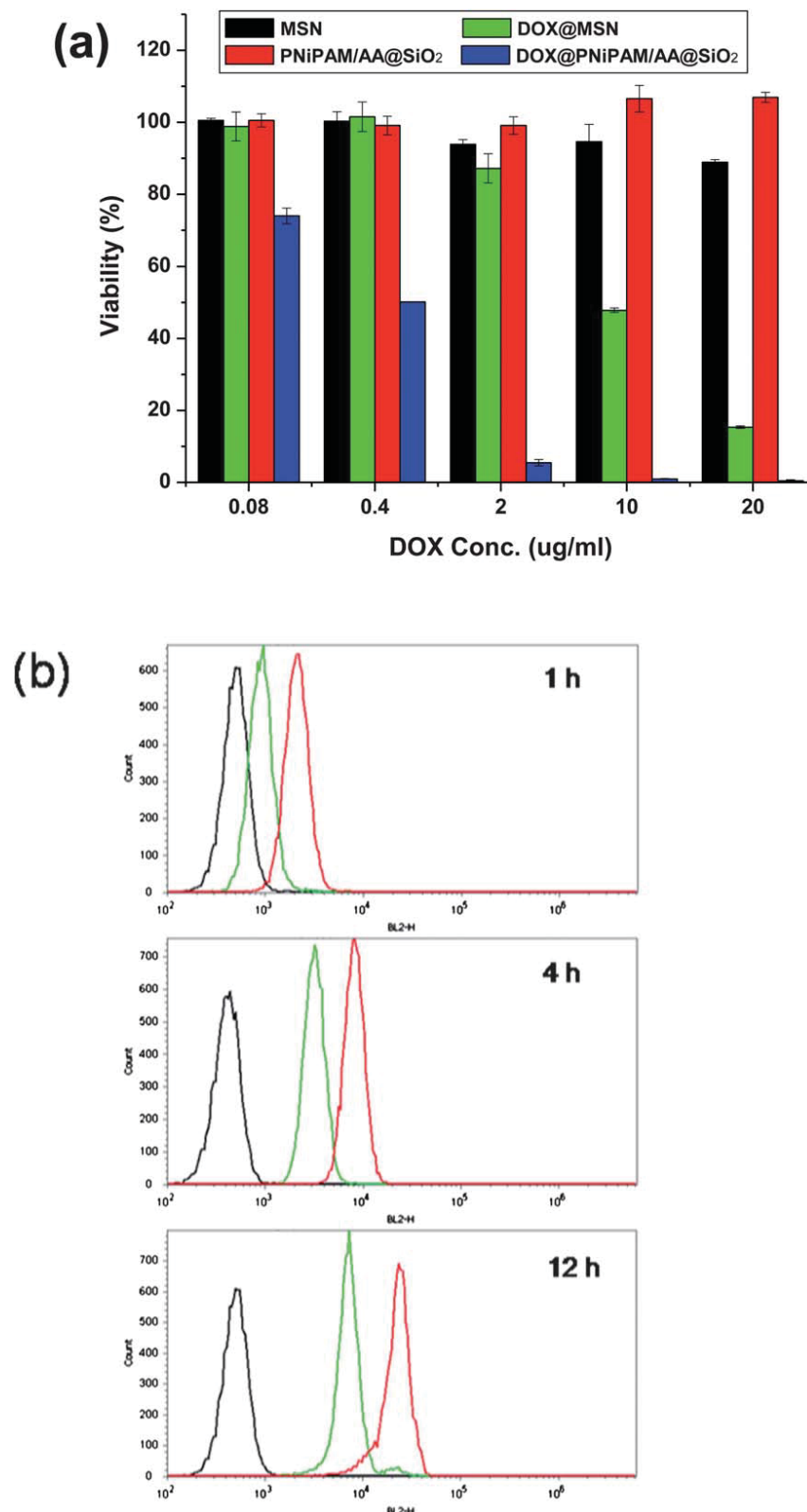


Fig. 8 The cytotoxicity and cellular uptake of different nanoparticles to MCF-7 cells. (a) Viability of cells cultured *in vitro* with DOX loaded PNiPAM@SiO₂, MSN and blank carriers; (b) flow cytometric analyses of DOX@PNiPAM/AA@SiO₂ (red line) and DOX@MSN (green line) at different time.

about 50% and 67%. However, at pH 7.4 the amount of cumulative drug released from PNiPAM/AA@SiO₂ (about 20%) is significantly lower than that of MSN and PNiPAM/AA particles (about 60%, Fig. 7b). When the medium pH value was reduced to 5.0, the accumulated released drug from PNiPAM/AA@SiO₂ quickly improved to 80%. The results clearly show that PNiPAM/AA@SiO₂ improved drug release efficiency in acidic medium and decreased the amount of cumulative drug released from PNiPAM/AA cores in neutral medium. The reason for the result is that the protons in the acidic buffer solution can easily get into the core through the gap of shell to protonate the amino group of DOX, which accelerate the drug release. This release behavior is desirable for cancer treatment, *i.e.* most of the drug

remains encapsulated in the nanocarrier during circulation, but when it reaches the acidic tumor tissue, the low pH triggers drug release.

3.6 Cell viability assay

To evaluate the potential of PNiPAM@SiO₂ nanoparticles as effective drug carriers for cancer therapy, *in vitro* cytotoxicity of DOX@MSN and DOX@PNiPAM/AA on MCF-7 cells was investigated. MCF-7 cells were incubated with DOX@MSN and DOX@PNiPAM/AA@SiO₂ at equivalent doxorubicin doses for 48 h, respectively. As shown in Fig. 8a, significant dose-dependent inhibition of MCF-7 cells' proliferation was observed when the

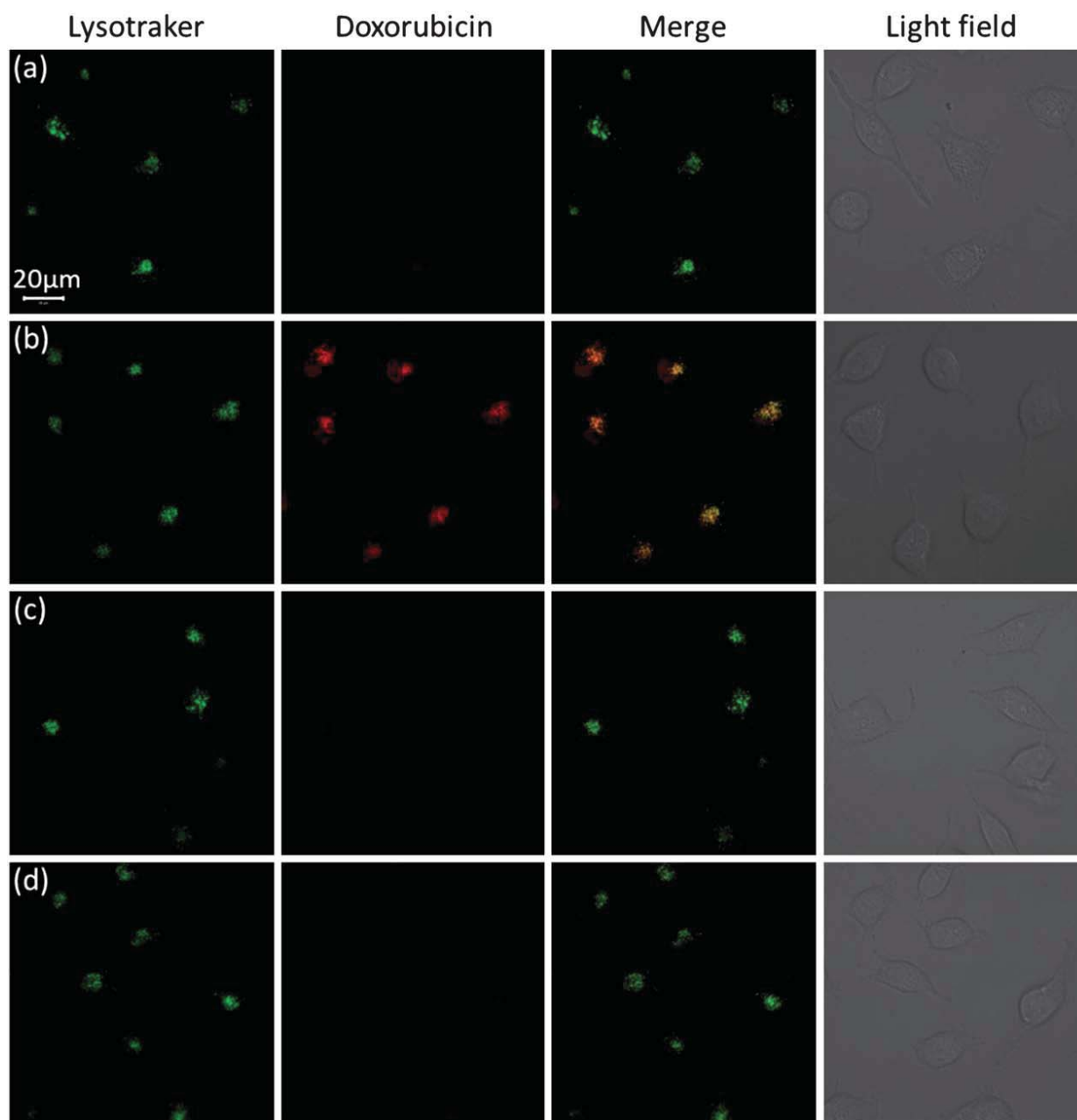


Fig. 9 Intracellular location of free DOX, DOX@PNiPAM/AA@SiO₂ and DOX@MSN. MCF-7 cells incubated with DOX@PNiPAM/AA@SiO₂ after 1 h (a) and 4 h (b) and MCF-7 cells incubated with DOX@MSN after 1 h (c) and 4 h (d).

cells were treated with DOX@PNiPAM/AA@SiO₂, but DOX@MSN showed mild toxicity to MCF-7 cells. On the other hand, the blank carrier of PNiPAM/AA@SiO₂ nanoparticles at the same concentration as drug carrier showed no cytotoxicity toward HEK293 cells (Fig. S2†), which differs from MSN, indicative of its better biocompatibility than MSN. Higher releasing efficiency of DOX from DOX@PNiPAM@SiO₂ particles taken up by MCF-7 cells might have contributed to the enhanced cytotoxicity of DOX@PNiPAM/AA@SiO₂.

The endocytosis of DOX loaded MSN and PNiPAM/AA@SiO₂ was evaluated by flow cytometry analysis after incubation for 1 h, 4 h and 12 h, respectively. As DOX is a fluorophore, the fluorescence intensity is proportional to the amount of DOX in MCF-7 cells. It could be seen from Fig. 8b that the cells without any treatment showed only autofluorescence. The fluorescence intensity of DOX@MSN and DOX@PNiPAM/AA@SiO₂ increased with the prolonging cultivation time. Although the DOX concentration and cell incubation time were the same, the fluorescence intensity of DOX loaded by PNiPAM/AA@SiO₂ was higher than that of DOX loaded by MSN at each time point, respectively. The flow cytometry results indicated that the DOX concentration loaded into the cells by PNiPAM/AA@SiO₂ was higher than that of DOX loaded by MSN, which was in agreement with the result of cellular toxicity.

To verify the pH responsive release behavior of DOX@PNiPAM/AA@SiO₂ in cells, the intracellular DOX distribution was analyzed by using DOX auto-fluorescence after incubation for 1 or 4 h. LysoTracker Green, a specific probe for acidic compartments, was used to confirm the lysosome colocation of DOX@PNiPAM/AA@SiO₂. In the group of cells treated with DOX@PNiPAM/AA@SiO₂, partial DOX gathered in the lysosomes, the fluorescence of which overlapped with that of the LysoTracker, and partial DOX dispersed in cytoplasm, surrounding the lysosomes, as shown in Fig. 9a and b. In distinct contrast, in DOX@MSN treatment the red fluorescence of DOX was much weaker and mainly colocalized with that of the LysoTracker, and DOX fluorescence in cytoplasm was barely visible (Fig. 9c and d). This experiment further proved that PNiPAM/AA@SiO₂ outperformed MSN in drug release at cellular level.

The difference in cytotoxicity of DOX@PNiPAM/AA@SiO₂ and DOX@MSN might be related to the following two factors. Superior dispersity of PNiPAM/AA@SiO₂ results in the size of the nanoparticles in solution being smaller than that of MSN, which makes it easier for the former to enter cells.^{42–44} Furthermore, DOX@PNiPAM/AA@SiO₂ particles have higher drug releasing efficiency in the acidic intracellular microenvironment than DOX@MSN.

4 Conclusions

In summary, PNiPAM/AA@SiO₂ nanoparticles with good dispersity and the ability to be modified were fabricated through self-assembly of PNiPAM/AA particles and TEOS in water. Many gaps were observed in the aggregated silica shell by TEM. The drug of doxorubicin not only could be loaded into the DOX@PNiPAM/AA@SiO₂ nanoparticles at lower

temperature and encapsulated inside PNiPAM@SiO₂ particles by a silica shell at 37 °C and neutral pH, but also could be released quickly from the nanoparticles at pH 5.0. The drug release results indicate that PNiPAM/AA@SiO₂ particles have pH responsive characteristics and higher releasing efficiency than MSN particles, which is very attractive for cancer treatment. In *in vitro* cell assays, significant growth inhibition of MCF-7 cells was observed when the cells were treated with DOX@PNiPAM/AA@SiO₂ particles, which was higher than that of DOX@MSN. The result of lysosome location and flow cytometry analysis demonstrated PNiPAM/AA@SiO₂ loaded with DOX was efficiently taken up by MCF-7 cells and had higher drug releasing efficiency in the acidic intracellular microenvironment than DOX@MSN. The results demonstrated that thermo/pH-sensitive PNiPAM/AA@SiO₂ particles could have great potential of selective release in tumor tissue.

Acknowledgements

This work was supported in part by Chinese Natural Science Foundation project (no. 30970784, 81171455, 31200717, 21271059 and 20971034), National Key Basic Research Program of China (2009CB930200), Chinese Academy of Sciences (CAS) “Hundred Talents Program” (07165111ZX), Research Fund for the Doctoral Program of Higher Education of China (no. 20111301110004) and CAS Knowledge Innovation Program. This work was supported in part by NIH/NCRR 3 G12 RR003048, NIH/NIMHD 8 G12 MD007597, and USAMRMC W81XWH-10-1-0767 grants. It was supported with the joint lab of nanotechnology for bioapplication, which was established with Life Technologies Corp. in the National Center for Nanoscience and Technology of China.

Notes and references

- 1 C. Choi, S. Y. Chae and J. W. Nah, *Polymer*, 2006, **47**, 4571–4580.
- 2 F. Kohori, K. Sakai, T. Aoyagi, M. Yokoyama, Y. Sakurai and T. Okano, *J. Controlled Release*, 1998, **55**, 87–98.
- 3 J. E. Chung, M. Yokoyama, M. Yamato, T. Aoyagi, Y. Sakurai and T. Okano, *J. Controlled Release*, 1999, **62**, 115–127.
- 4 D. Schmaljohann, *Adv. Drug Delivery Rev.*, 2006, **58**, 1655–1670.
- 5 C. J. Lefaux, J. A. Zimmerlin, A. V. Dobrynin and P. T. Mather, *J. Polym. Sci., Part B: Polym. Phys.*, 2004, **42**, 3654–3666.
- 6 S. K. Oiseth, A. Krozer, J. Lausmaa and B. Kasemo, *J. Appl. Polym. Sci.*, 2004, **92**, 2833–2839.
- 7 B. S. Kim, J. M. Qiu, J. P. Wang and T. A. Taton, *Nano Lett.*, 2005, **5**, 1987–1991.
- 8 S. F. Medeiros, A. M. Santos, H. Fessi and A. Elaissari, *Int. J. Pharm.*, 2011, **403**, 139–161.
- 9 T. Y. Liu, S. H. Hu, T. Y. Liu, D. M. Liu and S. Y. Chen, *Langmuir*, 2006, **22**, 5974–5978.
- 10 K. Engin, D. B. Leeper, J. R. Cater, A. J. Thistlethwaite, L. Tupchong and J. D. Mcfarlane, *Int. J. Hyperthermia*, 1995, **11**, 211–216.

- 11 E. S. Lee, K. T. Oh, D. Kim, Y. S. Youn and Y. H. Bae, *J. Controlled Release*, 2007, **123**, 19–26.
- 12 P. Satturwar, M. N. Eddine, F. Ravenelle and J. C. Leroux, *Eur. J. Pharm. Biopharm.*, 2007, **65**, 379–387.
- 13 K. Na, K. H. Lee and Y. H. Bae, *J. Controlled Release*, 2004, **97**, 513–525.
- 14 Y. Qiu and K. Park, *Adv. Drug Delivery Rev.*, 2001, **53**, 321–339.
- 15 M. Vallet-Regi, F. Balas and D. Arcos, *Angew. Chem., Int. Ed.*, 2007, **46**, 7548–7558.
- 16 M. Vallet-Regi, A. Ramila, R. P. del Real and J. Perez-Pariente, *Chem. Mater.*, 2001, **13**, 308–311.
- 17 K. P. Singh, P. Panwar, P. Kohli and Sanjesh, *J. Biomed. Nanotechnol.*, 2011, **7**, 60–62.
- 18 C. E. Ashley, E. C. Carnes, G. K. Phillips, D. Padilla, P. N. Durfee, P. A. Brown, T. N. Hanna, J. W. Liu, B. Phillips, M. B. Carter, N. J. Carroll, X. M. Jiang, D. R. Dunphy, C. L. Willman, D. N. Petsev, D. G. Evans, A. N. Parikh, B. Chackerian, W. Wharton, D. S. Peabody and C. J. Brinker, *Nat. Mater.*, 2011, **10**, 389–397.
- 19 H. Y. Tang, J. Guo, Y. Sun, B. S. Chang, Q. G. Ren and W. L. Yang, *Int. J. Pharm.*, 2011, **421**, 388–396.
- 20 C. Y. Lai, B. G. Trewyn, D. M. Jeftinija, K. Jeftinija, S. Xu, S. Jeftinija and V. S. Y. Lin, *J. Am. Chem. Soc.*, 2003, **125**, 4451–4459.
- 21 C. H. Lee, S. H. Cheng, I. P. Huang, J. S. Souris, C. S. Yang, C. Y. Mou and L. W. Lo, *Angew. Chem., Int. Ed.*, 2010, **49**, 8214–8219.
- 22 Y. L. Zhao, Z. X. Li, S. Kabehie, Y. Y. Botros, J. F. Stoddart and J. I. Zink, *J. Am. Chem. Soc.*, 2010, **132**, 13016–13025.
- 23 A. Baeza, E. Guisasola, E. Ruiz-Hernandez and M. Vallet-Regi, *Chem. Mater.*, 2012, **24**, 517–524.
- 24 Z. Luo, K. Y. Cai, Y. Hu, L. Zhao, P. Liu, L. Duan and W. H. Yang, *Angew. Chem., Int. Ed.*, 2011, **50**, 640–643.
- 25 H. P. Rim, K. H. Min, H. J. Lee, S. Y. Jeong and S. C. Lee, *Angew. Chem., Int. Ed.*, 2011, **50**, 8853–8857.
- 26 F. Porta, G. E. M. Lamers, J. I. Zink and A. Kros, *Phys. Chem. Chem. Phys.*, 2011, **13**, 9982–9985.
- 27 B. G. Trewyn, I. I. Slowing, S. Giri, H. T. Chen and V. S. Y. Lin, *Acc. Chem. Res.*, 2007, **40**, 846–853.
- 28 R. Guo, L. L. Li, W. H. Zhao, Y. X. Chen, X. Z. Wang, C. J. Fang, W. Feng, T. L. Zhang, X. Ma, M. Lu, S. Q. Peng and C. H. Yan, *Nanoscale*, 2012, **4**, 3577–3583.
- 29 N. Singh, A. Karambelkar, L. Gu, K. Lin, J. S. Miller, C. S. Chen, M. J. Sailor and S. N. Bhatia, *J. Am. Chem. Soc.*, 2011, **133**, 19582–19585.
- 30 J. E. Lee, D. J. Lee, N. Lee, B. H. Kim, S. H. Choi and T. Hyeon, *J. Mater. Chem.*, 2011, **21**, 16869–16872.
- 31 L. L. Li, Q. Yin, J. Cheng and Y. Lu, *Adv. Healthcare Mater.*, 2012, **1**, 567–572.
- 32 M. Liong, J. Lu, M. Kovochich, T. Xia, S. G. Ruehm, A. E. Nel, F. Tamanoi and J. I. Zink, *ACS Nano*, 2008, **2**, 889–896.
- 33 J. Lu, M. Liong, Z. X. Li, J. I. Zink and F. Tamanoi, *Small*, 2010, **6**, 1794–1805.
- 34 H. A. Meng, M. Xue, T. A. Xia, Y. L. Zhao, F. Tamanoi, J. F. Stoddart, J. I. Zink and A. E. Nel, *J. Am. Chem. Soc.*, 2010, **132**, 12690–12697.
- 35 Y. H. Deng, W. L. Yang, C. C. Wang and S. K. Fu, *Adv. Mater.*, 2003, **15**, 1729–1732.
- 36 J. X. Gu, F. Xia, Y. Wu, X. Z. Qu, Z. Z. Yang and L. Jiang, *J. Controlled Release*, 2007, **117**, 396–402.
- 37 X. Z. Qu, Y. Shi, Y. L. Tang, L. S. Chen and X. G. Jin, *J. Colloid Interface Sci.*, 2002, **250**, 484–491.
- 38 A. Vanblaaderen and A. Vrij, *Langmuir*, 1992, **8**, 2921–2931.
- 39 M. Jang, J. K. Park and E. W. Shin, *Microporous Mesoporous Mater.*, 2004, **75**, 159–168.
- 40 K. Moller, T. Bein and R. X. Fischer, *Chem. Mater.*, 1998, **10**, 1841–1852.
- 41 Y. S. Lin, N. Abadeer, K. R. Hurley and C. L. Haynes, *J. Am. Chem. Soc.*, 2011, **133**, 20444–20457.
- 42 W. K. Oh, S. Kim, M. Choi, C. Kim, Y. S. Jeong, B. R. Cho, J. S. Hahn and J. Jang, *ACS Nano*, 2010, **4**, 5301–5313.
- 43 B. D. Chithrani, A. A. Ghazani and W. C. W. Chan, *Nano Lett.*, 2006, **6**, 662–668.
- 44 H. E. Chung, D. H. Park, J. H. Choy and S. J. Choi, *Appl. Clay Sci.*, 2012, **65–66**, 24–30.

An Anti-PSMA Bivalent Immunotoxin Exhibits Specificity and Efficacy for Prostate Cancer Imaging and Therapy

Fayun Zhang, Liang Shan, Yuanyi Liu, David Neville, Jung-Hee Woo, Yue Chen, Alexandru Korotcov, Stephen Lin, Sophia Huang, Rajagopalan Sridhar, Wei Liang, and Paul C. Wang*

Prostate specific membrane antigen (PSMA) is overexpressed on prostate tumor cells and the neovascular endothelia various solid tumors. A bivalent immunotoxin generated by fusing a fold-back single-chain diabody derived from the Fv fragments of an anti-PSMA monoclonal antibody with a truncated diphtheria toxin (DT) containing the activity and translocation domains [A-dmDT390-scfbDb(PSMA)] might be suitable for targeted therapy of tumors that overexpress PSMA. In this study, a PSMA-positive and a PSMA-negative prostate cancer cell lines were treated with immunotoxin A-dmDT390-scfbDb(PSMA) in order to study the tumor targeting specificity and therapeutic potential of the immunotoxin. The cellular uptake and selective toxicity of the immunotoxin were evident in monolayer cultures of PSMA-positive LNCaP prostate cancer cells but not in cultures of PSMA-negative PC-3 prostate cancer cells. Cellular accumulation of A-dmDT390-scfbDb(PSMA) increased with increasing incubation times and concentrations in LNCaP cells. The proportion of apoptotic LNCaP cells increased upon incubation with increasing doses of the fold-back immunotoxin. Optical imaging and MRI with the Alexa Fluor 680-labeled A-dmDT390-scfbDb(PSMA) confirmed the specific targeting and therapeutic efficacy of this immunotoxin towards PSMA-positive LNCaP solid tumor xenografts in athymic nude mice.

1. Introduction

Prostate cancer is the most common solid tumor and one of the leading causes of cancer-related death among American men.^[1] Radiotherapy and/or surgery with or without androgen deprivation are used for management of early stage, organ-confined prostate cancer. A subset of early stage cancer may progress to an aggressive metastatic disease, which does not respond to androgen deprivation. Chemotherapeutic approaches are used for treating metastatic prostate cancer. The development of androgen resistance and systemic off-target toxicities of conventional chemotherapeutic drugs such as docetaxel and mitoxantrone are major clinical challenges.^[2,3] There is a need for safe and effective therapies that are based on specific targeting of immunotoxins to tumors. Tumor cells often express high levels of surface receptors or other molecules that distinguish them from other cells. Ligands designed to bind to tumor-specific receptors can be conjugated to cytotoxic drugs or toxins and the resulting

conjugates provide a tumor targeted drug delivery system for safe and effective therapy.^[4] Further research along these lines may lead to molecularly targeted individualized therapy.

Prostate-specific membrane antigen (PSMA) is over-expressed on the surface of certain prostate cancer cells. It is noteworthy that PSMA expression is particularly pronounced when prostate cancer progresses to late stage and becomes androgen-independent and metastatic.^[5] PSMA expression in certain prostate cancer cells is 1000-fold higher than in normal prostate tissue.^[6] PSMA is also expressed on the neovascular endothelium of a wide variety of human solid tumors, but is not expressed in the blood vessels of normal tissue.^[7] These findings have prompted the use of monoclonal antibody (mAb) of PSMA for sensitive and specific tumor imaging^[8] as well as targeted drug delivery for treating prostate cancer and other solid tumors.^[9]

PSMA antibody or its fragments, such as single-chain antibody fragments (scFv), can deliver cytotoxic agents into PSMA-expressing cells.^[10] scFv consists of the variable heavy chain (V_H) and the variable light chain (V_L) of an antibody connected by a flexible peptide linker and, due to its small size, exhibits

F. Zhang, L. Shan, Y. Chen, A. Korotcov, S. Lin,
S. Huang, R. Sridhar, P. C. Wang
Molecular Imaging Laboratory
Department of Radiology
Howard University
Washington, DC, 20060, USA
E-mail: pwang@howard.edu

F. Zhang, W. Liang
Protein & Peptide Pharmaceutical Laboratory
National Laboratory of Biomacromolecules
Institute of Biophysics
Chinese Academy of Sciences, Beijing, 100101, China

L. Shan
National Center for Biotechnology Information
National Institutes of Health
Bethesda, MD, 20892, USA

Y. Liu, D. Neville
Angimmune LLC, Bethesda, MD, 20852, USA

J.-H. Woo
Cancer Research Institute of Scott and White Healthcare
Texas A&M Health Science Center
Temple, TX 76702, USA



DOI: 10.1002/adhm.201200254

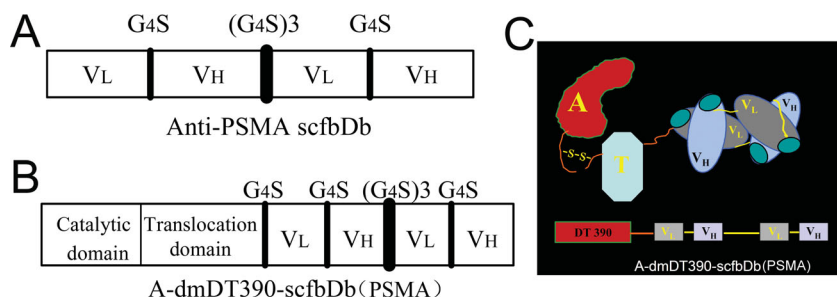


Figure 1. The scheme of A-dmDT390-scfDb comprising the A-dmDT390 moiety and the anti-PSMA scfDb. (A): The diabody consists of two scFv fragments separated by optimized lengths of Gly-Ser linkers. (B): The immunotoxin comprises the A-dmDT390 moiety and the anti-PSMA scfDb. The sequence from left to right is dmDT- VL-L1-VH-L2-VL-L1-VH. G4S are linkers, and VL and VH are the variable domains of light and heavy chains, respectively; A-dmDT390 is the first 390 amino acid residues of diphtheria toxin with an addition of alanine to the N-terminus and two mutations for de-glycosylation. (C): The cartoon structure of A-dmDT390-scfDb(PSMA) immunotoxin.

better tumor penetration, improved tumor distribution, and faster blood clearance than a full antibody when it is used as a ligand for targeted drug delivery.^[11]

The truncated form of diphtheria toxin (DT390) constructs incorporated in the immunotoxin exhibits targeted cytotoxicity^[12,13] and bioactivity *in vivo*.^[14,15] The DT-based anti-CD3 bivalent immunotoxin, A-dmDT390-bisFv (UCHT1), has been shown to bind to its target and depletes T cells effectively.^[16] This immunotoxin has undergone preclinical studies^[17,18] and is currently in clinical trials for treating cutaneous T-cell lymphoma (clinical trial identifier NCT00611208). In general, bivalent immunotoxins containing two scFv units have higher affinity and efficacy towards the targeted cells than those containing one scFv.^[13,19] It has also been shown that the format of scFv bivalency strongly affects binding affinity and immunotoxin cytotoxicity, depending on the antibody Fv sequences. The anti-mouse CD3 bivalent immunotoxin with a fold-back single-chain diabody, A-dmDT390-scfDb(207), showed a 5- to 7-fold enhanced bioactivity over that containing two tandem units of scFv (biscFv).^[19] To effectively deliver DT390 and enhance the specificity of its targeting to PSMA-expressing cells, we constructed an anti-PSMA fold-back single-chain diabody (scfDb, **Figure 1A**) based on the Fv sequences of the murine anti-PSMA antibody J591 and fused it to the C-terminus of DT390 using the approach similar to that for constructing anti-CD3 immunotoxin A-dmDT390-scfDb(207).^[19] As shown in **Figure 1B** and **C**, the bivalent anti-PSMA immunotoxin, A-dmDT390-scfDb(PSMA), has a sequence of DT390-L1-VL-L1-VH-L2-VL-L1-VH where L1 is a five-residue linker and L2 is the longer (G4S)₃ linker, permitting interactions between the distal and proximal VL/VH domains. Preliminary studies showed that the scfDb bound to the extracellular domain of PSMA with a higher affinity than biscFv and single scFv formats at a ratio of 7:2.5:1 (scfDb:biscFv:scFv). This finding indicates that the scfDb (PSMA) may be more sensitive and specific for targeted imaging and therapy. Previous *in vitro* studies have further demonstrated that the anti-PSMA fold-back diabody efficiently mediates the entry of the truncated toxin across the cell membrane into the cytosol and the fold-back format immunotoxin is 18- to 30-fold more potent than the biscFv format against monolayer LNCaP cancer cells.^[20]

For targeted immunotoxin therapy, it is important to determine the response of tumor cells to therapy. It would be useful if the target molecules expressed on the tumor cells could be identified before treatment, and the therapeutic dynamics and mechanisms could be imaged noninvasively during the targeted immunotoxin therapy. In this report, we laid the groundwork for evaluating the targeting specificity and therapeutic potential of the immunotoxin construct A-dmDT390-scfDb(PSMA) with noninvasive optical imaging.

In this study, A-dmDT390-scfDb(PSMA) was conjugated to Alexa Fluor 680 dye and used to investigate its utility for tumor-specific imaging and treatment. For this purpose, prostate cancer cells were grown *in vitro* as monolayer cultures and *in vivo*

as solid tumor xenografts in athymic nude mice. The results confirmed that A-dmDT390-scfDb(PSMA) immunotoxin had specific tumor targeting property in addition to a distinct and potent anticancer activity against PSMA-positive prostate cancer but not against PSMA-negative prostate cancer.

2. Results and Discussion

PSMA is known to be highly expressed and rapidly internalized in malignant prostate cancer cells. However, it is minimally expressed in benign tumors and normal tissues. The PSMA antibody fragment scFv has been used to bind specifically to prostate cancer cells for prostate cancer therapy^[21,22] and some PSMA-targeted therapeutics have been investigated in clinical trials.^[23,24] In this study, we demonstrated that the conjugate of a fold-back single-chain diabody of anti-PSMA monoclonal antibody fused to the translocation domains of diphtheria toxin (A-dmDT390-scfDb(PSMA)) inhibited the growth of PSMA-positive LNCaP cancer cells both *in vitro* and *in vivo* but not the growth of PSMA-negative PC-3 cells. The specific toxicity towards LNCaP cells indicated that scfDb(PSMA) bound specifically to the PSMA antigen on the cell membrane and effectively delivered DT390 into the PSMA-expressing cells to induce cytotoxicity.

2.1. PSMA is Overexpressed in LNCaP but not in PC-3 Cells

The expression of PSMA in LNCaP and PC-3 cells was determined with immunofluorescence staining and Western blotting. The results showed high levels of PSMA expression in LNCaP cells, but not in PC-3 cells (**Figure 2**).

2.2. A-dmDT390-scfDb(PSMA) Inhibits Proliferation of LNCaP Cells

The inhibitory effects of A-dmDT390-scfDb(PSMA) on the proliferation and viability of LNCaP cells and PC-3 cells were

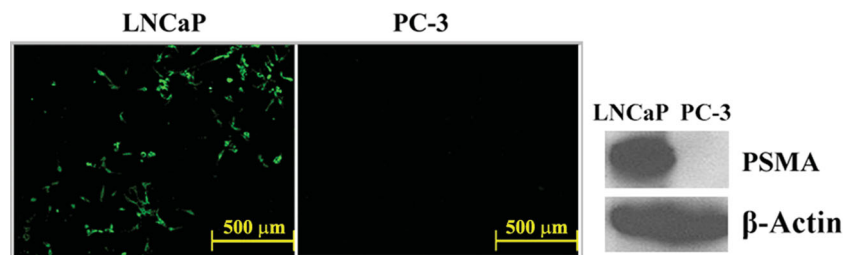


Figure 2. Expression of PSMA in prostate cancer cells. Left: LNCaP and PC-3 cells were fixed on slides, and incubated with anti-PSMA antibody and with FITC-labeled secondary antibody (green) sequentially. Right: Whole cell lysates from LNCaP and PC-3 cells were analyzed with Western blotting.

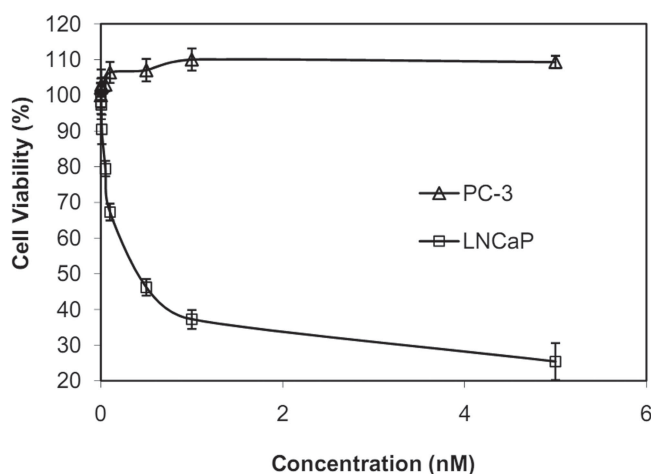


Figure 3. Cytotoxic effect of A-dmDT390-scfbDb(PSMA) on LNCaP cells and PC-3 cells. The viabilities of PSMA-positive (LNCaP) and PSMA-negative (PC-3) cells were determined with MTT assay after 48-hour treatment with A-dmDT390-scfbDb(PSMA). Data represent the mean \pm SD of triplicate determinations.

investigated with a methylthiazolyl tetrazolium (MTT) assay. Cells were treated with various concentrations of A-dmDT390-scfbDb(PSMA) immunotoxin for 48 hours. LNCaP cells were found to be highly sensitive to A-dmDT390-scfbDb(PSMA) immunotoxin, showing an IC_{50} of 0.57 nM (Figure 3). MTT assay showed 75% killing of the LNCaP cells after 48 hours of treatment. The viability of PC-3 cells was not affected by the immunotoxin, even at a relatively high concentration of 100 nM.

2.3. Cellular Uptake and Accumulation are High in LNCaP Cells but not in PC3 Cells

A-dmDT390-scfbDb(PSMA) was labeled with Alexa Fluor 680. The cellular uptakes and accumulations of the Alexa Fluor 680-labeled immunotoxin were detected with fluorescence microscopy and flow cytometry. As shown in Figure 4, the intensity of Alexa Fluor 680 fluorescence increased under microscopy with increasing concentrations of A-dmDT390-scfbDb(PSMA) (from 0.01 μ M to 0.1 μ M). Similarly, increased red fluorescence was observed in LNCaP cells treated with the

labeled A-dmDT390-scfbDb(PSMA) (0.1 μ M) when incubated for longer periods (Figure 5). In contrast, no Alexa Fluor 680 fluorescence signal could be detected in PC-3 cells, even after 4 hours of incubation with Alexa Fluor 680-labeled A-dmDT390-scfbDb(PSMA) and at a relatively high concentration (0.2 μ M) (Figure S1). Flow cytometry showed that an increase in the concentration and incubation time resulted in more accumulation of labeled A-dmDT390-scfbDb(PSMA) in LNCaP cells (Figure 6). Incubation with labeled A-dmDT390-scfbDb(PSMA) (0.1 μ M) for 6 hours caused significant accumulation of the labeled immunotoxin in the LNCaP cells, but not in the PC-3 cells (Figure S2). The heterogeneous distribution of the signal observed under microscopy is largely due to the different stages of cell proliferation and various expression levels of PSMA of the cells.

2.4. A-dmDT390-scfbDb(PSMA) Induces Cell Arrest and Apoptosis of LNCaP Prostate Cancer Cells

LNCaP cells were incubated with graded concentrations (0 to 5 nM) of A-dmDT390-scfbDb(PSMA) for 24 hours and stained with propidium iodide (PI), which binds with DNA. The fraction of cells with sub-diploid DNA content was measured with flow cytometry. As shown in Figure 7A, treatment with increasing doses of unlabeled immunotoxin resulted in dose-dependent increases in the S phase population with concomitant decreases in the G2 phase population of LNCaP cells. However, this effect of the immunotoxin was not evident in PC-3 cells. Similarly, trypan blue dye staining showed significantly increased staining of nonviable cells in LNCaP cultures, but not in PC-3 cell cultures treated with the immunotoxin. The 48 hours DNA content frequency histogram was similar to 24 hour histogram and shown in Figure S3. Light microscopy also showed higher rates of apoptosis in LNCaP cells after incubation with increasing amounts of A-dmDT390-scfbDb(PSMA) (Figure 7B). Fluorescence microscopy showed an increase of green fluorescence signal on the cell membrane due to apoptosis (FITC-labeled annexin V antibody bound with apoptotic cells) when the concentration of the immunotoxin was increased from 0.1 nM to 1 nM. The red fluorescence signal increased (due to DNA binding to PI in necrotic cells) when cells were treated with increased dose of immunotoxin, i.e., from 5 nM and 10 nM immunotoxin (Figure 7B).

Diphtheria toxin exerts its toxicity towards eukaryotic organisms through inactivation of the polypeptide chain EF-2 (Elongation Factor 2). The inactivation results in inhibition of protein synthesis and induction of apoptosis.^[25] As a truncated form of diphtheria toxin, DT390, is widely known for inducing cellular toxicity through targeted delivery *via* a ligand component. The immunotoxins constructed with DT390 are reported to have high toxicity to activated T cells.^[14,26] However, little is known about the process of targeted cell apoptosis induced by DT390 in tumor cells. In this study, the immunotoxin of A-dmDT390-scfbDb(PSMA) efficiently induced apoptosis in

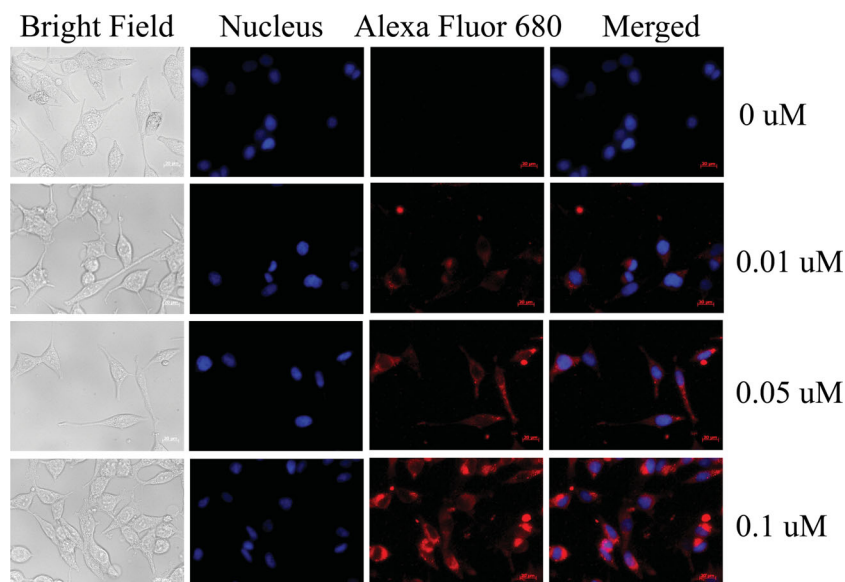


Figure 4. Fluorescence microscopy of A-dmDT390-scfbDb(PSMA) internalization in LNCaP cells. Cells were treated with 0.01, 0.05, or 0.1 μM of Alexa Fluor 680-labeled A-dmDT390-scfbDb(PSMA) for 3 hours. After washing with DPBS, cells were fixed and incubated with DAPI, and observed under a fluorescence microscope (magnification 400 \times).

PSMA-positive LNCaP cells. Flow cytometry analysis of the cell cycle parameters showed that the immunotoxin caused an increase in S phase population and a decrease in G2 phase

imaging technique for monitoring the uptake of fluorescent probes in tumor-bearing animals. This optical approach can be used to monitor gene delivery and drug accumulation

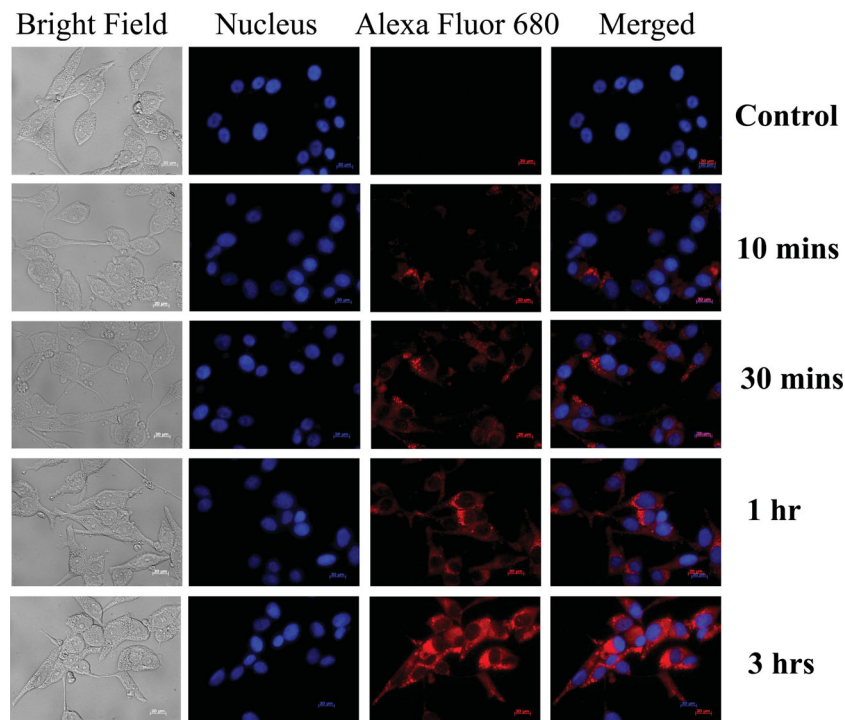


Figure 5. Fluorescence microscopy of the time course of A-dmDT390-scfbDb(PSMA) internalization in LNCaP cells. Cells were treated with 0.1 μM of Alexa Fluor 680-labeled A-dmDT390-scfbDb(PSMA) for different durations, *i.e.*, 10 min, 30 min, 1 h, and 3 h. After washing with DPBS, cells were fixed and incubated with DAPI, and observed under a fluorescence microscope (magnification 400 \times).

population in LNCaP cell cultures. These may have some implications for the cytotoxicity of the immunotoxin *in vitro*.

2.5. A-dmDT390-scfbDb(PSMA) Targets LNCaP but not PC-3 Solid Tumor Xenografts in Live Mice

LNCaP cells and PC-3 cells were implanted on the lower left flank of athymic nude mice to test the targeting efficiency of A-dmDT390-scfbDb(PSMA) in prostate tumors. The tumor was allowed to grow to about 5 mm in diameter. Alexa Fluor 680 dye labeled A-dmDT390-scfbDb(PSMA) (100 μL , 200 $\mu\text{g/mL}$) or Alexa Fluor 680 dye alone was administered as a single bolus *via* tail vein injection. The whole animal was then imaged at different time points after injection. In this study, near infrared fluorescent imaging was used to confirm the tumor targeting effectiveness of the immunotoxin in LNCaP tumors. Optical imaging provides a dynamic, noninvasive real-time *in vivo*

imaging technique for monitoring the uptake of fluorescent probes in tumor-bearing animals. This optical approach can be used to monitor gene delivery and drug accumulation in tumors.^[27–29] As shown in **Figure 8**, accumulation of the fluorescence signal from the labeled immunotoxin was detectable in LNCaP tumors as early as 30 minutes after injection. The fluorescent signal in LNCaP tumors showed an increase during the first 6 hours after injection, followed by a gradual decrease (**Figure 8A**). The signal from the free Alexa Fluor 680 dye was rapidly detectable throughout the whole body. However, no obvious accumulation of the Alexa Fluor 680 dye was observed in the tumors (**Figure 8B**). In PC-3 tumor models, both Alexa Fluor 680 labeled A-dmDT390-scfbDb(PSMA) and Alexa Fluor 680 dye showed increased fluorescent signals throughout the whole body during the first 8 hours after injection. However the fluorescent signal showed no obvious targeting to and accumulation in the tumors (**Figure S4**).

2.6. A-dmDT390-scfbDb(PSMA) Inhibits LNCaP Tumor Growth

The tumor-specific inhibitory effect of A-dmDT390-scfbDb(PSMA) was studied on the PSMA-positive LNCaP tumors and the PSMA-negative PC-3 tumors grown as solid tumor xenografts in athymic nude mice.

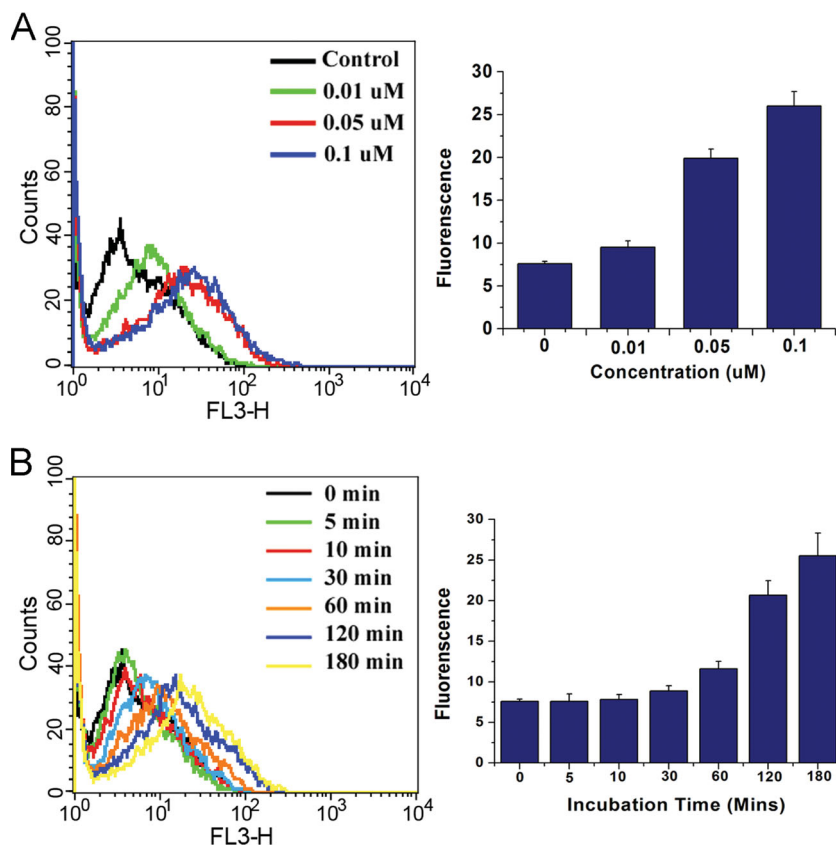


Figure 6. Flow cytometry quantification of A-dmDT390-scfDb(PSMA) accumulation in LNCaP cells. Cells were treated with 0.01, 0.05, or 0.1 μM of Alexa Fluor 680-labeled A-dmDT390-scfDb(PSMA) for 3 hours (A) or with 0.1 μM of Alexa Fluor 680-labeled A-dmDT390-scfDb(PSMA) for different durations, i.e., 5, 10, 30, 60, 120, and 180 min (B). After washing with DPBS, cells were collected and analyzed with flow cytometry.

Each mouse was given A-dmDT390-scfDb(PSMA) (10 μg) *via* intraperitoneal injection for six consecutive days. A-dmDT390-scfDb(PSMA) significantly inhibited LNCaP tumor growth while not affecting PC-3 tumor growth (Figure 9A and B, Figure 10). At the end of treatment, the tumors were surgically removed and weighed. The average LNCaP tumor weight in the treatment group was 0.27 ± 0.09 g, which was significantly lower than the tumor weight in the untreated control group (0.67 ± 0.11 g) ($P < 0.05$, Figure 9C). The average weight of the treated PC-3 tumors was not significantly different from the average weight of untreated PC-3 tumors in the control group ($P > 0.05$, Figure 9C). There was no difference for the body weights between the LNCaP tumor-bearing mice and PC-3 tumor-bearing mice, whether or not the animals were treated with the immunotoxin ($P > 0.05$).

Figure 8 shows rapid accumulation of A-dmDT390-scfDb(PSMA) immunotoxin in LNCaP tumors, whereas no fluorescent signal was detected in PC-3 tumors. High intensity of fluorescent signals from Alexa Fluor 680 labeled A-dmDT390-scfDb(PSMA) immunotoxin was also observed in the kidneys, suggesting that the immunotoxin or degraded fragments might be excreted through the kidneys. The selective cytotoxicity of A-dmDT390-scfDb(PSMA) immunotoxin both

in vitro (Figure 3) and *in vivo* (Figure 9) suggests that the immunotoxin can selectively bind to, and be internalized into, PSMA-expressing cells. This specific targeting *in vivo* may be responsible for the inhibitory effect of A-dmDT390-scfDb(PSMA) on the PSMA-positive LNCaP tumor growth, but not on the PSMA-negative PC-3 tumor growth. The findings suggest that this immunotoxin construct has considerable promise and potential for prostate cancer treatment.

Immunotoxins generated by full length anti-PSMA monoclonal antibody^[30,31] or its scFv^[32] exhibit specific cytotoxicity and capability to inhibit PSMA-positive prostate tumor growth. However, there are few clinical trials evaluating the clinical potential of immunotoxins linked to PSMA antibody. An important finding of this study was the efficacy of the A-dmDT390-scfDb(PSMA) immunotoxin against PSMA-positive prostate cancer cells and the lack of binding and cytotoxic effect against PSMA-negative prostate cancer cells. This suggests that inappropriate use of this immunotoxin for treating PSMA-negative tumors may run the risk of unintended systemic toxicity. It is imperative to confirm the presence of PSMA on the tumor cells before initiating therapy with the immunotoxin used in our studies because some prostate cancers do not express PSMA.

3. Conclusion

The A-dmDT390-scfDb(PSMA) immunotoxin used in this study selectively accumulates in LNCaP cells and tumors that overexpress PSMA. As a consequence of this uptake, LNCaP cells underwent S phase arrest and apoptosis. Intraperitoneal injection of the immunotoxin caused regression of LNCaP solid tumor xenografts in nude mice. Such accumulation and therapeutic response was not seen in PC3 cells and xenografts. This is due to the fact that PC3 cells and tumors are deficient in PSMA expression. Optical imaging experiments confirmed efficient targeted uptake of NIR labeled immunotoxin by PSMA expressing LNCaP cells and solid tumor xenografts in nude mice.

Our study showed that the use of this immunotoxin might be beneficial to individuals with a PSMA-positive prostate tumor. Optical imaging on the individual patient may be processed to determine the expression of PSMA and monitor the efficacy of immunotoxin therapy using the methods described in this paper. This approach will enable us to identify patients who are likely to benefit from treatment with A-dmDT390-scfDb(PSMA). The fluorescently-labeled immunotoxin is potentially useful for targeted theranostics and personalized medicine.

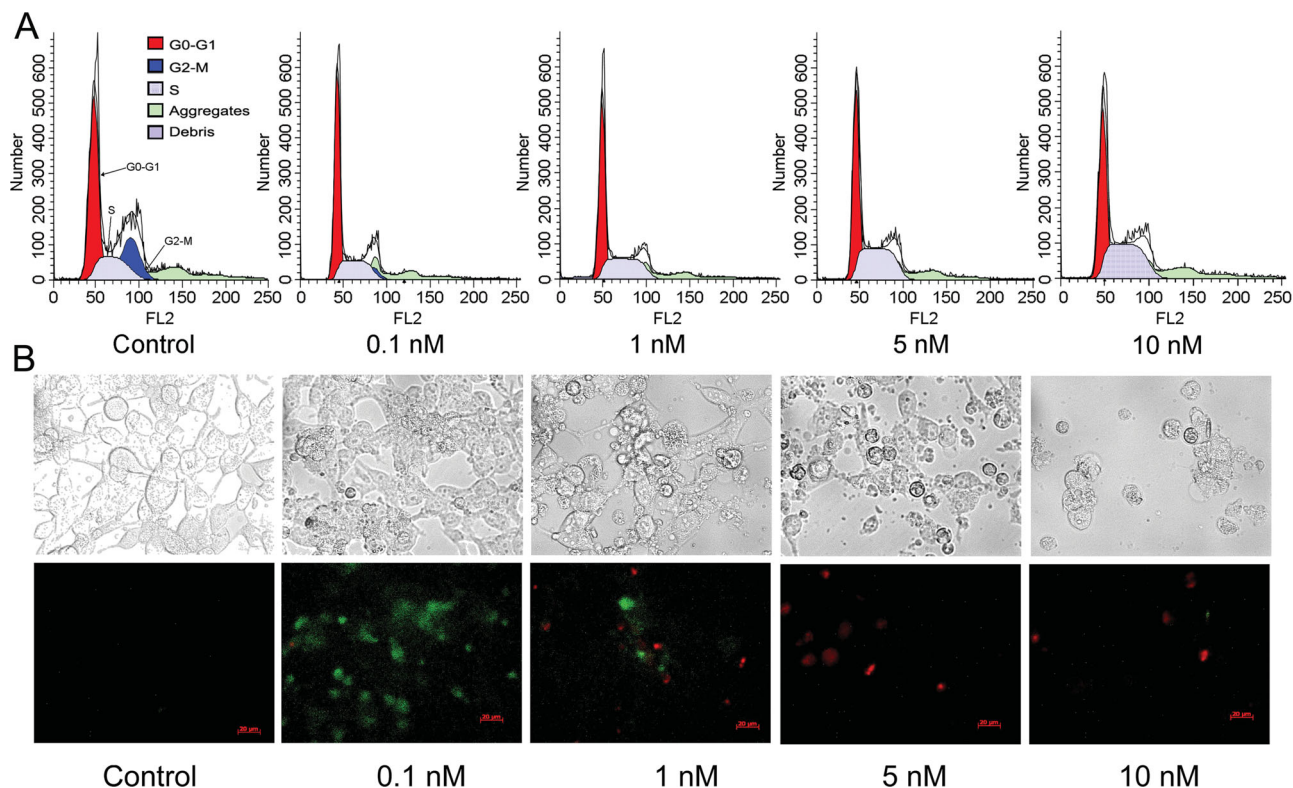


Figure 7. Cell cycle analysis and apoptosis assay of LNCaP cells after A-dmDT390-scfbDb(PSMA) treatment. (A) LNCaP cells were treated for 24 hours with 0.1, 1, 5, and 10 nM of A-dmDT390-scfbDb(PSMA), respectively, and then stained with PI. Cell cycle distribution was analyzed with flow cytometry. (B) LNCaP cells treated with 0 to 10 nM of A-dmDT390-scfbDb(PSMA) for 48 hours were stained with Annexin V-FITC antibody, washed with buffer and observed under a fluorescent microscope (magnification 400 \times).

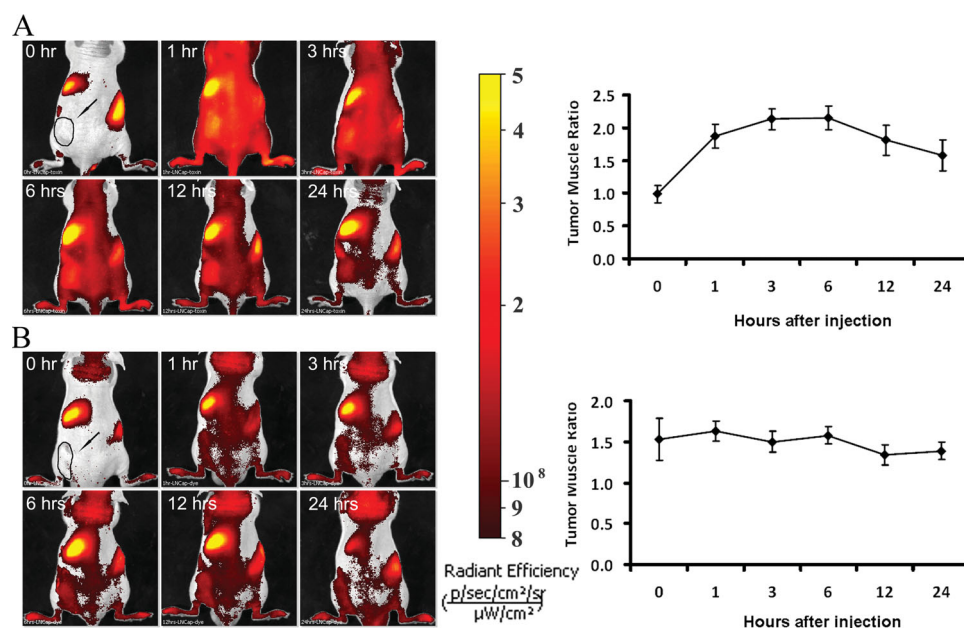


Figure 8. Animal whole body optical imaging after intravenous injection of Alexa Fluor 680-labeled A-dmDT390-scfbDb(PSMA) into LNCaP tumor-bearing mice, showing preferential accumulation of fluorescent signal in tumors. (A) Images obtained after injection of Alexa Fluor 680-labeled A-dmDT390-scfbDb(PSMA) (100 μ L) into mice. (B) Images obtained at 0, 1, 3, 6, 12, and 24 hours, respectively, after injection of Alexa Fluor 680 dye alone (100 μ L) into mice. The chart on the right shows the changes of the tumor (marked with arrow) to muscle ratio for the fluorescence intensity over time.

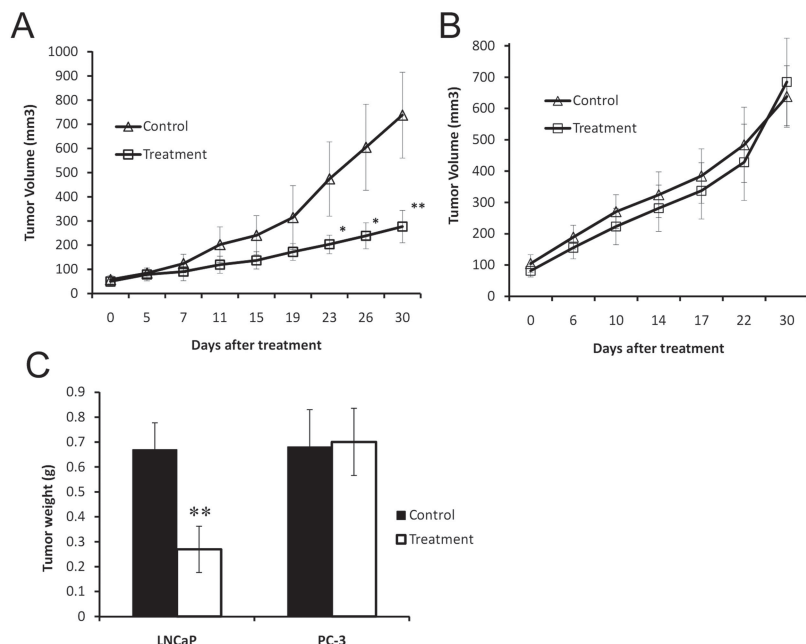


Figure 9. Effect of A-dmDT390-scfbDb(PSMA) immunotoxin on LNCaP and PC-3 prostate carcinomas. A-dmDT390-scfbDb(PSMA) (200 $\mu\text{g}/\text{kg}$, 5 $\mu\text{g}/\text{mice}$, per dose) immunotoxin was given via intraperitoneal injection, two doses a day with 6 hour interval for 6 days, compared to equivalent dose of BSA diluted in DPBS for control mice ($n = 10$ mice per group, $*P < 0.1$, $**P < 0.01$). (A) LNCaP tumor volume measurement with MRI. (B) PC-3 tumor volume measurement with MRI. (C) Tumor weight after treatment for 30 days.

4. Experimental Section

Cell Lines: Human prostate cancer cell lines LNCaP and PC-3 were purchased from ATCC (American Type Culture Collection, Manassas, VA). LNCaP and PC-3 cells were maintained as exponentially growing monolayer cultures in RPMI 1640 medium and DMEM, respectively. Both media were supplemented with L-glutamine (2 mM), penicillin and streptomycin (50 $\mu\text{g}/\text{mL}$ each), and 10% heat-inactivated fetal bovine serum. The cells were maintained in culture at 37 $^{\circ}\text{C}$ with 5% CO_2 in air and 95% humidity.

Expression and Purification of A-dmDT390-scfbDb(PSMA) Protein: A-dmDT390-scfbDb(PSMA) was expressed in a DT-resistant *Pichia pastoris* strain. The immunotoxin was produced in shake flask culture and purified by three purification steps, Phenyl Sepharose hydrophobic interaction chromatography, Q Sepharose anion exchange chromatography and Superdex 200 gel filtration chromatography.^[20]

Cellular PSMA Staining: LNCaP and PC-3 cells were plated in 8-well chamber slides with 1×10^4 cells in medium (0.5 mL) in each well. After 24 hours, cells were washed with Dulbecco's phosphate-buffered saline (DPBS) and fixed in 3.7% paraformaldehyde. The cells were permeabilized with 0.2% Triton-X 100 and blocked with 1% bovine serum albumin (BSA) in Hank's buffered salt solution (HBSS) for 1 hour. The cells were then incubated with a rabbit monoclonal anti-PSMA antibody (Abcam, Cambridge, MA) at a dilution of 1:200 to a final concentration of 1 $\mu\text{g}/\text{mL}$. After washing the cells with HBSS, goat anti-rabbit immunoglobulin G conjugated with Alexa Fluor 680 (Invitrogen, Carlsbad, CA) was added to the blocking solution at a final concentration of 2 $\mu\text{g}/\text{mL}$ and incubated at room temperature for 1 hour in the dark. The slides were washed three times with DPBS, and examined with a fluorescence microscope.

Western Blot Analysis: LNCaP and PC3 cells were washed with DPBS and lysed with RIPA lysis and extraction buffer (Pierce Biotech, Rockford, IL). Protein concentrations were determined with the Bio-Rad Protein Assay

Dye Reagent Concentrate (Bio-Rad, Hercules, CA). Fifty micrograms of proteins were separated by 8% SDS-PAGE electrophoresis and transferred to PVDF membranes. The membranes were blocked using 5% nonfat milk and probed separately for 2 hours at room temperature with primary antibodies for PSMA (Abcam) and β -Actin (Santa Cruz Biotechnology, Santa Cruz, CA). The membranes were then washed and probed with a 1:2000 dilution of peroxidase-conjugated secondary antibody, and detected with enhanced chemiluminescence (Amersham Life Sciences, Amersham, UK).

Cell Viability Assays: Cells were seeded in 96-well plates and cultured for 24 hours. The cells were then exposed to a graded range of concentrations of A-dmDT390-scfbDb(PSMA) (from 0 nM to 5 nM) for 48 hours. The viability of cells was measured with a MTT assay. MTT solution (100 μL , 0.5 mg/mL in PBS) was added to each well. The plates were incubated for 4 hours at 37 $^{\circ}\text{C}$, and then dimethyl sulfoxide (100 μL) was added to each well and incubated for 10 minutes at room temperature. The absorbance was measured at 570 nm using a plate reader. The half maximal inhibitory concentration (IC_{50}) of the immunotoxin was calculated using the SPSS software for performing statistical analysis.

Endocytosis and Quantification of A-dmDT390-scfbDb(PSMA) in Cells: A-dmDT390-scfbDb(PSMA) was labeled with Alexa Fluor 680 using Invitrogen Protein Labeling Kit A20172. LNCaP and PC-3 prostate cancer cells grown to 60 to 70% confluence on four-chamber glass slides were used for endocytosis analysis. The cells were incubated with Alexa Fluor 680-labeled A-dmDT390-scfbDb(PSMA) (0.1 μM) in complete medium for different durations

(from 10 minutes to 3 hours), or incubated with graded concentrations of Alexa Fluor 680-labeled A-dmDT390-scfbDb(PSMA) (from 0.01 μM to 0.1 μM) for 3 hours. After removal of the media, the cells were washed three times using DPBS, fixed with 10% formalin for 10 minutes, stained with 4',6-diamidino-2-phenylindole (DAPI) for 5 minutes, and rinsed three times with DPBS. The cells were then observed under fluorescent microscopy. For quantitative measurement of the Alexa Fluor 680-labeled A-dmDT390-scfbDb(PSMA) internalization, a BD flow cytometer (Becton Dickinson, San Jose, CA) with excitation/emission wavelengths of 635 nm/679 nm was used.

Assessment of Apoptosis: Annexin V binding was used to estimate apoptosis. Cells were first exposed to a DNA-binding dye (PI) to detect sub-diploid population. The two prostate cancer cell lines (LNCaP and PC-3) were treated with 0.1, 0.5, and 1.0 μM of A-dmDT390-scfbDb(PSMA) immunotoxin for 24 hours. Then, the cells were harvested with trypsinization, collected by centrifugation, and washed with DPBS. The collected cells were fixed with 70% ethanol for 1 hour at 4 $^{\circ}\text{C}$. The fixed cells were washed twice in DPBS, incubated with a solution containing RNase (100 $\mu\text{g}/\text{mL}$) at 37 $^{\circ}\text{C}$ in a water bath for 30 minutes, and then gently re-suspended in PI solution (1 mL, 50 $\mu\text{g}/\text{mL}$ with 3.8 μM sodium citrate in DPBS). Lastly, the cells were incubated for 15 minutes in the dark at room temperature and analyzed using flow cytometry. The red fluorescence signal from PI staining of individual cells was collected. Ten thousand cells of each sample were counted. For fluorescence microscopy detection, 10,000 LNCaP cells were plated onto an 8-well chamber slide for 24 hours. After incubation with different concentrations of A-dmDT390-scfbDb(PSMA) for 48 hours, the cells were incubated with Annexin binding buffer (500 μL). Annexin V-FITC (5 μL) and PI (Abcam) (5 μL) were added onto the cells, and cells were fixed in 2% formaldehyde before visualization. The fixed cells were examined under a fluorescence microscope using separate filters for FITC and PI. The cells that bound Annexin V-FITC, which had undergone apoptosis, showed green staining on the plasma membrane, whereas

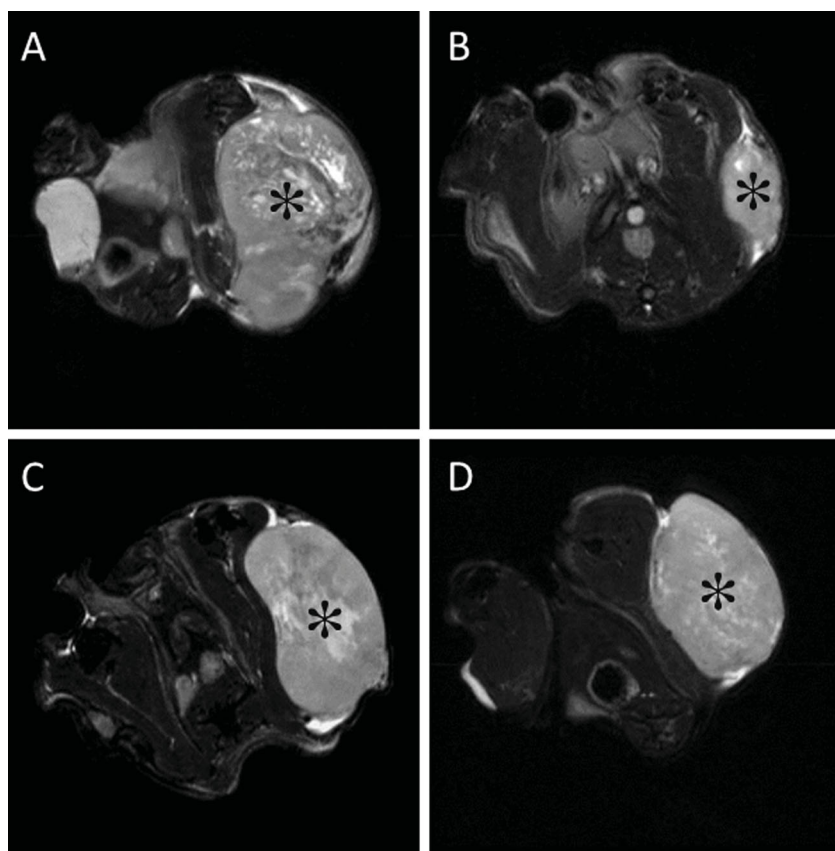


Figure 10. MR images showing the effects of A-dmDT390-scfbDb(PSMA) immunotoxin on LNCaP and PC-3 prostate tumors (marked with *). (A) and (B) are representative MR images through the largest cross section of an untreated control and a treated LNCaP tumor in mice 30 days after treatment. (C) and (D) are MR images of an untreated control and a treated PC-3 tumor.

the cells that had lost membrane integrity due to necrosis showed red PI staining throughout the nuclei. To further determine the cytotoxicity of A-dmDT390-scfbDb(PSMA), the cells were routinely examined using trypan blue staining and under light microscopy. The cells permeable to trypan blue were considered nonviable.

Animal Tumor Model and Optical Imaging: All animal studies were carried out in accordance with the guidelines of the Howard University Institutional Animal Care and Use Committee. Five-week-old athymic male nude mice were inoculated subcutaneously with 5×10^6 LNCaP cells or 2×10^6 PC-3 cells mixed with matrigel (BD Biosciences, Bedford, MA) (0.2 mL) into the lower left flank. The tumors were allowed to reach 5–7 mm in diameter for imaging study. Six mice with LNCaP tumors and five mice with PC-3 tumors were used to test the detection sensitivity and specificity of imaging and the dynamic uptake of Alexa Fluor 680-labeled A-dmDT390-scfbDb(PSMA) *in vivo*. Three mice with LNCaP tumors and three mice with PC-3 tumors were used to test specific targeting of tumor by Alexa Fluor 680 labeled A-dmDT390-scfbDb(PSMA). Three mice with LNCaP tumors and two mice with PC-3 tumors were given an identical volume of DPBS and served as controls.

In vivo fluorescence imaging of tumor-bearing mice was performed using the IVIS 200 Imaging System and Living Image software (Caliper Life Sciences, Hopkinton, MA). The mice were placed on a warmed (25 °C) stage inside a light-tight camera box with continuous exposure to 2% isoflurane. The mice were given the Alexa Fluor 680 labeled A-dmDT390-scfbDb(PSMA) (100 μ L 2.06 μ M or 100 μ L 4.12 μ M) or Alexa Fluor 680 dye via tail vein injection. The mouse was imaged every 10 minutes for the first hour and then imaged every hour for 24 hours. The acquisition time

for each image was 2 seconds. Regions of interest around tumor sites from the displayed images were identified and emitted light was measured. The signal intensity was expressed as radiant efficiency in photons/second/cm²/steradian/(μ Watt/cm²) (p/s/cm²/sr/(μ W/cm²)). The contralateral non-tumor-bearing leg muscle was selected as the background.

Evaluation of Therapeutic Efficacy: Tumor xenograft models were developed by subcutaneous inoculation of 5×10^6 LNCaP cells or 2×10^6 PC-3 cells mixed with matrigel (0.2 mL) into the lower left flank of five-week-old male athymic nude mice. LNCaP tumors were allowed to develop for six weeks and PC-3 tumors for three weeks to reach the diameter of about 5 mm. The mice with LNCaP tumors or PC-3 tumors were divided randomly into two groups ($n = 10$). A-dmDT390-scfbDb(PSMA) immunotoxin (200 μ g/kg) or BSA diluted in DPBS was administered *via* intraperitoneal injection to twice a day at 6 hour intervals (10 am and 4 pm) for 6 days. Tumor growth was monitored twice a week with MRI. The mice were anesthetized with 2% isoflurane in oxygen, positioned in the MRI probe, and taped with polyurethane foam to avoid involuntary motion. A Bruker 400MHz NMR machine (Bruker-Biospin, Billerica, MA) was used for MRI. A rapid acquisition with refocused echoes (RARE) sequence was used to acquire T2-weighted coronal images. The imaging parameters were: echo time 7.8 ms, RARE factor 16, effective echo time 39 ms, repetition time 3600 ms, number of averages 12, field-of-view 27.0 mm \times 25.6 mm, matrix size 192 \times 256, and slice thickness 0.5 mm. The Medical Image Processing, Analysis, and Visualization application (CIT/NIH, Bethesda, MD) was used for image analysis. The tumor was manually segmented in each MRI image, the number of voxels within the boundary of tumor was counted and the total tumor volume was calculated.

Statistical Analysis: Statistical analysis was performed with the Student's *t*-test. Survival was assessed with the Kaplan–Meier method. A significant correlation was inferred if a *P* value was < 0.05 by correlation analysis. All statistical tests were two-sided.

Supporting Information

Supporting Information is available from the Wiley Online Library or from the author.

Acknowledgements

This work was supported in part by NIH/NCRR 3 G12 RR003048, NIH/NIMHD 8 G12 MD007597, and USAMRMC W81XWH-10-1-0767 grants.

Received: June 30, 2012

Revised: August 22, 2012

Published online:

[1] A. Jemal, R. Siegel, E. Ward, Y. Hao, J. Xu, T. Murray, M. J. Thun, *CA Cancer J. Clin.* **2008**, *58*, 71.

[2] C. N. Sternberg, *Ann. Oncol.* **2008**, *19*, vii91.

- [3] L. C. Pronk, P. H. Hilken, M. J. van den Bent, W. L. van Putten, G. Stoter, J. Verweij, *Anticancer Drugs* **1998**, 9, 759.
- [4] T. M. Allen, *Nat. Rev. Cancer* **2002**, 2, 750.
- [5] W. R. Fair, R. S. Israeli, W. D. Heston, *Prostate* **1997**, 32, 140.
- [6] S. F. Slovin, *Expert. Opin. Ther. Targets* **2005**, 9, 561.
- [7] S. S. Chang, D. S. O'Keefe, D. J. Bacich, V. E. Reuter, W. D. Heston, P. B. Gaudin, *Clin. Cancer Res.* **1999**, 5, 2674.
- [8] C. A. Foss, R. C. Mease, H. Fan, Y. Wang, H. T. Ravert, R. F. Dannals, R. T. Olszewski, W. D. Heston, A. P. Kozikowski, M. G. Pomper, *Clin. Cancer Res.* **2005**, 11, 4022.
- [9] G. Fracasso, G. Bellisola, S. Cingarlini, D. Castelletti, T. Prayer-Galetti, F. Pagano, G. Tridente, M. Colombatti, *Prostate* **2002**, 53, 9.
- [10] N. Schulke, O. A. Varlamova, G. P. Donovan, D. Ma, J. P. Gardner, D. M. Morrissey, R. R. Arrigale, C. Zhan, A. J. Chodera, K. G. Surowitz, P. J. Maddon, W. D. Heston, W. C. Olson, *Proc. Natl. Acad. Sci. USA* **2003**, 100, 12590.
- [11] A. M. Wu, P. D. Senter, *Nat. Biotechnol.* **2005**, 23, 1137.
- [12] N. Arora, R. Masood, T. Zheng, J. Cai, D. L. Smith, P. S. Gill, *Cancer Res.* **1999**, 59, 183.
- [13] Y. Y. Liu, I. Gordienko, A. Mathias, S. Ma, J. Thompson, J. H. Woo, D. M. Neville, *Protein Expr. Purif.* **2000**, 19, 304.
- [14] Y. Jia, H. Li, W. Chen, M. Li, M. Lv, P. Feng, H. Hu, L. Zhang, *Gene Therapy* **2006**, 13, 1351.
- [15] C. H. Chan, B. R. Blazar, L. Greenfield, R. J. Kreitman, D. A. Vallera, *Blood* **1996**, 88, 1445.
- [16] Z. Wang, G. B. Kim, J. H. Woo, Y. Y. Liu, A. Mathias, S. Stavrou, D. M. Neville, *Bioconjug Chem.* **2007**, 18, 947.
- [17] J. H. Woo, S. H. Bour, T. Dang, Y. J. Lee, S. K. Park, E. Andreas, S. H. Kang, J. S. Liu, D. M. Jr. Neville, A. E. Frankel, *Cancer Immunol. Immunother.* **2008**, 57, 1225.
- [18] J. H. Woo, Y. J. Lee, D. M. Neville, A. E. Frankel, *Methods Mol. Biol.* **2010**, 651, 157.
- [19] G. B. Kim, Z. Wang, Y. Y. Liu, S. Stavrou, A. Mathias, K. J. Goodwin, J. M. Thomas, D. M. Neville, *Protein Eng. Des. Sel.* **2007**, 20, 425.
- [20] D. M. Neville, J. T. Thompson, H. Hu, J. H. Woo, S. Ma, J. M. Hexham, M. E. Digan, July **2012**, *US Patent Number* 8217158.
- [21] C. Liu, K. Hasegawa, S. J. Russell, M. Sadelain, K. W. Peng, *Prostate* **2009**, 69, 1128.
- [22] K. Fortmüller, K. Alt, D. Gierschner, P. Wolf, V. Baum, N. Freudenberger, U. Wetterauer, U. Elsässer-Beile, P. Bühler, *Prostate* **2011**, 71, 588.
- [23] D. M. Nanus, M. I. Milowsky, L. Kostakoglu, P. M. Smith-Jones, S. Vallabhaajosula, S. J. Goldsmith, N. H. Bander, *J. Urol.* **2003**, 170, S84.
- [24] W. C. Olson, W. D. Heston, A. K. Rajasekaran, *Rev. Recent Clin. Trials* **2007**, 2, 182.
- [25] S. K. Kochi, R. J. Collier, *Exp. Cell Res.* **1993**, 208, 296.
- [26] J. Jia, H. Li, S. Tai, M. Lv, M. Liao, Z. Yang, B. Zhang, B. Zhou, G. Zhang, L. Zhang, *DNA Cell Biol.* **2008**, 27, 279.
- [27] M. Veisheh, P. Gabikian, S. B. Bahrami, O. Veisheh, M. Zhang, R. C. Hackman, A. C. Ravanpay, M. R. Stroud, Y. Kusuma, S. J. Hansen, D. Kwok, N. M. Munoz, R. W. Sze, W. M. Grady, N. M. Greenberg, R. G. Ellenbogen, J. M. Olson, *Cancer Res.* **2007**, 67, 6882.
- [28] E. L. Kaijzel, G. van der Pluijm, C. W. Lowik, *Clin. Cancer Res.* **2007**, 13, 3490.
- [29] J. Thompson, S. Stavrou, M. Weetall, J. M. Hexham, M. E. Digan, Z. Wang, J. H. Woo, Y. Yu, A. Mathias, Y. Y. Liu, S. Ma, I. Gordienko, P. Lake, D. M. Neville Jr., *Protein Eng.* **2001**, 14, 1035.
- [30] D. Ma, C. E. Hopf, A. D. Malewicz, G. P. Donovan, P. D. Senter, W. F. Goeckeler, P. J. Maddon, W. C. Olson, *Clin. Cancer Res.* **2006**, 12, 2591.
- [31] K. Kuroda, H. Liu, S. Kim, M. Guo, V. Navarro, N. H. Bander, *Prostate* **2010**, 70, 1286.
- [32] P. Wolf, K. Alt, D. Wetterauer, P. Bühler, D. Gierschner, A. Katzenwadel, U. Wetterauer, U. Elsässer-Beile, *J. Immunother.* **2010**, 33, 262.



Supporting Information

for *Adv. Healthcare Mater.*, DOI: 10.1002/adhm.201200254

**An Anti-PSMA Bivalent Immunotoxin Exhibits Specificity
and Efficacy for Prostate Cancer Imaging and Therapy**

*Fayun Zhang, Liang Shan, Yuanyi Liu, David Neville, Jung-
Hee Woo, Yue Chen, Alexandru Korotcov, Stephen Lin,
Sophia Huang, Rajagopalan Sridhar, Wei Liang, and Paul C.
Wang**

Copyright WILEY-VCH Verlag GmbH & Co. KGaA, 69469 Weinheim, Germany, 2010.

Supporting Information

for Adv. Healthcare Mater., DOI: 10.1002/adhm.201200254

Title: An Anti-PSMA Bivalent Immunotoxin Exhibits Specificity and Efficacy for Prostate Cancer Imaging and Therapy

Authors: F. Zhang, L. Shan, Y. Liu, D. Neville, J-H Wu, Y. Chen, A. Korotcov, S. Lin, S. Huang, R. Sridhar, W. Liang, P. C. Wang

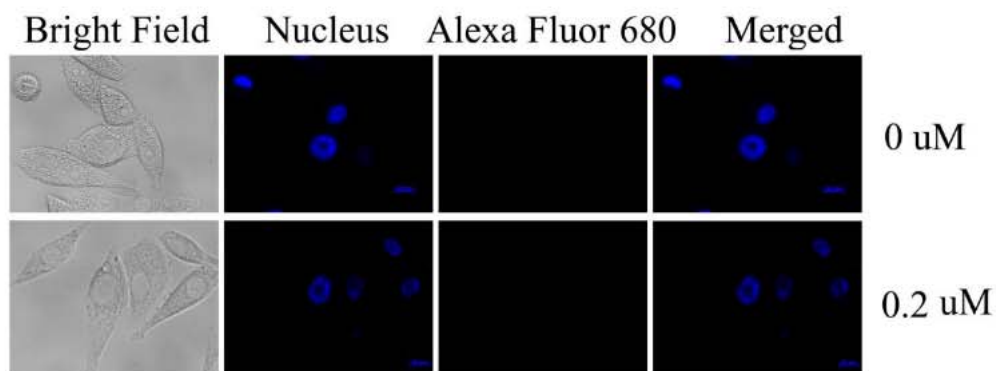


Figure S1. Fluorescence microscopy of A-dmDT390-scfDb(PSMA) internalization in PC-3 cells. Cells were treated with Alexa Fluor 680-labeled A-dmDT390-scfDb(PSMA) ($0.2 \mu\text{M}$) for 4 hours. After washing with DPBS, cells were fixed, incubated with DAPI, and observed under a fluorescence microscope (magnification $1000\times$).

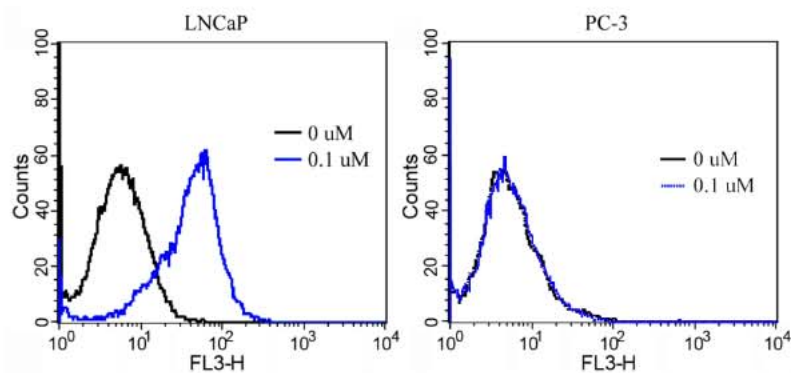


Figure S2. Flow cytometry quantification of A-dmDT390-scfbDb(PSMA) accumulation in PC-3 and LNCaP cells. Cells were treated with of Alexa Fluor 680-labeled A-dmDT390-scfbDb(PSMA) (0.1 μ M) for 6 hours. After washing with DPBS, cells were collected and analyzed with flow cytometry.

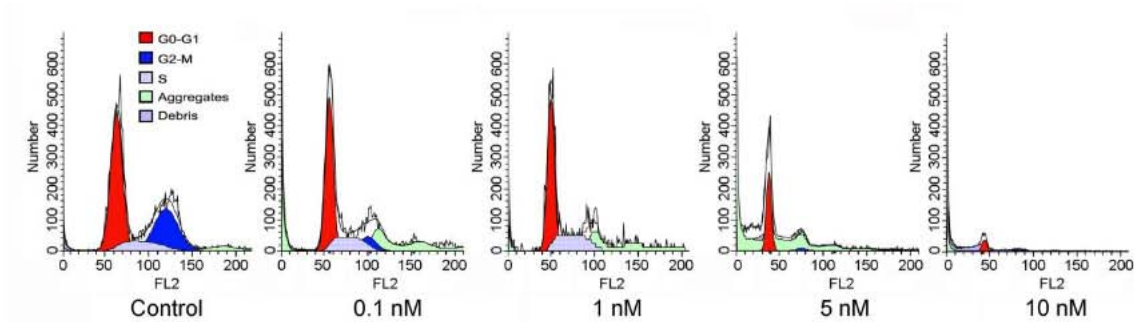


Figure S3. Cell cycle analysis of LNCaP cells after 48 hours treatment with 0.1, 1, 5, and 10 nM of A-dmDT390-scfbDb(PSMA), and then stained with PI. Cell cycle distribution was analyzed with flow cytometry.

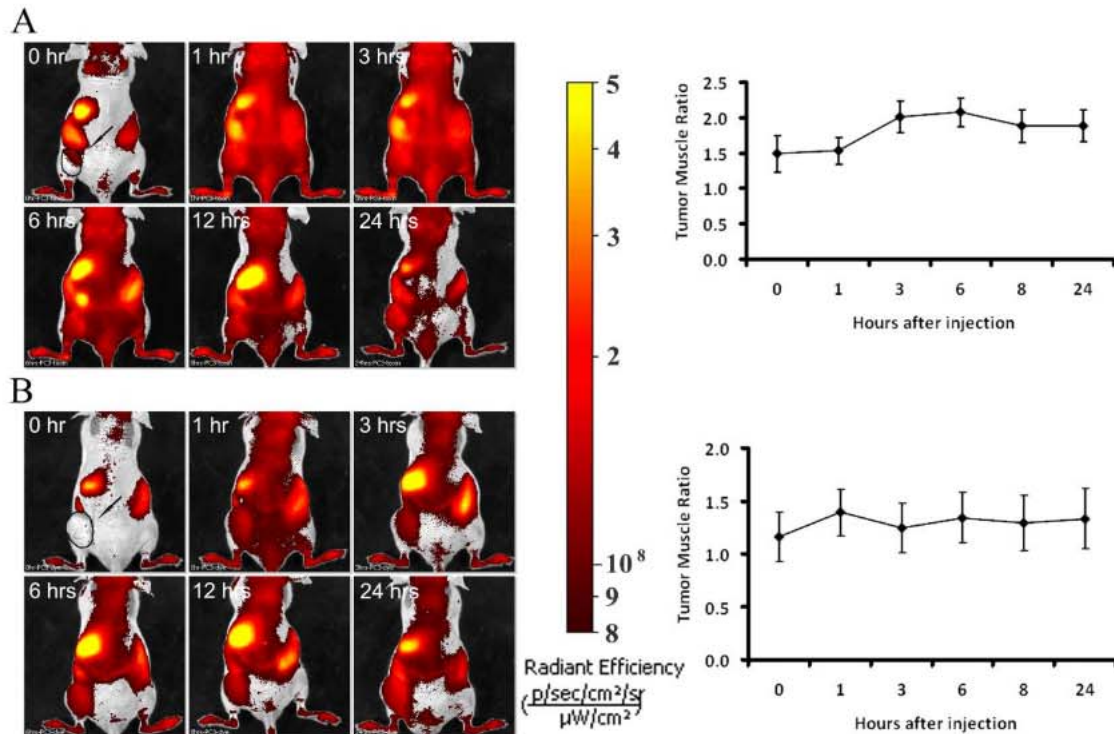


Figure S4. Whole animal imaging after intravenous injection of Alexa Fluor 680-labeled A-dmDT390-scfbDb(PSMA) into PC-3 tumor-bearing mice. (A) Images were acquired after injection of Alexa Fluor 680-labeled A-dmDT390-scfbDb(PSMA) (100 μL) into mice. (B) Images were acquired after injection of Alexa Fluor 680 dye (100 μL) into mice. Images were taken at 0, 1, 3, 6, 8, and 24 hours after injection, respectively. The charts on the right show the changes in the ratio of tumor (marked with arrow) to muscle fluorescence intensity over time.

REVIEW

Innovative pharmaceutical development based on unique properties of nanoscale delivery formulation

Cite this: *Nanoscale*, 2013, 5, 8307

Anil Kumar,^{†,ab} Fei Chen,^{†,ab} Anbu Mozhi,^{ab} Xu Zhang,^a Yuanyuan Zhao,^a Xiangdong Xue,^{ab} Yanli Hao,^c Xiaoning Zhang,^c Paul C. Wang^d and Xing-Jie Liang^{*a}

The advent of nanotechnology has reignited interest in the field of pharmaceutical science for the development of nanomedicine. Nanomedicinal formulations are nanometer-sized carrier materials designed for increasing the drug tissue bioavailability, thereby improving the treatment of systemically applied chemotherapeutic drugs. Nanomedicine is a new approach to deliver the pharmaceuticals through different routes of administration with safer and more effective therapies compared to conventional methods. To date, various kinds of nanomaterials have been developed over the years to make delivery systems more effective for the treatment of various diseases. Even though nanomaterials have significant advantages due to their unique nanoscale properties, there are still significant challenges in the improvement and development of nanoformulations with composites and other materials. Here in this review, we highlight the nanomedicinal formulations aiming to improve the balance between the efficacy and the toxicity of therapeutic interventions through different routes of administration and how to design nanomedicine for safer and more effective ways to improve the treatment quality. We also emphasize the environmental and health prospects of nanomaterials for human health care.

Received 27th March 2013

Accepted 22nd May 2013

DOI: 10.1039/c3nr01525d

www.rsc.org/nanoscale

^aCAS Key Laboratory for Biological Effects of Nanomaterials and Nanosafety, National Center for Nanoscience and Technology, Chinese Academy of Sciences, No. 11, First North Road, Beijing 100190, P. R. China. E-mail: liangxj@nanoctr.cn; Fax: +86 10 62656765; Tel: +86 1082545569

^bUniversity of Chinese Academy of Science, Beijing, P. R. China

^cDepartment of Pharmacology and Pharmaceutical Sciences, School of Medicine, Tsinghua University, Beijing, China

^dLaboratory of Molecular Imaging, Department of Radiology, Howard University, Washington DC 20060, USA

[†] Anil Kumar and Fei Chen contributed equally to this paper.



Anil Kumar is currently working as a Research Fellow in the research group of Prof. Xing-jie Liang at the CAS Key Laboratory for Biological effects of Nanomaterials and Nanosafety, National Center for Nanoscience and Technology, Chinese Academy of Sciences. Previously, he graduated from Bangalore University with major in Biotechnology, Chemistry and Zoology. He completed his

Masters degree in Microbial Science and Technology from Amity University, Noida, India. His main research interest focuses on applied nanotechnology for the study of nano-drug delivery systems (gold nanomaterials for targeted drug delivery system) and to overcome drug resistance in cancer.



Fei Chen received his BS of Biopharmaceutics at Huazhong University of Science & Technology in 2012. Currently he is pursuing his master's degree under the guidance of Prof. Xing-jie Liang at the National Center for Nanoscience and Technology (NCNST). His main research interest focuses on nanomaterial-based controllable drug delivery systems.

1 Introduction

In 1959, Richard Feynman proposed that the future of humans will be fully occupied by machines, small machines will be used to make further smaller machines, and these in turn, will be used to make even tinier machines, all the way down to the atomic level.¹ Interestingly, with the advent of nanotechnology, the vision of Professor Feynman has been partially realized today. The advances in nanoscience have propelled innovations in a number of scientific disciplines, including pharmaceutical development for the treatment of various diseases. Nanotechnology has the potential to revolutionize medicine, and has already presented new regulatory challenges for scientific communities. Innovations are occurring rapidly, as demonstrated by the exponential increase in nanotechnology-related pharmaceutical patents over the past 20 years.²

The European Science Foundation (ESF) launched its forward vision on nanomedicine and provided the new definition: "Nanomedicine uses nano-sized tools for the diagnosis, prevention and treatment of disease and to gain increased

understanding of the underlying complex patho-physiology of the disease. The ultimate goal is to improve the quality of human life".

Nanomedicine encompasses the production and application of physical, chemical, and biological systems (Fig. 1) at scales, ranging from individual atoms or molecules to around 100 nanometers in diameter, as well as the integration of the resulting nanostructures into larger systems for real-time application (Box 1).

Over the past decades, nanomedicines have been translated into various commercial products, from the lab to the market. Many pharmaceutical companies are paying more attention to nanotechnology than before, in order to find new solutions for pharmaceutical innovation with lower cost, lower risks and much higher efficiency compared to traditional drug development.³ Currently, nanomedicine is dominated by nanoscale drug delivery systems.³ As we know, materials have unique properties at nanoscale dimensions that meet important medical needs and are already being used as the basis for new drug delivery formulation.⁴ Nanoscale particle/molecule based



Anbu Mozhi received her Bachelor of advanced Zoology and Biotechnology in 2007 and obtained her M.Tech of Nanoscience and Nanotechnology in 2010, both at the University of Madras, India. She is pursuing her PhD under the guidance of Prof. Xing-jie Liang's lab at the National Center for Nanoscience and Nanotechnology (NCNST) at Chinese academy of Science, China. Her research interest is

focussed on design and development of stimuli-responsive polymer based nanomaterials for gene therapy and drug delivery.



Yuanyuan Zhao graduated in Applied Chemistry. She completed her M.S. study in Physical Chemistry and obtained a Ph.D. in Polymeric Chemistry and Physics at Jilin University in 2010. Since 2011 she has been doing her Post-doctoral studies on design and application of nanoscale biomaterials in Prof. Xing-jie Liang's group.



Xu Zhang received in BS of Biology from Qufu Normal University, College of Life Science. Since 2008, he became a Ph.D. candidate at National Center for Nanoscience and Technology, Chinese Academy of Science in the group of Prof. Xing-jie Liang. His research interests include the design and applications of self-assembled peptides and peptide-based functional aggregation-induced emission molecules.



Dr Xing-jie Liang received his Ph.D. at the National Key Laboratory of Bio-macromolecules, Institute of Biophysics at CAS. He finished his postdoctoral studies at the Center for Cancer Research, NCI, NIH, and worked as a Research Fellow at the Surgical Neurology Branch, NINDS. He worked on molecular imaging at the School of Medicine, Howard University before he became deputy director of the

CAS Key Laboratory for Biomedical Effects of Nanomaterials and Nanosafety, NCNST. Developing drug delivery strategies for prevention/treatment of AIDS and cancers are current programs ongoing in Dr Liang's lab based on understanding the basic physio-chemical and biological processes in nanomedicine.

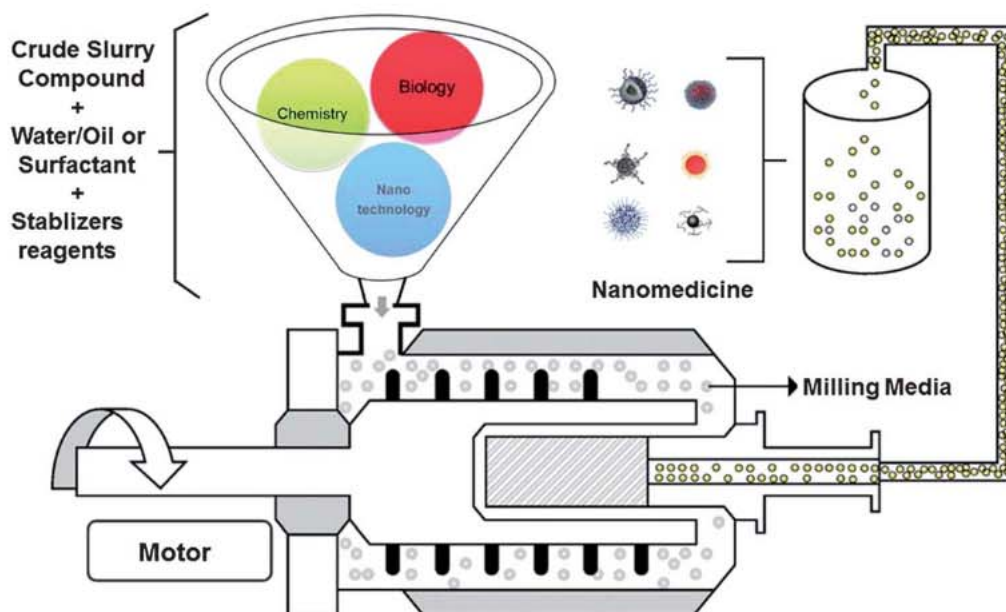


Fig. 1 Schematic diagram for the future-nanomedicine production system.

drug delivery formulations improve the bioavailability and pharmacokinetics for better therapy, such as liposomes,⁵ nanosuspensions⁶ and polymeric nanoparticles.⁷ Some of the nanoparticles (NPs) are effective in improving safety and

efficacy, and also decreasing the toxicity. For a better understanding of innovative pharmaceutical development based on nanoscale drug delivery formulation, we attempt to review the history and development of nanomedicine in the

Box 1 Real applications of nanotechnology for health care

An important area to focus on for bionanomedical applications has been investigated recently. We adopted all these concepts with the help of various literatures reports. This box summarizes the key points.

Drug delivery: nanoscale particles/molecules have been developed to target specific sites in the body, to improve the bioavailability and pharmacokinetics of therapeutics. Multifunctional targeted devices are capable of bypassing biological barriers to deliver multiple therapeutic agents directly to the cancer cells and also to tissues in the microenvironment.

Drug therapy: the nanostructure/molecules themselves have unique medical properties, which show therapeutic effects in biological systems. Such molecules differ from traditional small-molecule drugs. Examples include drugs based on fullerenes or dendrimers.

Imaging: nanoparticles, which are used particularly for MRI and ultrasound scans, provide an improved contrast and favorable biodistribution. For example, super paramagnetic iron oxide nanoparticles have been used as MRI contrast agents.

Repair and replacement: damaged tissues and organs are often replaced by artificial substitutes, and nanotechnology offers a range of new biocompatible coatings for the implants that improves their adhesion, durability and lifespan. New types of nanomaterials are being evaluated as implant coatings to improve interface properties for bone replacement and tissue regeneration. For example, nanopolymers can be used to coat devices in contact with blood (*e.g.* artificial hearts, catheters) to disperse clots or prevent their formation.

Hearing and vision: nanotechnology is being used to develop a potentially more powerful device to restore lost vision and hearing. One approach uses a miniature video camera attached to glasses to capture visual signals which are then transmitted to an array of electrodes placed in the eye. Another approach uses an array of electrodes at the tip of the device to solve hearing problems, with five times greater amplification than that of current devices.

Implants, surgery and coatings: nanotechnology has the capability to improve implant biocompatibility, either by coating implants with nanomaterials or by using nanomaterials as implant materials. They can also be used to create smaller, rechargeable batteries for use in active implants. The technology has also been applied to create corrosion free suture needles with improved strength and ductility. Nanoparticles have also been incorporated into fibers to be used for wound dressings and for dental cavity filling. The ultimate aim of using these novel technologies in implants, surgery or wound care is to heal the body quickly and efficiently without creating excessive pain or irritation.

pharmaceutical field, and we also discuss about its advantages, delivery through different routes of administration and toxicological issues to develop more efficient nanoformulations for better health care.

2 History and development

The nanomedicines can be divided into three groups. The first group consists of the marketed nanomedicine products, which are already in routine clinical use, while the members of the second group of nanomedicines are mostly in the clinic stage.⁸ In 1965, researchers started to utilize nanotechnology in pharmaceutical research, they created a novel lipid vesicle for drug delivery, now known as a liposome.⁹ Later in 1976, the first control-released polymeric system for the delivery of macromolecules was described,⁹ and in 1978, dendrimers were described as a delivery vehicle.¹⁰ Doxil¹¹ (a doxorubicin carrying nano-drug) was the first Food and Drug Administration (FDA)-approved nanomedicine used in the treatment of cancer patients. In 1995, liposome injection was approved to treat a wide range of cancers like ovarian cancer, AIDS (acquired immunodeficiency syndrome)-related Kaposi's sarcoma and myeloma.¹² All these early innovations provide valuable information to the researchers to design novel nanomedicines that would be helpful in treating multiple diseases. Long circulating PLGA-PEG NPs¹³ were first described in 1994 as biodegradable polymeric nanospheres for drug delivery. In 1996, the FDA approved Ferumoxide (iron oxide) to be applied for clinical use as MRI contrast agent.¹⁴ In addition to this, polymer coated iron oxide NPs have also been approved by the FDA as MRI contrast agents. In 2005, Abraxane¹⁵ (a protein based drug delivery system) was approved by the FDA. In 2007, targeted nanomedicines like Genexol-PM¹⁶ (polymeric micelle NPs), CALAA-01¹⁷ (a targeted cyclodextrin-polymer hybrid NP), BIND-014¹⁸ (targeted polymeric NPs) and SEL-068¹² (integrated polymeric nanoparticle vaccines) for cancer therapy have already entered into human clinical study.

Finally, the third group consists of some nanoscale materials for drug delivery, such as gold (Au), silica nanoparticles, have been developed with more advanced nanotechniques, which may have the potential to help the conventional drugs to be more effective and cause adverse side effects. For example, mesoporous silica nanoparticles (MSNPs) can be used as an ideal drug delivery vehicle with its excellent drug loading capacity, easily synthesis, biocompatibility, but many details about MSNPs still remain unclear for clinical use. It is easy to conclude that the successful application of nanotechnology in drug delivery could draw the attention of scientists, governments and industrial investigators, which in turn is helpful for the development of nanomedicine and accelerates the speed of discovery of novel nanoscale drug formulations.

3 Advantages of nanomedicine over conventional medicine

In conventional medicine, treatment is based on the symptoms created by the disease and the adverse problems occurring at

the tissue/organ level, (*e.g.* due to metabolic problems, or other infectious agents). At a certain stage, the disease may often be at an advanced and most dangerous stage, in such a condition that the symptoms become apparent in the patient and the clinician becomes confused over which way they can treat the patient to get rid of the disease.¹⁹ Conventional medicine and techniques have left many of the problems, which are hard to penetrate due to lack of information and appropriate techniques.

When the drug is being assessed for clinical use, both the therapeutic efficacy and toxicity should be taken into account. Some drugs are poorly soluble in water, but they can be dissolved in other organic solvents, which trigger severe allergic effects in the human body after administration.²⁰ During cancer treatment, cisplatin and other drugs all have the drawback of high toxicity. One reason for this is the unspecific recognition and interaction with cells and organs.²¹ There are so many prevailing drawbacks, including: limited solubility, poor distribution within the body, a lack of selectivity, and unfavorable pharmacokinetics behavior can damage the healthy tissues.²²

Due to the significant properties of materials at the nanoscale, nanomedicine shows different behavior from conventional medicine.¹⁹ Advancement of nanoformulation techniques has offered a new hope for incurable, severe diseases like cancer, human immunodeficiency virus (HIV)^{23,24} and for the treatment of some infectious pathogens.²⁵ Based on nanoscale particles, nanomedicines represent many benefits over conventional drugs and here we have characterized the advantages of nanomedicine according to two aspects (Table 1). In addition, nanotechnology could give conventional materials or drugs additional functionality based on their unique properties at the nanoscale. For example, QDs have far brighter and more stable fluorescence than conventional fluorescent dyes for cell labeling. Gold nanorods (AuNRs), nanoshells (NSs) and nanocages (NCs) have unique properties for imaging-guided cancer therapy.^{26–28}

However, current nanotechnology based drug molecules continue to dominate the pharmaceutical market despite conventional therapeutic and diagnostic agents, making a distinct niche for themselves. It offers an immense vision of enhanced, tailored treatment of disease, with monitoring, repairing, construction and control of human biological systems at the molecular level, using engineered nanodevices and nanostructures for human health care.

4 Techniques involve for the development and production of nanoscale drug formulation

Basically, there are two types of technique for the production of nanoscale formulations, one is top-down, and the other is bottom-up. The bottom-up techniques include chemical reactions and molecular assemblies, such as supercritical fluid techniques, precipitation, nanoemulsion, spray-drying, polymerization and synthesis. The top-down techniques include wet

Table 1 Advantages of nanomedicine over conventional medicine

Advantages of nanomedicine according to physical aspects	Advantages of nanomedicine according to biological aspects
<ul style="list-style-type: none"> • Increase the aqueous solubility of pharmaceuticals • Protect the drugs from degradation • Ability to encapsulate high drug content, <i>e.g.</i> polymeric nanoparticles • Feasibility of carrying both lipophilic and hydrophilic drugs • High surface activity and adsorption ration rate • Increasing specificity towards disease • Deliver drug for slow release to maintain the therapeutic dose • Produce a prolonged release of drugs to control systemic transportation • Stimuli release (pH, temperature, heat, light, radiation, magnetic field <i>etc.</i>) • Easily design and engineer to load different drugs for combination therapy 	<ul style="list-style-type: none"> • Improve the bioavailability and biocompatibility of drugs, non-toxic, non-allergenic and non-irritating • Improve the active/passive target specificity in drug delivery • Penetrate the cell membrane and biological barriers. <i>e.g.</i> Blood-brain barrier (BBB) • Enhance the permeability and retention (EPR) of tumors for accumulation of large molecules and small particles • Prolong the circulation time of drugs towards the therapeutic window • Possibility to overcome resistance factors. <i>e.g.</i> P-glycoprotein and MDR factors • Combined treatment of multiple diseases or theranostics application • It is possible to target individual pathogens or biomolecules according to the nature of the disease

media milling and high-pressure homogenization. The resulting nanoparticles are referred to as nanosuspensions.^{6,29,30}

Nanosuspensions are stabilized submicron colloidal dispersions of nanosized drug particles.³⁰ Various technologies have been utilized in the development and production of nanosuspensions. As for top-down strategies, one important technique is high-pressure homogenization. The first method for high pressure homogenization was invented by employing a piston-gas homogenizer and processing in aqueous media at room temperature,³¹ and later in non-aqueous media (patent number: WO2001003670, 2001). J. Kluge and M. Mazzotti produced S-ketoprofen poly(lactic-co-glycolic acid) (PLGA) drug-polymer nanocomposites with CO₂ assisted high pressure homogenization that greatly improved the bioavailability of the drug.³² Pereda *et al.* found that after treatment by high-pressure

homogenization, the storage of milk fat was significantly improved.³³

Other types of high-pressure homogenization, such as media milling²⁹ and Nanoedge (US Patent 6018080, 2000), were also involved in the production of nanoscale drug formulations. Several pharmaceutical companies have developed a certain kind of processing standard operating procedures (SOPs) based on high pressure homogenization techniques, for example the Nanomorph™ from Abbott, Nanocrystal™ from Elan Nano-systems and Nanoedge from Baxter. Another important method to reduce the particle size in the industry is wet ball milling. Currently, there are more than 5 nanoscale drug formulations produced by this method in the market, and still some are in the developmental stage. One interesting point is that all of the FDA approved top-down-strategy nanoscale drug formulations are for oral delivery.³⁴

As for the bottom-up strategy, apart from classical synthesis and polymerization, one powerful technique is the formation of nanoemulsions. As a nanoemulsion is itself a drug, it can serve as a template for the production of nanosuspensions.^{35,36} Solvent emulsification diffusion (SED) is the most commonly used method for the preparation of solid-lipid and polymeric nanoparticles.³⁷ The ease and convenience in fabrication of nanoemulsions can precisely control drug loading and positioning (spatial placement), therefore, thousands of drugs and active pharmaceutical ingredients (APIs) have been extensively investigated and developed. For example, the nanosuspensions of ibuprofen, diclofenac and acyclovir are now available from the market (<http://www.reportlinker.com/report/search/theme/ibuprofen>).

Supercritical fluid techniques are also important, which have drawn great attention in the literature as well as the pharmaceutical industry in the early 2000s.^{38,39} SC (supercritical)-CO₂ is commonly used as a supercritical fluid. Above its supercritical point, CO₂ can serve as a solvent with low density, and this unique property was developed to increase nanoparticle production from a lab scale to pilot scale. One of the most popular supercritical fluid techniques is the rapid expansion of supercritical solution (RESS).⁴⁰ RESS can produce nanoparticles with diameter less than 100 nm⁴¹ and free of solvents, which is quite promising for the fabrication of nanosuspensions. The combination of a supercritical fluid with an emulsion process offers greater benefit than the use of a single technique alone. For example, Porta *et al.* produced PLGA polymers loaded with 2 different nonsteroidal anti-inflammatory drugs (NSAIDs) by using supercritical CO₂ fluid to extract drug molecules from the oily phase of an emulsion. The loading efficiency of this technique is 3 times greater compared to common emulsion techniques.⁴²

4.1 Pharmaceuticals importance of different formulation molecules

The rapid development of nanotechnology has been changing the face of the pharmaceutical industry, including the concept of new drug innovation and development as well as the designing of new techniques for drug formulation. The drug

formulation studies mainly focus on preparation of a drug which is both stable and acceptable to the patient. Generally, the tablets and capsules improve the convenience and compliance for oral delivery, and the PEGylated adjuvants prolong circulation and reduce side effects such as allergies and toxicity.^{43,44} Various nanoparticles have been extensively studied for the development of “block-buster” drugs, based on proteins, polymers, liposomes, micelles, nano-emulsions, gold nanoparticles, *etc.*. Several formulations are in the pipeline, and few of them have FDA approval.⁴⁵

4.2 Advantages of protein formulations

Proteins are naturally the first choice for developing nanoscale drug formulations because their safety, biocompatibility and ease of availability is superior. Most proteins are nanoscale macromolecules. The hydrophilic and hydrophobic sequences could be loaded with different drugs, thus serving as drug carriers. Albumin has been extensively explored because it is the most abundant protein in human serum and it is extremely stable during bioprocessing and pharmaceutical preparations compared to the other proteins.⁴⁶ Most importantly, it can accumulate in tumor tissues and inflammation sites, thus would be preferred in the design of passive targeted drug delivery systems against cancer and inflammations. Abraxane was the first protein-based nanoscale drug formulation approved by the FDA in 2005 for breast cancer treatment, which has a superior antitumor efficacy over conventional paclitaxel and cremophor formulations.⁴⁷ The global pharmaceutical sales in 2012 were 485 million USD (annual revenue in 2012), which is a real “block-buster” drug available for cancer patients. The success of Abraxane has led to other investigations into albumin-based drug formulations, such as rapamycin and docetaxel, both in phase-1 clinical trials.⁴⁸ However, not all drugs are suitable for albumin-based drug formulation. Some drugs interact with albumin and lose their activity such as camptothecin.^{49,50} These protein–drug interactions hindered the application of albumin as a general drug carrier, but still there is great potential for this strategy to develop new drug formulations for the market.

Another protein candidate called apoferritin, which is a large protein molecule with 24 subunits, a diameter around 10–12 nm and a 2 nm central cavity.⁵¹ Their cycle of assembly and disassembly can be controlled by tuning pH, which would be favorable for controlled drug loading and release. Zhen *et al.* encapsulated the anti-cancer drugs cisplatin and carboplatin into apoferritin at neutral pH and released the platinum drugs under acidic pH,⁵² with improved toxicity against cancerous cells. Kilic *et al.* developed a Dox-loaded apoferritin delivery system and found that approximately 28 Dox molecules were encapsulated within 1 apoferritin molecules and the nano-formulation was stable for at least 48 h at neutral pH.⁵¹

4.3 Importance of liposomal formulations as drug carriers

In drug formulation development liposomes are the dominating nanocarrier systems. They are easily fabricated, modified, and most importantly they can be adopted to deliver nearly

any biomolecules and drugs, such as small molecules, proteins, peptides, nucleotides, and so on. Meanwhile, the large production of liposomes is available for the pharmaceutical industry, which would definitely accelerate the transition from bench-side to bedside. However, one drawback of liposome technology is the “accelerated blood clearance” (ABC) effect.⁵³ Usually one effective method to avoid the ABC effect is PEGylated technology, which would significantly reduce the ABC effect and improve the biodistribution of liposome-formulated drugs. Another effective method is “active targeting”, that is modifying the liposomes with targeting ligands that specifically deliver the liposome to its designed destination.⁵⁴ Currently there are 21 liposome-based drug formulations which are in different developmental stages, and the FDA has approved 12 liposome-based drugs.^{5,55}

4.4 Advantages of polymer formulations

Polymers are another major direction in nanoscale drug formulation development. Either natural polymers or synthetic polymers are extensively investigated in the development of new drug formulations, and the various resources of polymers encourage scientists as well as pharmaceutical companies to design more smart polymer-based drug delivery systems. With the help of highly flexible and tunable polymers, currently there are 12 candidates in various stages of clinical trials,^{55,56} and 1 has been approved by the FDA.⁴⁵ For the formulation of polymer-based drug delivery systems, it is best to employ FDA approved biodegradable polymers such as PLA, PGA, PLGA, *etc.* There are two kinds of polymer-based formulations, one is polymer–drug composites, and the other is polymer–drug conjugates.⁵⁷ However, with the bright outlook of polymer formulations, there is a concern about quality control in the pharmaceutical production.⁵⁷ Most of the polymer-based formulations are multicomponent nanoparticles, such kinds of nanoparticles are likely to encounter technical difficulties during large-scale production, as well as the expensive instruments and materials. Unlike a fully developed large-scale liposome manufacture process which is easy to transfer and adopt, polymer based formulations tend to be more specific in large-scale production. The key to solving such problems may rely on the process of industrial standardization and the collaboration between pharmaceutical and research institutes.

4.5 Formulation of composite nanomaterials for medicinal application

Recently, the advances in material science and pioneering research have greatly broadened the scope for the development of new pharmaceutical formulations, and the emergence of “composite pharmaceutical formulations” is expected. Composite pharmaceutical formulations are combinations of more than one nanoscale drug formulation technique, which includes all of the available materials such as polymers, proteins, nucleotides (DNA, aptamers, siRNA, mRNA) and inorganic nanoparticles. The complexity for manufacturing such new formulations would definitely be beyond currently

available pharmaceutical formulation techniques; therefore, there is no FDA approval for any formulations based on this concept. For pursuing the successful development of composite pharmaceutical formulations, one useful strategy is adopting the FDA approved materials in the design, such as polymer-liposome and protein-liposome composites.⁵⁸ This strategy could significantly reduce the risk of failure and unnecessary biosafety issues. Chan *et al.* developed the core-shell nanoparticle delivery system composed of a PLGA core, soybean lectin monolayer and polyethylene glycol (PEG) shell. The anti-cancer chemotherapeutic Docetaxel was loaded in PLGA core, protected by a lectin layer, and PEG shell was assembled onto the nanoparticle surface.⁵⁹ This composite formulation greatly enhanced the therapeutic outcome of Docetaxel, which would be of benefit in clinical applications over the classical anti-cancer drugs. Another advantage of composite formulation is multifunctionality; therapy, imaging and diagnosis could be accomplished in one formulation.^{60,61} Howell *et al.* encapsulated MnO (manganese oxide) nanoparticles and doxorubicin in lipid micelles for lung cancer treatment and imaging. The designed nanoparticles could significantly accumulate within tumour tissues and indicate exact locations through MRI imaging.⁶² In cancer therapy, one rapidly developing field is silence therapy based on the lipid-based polymer system for siRNA delivery, also known as siRNA-lipoplex platform technologies.⁶³ This unique silence therapy based on properties of proprietary lipid components, which embed the siRNA molecules into lipid-bi-layer.⁶⁴ The siRNA is combined with various developed lipid moieties containing cationic lipids, co-lipids (fusogenic) and PEGylated lipids, to form nanoparticles enabling functional delivery to various cell types upon systemic delivery.⁶⁵ Interestingly, the first clinical trials of this class of therapy in age-related macular degeneration (AMD) involved injecting the RNAi drugs directly to the diseased tissue in the eye. This direct delivery ensured that the RNAi drugs reached their target intact.^{66,67} With the rapid development of composite pharmaceutical formulations, it is possible that the “smart drugs” would be accessible for the patients in the near future.

5 Nanomedicine as an emerging therapeutic approach for real solutions through different routes of administration

Conventional therapies have been used in the treatment of diseases for many years through different routes of administration. The existing treatment of severe diseases like cancer, highly pathogenic, infectious and also several other metabolic diseases are limited by general toxicity or low bioavailability of the drug or by both of these limitations. These treatments may be further improved as a new era of therapy, based on nanomedicine. As we know there are many potential advantages of using nanomedicine over conventional therapies as we described above, associating drugs with different nanocarriers or formulation systems is relevant to develop new effective and safe therapies.⁶⁸ The benefit of using such delivery systems lies in the fact that a carrier can modify *in vivo* the fate of the drug by changing the biodistribution profile of drugs and modulating

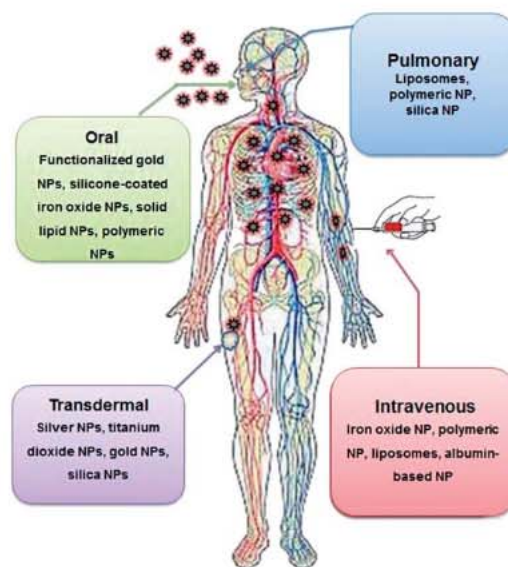


Fig. 2 Important routes of nanoparticle based drug administration.

the different control phase of therapeutic molecules to improve the delivery through different routes of administration (Fig. 2).⁶⁹ In fact, combining our new knowledge of nanomaterials with an understanding of the cellular and molecular functions can be used to change the absorption, metabolism and elimination of a drug when it is administered *via* different routes. Here, we have emphasized the role of nanomaterial formulation through different and important routes of administration to develop better and safer therapies.

5.1 Nanoparticle formulations for intravenous drug delivery

The primary purpose of intravenous (*I.V.*) medication is to initiate a rapid systemic response against the given medication. It is one of the fastest ways to deliver medication directly into a patient's blood stream. By this method, the drug is immediately available to the whole body. It is easier to control the actual amount of drug delivered to the body by using the *I.V.* method and it is easier to maintain drug level in the blood for therapeutic response (<http://www.healthline.com/galecontent/intravenous-medication-administration>).

Despite the various advantages of the *I.V.* route of administration, there still exists many problems for proper therapy:⁷⁰

- ◆ The medication to be delivered would be destroyed by digestive enzymes.
- ◆ The drug is poorly absorbed by the tissue.
- ◆ It is painful or irritating and could result in speed shock when given to a patient.
- ◆ Onset of action is quick, facilitating a greater risk of addiction and overdose when injecting illicit drugs.
- ◆ Intravenous catheters are complicated to maintain drug interaction, because of incompatibilities.
- ◆ It is the most dangerous route of administration because it bypasses most of the body's natural defences (immune system), exposing the user to health problems such as hepatitis,

abscesses, infections, and undissolved particles or additives/contaminants.

◆ Errors in compounding of medication *e.g.* chemical phlebitis (clotting/deposition).

In contrast to microparticles with a diameter of more than 1 μm that cannot be administered *via* intravascular routes of administration, nanoparticles are small enough to allow intracapillary passage followed by efficient cellular uptake.⁷¹ When nanoparticles are administered intravenously, they follow the same route as most other foreign particulates when enter into the body and are easily recognized by the body immune systems, and then will be cleared by phagocytes through circulation.⁷² Apart from the size and shape of the nanomaterials, their surface properties such as hydrophobicity determine the amount of adsorbed blood components, mainly with serum proteins (opsonins) and a process known as opsonization. This process in turn influences the *in vivo* fate of drugs and nanoparticles in reaching their target site.^{73,74} The binding of these opsonins onto the surface of nanomaterials, called opsonization, acts as a bridge between drugs, nanomaterials and phagocytes. The association of a drug to conventional carriers leads to modification of the drug distribution profile, as it is mainly delivered to mononuclear-phagocyte systems (MPS) such as the liver, spleen, lungs and bone marrow.⁷⁴ After intravenous injection, surface unmodified nanoparticles or naked drugs and non-specific delivery systems are rapidly opsonized and found mostly in the liver. They are called 'non-stealth' delivery system that are cleared by the macrophages of MPS rich organs.⁷⁵ Hence, to increase the likelihood of the drug delivery and targeting, it is necessary to understand the distance between the site of the drug administration (site of injection) and the location of the disease in the body. At the same time, it is also necessary to minimize the opsonization and to prolong the circulation of nanoparticles *in vivo*. This can be achieved by using various design approaches with the advancement of nanoformulation techniques:

◆ Loading and protecting the drug inside different nano-carrier systems.

◆ Surface coating of nanoparticles with loaded drugs with hydrophilic polymers/surfactants.

◆ Applying the difference formulation with biodegradable copolymers with hydrophilic segments such as polyethylene glycol (PEG), polyethylene oxide, polyoxamer, poloxamine and so on.

◆ Preparation of 'stealth' nanoparticles which can bypass the defense system.

◆ Engineering of nanomaterial that can bypass the capillary endothelial or escape from the blood compartment and reach to the target site.

Several studies have shown that PEG conformation at the nanoparticle surface is of utmost importance for the opsonin repelling function of the PEG layer.⁷⁶ If the surface of the PEG is brush shaped, such configurations reduce the phagocytosis and complement activation, whereas PEG surfaces in a mushroom-like configuration were potent to the complement activators and favored phagocytosis.⁷⁶⁻⁷⁸ Therefore, by applying a certain methodology, it might be possible to overcome the above

condition. Doxorubicin is a drug used to treat a wide range of cancers, but it damages the heart tissue. In 1995, an approved nanomedicine was Doxil, a doxorubicin-carrying drug that keeps the drug out of the heart. During the 1980s, researchers found that 100 nm particles cannot exit healthy blood vessels but can easily escape through the leaky tumor vasculature. Therefore, they loaded the doxorubicin into lipid bubbles about 100 nm in diameter, which can evade the immune system. Patients receiving Doxil have one-third congestive heart failure incidence of those given conventional doxorubicin. Again to improve the efficacy and decrease side effects of the drug delivery, companies such as BIND Biosciences in Cambridge, USA, use polymers to load the drug and also design how to control the drug release at the target site.⁷⁹ The leading candidate BIND-014 a 100 nm polymer sphere loaded with docetaxel, a drug that can kill the proliferative cells. The polymer center was engineered to control the drug release and has two outer layers, a PEG layer to evade immune system and binding molecules to recognize the tumor. BIND-014's phase I clinical trial results look promising after intravenous injection.⁷⁹

5.2 Nanoparticles for oral drug delivery system

Oral delivery is the most widely used, highly favorable, and readily accepted form of drug administration due to its convenience, the possibility of self-administration and improved patient compliance.⁸⁸ Significant advances in biotechnology and biochemistry have led to the discovery of a large number of bioactive molecules and vaccines based on peptides and proteins. Currently greater than 60% of marketed drugs are oral products.⁸⁹ However, because of their poor oral bioavailability,⁸⁸ most of the drugs administered *via* the oral route lose their designed dosage regimen and have limited effects. The intestinal layer of human epithelium cells is highly absorptive and is composed of villi that increase the total absorptive surface area (300–400 m^2) in the gastrointestinal (GI) tract.⁹⁰⁻⁹² The mucus layers that protect the epithelial surfaces have been highlighted as significant barriers for drug and nanoparticle delivery. In some instances, over 90% of the administered drug is lost due to epithelial barriers of the GI tract and their susceptibility to intestinal degradation by digestive enzymes.^{91,93} However, despite having several advantages, oral drugs face several problems, particularly for peptides and proteins, and some other bimolecular drugs delivery.⁹³

◆ Dose dumping, poor stability in the gastrointestinal tract, mucus layer and epithelial lining itself.

◆ Low solubility and/or bioavailability.

◆ The mucus barrier can prevent drug penetration and decrease the subsequent absorption rate of the drug.

◆ Proteolytic enzymes in the gut lumen like pepsin, trypsin and chymotrypsin, presence at the brush border the membrane.

◆ Bacterial gut flora.

All of the above factors reduce the potential for accurate dose adjustment of the final therapy. However, to overcome these limitations and barriers, the stability of nanocarriers offers a greater possibility of the drug to be successfully delivered through oral administration. The fate of the nanoparticles in the

Table 2 Design of nanocarrier with adhesive molecules to improve oral administration

Mucoadhesive nanoparticle System	Nanoparticles/component	Advantages	Ref.
Mucoadhesive polymeric systems	Poly(lactic acid) (PLA), poly(sebacic acid) (PSA), poly(lactic-co-glycolic acid) (PLGA) and poly(acrylic acid) (PAA)	Improved bioavailability of particles, prolonged retention in the gut, improved blood glucose regulation	Suk <i>et al.</i> (2011) ⁸⁰
Targeted mucoadhesive nanoparticle systems	Lectins, invasins, vitamin B12-derivatives, wheat germ agglutinin (WGA), bacterial enzymes and surface invasin protein (<i>e.g.</i> <i>Salmonella</i> and <i>Shigella</i>)	Particle uptake, increased binding efficiency, decreased rate of elimination, penetration of mucus barrier	Hussain <i>et al.</i> (1998) ⁸¹ Salman <i>et al.</i> (2005) ⁸²
Mucoadhesive pH-responsive systems	Acrylic-based polymers (methacrylic acid) (PMAA), polyethylacrylate (PMAA-PEA) and polymethacrylate (PMAA-PMA)	Retention of a collapsed state in the low pH of the stomach, penetration of the gastrointestinal (GI) tract, frequently localized drug molecules	Dai <i>et al.</i> (2000), ⁸³ Ganta <i>et al.</i> (2008) ⁸⁴
Mucoadhesive lipid-based systems	Liposomes, mixed micelles, micro and nanoemulsions, and solid lipid nanoparticles	Increased solubility and bioavailability of the encapsulated drugs	Fricker <i>et al.</i> (2010) ¹⁰³
Mucus penetrating systems	Component	Advantages	Ref.
Disrupting the mucus barrier	<i>N</i> -Acetyl-L-cysteine (NAC), a commonly used mucolytic, and some viscous molecules	Enhanced nanoparticle-based drug delivery, disruption of the barrier properties of the mucus lining	Carlstedt <i>et al.</i> (1998) ⁸⁵
Particles that penetrate the mucus barrier	Virus particles, bacterial lysine, bacterial grown hydrophobic surface	Increased diffusion rate, penetration of the mucosal layer	Stuart <i>et al.</i> (2001), ⁸⁶ Paerregaard <i>et al.</i> (1991) ⁸⁷

gastrointestinal tract has been investigated in number of studies, in general the uptake of nanoparticles occurs as follows:⁹⁴

- ◆ Transecytosis of the drug *via* microfold cells (M-cells, a specific cell type in the intestinal epithelium).

- ◆ Intracellular uptake and transport *via* the epithelial cells lining the intestinal mucosa.

- ◆ Uptake *via* Peyer's patches.

Polymeric nanoparticle based formulation methods are being developed⁹⁵ that encapsulate and protect (against enzymatic and hydrolytic degradation) drugs from damage and release them in a temporally or spatially controlled manner at the site of the disease.^{93,96–99} The surface of the nanoparticles can also be modified to enhance or reduce the bio-adhesion properties so the specific target cells should be recognized efficiently.⁹³ There are several new approaches and techniques (Table 2), based upon the unique properties of nanoscale materials and the basic properties of the mucus layer, which have significantly improved the efficacy of pharmaceuticals products after oral administration.^{100–104} Recently, it has been observed that insulin-loaded nanoparticles have preserved insulin activity and produced blood glucose reduction in diabetic rats for up to 14 days following oral administration.¹⁰⁵ Even after oral administration, drug loaded NPs still face several difficulties due to the presence of M-cells that have a tight junction of epithelial cells, which prevent the entry of foreign materials. Therefore targeting this region is necessary to cross the mucosal barrier for the efficient delivery of oral drugs.

5.2.1 Targeting of nanoparticles to epithelial cells in the gastrointestinal (GI) tract using ligands. To enhance the target specificity, it is necessary for the nanoparticles to interact with the enterocytes and M-cells of Payer's patches in the GI tract, because a large number of cell-specific carbohydrates is expressed on their cell surface, which serves as a binding site for the colloidal drug carrier containing specific ligands.¹⁰⁶ Certain glycoproteins and lectins have the necessary properties to bind specifically on their cell receptor surface.¹⁰⁷ In order to enhance oral peptide and vitamin B-12 absorption from the gut, different lectins (bean and tomato lectin) have been used.¹⁰⁸ This study was carried out under physiological conditions *via* receptor-mediated endocytosis. For further studies, they also used various peptides (*e.g.* granulocyte colony stimulating factor, erythropoietin). The mucus membrane in the stomach secretes mucoprotein, which can bind specifically with the cobalamin.¹⁰⁶ The mucoprotein reaches the ileum intact where transportation is facilitated by specific receptors.

5.2.2 Enhancing absorption using non-specific interactions in the gastrointestinal tract. In another approach, the absorption of macromolecules and certain materials in the gastrointestinal tract follows either a paracellular or endocytotic pathway. Nanoparticle absorption through the paracellular route utilizes 1% of the mucosal surface area. Macromolecules introduced *via* paracellular permeability can be increased by using polymeric materials such as chitosan, starch, or

poly(acrylate).^{109,110} The absorption of nanoparticles *via* the endocytotic pathway is either by receptor-mediated endocytosis (*i.e.* active targeting) or by adsorptive endocytosis, where the ligands do not take part. This process is initiated by electrostatic forces (such as hydrogen bonding or hydrophobic interactions) between the nanomaterial and the cell surface.¹¹¹ During the adsorptive endocytosis pathway, the size and surface properties of the material are important.¹¹² If the nanoparticles are positive or uncharged, they have a greater affinity towards the adsorptive enterocytes. If the NPs are hydrophilic in nature and negatively charged, they have a higher affinity towards the adsorptive enterocytes and M-cells.¹¹³

5.3 Transdermal drug delivery (TDD) system using nanotechnology

Transdermal drug delivery system is the most promising route of drug administration and offers many advantages over oral, intravenous and others routes of administration. The skin of the human body is one of the most physical barriers for the drug delivery. The outermost layer of the skin is called the *stratum corneum* (SC), the viable epidermis is seen underneath the *stratum corneum* and deeper is dermis, which is 1–2 mm thick, and contains rich capillary blood vessels for systemic absorption of drugs just below the dermal–epidermal junction. The function of the *stratum corneum* is to protect the underlying tissues from infection, dehydration, chemicals and mechanical stress.¹¹⁴ Therefore, several approaches have been made to defeat this barrier and enhance the *stratum corneum* permeability. Such strategies include physical, biochemical, and chemical methods.¹¹⁵ Over the past decades, developing controlled drug delivery has become increasingly important in the pharmaceutical industry.

In the present approaches, different techniques have been developed to enhance transdermal delivery. Such techniques are physical enhancers (non-cavitation ultrasound, cavitation ultrasound, microdermabrasion, thermal ablation,⁵⁸ iontophoresis, electroporation, magnetophoresis, microneedle), nano-scale-vesicle nanoparticulates (liposome, niosome, transfersome,

microemulsion, solid lipid nanoparticle) dendrimer systems and chemical enhancers (sulphoxides, azones, glycols, alkanols, terpenes *etc.*) to penetrate the skin frequently and transport the drug through this barrier.¹¹⁶ Recently different types of nano-carriers (Fig. 3) have been used to design an important delivery system for topical transdermal drug delivery and also various nanoformulation drugs have been investigated in the pharmaceutical field (Table 3).

Recently various works in the literature have demonstrated the enhancement of drug penetration across the skin. Basically, two favored trends have been developed with nanoparticle delivery systems. First, the high drug loading capacity of the vehicle due to the small size nanoparticle system can reduce the interfacial tension and ensure excellent surface contact between the skin and vehicle over the entire application area. Secondly, the fluctuating structure of nanoemulsions or microemulsions (NE/ME), with ultralow interfacial tension and high oil and water content, makes it possible for both lipophilic and hydrophilic drugs from the relatively hydrophilic vehicle to penetrate the lipophilic *stratum corneum* and move towards the targeted site (Fig. 4).¹¹⁷

Kreilgaard *et al.* developed a nanoparticle based emulsion system, which is loaded with lipophilic (lidocaine) and hydrophilic (prilocaine hydrochloride) drug molecules and compared its flux to conventional methods. They found that the transdermal flux of lidocaine and prilocaine hydrochloride was increased up to 4 and 10 times, respectively, as compared to conventional method of drug formulation. This drastic enhancement was achieved due to concentration gradients created by high solubilization of the drugs and the increased thermodynamic activity of drug.^{117,118} However, researchers also demonstrated the possibility of an enhancement effect of different individual constituents, such as oil, surfactants and different nanosized particulates and nanocarrier based delivery systems (Table 3), to bypass the barrier of skin. The carriers then preclude excessive local drug clearance through the peripheral blood plexus for a better therapeutic effect.¹¹⁹

5.4 Nanotechnology for pulmonary drug delivery

There are several lung diseases which serve as prime candidates for inhalation therapy, such as asthma, emphysema, chronic obstructive pulmonary disease (COPD), cystic fibrosis, primary pulmonary hypertension, lung cancer, pneumonia, and some of the new born respiratory diseases.¹²⁰ Since the drug avoids first-pass metabolism and is deposited at the disease site, it is advantageous in treating such diseases locally.

There are two major primary modes of pulmonary aerosol administration: nasal and oral inhalation.¹²¹ In respiratory system, the inhaled material deposits in different parts of lung regions mainly depending on the size and diameter of the particles and the overall inhalation process (Fig. 5). Discrimination between the deposition sites is realized by three different mechanisms: Brownian motion, sedimentation and impaction. According to Brownian motion, particles of a size smaller than 1 μm will deposit mainly in alveolar regions of the lung. Particles of size 1–5 μm are able to enter and sediment within

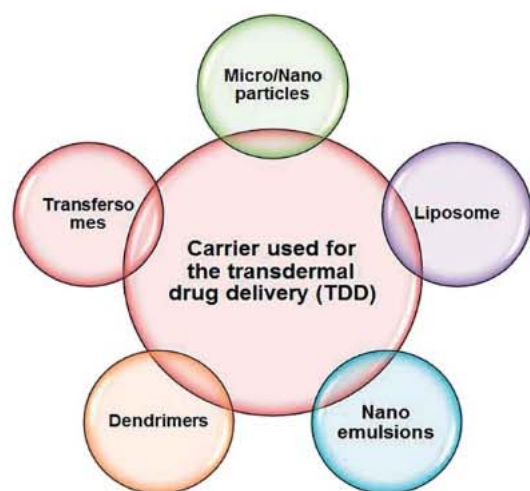


Fig. 3 Nanoformulations used as transdermal drug delivery systems.

Table 3 Examples of nanomedicine products on the market or under clinical trials with different routes of administration

Route of administration	Product or drug	Formulation	Therapeutic use	Status	Company or references
Oral drug delivery	Gastromark (ferumoxsil)	Silicon-coated iron oxide NPs	GI imaging	Marketed	AMAG Pharmaceuticals
	Rapamune (sirolimus)	Nanocrystal particles	Immunosuppressive	Marketed	Pfizer/Wyeth
	Emend (aprepitant)	Nanocrystal particles	Antiemetic	Marketed	Merck
	Tricor (fenofibrate)	Nanocrystal particles	Hypercholesterolemia	Marketed	Abbott
	Megace ES (megestrol)	Nanocrystal particles	Antianorectic	Marketed	Par Pharmaceuticals
	Triglide (fenofibrate)	Nanocrystal particles	Hypercholesterolemia	Marketed	ScielePharma
	Renagel (sevelamer)	Phosphate binding polymer	End stage renal failure	Marketed	Genzyme (Daiichi licensed)
	Welchol	Cholesterol binding polymer	Type 2 diabetes	Marketed	Genzyme
	AMG223	Phosphate binding polymer	Hyperphosphatemia in CKD patients on hemodialysis	Phase II	Amgen
	NKTR-118	PEG-naloxone	Opioid-induced constipation	Phase II	Nektar
Pulmonary drug delivery	SLIT cisplatin	Liposomes	Cancer—lung	phase II	Transave
	Budesonide	Nanoemulsion	Asthma	Reported	Jacobs <i>et al.</i> (2002) ¹³⁰
	Fluticasone	NPs	Asthma	Reported	Shekunov <i>et al.</i> (2005) ¹³¹
	Tobramycin	NPs	Infections	Reported	Joshi <i>et al.</i> (2003) ¹³²
	Insulin	Liposomes	Diabetes	Reported	Carpenter <i>et al.</i> (2005) ¹³³
	Leuprolide	Liposomes	Lung cancer	Reported	Khanna <i>et al.</i> (1997) ¹³⁴
	Low molecular weight heparin	Dendrimer	Thrombosis	Reported	Zhang <i>et al.</i> (2001) ¹³⁵
Transdermal drug delivery	Lignocaine	Liposomes	Local anesthetic	Reported	Sharma <i>et al.</i> (1994) ¹³⁶
	Methotrexate	pH-sensitive liposomes	Cancer	Reported	Dubey <i>et al.</i> (2007) ¹³⁷
	Indomethacin	Dendrimer	Anti-inflammatory	Reported	Chauhan <i>et al.</i> (2003) ¹³⁸
	5-Fluorouracil	Dendrimer	Cancer	Reported	Venuganti <i>et al.</i> (2008) ¹³⁹
	Insulin	NPs	Diabetes	Reported	Huang <i>et al.</i> (2009) ¹⁴⁰
	Celecoxib	NPs	Anti-inflammatory	Reported	Joshi <i>et al.</i> (2008) ¹⁴¹
	Triptolide	NPs	Anti-inflammatory, anticancer	Reported	Mei <i>et al.</i> (2003) ¹⁴²
Ocular drug delivery	GCV	Albumin NPs	Cytomegalovirus retinitis	Reported	Irache <i>et al.</i> (2005) ¹⁴³
	Oligonucleotides	Liposomes	Cancer	Reported	Bohot <i>et al.</i> (1998) ¹⁴⁴
	Pilocarpine HCl	Liposomes	Miotic	Reported	Sahoo <i>et al.</i> , (2008) ¹⁴⁵
	Timolol maleate	Diocomes	Glaucoma	Reported	Vyas <i>et al.</i> (1998) ¹⁴⁶
	Cyclopentolate	Niosomes	Mydriatic	Reported	Saettone <i>et al.</i> (1996) ¹⁴⁷
	Acetazolamide	Liposomes	Diuretic	Reported	El-Gazayerly <i>et al.</i> (1997) ¹⁴⁸
	Insulin	Liposomes	Diabetes	Reported	Sahoo <i>et al.</i> (2008) ¹⁴⁵

the trachea-bronchial region whereas, the particles larger than 5 mm will mainly be deposited in the pharyngeal airways due to impaction (blockage of the digestive tract).

Interestingly, ultrafine particles of 0.005–0.2 mm are efficiently deposited deep in the lungs, whereas most of the particles 0.2–1.0 mm in size are exhaled again. As mentioned before, the inhalation process (Fig. 6) or incorrectly entering the pulmonary path unsurprisingly results in reducing the therapeutic effects of the drug. However, most inhaled drugs are intended to reach the alveolar region, since the very thin epithelium (0.1–0.5 mm) and the huge alveolar surface (100–140 m²) offer superior conditions for drug absorption.¹²²

The advancement of nanotechnology has reignited interest in the treatment of lung disease because the lungs act as a major route of drug delivery for both systemic and local treatments. The large surface area of the lungs and the minimal

barriers impeding access to the lung periphery make this organ a suitable portal for a variety of therapeutic interventions.¹²² Nanotechnology has provided new formulation options for both dispersed liquid droplet dosage forms (such as metered dose inhalers and nebulizers) and dry powder formulations.^{123,124} There are various advantages in using nanocarrier systems in pulmonary⁴¹ drug delivery which are beneficial to the patient such as:

- ◆ The potential to achieve a relatively uniform distribution of drug dose among the alveoli.
- ◆ Enhanced solubility of the drug compared to its own aqueous solubility.
- ◆ The sustained-release of a drug which consequently reduces the dosing frequency.
- ◆ Suitability for delivery of macromolecules.
- ◆ Decreased incidence of side effects.

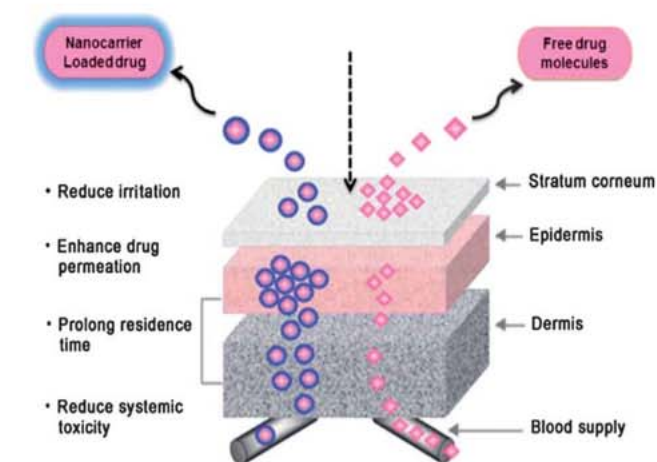


Fig. 4 Systemic delivery of free drugs and nanocarrier systems through the barriers of transdermal drug delivery.

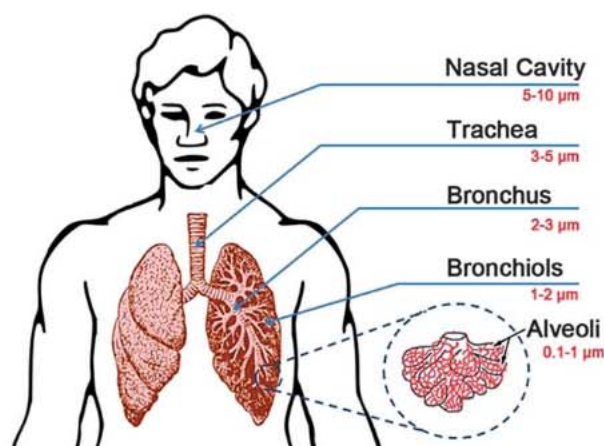


Fig. 5 The image represents the regional deposition of particles within the lungs, depending on the particle size and the overall inhalation process.

- ◆ Improved patient compliance.
- ◆ The potential for drug internalization by cells.

Recently, various drugs, pure molecules, proteins and peptides,^{83–86} polymeric nanoparticles, polyelectrolyte complexes, and drug-loaded liposomes have shown encouraging results for the delivery of drugs in the case of lung diseases.^{125–127} Several methods are also being developed to produce nanoparticles with properties suitable for improving access to the peripheral lung. Traditional techniques such as grinding, spray drying and with the help of more recent advances in supercritical fluid extraction procedure, precipitation, and solvent extraction methods have also been employed to produce more efficient nanoparticle formulations for the treatment of pulmonary diseases.^{128,129}

Today, researchers have put forth a great effort for the development of precise pulmonary drug delivery technology through combination with nanotechnology both in terms of inhaler design and using advanced methodologies. Particle engineering for improving the diagnosis and therapy for heart,

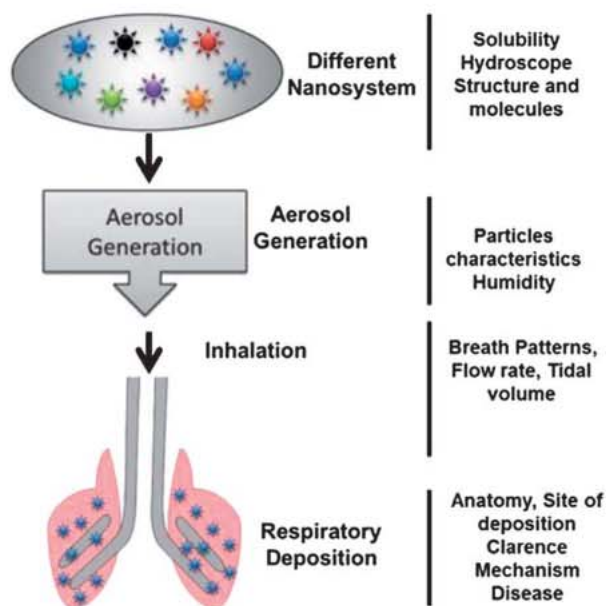


Fig. 6 Different factors influence on the pulmonary delivery of drug and nanoparticle systems.

lung and blood diseases, and drug delivery represents an area of particular promise.¹⁴⁹ Nanotechnology may provide novel treatments for a broad range of intractable pulmonary diseases, including bacterial biofilms, fungal infections, and tuberculosis and more promising targets for nanotechnology-based treatment for heart, lung and blood diseases through a pulmonary route of administration.^{149,150}

5.5 Nanotechnology in ocular drug delivery

The eyes are the most readily accessible organs in our body. Drug delivery to eye tissues is particularly problematic and highly risky. The poor bioavailability of drugs from ocular dosage forms is mainly due to pre-corneal loss factors (*e.g.*, tear dynamics, nonproductive absorption, transient residence time in the culdesac, and relative impermeability of the corneal epithelial membrane).¹⁵¹ Delivery of drugs to ocular region *via* nanotechnology based products satisfies three main objectives.¹⁵²

- ◆ Enhancement of drug permeation.
- ◆ Controlled release of the drug.
- ◆ Targeting the drug to the diseased site.

The nanotechnological formulations include micro/nanoparticles, nanoemulsions, nanosuspensions, niosomes^{145,153} liposomes, cyclodextrins¹³⁶ polymer scaffolds, solid lipid nanoparticles, light-sensitive nanocarrier systems, dendrimers *etc.* Treatment of posterior eye segment diseases, such as proliferative retinopathy or macular degeneration, remains dodgy, due to the presence of the tight junctions of the blood–retinal barrier (BRB), but advanced nanotechnology systems have demonstrated successful outcomes.^{154,155}

Recently, Mahmoud *et al.* have developed an efficient nano-based delivery system to achieve sustained therapeutic effects to treat ocular disease. In this study, they prepared chitosan

nanoparticles using sulfobutylether β -cyclodextrin as a polyphonic cross linker to investigate the potential of this nanostructure for ocular drug delivery systems in albino rabbits. The result shows that approximately 50% drug release over an 8 hour period from its original amount shows zero order pharmacokinetics behavior. The *in vivo* study revealed that the prepared mucoadhesive nanoparticles have a better ability to sustain antifungal effects.¹⁵⁶

In another work, Chaiyasan *et al.* developed self-assembled oppositely charged polymers, cationic chitosan (CS) and anionic dextran sulfate (DS), nanoparticles for drug delivery to the ocular surface. In this study, the mucoadhesive properties of the chitosan–dextran sulfate nanoparticles (CDNs) was evaluated by imaging the retention of the fluorescein isothiocyanate-labeled CDNs on the cornea. The *ex vivo* experiment indicated that cationic, biocompatible mucoadhesive CDNs, loaded with a drug such as Rhodamine B (RhB) or Nile Red (NR), are able to release the drug analog at the ocular surface. The nanoparticles were stable to lysozymes and showed prolonged adherence to the corneal surface.¹⁵⁷ Several other groups have also developed dendrimer based nanocarrier systems for the treatment of ocular disease.¹⁵⁸

To incorporate anti-inflammatory drugs for ophthalmic applications, several nanoparticle based drug carriers are available in the market and some of them are in clinical trials (Table 3).

6 The environmental, health and safety issues related to nanoparticles

Several decades have passed, and the implementation of nanomedicine concepts in broad clinical application still remains puzzling due to the limited knowledge about safety and toxicity. Although one inherent property of NP based drug delivery formulations is decreased adverse side effects and reduced toxicity, NPs themselves may account for the adverse biological response.^{159,160} As more and more nanomaterials are used as drug delivery vehicles, we should first make sure they are safe to utilize as a drug delivery carriers for human medical application, and also pay more attention to the potential safety hazards and toxicity issues.

Because of their nanoscale size, NPs which are left in the environment after synthesis can be easily transported into the human body by inhalation and have some unknown influences upon health. Ultrafine particles in the air are considered as the main cause of respiratory disease, and the NPs may be harmful when directly exposed to human beings. One report says that, workers who are exposed to polystyrene fumes and polyacrylate NPs for several months are expected to be affected by certain diseases like pulmonary fibrosis, pleural effusions and granuloma formation.¹⁶¹ Sometimes the above behavior has also been observed when NPs are used in clinical situations. It may also cause some undesirable effects in human by the interaction with various components inside the body, like platelet aggregation or cardiovascular effects. In the United States of America (USA), some organizations have made efforts to establish some standard programs for the determination of health and

environmental hazards caused by nanomaterials.¹⁶² The following are key reasons for toxicity of nanomaterials in human health applications.

Physicochemical properties (size, shape and surface charge)

NPs of <100 nm present ideal properties for drug delivery, which in turn to cause undesirable effects like crossing the blood–brain barrier, triggering immune reactions and damaging the membrane structure of human cells or organelles. The surface charge on the nanoparticles can cause organ accumulation and induce toxicity. Cationic lipids loaded with drugs, genes and siRNA used in laboratory research are not safe to be used in the clinic because of their dose dependent toxicity, pulmonary inflammation and potential hemolysis effects.¹⁶³

High surface area to volume ratio

Due to their high surface area to volume ratio, nanoparticles can efficiently interact with biological systems, which leads to potential toxicity.¹⁶⁴

Agglomeration and dispensability

Nanoparticles tend to agglomerate, due to their high surface to volume ratio. If agglomeration happens in the human body after drug administration, it will cause vascular or lymphatic blockage.¹⁶⁵

Biodegradation and biocompatibility

In drug delivery system, if the nanocarriers are not degraded quickly, they may accumulate in cells or tissue, and lead to a chronic inflammatory response.¹⁶⁶ Hence, excellent biodegradability must be one of the basic characteristics of NPs in drug delivery. Silver (Ag) NPs were reported to be toxic, due to the presence of residual CTAB from synthesis process.¹⁶⁶ Chang *et al.* have reported silica NPs to be toxic at high concentration, because of the observation of cell viability reduction.¹⁶⁷ Nanomaterials with poor biocompatibility would cause serious cell death and immunological effects.

Immunotoxicity

As we know, the immune system protects the body from possible harmful substances by recognizing and responding to antigens. When nanoparticles enter inside the human body as foreign agents, they may trigger a defense to protect the body. If a nanomaterial with immunotoxicity is applied in clinical use, it will cause a severe immune response, and show dangerous side effects. To measure nanoparticle-related toxicity *in vitro*, a plaque forming cell assay should be done.^{168,169}

Genotoxicity

Some nanoparticles, such as gold NPs of <10 nm, can cross the cell nucleus membrane, and deliver loaded drugs or siRNA within the nucleus. At the same time, they can also cause gene mutation in the DNA helix. Assessment strategies for nanoparticle genotoxicity are limited, such as the *salmonella* reverse

mutation assay, the micronucleus test, and the alkaline comet assay.¹⁷⁰

Hemolysis and anticoagulation

Nanoparticles can cause hemolysis or coagulation phenomena when administrated by intravenous injection.¹⁶⁸ Standard hemolysis and coagulation tests exist, and allow us to study these two properties of nanoparticles used in drug delivery.^{171,172} Early safety studies of the drug delivery nanoformulation are necessary to find and avoid the potential danger to the environment and toxicity to human health. Therefore, comprehensive studies of nanodrug formulation should be necessary, such as general toxicity assay, histocompatibility, complement activation, immunotoxicology, pharmacokinetics, toxicokinetics, and metabolic fate.⁸

Clearance and distribution

As mentioned above, nanoparticle based drug delivery formulation can target an active site, which can lead to a better bio-distribution. Once the drug is released from the nanocarriers, there is no need for the nanocarriers to stay further in the human body. Therefore, it is necessary to study in detail about the mechanisms of how body clears the left over nanomaterials. The clearance rate of the nanoparticles is important to evaluate the toxicity effects.¹⁷³ Moreover, the organ distribution should be studied to predict the potential hazards to the liver, kidney, spleen and so on.^{174,175}

6.1 The toxicity of nanoparticles through different routes of administration

Nanoparticles can be used in drug delivery systems for clinical therapy, *via* various routes of administration such as oral, injection or transdermal patch. After administration, nanoparticles with varying size, shape, surface and composition can penetrate and transfer to the organs and cells by either diffusion

or active intracellular transportation, or adsorb onto the surface of macromolecules,^{116,124} which could cause unknown interactions between the nanoparticles and biological systems, which decide the negative and positive aspects of materials for real therapeutic applications. In addition to this, the distribution, including regional deposition, retention, solubility, redistribution and translocation also need our attention as they all seriously affect the body. In the process of circulation, metabolism, accumulation and excretion pathways, nanoparticles with poor solubility or degradability would accumulate within the body and persist for a long time and cause undesirable adverse effects when higher concentrations are used. However, in most cases, the toxicity of the drug formulated nanocarriers is the due above mentioned factors but this is not the only region for the actual therapy. A number of cases and physiological factors (Fig. 7) of the host body decide the exact response of materials for real therapeutic applications.

7 What can we do for the reduction and assessment of toxicity through different modes of administration?

To improve the efficacy of *in vivo* drug delivery, certain basic rules have to be followed (Fig. 8) while designing nanocarriers. All types of nanocarriers must be formulated with biocompatible materials. For targeted drug delivery, the route of administration plays a major role. Before engineering the nanoparticles, suitable material selection has to be carried out for their *in vivo* compatibility and degradability.⁶⁹ Next, scientists should think about which type of nanoparticles to synthesize, ranging from nanospheres to nanocapsules. The shape of the material greatly controls the loading and release properties of the drug. After synthesizing the material, the nanospheres occur as plain nanoparticles whereas nanocapsules appear like a vesicular structure. From the literature survey, it has been found that the shape of the nanoparticles is also an important factor, which greatly influences their fate in biological systems. Having chosen the type of the nanoparticles,

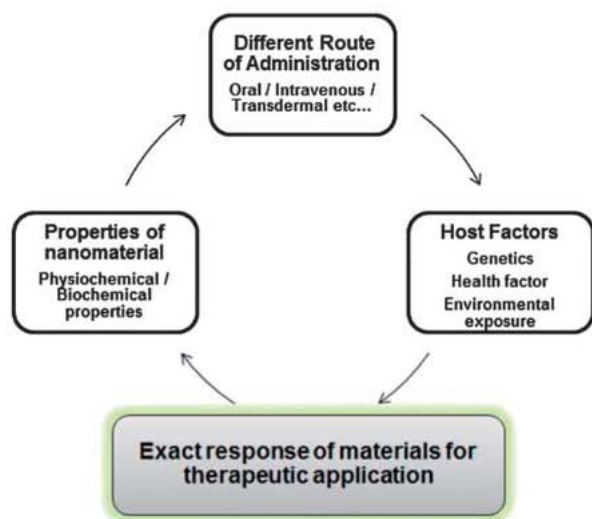


Fig. 7 A simplified depiction of potential factors that may influence the effects of engineered nanoparticles on the health system.

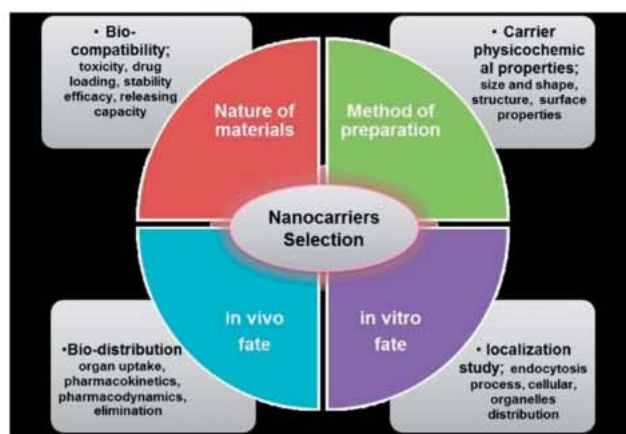


Fig. 8 Different parameters for the selection of nanocarriers for the formulation process.

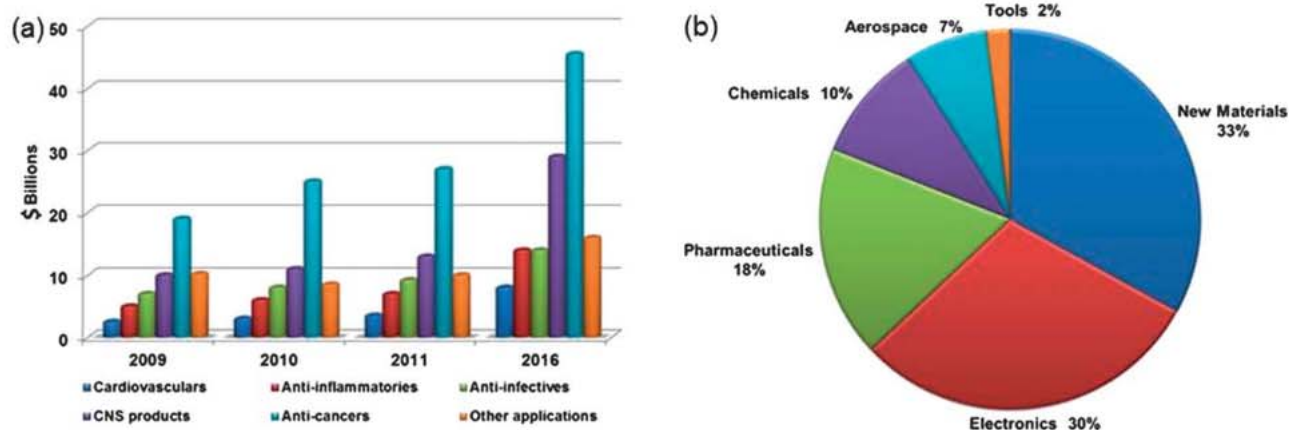


Fig. 9 (a) Nanomedical global sales by therapeutic area, 2009–2016; (source: BCC Research) (b) projected contributions in the field of nanomedicine or pharmaceutical fields for human health care, according to the US economy, 2015 (source: US Science Foundation, 2003).

the engineer has to decide which preparation process they wants to adopt, such as polymerization or some specific preparation procedure. The nature of the materials and the physicochemical properties of the drug-loading carrier directly influence their *in vivo* fate.¹⁷⁶ Due to the submicron size of the nanoparticles, surface properties are also considered as an important parameter to control the *in vivo* fate of the drug carrier.¹⁷⁷ The physicochemical properties of the nanocarrier are predicted obviously by the chemicals that are attached to their surface.

Surface chemistry also contributes to define the type of interaction with components of the surrounding medium.⁶⁹ However, the *in vivo* fate of the drug carrier is not only decided by their formulation, but the route of administration of the drug-loaded carrier is also considered. Hence, specific strategies of drug-carrier formulation have to be applied depending on the different routes of administration.

8 Nanomedicine in the market and industry

Nanotechnology has been hailed as the “next Industrial Revolution” (National Nanotechnology Initiative 2000) and promises to have substantial impacts on many areas of our lives.¹⁷⁸ As expected, pharmaceutical companies are already investing in nanotechnology (Fig. 9). Nanomedicines include nano-based contrast agents and various drug delivery formulations. Currently, drug delivery formulation makes up about 75% of the total sales of nanomedicine.³ Here we just show the details about drug delivery formulation. About 23 nanoscale drug formulations are available in the market. Of which, three polymeric products have been sold for around \$3.2 billion.³ Nanomedicine regulatory and standardisation methods have been initially built. Nowadays, the regulatory procedure of nanomedicine drug approval is similar to the conventional method. As time goes on, a new examination department may be needed for nanomedicine, with different requirements. Analysts have predicted that by 2014 the market for pharmaceutical applications of nanotechnology will be close to \$18 billion annually.¹⁷⁹ Another report indicates that the demand for medical products

incorporating nanotechnology in the United States will increase by more than 17% per year to \$53 billion in 2011 and \$110 billion in 2016.¹⁸⁰

9 Conclusion and future prospects

After over-viewing the innovative pharmaceutical developments based on the unique properties of nanoscale drug delivery formulation, we can conclude that nanomedicine will become more important and much broader in clinical diagnosis, imaging and therapeutics, detection and treatment of various diseases. Indeed, the National Institute of Health (NIH) roadmaps envisage that nanomedicine developed from nanoparticle based technology will begin to bring more medical benefits within the next 10 years. This dream includes the evolution of new nanoformulation materials like ocular implants and implanted transducers that can be used to restore lost vision and hearing, nanoscale polymer materials that mimic an artificial heart valve to treat cardiac problems and nanocomposites for bone scaffolds (Opportunities and risks of nanotechnologies, report in co-operation with the OECD International Futures Program). Furthermore, we already know that engineered nanoparticles with special structures and multifunctional nanodrug formulations for combined therapy will be the next step in the development.^{181,182} As we mentioned above, for better development of nanomedicine, the assessment of the toxicity of these drug carriers should be studied in detail through different routes of administration to avoid hazards to health and the environment issues.¹⁶⁵ In order to achieve immense success in this field of nanomedicine, scientists with diverse backgrounds must unite as one to create amazing pharmaceutical formulations from different nanomaterials for clinical trials for better human health.

Declaration of interest

The authors do not have any conflicts of interest to declare.

Acknowledgements

This work was financially supported in part by grants from the State High-Tech Development Plan (2012AA020804), National Natural Science Foundation of China project (no. 30970784, and 81171455), National Key Basic Research Program of China (MOST 973 project 2009CB930200), National Distinguished Young Scholars grant (31225009) from the National Natural Science Foundation of China and Chinese Academy of Sciences (CAS) "Hundred Talents Program" (07165111ZX) and the CAS Knowledge Innovation Program. This work was also supported in part by NIH/NIMHD 8 G12 MD007597, and USAMRMC W81XWH-10-1-0767 grants.

Notes and references

- 1 R. P. Feynman, *Engineer and Science*, 1960, **23**, 22–36.
- 2 F. Caruso, T. Hyeon and V. M. Rotello, *Chem. Soc. Rev.*, 2012, **41**, 2537–2538.
- 3 V. Wagner, A. Dullaart, A. K. Bock and A. Zweck, *Nat. Biotechnol.*, 2006, **24**, 1211–1217.
- 4 T. L. Doane and C. Burda, *Chem. Soc. Rev.*, 2012, **41**, 2885–2911.
- 5 H. I. Chang and M. K. Yeh, *Int. J. Nanomed.*, 2012, **7**, 49–60.
- 6 S. S. Chavhan, K. C. Petkar and K. K. Sawant, *Crit. Rev. Ther. Drug Carrier Syst.*, 2011, **28**, 447–488.
- 7 M. Elsalaby and K. L. Wooley, *Chem. Soc. Rev.*, 2012, **41**, 2545–2561.
- 8 R. Duncan and R. Gaspar, *Mol. Pharmaceutics*, 2011, **8**, 2101–2141.
- 9 A. D. Bangham, M. M. Standish and J. C. Watkins, *J. Mol. Biol.*, 1965, **13**, 238–252.
- 10 E. Buhleier, W. Wehner and F. Vogtle, *Synthesis*, 1978, **2**, 155–158.
- 11 A. Gabizon, H. Shmeeda and Y. Barenholz, *Clin. Pharmacokinet.*, 2003, **42**, 419–436.
- 12 N. Kamaly, Z. Xiao, P. M. Valencia, A. F. Radovic-Moreno and O. C. Farokhzad, *Chem. Soc. Rev.*, 2012, **41**, 2971–3010.
- 13 R. Gref, Y. Minamitake, M. T. Peracchia, V. Trubetskoy, V. Torchilin and R. Langer, *Science*, 1994, **263**, 1600–1603.
- 14 P. R. Ros, P. C. Freeny, S. E. Harms, S. E. Seltzer, P. L. Davis, T. W. Chan, A. E. Stillman, L. R. Muroff, V. M. Runge, M. A. Nissenbaum, *et al.*, *Radiology*, 1995, **196**, 481–488.
- 15 W. J. Gradishar, S. Tjulandin, N. Davidson, H. Shaw, N. Desai, P. Bhar, M. Hawkins and J. O'Shaughnessy, *J. Clin. Oncol.*, 2005, **23**, 7794–7803.
- 16 T. Y. Kim, D. W. Kim, J. Y. Chung, S. G. Shin, S. C. Kim, D. S. Heo, N. K. Kim and Y. J. Bang, *Clin. Cancer Res.*, 2004, **10**, 3708–3716.
- 17 M. E. Davis, *Mol. Pharmaceutics*, 2009, **6**, 659–668.
- 18 K. Bourzac, *Nature*, 2012, **491**, S58–S60.
- 19 A. Furnham and J. Lovett, *Journal of Applied Biobehavioral Research*, 2001, **6**, 39–63.
- 20 M. I. Montanez, A. J. Ruiz-Sanchez and E. Perez-Inestrosa, *Curr. Opin. Allergy Clin. Immunol.*, 2010, **10**, 297–302.
- 21 D. K. Kim and J. Dobson, *J. Mater. Chem.*, 2009, **19**, 6294–6307.
- 22 K. Riehemann, S. W. Schneider, T. A. Luger, B. Godin, M. Ferrari and H. Fuchs, *Angew. Chem., Int. Ed.*, 2009, **48**, 872–897.
- 23 J. Lisiewicz and E. R. Toke, *Nanomed.: Nanotechnol., Biol. Med.*, 2013, **9**, 28–38.
- 24 A. Kumar, B. M. Boruah and X. J. Liang, *J. Nanomater.*, 2011, **2011**, 1–17.
- 25 A. L. Armstead and B. Li, *Int. J. Nanomed.*, 2011, **6**, 3281–3293.
- 26 Y. Huang, S. He, W. Cao, K. Cai and X. J. Liang, *Nanoscale*, 2012, **4**, 6135–6149.
- 27 E. S. Shibu, M. Hamada, N. Murase and V. Biju, *J. Photochem. Photobiol., C*, 2013, **15**, 53–72.
- 28 A. Kumar, X. Zhang and X. J. Liang, *Biotechnol. Adv.*, 2013, **31**, 593–606.
- 29 B. Van Eerdenbrugh, L. Froyen, J. A. Martens, N. Bleton, P. Augustijns, M. Brewster and G. Van den Mooter, *Int. J. Pharm.*, 2007, **338**, 198–206.
- 30 B. E. Rabinow, *Nat. Rev. Drug Discovery*, 2004, **3**, 785–796.
- 31 R. H. Müller and K. Peters, *Int. J. Pharm.*, 1998, **160**, 229–237.
- 32 J. Kluge and M. Mazzotti, *Int. J. Pharm.*, 2012, **436**, 394–402.
- 33 J. Pereda, V. Ferragut, J. M. Quevedo, B. Guamis and A. J. Trujillo, *J. Agric. Food Chem.*, 2008, **56**, 7125–7130.
- 34 B. Van Eerdenbrugh, G. Van den Mooter and P. Augustijns, *Int. J. Pharm.*, 2008, **364**, 64–75.
- 35 V. R. Patel and Y. K. Agrawal, *J. Adv. Pharm. Technol. Res.*, 2011, **2**, 81–87.
- 36 V. B. Patravale, A. A. Date and R. M. Kulkarni, *J. Pharm. Pharmacol.*, 2004, **56**, 827–840.
- 37 B. Mishra, B. B. Patel and S. Tiwari, *Nanomed.: Nanotechnol., Biol. Med.*, 2010, **6**, 9–24.
- 38 P. York, *Pharm. Sci. Technol. Today*, 1999, **2**, 430–440.
- 39 J. Jung and M. Perrut, *J. Supercrit. Fluids*, 2001, **20**, 179–219.
- 40 A. C. Lima, P. Sher and J. F. Mano, *Expert Opin. Drug Delivery*, 2012, **9**, 231–248.
- 41 M. Türk, *J. Supercrit. Fluids*, 2009, **47**, 537–545.
- 42 G. Della Porta, N. Falco and E. Reverchon, *J. Pharm. Sci.*, 2010, **99**, 1484–1499.
- 43 L. S. Lee, C. Conover, C. Shi, M. Whitlow and D. Filpula, *Bioconjugate Chem.*, 1999, **10**, 973–981.
- 44 F. M. Veronese and G. Pasut, *Drug Discovery Today*, 2005, **10**, 1451–1458.
- 45 B. Y. Kim, J. T. Rutka and W. C. Chan, *N. Engl. J. Med.*, 2010, **363**, 2434–2443.
- 46 F. Kratz, *J. Controlled Release*, 2008, **132**, 171–183.
- 47 N. Desai, V. Trieu, Z. Yao, L. Louie, S. Ci, A. Yang, C. Tao, T. De, B. Beals, D. Dykes, P. Noker, R. Yao, E. Labao, M. Hawkins and P. Soon-Shiong, *Clin. Cancer Res.*, 2006, **12**, 1317–1324.
- 48 M. J. Hawkins, P. Soon-Shiong and N. Desai, *Adv. Drug Delivery Rev.*, 2008, **60**, 876–885.
- 49 T. G. Burke, C. B. Munshi, Z. Mi and Y. Jiang, *J. Pharm. Sci.*, 1995, **84**, 518–519.
- 50 T. G. Burke and Z. Mi, *J. Med. Chem.*, 1994, **37**, 40–46.
- 51 M. A. Kilic, E. Ozlu and S. Calis, *J. Biomed. Nanotechnol.*, 2012, **8**, 508–514.

- 52 Y. Zhen, X. Wang, H. Diao, J. Zhang, H. Li, H. Sun and Z. Guo, *Chem. Commun.*, 2007, 3453–3455.
- 53 M. C. Woodle, *Adv. Drug Delivery Rev.*, 1998, **32**, 139–152.
- 54 P. Sapra and T. M. Allen, *Cancer Res.*, 2002, **62**, 7190–7194.
- 55 A. Z. Wang, R. Langer and O. C. Farokhzad, *Annu. Rev. Med.*, 2012, **63**, 185–198.
- 56 L. Zhang, F. X. Gu, J. M. Chan, A. Z. Wang, R. S. Langer and O. C. Farokhzad, *Clin. Pharmacol. Ther.*, 2008, **83**, 761–769.
- 57 M. E. Davis, Z. G. Chen and D. M. Shin, *Nat. Rev. Drug Discovery*, 2008, **7**, 771–782.
- 58 M. R. Prausnitz and R. Langer, *Nat. Biotechnol.*, 2008, **26**, 1261–1268.
- 59 J. M. Chan, L. Zhang, K. P. Yuet, G. Liao, J. W. Rhee, R. Langer and O. C. Farokhzad, *Biomaterials*, 2009, **30**, 1627–1634.
- 60 S. Parveen, R. Misra and S. K. Sahoo, *Nanomed.: Nanotechnol., Biol. Med.*, 2012, **8**, 147–166.
- 61 S. S. Kelkar and T. M. Reineke, *Bioconjugate Chem.*, 2011, **22**, 1879–1903.
- 62 M. Howell, J. Mallela, C. Wang, S. Ravi, S. Dixit, U. Garapati and S. Mohapatra, *J. Controlled Release*, 2013, **167**, 210–218.
- 63 Q. Leng, M. C. Woodle, P. Y. Lu and A. J. Mixson, *Drugs Future*, 2009, **34**, 721.
- 64 C. Foged, *Curr. Top. Med. Chem.*, 2012, **12**, 97–107.
- 65 J. Wang, Z. Lu, M. G. Wientjes and J. L. Au, *AAPS J.*, 2010, **12**, 492–503.
- 66 P. K. Kaiser, R. C. Symons, S. M. Shah, E. J. Quinlan, H. Tabandeh, D. V. Do, G. Reisen, J. A. Lockridge, B. Short, R. Guercioli, Q. D. Nguyen and I. Sirna-027 Study, *Am. J. Ophthalmol.*, 2010, **150**, 33–39.e2.
- 67 J. C. Burnett, J. J. Rossi and K. Tiemann, *Biotechnol. J.*, 2011, **6**, 1130–1146.
- 68 A. J. Domb, Y. Tabata, M. N. V. Ravi Kumar and S. Farber, *Nanoparticles for Pharmaceutical Applications*, American Scientific Publishers, Stevenson Ranch, CA, 2007.
- 69 C. Vauthier, *Nanoformulation*, 2012, 3–19.
- 70 S. H. Yalkowsky, J. F. Krzyzaniak and G. H. Ward, *J. Pharm. Sci.*, 1998, **87**, 787–796.
- 71 Y. Hu, J. Xie, Y. W. Tong and C. H. Wang, *J. Controlled Release*, 2007, **118**, 7–17.
- 72 R. H. Müller and K. H. Wallis, *Int. J. Pharm.*, 1993, **89**, 25–31.
- 73 I. Brigger, C. Dubernet and P. Couvreur, *Adv. Drug Delivery Rev.*, 2002, **54**, 631–651.
- 74 I. Brigger, C. Dubernet and P. Couvreur, *Adv. Drug Delivery Rev.*, 2012, **64**, 24–36.
- 75 L. Grislain, P. Couvreur, V. Lenaerts, M. Roland, D. Deprezdecampeneere and P. Speiser, *Int. J. Pharm.*, 1983, **15**, 335–345.
- 76 N. K. Jain and M. Nahar, *Methods Mol. Biol.*, 2010, **624**, 221–234.
- 77 A. Jain and S. K. Jain, *Crit. Rev. Ther. Drug Carrier Syst.*, 2008, **25**, 403–447.
- 78 P. Chatikobo, T. Choga, C. Ncube and J. Mutambara, *Prev. Vet. Med.*, 2013, **109**, 327–333.
- 79 K. Bourzac, *Nature*, 2012, **491**, S58–S60.
- 80 J. S. Suk, S. K. Lai, N. J. Boylan, M. R. Dawson, M. P. Boyle and J. Hanes, *Nanomedicine*, 2011, **6**, 365–375.
- 81 N. Hussain and A. Florence, *Pharm. Res.*, 1998, **15**, 153–156.
- 82 H. H. Salman, C. Gamazo, M. A. Campanero and J. M. Irache, *J. Controlled Release*, 2005, **106**, 1–13.
- 83 S. Dai, K. C. Tam and R. D. Jenkins, *Eur. Polym. J.*, 2000, **36**, 2671–2677.
- 84 S. Ganta, H. Devalapally, A. Shahiwala and M. Amiji, *J. Controlled Release*, 2008, **126**, 187–204.
- 85 I. Carlstedt and J. K. Sheehan, *Ciba Foundation Symposium 109-Mucus and Mucosa*, John Wiley & Sons, Ltd., 2008, pp. 157–172.
- 86 S. S. Olmsted, J. L. Padgett, A. I. Yudin, K. J. Whaley, T. R. Moench and R. A. Cone, *Biophys. J.*, 2001, **81**, 1930–1937.
- 87 A. Paerregaard, F. Espersen, O. M. Jensen and M. Skurnik, *Infect. Immun.*, 1991, **59**, 253–260.
- 88 P. Fasinu, V. Pillay, V. M. Ndesendo, L. C. du Toit and Y. E. Choonara, *Biopharm. Drug Dispos.*, 2011, **32**, 185–209.
- 89 Y. Tanaka, Y. Masaoka, M. Kataoka, S. Sakuma and S. Yamashita, *Eur. J. Pharm. Sci.*, 2006, **29**, 240–250.
- 90 M. Schenk and C. Mueller, *Best Pract. Res. Clin. Gastroenterol.*, 2008, **22**, 391–409.
- 91 R. A. Cone, *Adv. Drug Delivery Rev.*, 2009, **61**, 75–85.
- 92 J. S. Crater and R. L. Carrier, *Macromol. Biosci.*, 2010, **10**, 1473–1483.
- 93 S. K. Lai, Y. Y. Wang and J. Hanes, *Adv. Drug Delivery Rev.*, 2009, **61**, 158–171.
- 94 V. Mohanraj and Y. Chen, *Trop. J. Pharm. Res.*, 2006, **5**, 561–573.
- 95 C. Prego, D. Torres, E. Fernandez-Megia, R. Novoa-Carballal, E. Quinoa and M. J. Alonso, *J. Controlled Release*, 2006, **111**, 299–308.
- 96 X. Q. Wang and Q. Zhang, *Eur. J. Pharm. Biopharm.*, 2012, **82**, 219–229.
- 97 D. K. Sahana, G. Mittal, V. Bhardwaj and M. N. Kumar, *J. Pharm. Sci.*, 2008, **97**, 1530–1542.
- 98 F. Cui, C. He, L. Yin, F. Qian, M. He, C. Tang and C. Yin, *Biomacromolecules*, 2007, **8**, 2845–2850.
- 99 A. S. Holpuch, G. J. Hummel, M. Tong, G. A. Seghi, P. Pei, P. Ma, R. J. Mumper and S. R. Mallery, *Pharm. Res.*, 2010, **27**, 1224–1236.
- 100 L. M. Ensign, R. Cone and J. Hanes, *Adv. Drug Delivery Rev.*, 2012, **64**, 557–570.
- 101 S. A. Shoyele and A. Slowey, *Int. J. Pharm.*, 2006, **314**, 1–8.
- 102 S. A. Shoyele, *Methods Mol. Biol.*, 2008, **437**, 149–160.
- 103 G. Fricker, T. Kromp, A. Wendel, A. Blume, J. Zirkel, H. Rebmann, C. Setzer, R. O. Quinkert, F. Martin and C. Müller-Goymann, *Pharm. Res.*, 2010, **27**, 1469–1486.
- 104 J. C. Bonner, J. W. Card and D. C. Zeldin, *Hypertension*, 2009, **53**, 751–753.
- 105 C. Damgé, C. Michel, M. Aprahamian, P. Couvreur and J. P. Devissaguet, *J. Controlled Release*, 1990, **13**, 233–239.
- 106 G. J. Russell-Jones, *Adv. Drug Delivery Rev.*, 2001, **46**, 59–73.
- 107 E. Haltner, J. H. Easson and C. M. Lehr, *Eur. J. Pharm. Biopharm.*, 1997, **44**, 3–13.
- 108 G. J. Russell-Jones, L. Arthur and H. Walker, *Int. J. Pharm.*, 1999, **179**, 247–255.

- 109 N. G. M. Schipper, K. M. Varum and P. Artursson, *Pharm. Res.*, 1996, **13**, 1686–1692.
- 110 Y. Akiyama, N. Nagahara, T. Kashihara, S. Hirai and H. Toguchi, *Pharm. Res.*, 1995, **12**, 397–405.
- 111 E. Bjork, U. Isaksson, P. Edman and P. Artursson, *J. Drug Targeting*, 1995, **2**, 501–507.
- 112 A. Albanese, P. S. Tang and W. C. Chan, *Annu. Rev. Biomed. Eng.*, 2012, **14**, 1–16.
- 113 M. Jepson, N. Simmons, T. Savidge, P. James and B. Hirst, *Cell Tissue Res.*, 1993, **271**, 399–405.
- 114 G. Cevc, *Adv. Drug Delivery Rev.*, 2004, **56**, 675–711.
- 115 P. M. Elias, M. R. Prausnitz, T. J. Franz, M. Schmuth, J.-C. Tsai, G. K. Menon, W. M. Holleran and K. R. Feingold, *Medical Therapy*, 2012, 2065–2073.
- 116 M. Aqil, M. Rizwan, S. Talegaonkar, A. Azeem, Y. Sultana and A. Ali, *Recent Pat. Drug Delivery Formulation*, 2009, **3**, 105–124.
- 117 A. K. Tiwary, B. Sapra and S. Jain, *Recent Pat. Drug Delivery Formulation*, 2007, **1**, 23–36.
- 118 M. Kreilgaard, E. J. Pedersen and J. W. Jaroszewski, *J. Controlled Release*, 2000, **69**, 421–433.
- 119 G. Cevc and U. Vierl, *J. Controlled Release*, 2010, **141**, 277–299.
- 120 M. Smola, T. Vandamme and A. Sokolowski, *Nanomedicine*, 2008, **3**, 1–19.
- 121 D. A. Groneberg, C. Witt, U. Wagner, K. F. Chung and A. Fischer, *Respir. Med.*, 2003, **97**, 382–387.
- 122 A. Henning, S. Hein, M. Schneider, M. Bur and C. M. Lehr, *Handb. Exp. Pharmacol.*, 2010, **197**, 171–192.
- 123 M. M. Bailey and C. J. Berkland, *Med. Res. Rev.*, 2009, **29**, 196–212.
- 124 H. M. Mansour, Y. S. Rhee and X. Wu, *Int. J. Nanomed.*, 2009, **4**, 299–319.
- 125 E. Rytting, J. Nguyen, X. Wang and T. Kissel, *Expert Opin. Drug Delivery*, 2008, **5**, 629–639.
- 126 I. M. El-Sherbiny and H. D. Smyth, *Int. J. Pharm.*, 2010, **395**, 132–141.
- 127 T. Takami and Y. Murakami, *Colloids Surf., B*, 2011, **87**, 433–438.
- 128 M. Odziomek, T. R. Sosnowski and L. Gradon, *Int. J. Pharm.*, 2012, **433**, 51–59.
- 129 B. K. Nanjwade, S. A. Adichwal, K. R. Gaikwad, K. A. Parikh and F. V. Manvi, *PDA J. Pharm. Sci. Technol.*, 2011, **65**, 513–534.
- 130 C. Jacobs and R. H. Muller, *Pharm. Res.*, 2002, **19**, 189–194.
- 131 B. Shekunov, *Idrugs*, 2005, **8**, 399–401.
- 132 M. Joshi and A. Misra, *Clin. Exp. Pharmacol. Physiol.*, 2003, **30**, 153–156.
- 133 M. Carpenter, M. W. Epperly, A. Agarwal, S. Nie, L. Hricisak, Y. Niu and J. S. Greenberger, *Gene Ther.*, 2005, **12**, 685–693.
- 134 C. Khanna, P. M. Anderson, D. E. Hasz, E. Katsanis, M. Neville and J. S. Klausner, *Cancer*, 1997, **79**, 1409–1421.
- 135 Q. Zhang, Z. Shen and T. Nagai, *Int. J. Pharm.*, 2001, **218**, 75–80.
- 136 B. B. Sharma, S. K. Jain and S. P. Vyas, *J. Microencapsulation*, 1994, **11**, 279–286.
- 137 V. Dubey, D. Mishra, T. Dutta, M. Nahar, D. K. Saraf and N. K. Jain, *J. Controlled Release*, 2007, **123**, 148–154.
- 138 A. S. Chauhan, S. Sridevi, K. B. Chalasani, A. K. Jain, S. K. Jain, N. K. Jain and P. V. Diwan, *J. Controlled Release*, 2003, **90**, 335–343.
- 139 V. V. Venuganti and O. P. Perumal, *Int. J. Pharm.*, 2008, **361**, 230–238.
- 140 X. Huang, Y. Z. Du, H. Yuan and F. Q. Hu, *Carbohydr. Polym.*, 2009, **76**, 368–373.
- 141 M. Joshi and V. Patravale, *Int. J. Pharm.*, 2008, **346**, 124–132.
- 142 Z. Mei, H. Chen, T. Weng, Y. Yang and X. Yang, *Eur. J. Pharm. Biopharm.*, 2003, **56**, 189–196.
- 143 J. M. Irache, M. Merodio, A. Arnedo, M. A. Camapanero, M. Mirshahi and S. Espuelas, *Mini-Rev. Med. Chem.*, 2005, **5**, 293–305.
- 144 A. Bochot, E. Fattal, A. Gulik, G. Couarraze and P. Couvreur, *Pharm. Res.*, 1998, **15**, 1364–1369.
- 145 S. K. Sahoo, F. Diinawaz and S. Krishnakumar, *Drug Discovery Today*, 2008, **13**, 144–151.
- 146 S. P. Vyas, N. Mysore, V. Jaitely and N. Venkatesan, *Pharmazie*, 1998, **53**, 466–469.
- 147 M. F. Saettone, G. Perini, M. Carafa, E. Santucci and F. Alhaique, *STP Pharma Sci.*, 1996, **6**, 94–98.
- 148 O. N. El-Gazayerly and A. H. Hikal, *Int. J. Pharm.*, 1997, **158**, 121–127.
- 149 J. W. Card, D. C. Zeldin, J. C. Bonner and E. R. Nestmann, *Am. J. Physiol.: Lung Cell. Mol. Phys.*, 2008, **295**, L400–L411.
- 150 D. Buxton, *Expert Opin. Drug Delivery*, 2006, **3**, 173–175.
- 151 A. Fernandez-Martinez, P. Mula, P. Cravo, P. Charle, A. Amor, P. Ncogo, A. Benito and P. Berzosa, *Am. J. Trop. Med. Hyg.*, 2013, **88**, 43–47.
- 152 F. Lallemand, P. Daull, S. Benita, R. Buggage and J. S. Garrigue, *J. Drug Delivery*, 2012, **2012**, 604204.
- 153 S. Wang, D. Li, Y. Ito, T. Nabekura, S. Wang, J. Zhang and C. Wu, *Curr. Eye Res.*, 2004, **29**, 51–58.
- 154 Y. Sultana, D. P. Maurya, Z. Iqbal and M. Aqil, *Drugs Today*, 2011, **47**, 441–455.
- 155 R. Gaudana, J. Jwala, S. H. Boddu and A. K. Mitra, *Pharm. Res.*, 2009, **26**, 1197–1216.
- 156 A. A. Mahmoud, G. S. El-Feky, R. Kamel and G. E. Awad, *Int. J. Pharm.*, 2011, **413**, 229–236.
- 157 W. Chaiyasan, S. P. Srinivas and W. Tiyaboonchai, *J. Ocul. Pharmacol. Ther.*, 2013, **29**, 200–207.
- 158 S. P. Kambhampati and R. M. Kannan, *J. Ocul. Pharmacol. Ther.*, 2013, **29**, 151–165.
- 159 B. Fadeel and A. E. Garcia-Bennett, *Adv. Drug Delivery Rev.*, 2010, **62**, 362–374.
- 160 A. Kunzmann, B. Andersson, T. Thurnherr, H. Krug, A. Scheynius and B. Fadeel, *Biochim. Biophys. Acta, Gen. Subj.*, 2011, **1810**, 361–373.
- 161 Y. Song, X. Li and X. Du, *Eur. Respir. J.*, 2009, **34**, 559–567.
- 162 M. R. Wiesner, G. V. Lowry, K. L. Jones, M. F. Hochella Jr, R. T. Di Giulio, E. Casman and E. S. Bernhardt, *Environ. Sci. Technol.*, 2009, **43**, 6458–6462.
- 163 N. E. Palmateer, V. D. Hope, K. Roy, A. Marongiu, J. M. White, K. A. Grant, C. N. Ramsay, D. J. Goldberg and F. Ncube, *Emerging Infect. Dis.*, 2013, **19**, 29–34.

- 164 A. Sharma, S. V. Madhunapantula and G. P. Robertson, *Expert Opin. Drug Metab. Toxicol.*, 2012, **8**, 47–69.
- 165 G. Oberdorster, *J. Intern. Med.*, 2010, **267**, 89–105.
- 166 W. H. D. Jong and P. J. Borm, *Int. J. Nanomed.*, 2008, **3**, 133–149.
- 167 J.-S. Chang, K. L. B. Chang, D.-F. Hwang and Z.-L. Kong, *Environ. Sci. Technol.*, 2007, **41**, 2064–2068.
- 168 J. B. Hall, M. A. Dobrovolskaia, A. K. Patri and S. E. McNeil, *Nanomedicine*, 2007, **2**, 789–803.
- 169 X. J. Liang, A. Kumar, D. L. Shi and D. X. Cui, *J. Nanomater.*, 2012, **2012**, 127–129.
- 170 R. Landsiedel, M. D. Kapp, M. Schulz, K. Wiench and F. Oesch, *Mutat. Res., Rev. Mutat. Res.*, 2009, **681**, 241–258.
- 171 Y.-S. Lin and C. L. Haynes, *J. Am. Chem. Soc.*, 2009, **132**, 4834–4842.
- 172 T. Yu, A. Malugin and H. Ghandehari, *ACS Nano*, 2011, **5**, 5717–5728.
- 173 A. Dhawan and V. Sharma, *Anal. Bioanal. Chem.*, 2010, **398**, 589–605.
- 174 K. R. Vega-Villa, J. K. Takemoto, J. A. Yanez, C. M. Remsberg, M. L. Forrest and N. M. Davies, *Adv. Drug Delivery Rev.*, 2008, **60**, 929–938.
- 175 M. L. Schipper, N. Nakayama-Ratchford, C. R. Davis, N. W. Kam, P. Chu, Z. Liu, X. Sun, H. Dai and S. S. Gambhir, *Nat. Nanotechnol.*, 2008, **3**, 216–221.
- 176 J. A. Champion and S. Mitragotri, *Proc. Natl. Acad. Sci. U. S. A.*, 2006, **103**, 4930–4934.
- 177 K. Xiao, Y. Li, J. Luo, J. S. Lee, W. Xiao, A. M. Gonik, R. G. Agarwal and K. S. Lam, *Biomaterials*, 2011, **32**, 3435–3446.
- 178 S. Johnson, *Am. J. Bioeth.*, 2009, **9**, 1–2.
- 179 F. Allhoff, *Am. J. Bioeth.*, 2009, **9**, 3–11.
- 180 R. Bawa and S. Johnson, *Med. Clin. North Am.*, 2007, **91**, 881–887.
- 181 J. Gao, H. Gu and B. Xu, *Acc. Chem. Res.*, 2009, **42**, 1097–1107.
- 182 N. Nasongkla, E. Bey, J. Ren, H. Ai, C. Khemtong, J. S. Guthi, S. F. Chin, A. D. Sherry, D. A. Boothman and J. Gao, *Nano Lett.*, 2006, **6**, 2427–2430.